A STUDY OF EVOLUTION OF COSMOLOGICAL PARAMETERS BASED ON A DARK ENERGY MODEL IN THE FRAMEWORK OF BRANS-DICKE GRAVITY[†]

Sudipto Roy[a,*], Rivu Kayal[b,†], Simran Ali[b,§], Srinjoyee Bandyopadhyay[b,#], Debamita Bhattacharya[b,‡]

[a]Department of Physics, St. Xavier's College, Kolkata, West Bengal, India
[b]St. Xavier's College, M.Sc. Student (2021-2023), Subject: Physics, Kolkata, India
*Corresponding Author e-mail: roy.sudipto@sxccal.edu
[†]e-mail: rivukayaljoy50@gmail.com; [§]e-mail: simran.reads@gmail.com, [#]e-mail: srinjoyee.banerjee@gmail.com
[‡]e-mail: debamitabhattacharya99@gmail.com

The objective of the present study is to find the characteristics of evolution of a homogeneous and isotropic universe in the framework of Brans-Dicke (BD) theory of gravity. FLRW space-time, with zero spatial curvature, has been used to obtain BD field equations. Scale factor and Hubble parameter have been obtained from an ansatz for the deceleration parameter, assumed on the basis of its property of signature flip indicating a change of phase from deceleration to acceleration. Validation of the model has been achieved by a suitable parametrization of that ansatz. Expressions for energy density, pressure, equation of state (EoS) parameter, cosmological constant, gravitational constant have been derived and depicted graphically. The gravitational constant is found to decrease with time at a gradually decreasing rate. The Hubble parameter, deceleration parameter and energy density decrease with time, which is in agreement with many other studies. The value of the EoS parameter at the present epoch is negative, and it becomes more negative with time. The cosmological constant increases very rapidly in the early universe from negative to smaller negative values, becoming positive finally, with a much slower change thereafter. A cosmographic and a geometrical analysis have been carried out. It is observed that a gradual transition takes place from a regime of quintessence to phantom dark energy. An important finding of this study is that the signature flip of the deceleration parameter takes place almost simultaneously with the signature flip of the cosmological constant, implying a connection between accelerated expansion and dark energy, which is represented here by the cosmological constant. Unlike the common practice of using arbitrary units, proper SI units for all measurable quantities have been used. This theoretical investigation provides the reader with a simple method to formulate models in the framework of BD theory.

Keywords: *Brans-Dicke gravity; Dark Energy; Gravitational constant; Cosmological constant; Cosmographic analysis; Om diagnostic; Statefinder diagnostic*
PACS: 04.50.−h, 98.80.Es, 98.80.−k, 95.36.+x, 04.50.Kd, 95.30.Sf, 03.30.+p

1. INTRODUCTION

Based on the observations regarding the Type 1a supernova, it was established that the universe is expanding with acceleration and the present phase of acceleration was preceded by a phase of deceleration [1-5]. It has been a great challenge since then to explain the cosmic acceleration. According to the general theory of relativity (GTR), there is a strange form of energy, named Dark Energy (DE), which causes this acceleration. One of the parameters representing DE is the cosmological constant (Λ) in ΛCDM model which is known to be consistent with several important astrophysical observations related with supernova, baryon acoustic oscillation and cosmic microwave background. But it cannot account for the structure formation at small scales. DE models with scalar fields, such as phantom, quintessence and tachyon models were formulated to account for the phenomenon of late-time acceleration by Copeland et al. [6].

Several models were formulated to explain the dynamical behavior of DE [7-9]. One of the most significant among the theories which are modified versions of GTR is the one formulated by Brans and Dicke, which supports Mach's principle and weak equivalence principle [10]. The theory of $f(R,T)$ gravity is another such important theory of modified gravity [11, 12]. Brans and Dicke made a pioneering contribution to the theoretical exploration of the scalar tensor theories, and the elegant theoretical framework built up by them is known as Brans-Dicke theory of gravity. The scalar field (ϕ) in this theory evolves with time and we have $\phi = 1/G$ where G stands for the gravitational constant. A dimensionless constant ω in BD theory couples the scalar field with gravity. BD theory can generate the results of GTR if ϕ is constant and ω is infinitely large [13]. An important role is played by the scalar field ϕ in explaining the characteristics of the inflationary universe [10, 14, 15]. Based on BD theory, various cosmological models have been formulated by several researchers to account for the observed features [16-20]. The dynamics of Bianchi Type-V universe have been studied by Prasad et al. under the framework of BD theory [21]. DE models in BD theory have also been constructed where the dimensionless parameter ω is a function of the scalar field (ϕ) [22].

The main objective of the present study is to construct a cosmological model, in the framework of Brans-Dicke theory of gravity, to find and analyze the features of time evolution of different cosmological quantities. For this purpose, we have built a model starting from an empirical expression for the deceleration parameter (q) which is based upon the fact that q undergoes a signature flip as time goes on. Expressions for Hubble parameter (H) and scale factor (a) have

been derived from that ansatz for q which clearly demonstrates (as a function of time) the change of the mode of expansion of the universe from deceleration to acceleration. The values of the arbitrary constants involved in this model have been calculated by using the presently accepted values of some cosmological quantities obtained from observational data. Considering the homogeneity and isotropy of the universe at large scale, we have used FLRW metric to obtain the field equations. To extract information from these equations, a power-law relation between the scalar field (ϕ) and the scale factor (a) has been used in the present study. Employing these equations, we have derived expressions for energy density, cosmic pressure, cosmological constant, gravitational constant, equation of state (EoS) parameter and shown their time variation graphically. For a cosmographic analysis, we have shown the variation of *jerk*, *snap* and *lerk* parameters in terms of redshift (z) graphically. To analyze the DE model characteristics, we have employed the theoretical tools named Statefinder diagnostic and *Om* diagnostic. It is observed that there is a gradual transition from quintessence dark energy regime to a phantom dark energy regime in the universe. A novel finding is that, the signature flip of the cosmological constant is almost simultaneous with the signature flip of the deceleration parameter, pointing towards a role of dark energy (represented by the cosmological constant) in causing cosmic acceleration.

2. FIELD EQUATIONS

The action for the Brans-Dicke theory of gravity is expressed as,

$$S = \int_{\mathcal{R}} \left\{ \phi(R - 2\Lambda) + \omega \phi^{-1} \phi^{\mu} \phi_{\mu} + \frac{16\pi}{c^4} L_m \right\} \sqrt{-g} \, d^4 x, \tag{1}$$

where, ϕ represents the BD scalar field, which is reciprocal of the gravitational constant ($G = 1/\phi$). R stands for the Ricci scalar. The symbol Λ represents the cosmological constant. ω is called the BD parameter which represents a dimensionless coupling constant. The symbol ϕ_{μ} denotes the ordinary derivative of ϕ with respect to x^{μ}. The matter Lagrangian density is denoted by the symbol L_m.

The field equation, which is given below, is obtained by the variation of action (i.e., S in eqn. 1) through infinitesimal changes in the metric tensor $g^{\mu\nu}$.

$$R_{\mu\nu} - \frac{1}{2} g_{\mu\nu} R = -\frac{8\pi}{\phi c^4} T_{\mu\nu} - \frac{\omega}{\phi^2} \left(\phi_{\mu} \phi_{\nu} - \frac{1}{2} g_{\mu\nu} \phi^{\gamma} \phi_{\gamma} \right) - \frac{1}{\phi} \left(\phi_{\mu;\nu} - g_{\mu\nu} \Box \phi \right) - \Lambda g_{\mu\nu} \tag{2}$$

In the above equation, $T_{\mu\nu}$ denotes the energy-momentum tensor, $g_{\mu\nu}$ is the metric tensor and $R_{\mu\nu}$ stands for the Ricci tensor. The semicolon (;) in this equation stands for the covariant derivative and the symbol $\Box$ represents the d'Alembert operator.

Through a variation of the scalar field (ϕ) in BD action (i.e., S in eqn. 1) we get the following equation.

$$\Box \phi = \frac{1}{3 + 2\omega} \left(\frac{8\pi T}{c^4} + 2\Lambda \phi \right) \tag{3}$$

where, $T = g^{\mu\nu} T_{\mu\nu}$ is the trace of energy-momentum tensor $T_{\mu\nu}$.

The matter content of the universe is considered to be that of a perfect fluid distribution, which is given by,

$$T_{\mu\nu} = \rho u_{\mu} u_{\nu} + p h_{\mu\nu} \tag{4}$$

where, ρ and p are cosmic fluid's energy density and pressure respectively. $h_{\mu\nu} = u_{\mu} u_{\nu} - g_{\mu\nu}$ where u_{μ} represents the four-velocity vector of cosmic fluid with $g_{\mu\nu} u^{\mu} u^{\nu} = 1$.

It has been concluded from recent cosmological findings that the observable universe is homogeneous and isotropic at large scales. To take into account this aspect of the cosmos, we have chosen FLRW metric to represent the space-time geometry of the universe. This metric is given by,

$$ds^2 = c^2 dt^2 - a^2 \left(\frac{1}{1 + kr^2} dr^2 + r^2 d\theta^2 + r^2 \sin^2 \theta \, d\phi^2 \right) \tag{5}$$

In equation (5), the symbol a denotes the scale factor. The coordinates (co-moving) of the spherical polar system are (r, θ, ϕ). The symbol k is regarded as the curvature parameter which has three values $1, 0, -1$, denoting respectively three characteristics of the expanding universe, namely *open*, *flat* and *closed*.

In co-moving coordinate system, Brans-Dicke field equations (eqns. 2, 3) and the energy-momentum tensor (eqn. 4) for a FLRW metric (eqn. 5) with zero curvature (i.e., $k = 0$) lead to the set of differential equations given below (eqns. 6-8).

$$H^2 + H \frac{\dot{\phi}}{\phi} - \frac{\omega}{6} \left(\frac{\dot{\phi}}{\phi} \right)^2 = \frac{8\pi \rho}{3 \phi c^2} + \frac{\Lambda c^2}{3} \tag{6}$$

$$2\dot{H} + 3H^2 + 2H\frac{\dot{\phi}}{\phi} + \frac{\omega}{2}\left(\frac{\dot{\phi}}{\phi}\right)^2 + \frac{\ddot{\phi}}{\phi} = -\frac{8\pi p}{\phi c^2} + \Lambda c^2 \tag{7}$$

$$(3 + 2\omega)\left(3H\frac{\dot{\phi}}{\phi} + \frac{\ddot{\phi}}{\phi}\right) = \frac{8\pi(\rho - 3p)}{\phi c^2} + 2\Lambda c^2 \tag{8}$$

In equations (6), (7) and (8), H represents the Hubble parameter (given by, $H = \frac{\dot{a}}{a}$). A dot over any parameter represents the conventional derivative of that parameter with respect to time (t).

Based on the three above equations, we have obtained the following expressions for the parameters Λ, ρ and p, represented as functions of a, ϕ and their time derivatives.

$$\Lambda(t) = \frac{1}{2c^2}\left[6\left(\frac{\dot{a}}{a}\right)^2 + \omega\left(\frac{\dot{\phi}}{\phi}\right)^2 + 6\frac{\ddot{a}}{a} - 2\omega\frac{\ddot{\phi}}{\phi} - 6\omega\frac{\dot{a}}{a}\frac{\dot{\phi}}{\phi}\right] \tag{9}$$

$$\rho(t) = \frac{\phi c^2}{8\pi}\left[3\left(\frac{\dot{a}}{a}\right)^2 + 3\frac{\dot{a}}{a}\frac{\dot{\phi}}{\phi} - \frac{\omega}{2}\left(\frac{\dot{\phi}}{\phi}\right)^2 - \Lambda c^2\right] \tag{10}$$

$$p(t) = \frac{\phi c^2}{8\pi}\left[\Lambda c^2 - 2\frac{\ddot{a}}{a} - \left(\frac{\dot{a}}{a}\right)^2 - \frac{\ddot{\phi}}{\phi} - 2\frac{\dot{a}}{a}\frac{\dot{\phi}}{\phi} - \frac{\omega}{2}\left(\frac{\dot{\phi}}{\phi}\right)^2\right] \tag{11}$$

3. SOLUTION OF FIELD EQUATIONS

Considering the change of phase of the cosmic expansion from deceleration to acceleration [1-5], we assume an ansatz regarding the time evolution of the deceleration parameter (q). It is given by,

$$q(t) = At^{-n} - B \tag{12}$$

where $A, B, n > 0$. This function of time, $q(t)$, undergoes a change of sign (with time) from positive to negative.

Since $q(t) = -1 - \frac{\dot{H}}{H^2}$, where H is the Hubble parameter, we may write equation (12) as,

$$\frac{\dot{H}}{H^2} = B - 1 - At^{-n} \tag{13}$$

Integrating equation (13), we get the following expression for the Hubble parameter.

$$H = \left[(1 - B)t + \frac{At^{1-n}}{1-n} + C\right]^{-1} \tag{14}$$

where C is a constant of integration.

Substituting $H = \frac{\dot{a}}{a}$ in equation (14) we get the following differential equation.

$$\frac{\dot{a}}{a} = \left[(1 - B)t + \frac{At^{1-n}}{1-n} + C\right]^{-1} \tag{15}$$

Equation (15) can be solved analytically for $C = 0$, which corresponds to its simplest solution. That solution leads to the following expression for the scale factor (a).

$$a(t) = b[(B - 1)(n - 1)t^n + A]^{\frac{1}{n(1-B)}} \tag{16}$$

where b is a constant of integration.

The expressions for a, H and q (in terms of time) are dependent upon the parameters A, B, b and n. The inter-dependence of these parameters can be determined by using the values of the cosmological quantities (H_0, q_0, ρ_0) obtainable from observational data. The symbols, H_0, q_0, ρ_0 denote respectively the values of H, q, ρ at the present time (i.e., $t = t_0$) where t_0 is the present age of the universe.

Using the fact that $q = q_0$ at $t = t_0$ in equation (12), we get,

$$A = (q_0 + B)t_0^n \tag{17}$$

Similarly, using the fact that $H = H_0$ at $t = t_0$ in equation (14), we get,

$$B = 1 + \frac{At_0^{-n}}{1-n} - \frac{1}{H_0 t_0} \tag{18}$$

Solving equations (17) and (18) for A and B one gets,

$$A = \left[q_0 + \frac{(1-n)(1-H_0 t_0) - q_0 H_0 t_0}{n H_0 t_0} \right] t_0^n \tag{19}$$

$$B = \frac{(1-n)(1-H_0 t_0) - q_0 H_0 t_0}{n H_0 t_0} \tag{20}$$

Thus, A and B are found to be dependent upon the parameter n.
Using the fact that $a = a_0$ at $t = t_0$, in equation (16), we get,

$$a_0 = b[(B-1)(n-1)t_0^n + A]^{\frac{1}{n(1-B)}} \tag{21}$$

where, a_0 is the value of the scale factor at the present time. Using equation (21), we obtain b in terms of n and a_0, as given below.

$$b = a_0[(B-1)(n-1)t_0^n + A]^{-\frac{1}{n(1-B)}} \tag{22}$$

Substituting the equations (19) and (20) in equation (22) we get,

$$b = a_0 \left[\left(\frac{(1-n)(1-H_0 t_0) - q_0 H_0 t_0}{n H_0 t_0} - 1 \right)(n-1)t_0^n + \left[q_0 + \frac{(1-n)(1-H_0 t_0) - q_0 H_0 t_0}{n H_0 t_0} \right] t_0^n \right]^{-\frac{1}{n\left[1 - \frac{(1-n)(1-H_0 t_0) - q_0 H_0 t_0}{n H_0 t_0}\right]}} \tag{22A}$$

Thus, among the four arbitrary parameters of this model (A, B, b and n), it is observed from equations (19), (20) and (22A) that A, B, b can be expressed as functions of n. We have chosen $a_0 = 1$ in the present study. Hence q, H and a are dependent on n only. Taking $H_0 t_0 \approx 1$ [18], we obtain $B \approx -\frac{q_0}{n}$ from equation (20), satisfying the condition $B > 0$, since $q_0 < 0$ for an accelerating universe and $n > 0$ by definition. For A to be positive, we must have $(q_0 + B)t_0^n > 0$ (according to eqn. 17). It means $q_0 - \frac{q_0}{n} > 0$, leading to $n < 1$ (using $B = -\frac{q_0}{n}$ and $q_0 < 0$). Thus, the range of values for n is obtained as, $0 < n < 1$.

An ansatz for the scalar field parameter (ϕ), where it has a power-law relation with the scale factor (a), has been used in the present formulation, based on some recent studies [17-20]. This ansatz is,

$$\phi = \phi_0 \left(\frac{a}{a_0} \right)^m \tag{23}$$

where, m is an arbitrary constant and $\phi_0 = \frac{1}{G_0}$, where G_0 is the present value of the gravitational constant G. In BD theory, the gravitational term $G(t) = 1/\phi(t)$. Based on equation (23), the first and the second order time-derivatives of ϕ are given by the following two equations.

$$\dot{\phi} = mH\phi \tag{24}$$

$$\ddot{\phi} = mH^2\phi\{(m-1) - q\} \tag{25}$$

Equation (24) and (25) have been obtained by using the relations: $\frac{\dot{a}}{a} = H$ and $\frac{\ddot{a}}{a} = -qH^2$. Using equations (24) and (25) in equations (9), (10) and (11), we obtain the following expressions for cosmological term (Λ), energy density (ρ) and pressure (p).

$$\Lambda(t) = \frac{H^2}{2c^2} [(6 - \omega m^2 - 4\omega m) + 2q(\omega m - 3)] \tag{26}$$

$$\rho(t) = \frac{\phi c^2 H^2}{8\pi} [(3m + 2\omega m) + q(3 - \omega m)] \tag{27}$$

$$p(t) = \frac{\phi c^2 H^2}{8\pi} [(2 - \omega m^2 - 2\omega m - m^2 - m) + q(\omega m + m - 1)] \tag{28}$$

Putting $\rho = \rho_0$, $\phi = \phi_0$, $H = H_0$, $q = q_0$ in equation (27), we get the following expression for m in terms of ω.

$$m = \frac{8\pi\rho_0 - 3q_0(\phi_0 c^2 H_0{}^2)}{(\phi_0 c^2 H_0{}^2)(3 + 2\omega - q_0\omega)} \quad (29)$$

Hence, along with n, ω is also a free parameter in this model. Λ, ρ and p are dependent on both n and ω, while q, H and a are dependent on n only.

The equation of state (EoS) parameter (η) is defined as $\eta = \frac{p}{\rho}$. Using equations (27) and (28), η can be expressed as,

$$\eta = \frac{(2 - \omega m^2 - 2\omega m - m^2 - m) + q(\omega m + m - 1)}{(3m + 2\omega m) + q(3 - \omega m)} \quad (30)$$

Using equation (12) in (26), (27), (28) and (30), the expressions for Λ, ρ, p and η take new forms represented by equations (31), (32), (33) and (34), respectively, as given below.

$$\Lambda(t) = \frac{1}{2c^2}\left((1 - B)t + \frac{At^{1-n}}{1-n}\right)^{-2}\begin{bmatrix}(6 - \omega m^2 - 4\omega m) + \\ 2(At^{-n} - B)(\omega m - 3)\end{bmatrix} \quad (31)$$

$$\rho(t) = \frac{\phi_0 c^2}{8\pi}\left(\frac{a}{a_0}\right)^m\left((1 - B)t + \frac{At^{1-n}}{1-n}\right)^{-2}\begin{bmatrix}(3m + 2\omega m) + \\ (At^{-n} - B)(3 - \omega m)\end{bmatrix} \quad (32)$$

$$p(t) = \frac{\phi_0 c^2}{8\pi}\left(\frac{a}{a_0}\right)^m\left((1 - B)t + \frac{At^{1-n}}{1-n}\right)^{-2}\begin{bmatrix}(2 - \omega m^2 - 2\omega m - m^2 - m) + \\ (At^{-n} - B)(\omega m + m - 1)\end{bmatrix} \quad (33)$$

$$\eta(t) = \frac{p(t)}{\rho(t)} = \frac{(2 - \omega m^2 - 2\omega m - m^2 - m) + (At^{-n} - B)(\omega m + m - 1)}{(3m + 2\omega m) + (At^{-n} - B)(3 - \omega m)} \quad (34)$$

4. COSMOGRAPHIC ANALYSIS

For a cosmographic analysis, we have determined the time dependence of jerk(j), snap(s) and lerk(l) parameters, which are defined as, $j(t) = a^2\frac{d^3a}{dt^3}\left(\frac{da}{dt}\right)^{-3}$, $s(t) = a^3\frac{d^4a}{dt^4}\left(\frac{da}{dt}\right)^{-4}$ and $l(t) = a^4\frac{d^5a}{dt^5}\left(\frac{da}{dt}\right)^{-5}$ respectively [23, 24]. These are dimensionless quantities which depend upon the scale factor (a) and its third, fourth and fifth order time derivatives. They allow us to determine the rate of cosmic expansion more accurately by a model independent analysis of the evolution of the universe. Using equation (16) we get the following expressions (eqns. 35, 36 and 37) for j, s and l respectively.

$$j(t) = \frac{C_1 t^{2n} + C_2 t^n + C_3}{(n-1)t^{2n}} \quad (35)$$

where $C_1 = 2B^2n - Bn - 2B^2 + B$,

$C_2 = -ABn^2 + An^2 - 3ABn + 4AB - A$,

and $C_3 = A^2n - 2A^2$.

$$s(t) = \frac{C_4 t^{3n} + C_5 t^{2n} + C_6 t^n + C_7}{(n-1)^2 t^{3n}} \quad (36)$$

where $C_4 = 6B^3n^2 - 7B^2n^2 + 2Bn^2 - 12B^3n + 14B^2n - 4Bn + 6B^3 - 7B^2 + 2B$,

$C_5 = -AB^2n^4 + 2ABn^4 - An^4 - 5AB^2n^3 + 6ABn^3 - An^3 - 5AB^2n^2 - 4ABn^2 + 3An^2 + 29AB^2n - 18ABn + An - 18AB^2 + 14AB - 2A$,

$C_6 = 4A^2Bn^3 - 4A^2n^3 + 7A^2n^2 - 22A^2Bn + 4A^2n + 18A^2Bt^n - 7A^2$,

and $C_7 = -A^3n^2 + 5A^3n - 6A^3$.

$$l(t) = \frac{C_8 t^{4n} + C_9 t^{3n} + C_{10}t^{2n} + C_{11}t^n + C_{12}}{(n-1)^3 t^{4n}} \quad (37)$$

where $\quad C_8 = 24B^4n^3 - 46B^3n^3 + 29B^2n^3 - 6Bn^3 - 72B^4n^2 + 138B^3n^2 - 87B^2n^2 + 18Bn^2 + 72B^4nt^{4n} - 138B^3n + 87B^2n - 18Bn - 24B^4 + 46B^3 - 29B^2 + 6B$,

$C_9 = -AB^3n^6 + 3AB^2n^6 - 3ABn^6 + An^6 - 8AB^3n^5 + 19AB^2n^5 - 14ABn^5 + 3An^5 - 16AB^3n^4 + 18AB^2n^4 + 2ABn^4 - 4An^4 + 10AB^3n^3 - 60AB^2n^3 + 50ABn^3 - 10An^3 + 161AB^3n^2 - 163AB^2n^2 + 23ABn^2 + 9An^2 - 242AB^3n + 321AB^2n - 116ABn + 7An + 96AB^3 - 138AB^2 + 58AB - 6A,$

$C_{10} = 11A^2B^2n^5 - 22A^2Bn^5 + 11A^2n^5 + +19A^2B^2n^4 - 8A^2Bn^4 - 11A^2n^4 - 65A^2B^2n^3 + 130A^2Bn^3 - 40A^2n^3 - 115A^2B^2n^2 - 10A^2Bn^2 + 40A^2n^2 + 294A^2B^2n - 228A^2Bn + 29A^2n - 144A^2B^2 + 138A^2B - 29A^2,$

$C_{11} = -11A^3Bn^4 + 11A^3n^4 + 30A^3Bn^3 - 45A^3n^3 + 35A^3Bn^2 + 35A^3n^2 - 150A^3Bn + 45A^3n + 96A^3B - 46A^3,$

and $C_{12} = A^4n^3 - 9A^4n^2 + 26A^4n - 24A^4.$

5. STATEFINDER AND Om DIAGNOSTICS

Sahni et al. introduced two parameters r and s which are defined as [25],

$$r = a^2 \frac{d^3a}{dt^3} \left(\frac{da}{dt}\right)^{-3} \tag{38}$$

$$s = \frac{2(1-r)}{3(1-2q)} \tag{39}$$

The expression for r is the same as the expression for the jerk parameter $j(t)$.

Like H and q, these dimensionless parameters are functions of the scale factor (a) and its higher order derivatives. These parameters help us to differentiate between any DE model and the ΛCDM model. As per statefinder diagnostic, (s,r) and (q,r) trajectories are plotted in $s-r$ and $q-r$ planes, respectively, to analyze the evolution of the universe under the frameworks of different models of dark energy. Since q, r and s involve only the scale factor (a) and its time derivatives of higher orders, this method is independent of the framework of gravity. Thus, this diagnostic is model independent.

Using equations (12) and (16) in equations (38) and (39), r and s are expressed as,

$$r = \frac{C_1t^{2n}+C_2t^n+C_3}{(n-1)t^{2n}} \tag{40}$$

$$s = \frac{2\left\{1-\frac{C_1t^{2n}+C_2t^n+C_3}{(n-1)t^{2n}}\right\}}{3\{1-2(At^{-n}-B)\}} \tag{41}$$

where, $C_1 = 2B^2n - Bn - 2B^2 + B$, $C_2 = -ABn^2 + An^2 - 3ABn + 4AB - A$ and $C_3 = A^2n - 2A^2.$

ΛCDM model is represented by the point $(s,r) = (0,1)$ in $s-r$ plane. Standard cold dark matter (SCDM) model is represented by the point $(s,r) = (1,1)$ in FLRW background. The point $(q,r) = (-1,1)$ stands for steady state (SS) model and $(q,r) = (0.5,1)$ stands for SCDM model in $q-r$ plane.

Om diagnostic has been used in recent cosmological studies to distinguish between the standard ΛCDM model and various other DE models [26]. In this theory, a parameter called $Om(z)$ is defined as

$$Om(z) = \frac{[E(z)]^2-1}{z^3+3z^2+3z} \tag{42}$$

where, $E(z) = \frac{H(z)}{H_0}$ and $z(\equiv \frac{a_0}{a} - 1)$ is the redshift parameter. The positive curvatures of $Om(z)$ trajectories imply phantom behaviour while negative curvatures of $Om(z)$ trajectories indicate quintessence behaviour of dark energy. Constant value of $Om(z)$ for a model indicates that its behaviour is the same as that of the ΛCDM model.

6. RESULTS AND DISCUSSION

To plot some cosmological quantities graphically with respect to redshift (z), we have derived the following relation (redshift versus time) based on equation (16).

$$z = \frac{a_0}{a} - 1 = \frac{a_0}{b}[(B-1)(n-1)t^n + A]^{-\frac{1}{n(1-B)}} - 1 \tag{43}$$

Since the behaviour of the deceleration parameter (q) determines how the phase of decelerated expansion of the universe changes into the phase of accelerated expansion, we have derived the following expression for Λ as a function of q, using equations (12), (14) and (26).

$$\Lambda(q) = \frac{[(6-\omega m^2 - 4\omega m) + 2q(\omega m - 3)]}{2c^2} \left[(1-B)\left\{ \left(\frac{q+B}{A}\right)^{-\frac{1}{n}} \right\} + \frac{A\left\{ \left(\frac{q+B}{A}\right)^{-\frac{1}{n}} \right\}^{1-n}}{1-n} + C \right]^{-2}$$ (44)

To validate the present model, the arbitrary constants associated with the formulation have been so adjusted that the values of $H_0, q_0, \rho_0, G_0, t_0$ are obtained correctly from the model, as discussed in Section-3 of this article. For this purpose, we have used the following values of these parameters [18].

$H_0 = 2.34 \times 10^{-18} \, sec^{-1}$, $q_0 = -0.55$, $\rho_0 = 8.91 \times 10^{-10} \, J/m^3$, $G_0 = 6.67 \times 10^{-11} N \, m^2 \, Kg^{-2}$, $t_0 = 4.13 \times 10^{17} \, sec$.
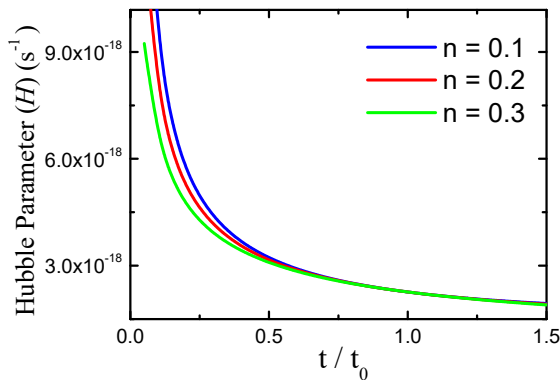
Figure 1. Plots of Hubble parameter (H) versus time
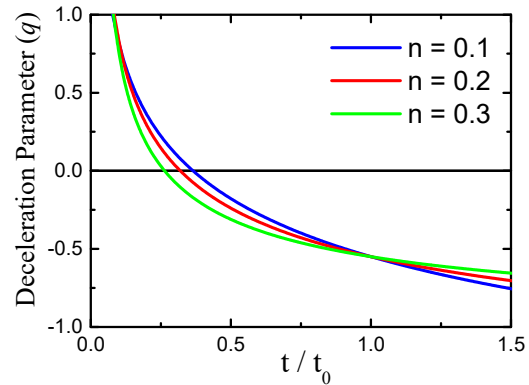
Figure 2. Plots of deceleration parameter (q) versus time

Figures 1 and 2 show the time evolution of Hubble parameter (H) and deceleration parameter (q) respectively, for three values of the parameter n. It is observed that H decreases with time, which is consistent with recent studies based on various models [7, 17-19]. The deceleration parameter shows a signature flip indicating a change from decelerated expansion to accelerated expansion, in accordance with the observed features [7, 17-19].
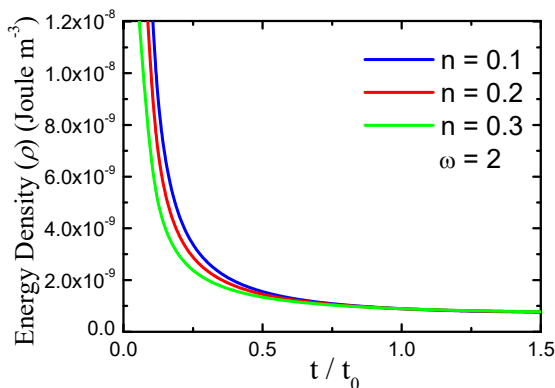
Figure 3. Plots of energy density (ρ) versus time
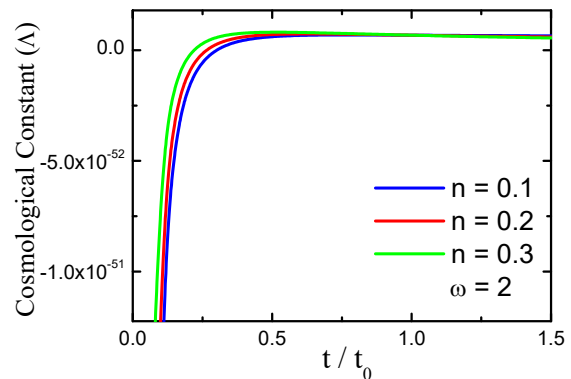
Figure 4. Plots of cosmological Constant (Λ) versus time

Figures 3, 4, 5 and 6 show respectively the behavior of energy density (ρ), cosmological constant (Λ), Gravitational constant (G) and EoS parameter (η) with respect to time, for three values of the parameter n. These four cosmological quantities depend also on the Brans-Dicke parameter ω. It is found from equation (29) that $m > 0$ for $\omega > -1.11$. Using equation (32) we have found that, for some values of ω, in the range of $\omega < -1.11$, ρ becomes negative. Due to this discrepancy regarding the sign of ρ values, we have chosen to use ω values belonging to the range of $\omega > -1.11$. For all calculations we have used $\omega = 2$, leading to $m = 0.61$, which are consistent with a recent study in the framework of BD theory [19]. Another study by Goswami et al, in BD framework, also used positive values of ω [18]. As per equation (23), ϕ increases with time if $m > 0$, implying that $G \ (\equiv 1/\phi)$ decreases with time, as shown by Figure 5, which is in agreement with some recent studies based on different theoretical models and experimental observations [18, 27, 28]. Figure 3 shows that ρ decreases with time, as obtained from many other studies [9, 17, 19, 29, 30]. Figure 4 shows that Λ rises very steeply in the early universe, becoming positive from negative and then changes slowly. This behavior is consistent with the findings of various other studies [31-34]. As per Figure 6, η is negative and decreases gradually with time, with $\eta(t = t_0) = -0.8$, which is consistent with values obtained from observational data [35, 36]. According to the plots of Figure 6, the universe presently has a quintessence dark energy regime ($\eta > -1$) and it is making a gradual transition towards a phantom dark energy regime ($\eta < -1$).
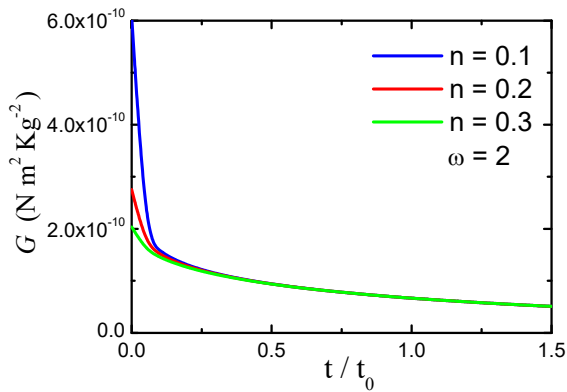
Figure 5. Plots of gravitational constant (G) versus time
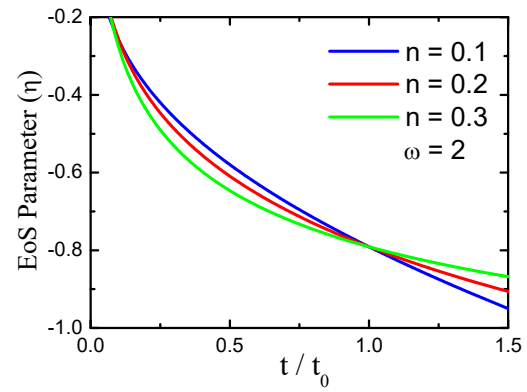
Figure 6. Plots of EoS Parameter (η) versus time

Figure 7 depicts the variation of cosmic pressure (p) with respect to time for three values of n. It is negative and it becomes less negative with time. Negative pressure is associated with DE, causing the accelerated expansion of the universe. This behavior is consistent with the findings of several studies [37, 38].
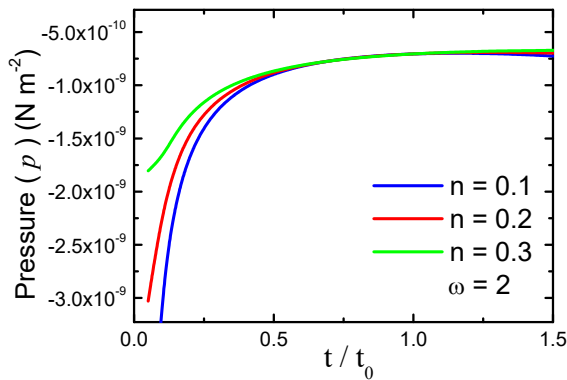
Figure 7. Plots of pressure (p) versus time
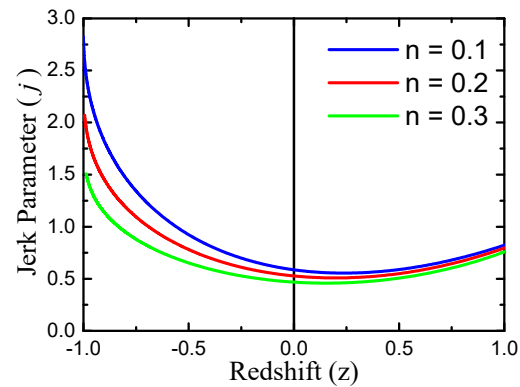
Figure 8. Plots of jerk parameter (j) versus redshift (z)

Figures 8, 9 and 10 represent respectively the plots of jerk (j), snap (s) and lerk (l) parameters against redshift (z). Their behaviours are similar to the results of a recent study under BD framework [19].
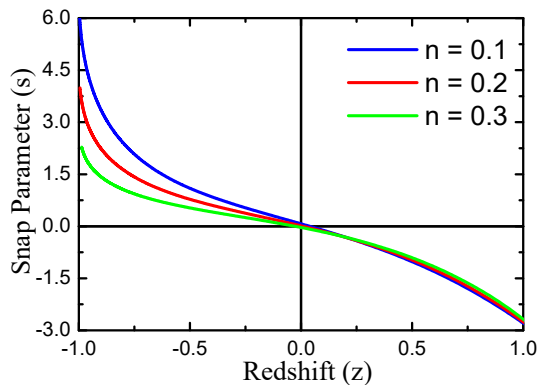
Figure 9. Plots of snap parameter (s) versus redshift (z)
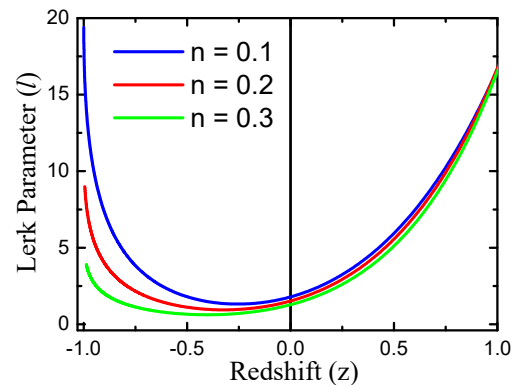
Figure 10. Plots of lerk parameter (l) versus redshift (z)

Positive values for j and l and negative values for s represent accelerated expansion [39]. Figures 8 and 10 show j and l to have positive values for all values of n. As per Figure 9, the values of the snap parameter (s) undergo a transition with time from negative to positive (based on the fact that z decreases as t increases). From equation (36) it is found that the value of the snap parameter at the present time (i.e., at $t = t_0$) is negative for $n > 0.227$, which is consistent with the plot for $n = 0.3$ in Figure 9 where s is negative at $t = t_0$ (i.e., $z = 0$). It provides a clear guideline for choosing the values of n for an accelerating universe. It has been shown in Section-3 of this article that $0 < n < 1$, based on the requirements for a proper parameterization of the ansatz that we have chosen for the deceleration parameter (represented by eqn. 12). Figure 8 shows that, the rate of increase of j with time (i.e., as z decreases) is larger for smaller values of the parameter n. We observe almost the same behaviour for the plots of s in Figure 9. In Figure 10, the values of l initially decrease with time and, at some point of time in future (i.e., $z < 0$) the values increase with time, having the largest rate of rise for

the lowest value of the parameter n. For plotting the graphs in Figures 8-10, we did not have to express jerk (j), snap (s) and lerk (l) parameters as functions of redshift (z). Expressions for these parameters, in terms of z, would have been extremely complicated and difficult to handle. We generated datasets for j, s, l and z as functions of time (using eqns. 35-37, 43 respectively) for three different values of the parameter n, using Microsoft Excel. Based on these datasets, we have plotted j, s, l as functions of z.

Figures 11 and 12 show the plots of (s, r) and (q, r) trajectories. Their natures are found to be close to those obtained from a different model in the BD framework [19]. In Figure 11, trajectories begin in the Chaplygin gas (CG) region ($s < 0, r > 1$), and enter the quintessence region ($s > 0, r < 1$). Then they merge together and reach the Chaplygin gas region again after passing through the point (0, 1) which stands for the ΛCDM model, for all values of n. In Figure 12, the line $r = 1$ represents the evolution of ΛCDM model. The trajectories, starting from the region of decelerated expansion ($q > 0$), are found to reach and cross the $r = 1$ line for all three values of n. Here, $q = 0.5$ line represents matter-dominated era. These two figures show that the constructed model is presently behaving as a quintessence dark energy model. Its predictions for the future evolution of the universe will be like the Chaplygin gas model, after passing through an intermediate stage having the behavior which is consistent with that of the ΛCDM model.
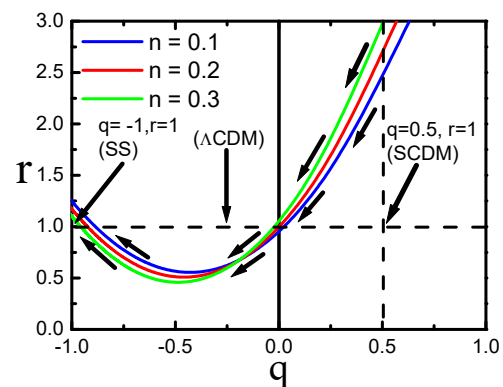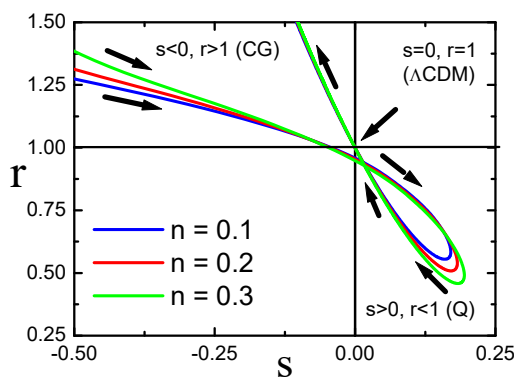
Figure 11. Plots of (s, r) trajectories for statefinder diagnostic

Figure 12. Plots of (q, r) trajectories for statefinder diagnostic

Figure 13 depicts the variation of $Om(z)$ as a function of z for different values of n. It is known that, if the curvature of $Om(z)$ is positive with respect to z, the model is a phantom dark energy model ($\eta < -1$) and, if the curvature is negative, it is a quintessence dark energy model ($\eta > -1$). For zero curvature, it represents the ΛCDM model [40-42]. It is observed that, $Om(z)$ rises steeply as z increases and it decreases slowly beyond $z = -0.75$ (approximately). Its decreasing behavior at $z = 0$ (i.e., the present time) indicates that our model has the characteristics of a quintessence DE model at the present time. Since z decreases with time, Figure 13 shows a transition of the model characteristics from those of a quintessence DE model to those of a phantom DE model, which is consistent with the inferences drawn from Figure 6. This transition takes more time to occur for greater values of the parameter n.
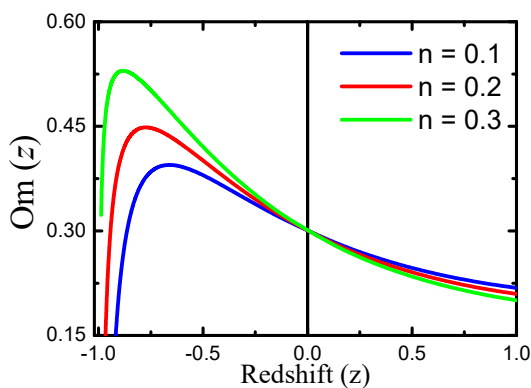
Figure 13. Plots of Om (z) versus redshift (z)
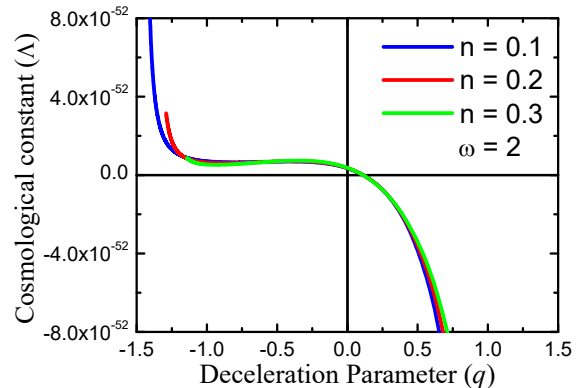
Figure 14. Plots of cosmological constant (Λ) versus deceleration parameter (q)

Figure 14 shows the variation of the cosmological constant (Λ) as a function of the deceleration parameter (q). These plots are based on equation (44). It is observed that, as Λ changes its sign from negative to positive, q undergoes a signature flip from positive to negative, indicating the phase transition (i.e., deceleration to acceleration) to be associated with some phenomena involving dark energy which is represented by Λ.

7. CONCLUSION

In the present article, we have constructed a cosmological model using FLRW metric for zero spatial curvature, in the Brans-Dicke framework with cosmological constant (Λ). Solutions of the field equations have been obtained from a proper parameterization of the deceleration parameter $q(t) = At^{-n} - B$ with $A, B, n > 0$. The choice of this expression is based on the phenomenon of signature flip of the deceleration parameter as obtained from astrophysical observations. The characteristics of the physical and geometrical parameters have been depicted graphically. We have a detailed interpretation of these graphs in Section-6 of this article. A significant finding of the present study is that the time at which the deceleration parameter changes its sign (from positive to negative) is almost the same as the time at which the cosmological parameter changes its sign (from negative to positive), indicating clearly that the change of phase from decelerated expansion to accelerated expansion is governed by some dark energy dynamics which is generally regarded as being represented by the characteristics of the cosmological parameter (Λ), in calculations under different gravitational frameworks. The plots based on the statefinder parameters show that, for all values of the parameter n, the (s, r) trajectories enter the quintessence region from Chaplygin gas region, ending up finally in the Chaplygin gas region after passing through the point representing ΛCDM. Thus, the future characteristics of the universe, based on this model, is like those obtained from Chaplygin gas model. The (q, r) trajectories start evolving from a region close to SCDM and move ahead crossing the line representing ΛCDM. The findings of the present study are sufficiently consistent with the findings of models constructed under various other theoretical frameworks, and they are also in reasonable agreement with observational data. As a future extension of the present work, we have plans to use some new ansatzes representing deceleration parameter to determine the time evolution of various cosmological quantities and find their average behaviour under different theoretical frameworks of gravitation. The construction of the present model might be helpful to the researchers in studying the evolution of the universe under the Brans-Dicke framework by formulating more such models in future.

ORCID

Sudipto Roy, https://orcid.org/0000-0002-8811-2511; **Rivu Kayal,** https://orcid.org/0009-0009-4417-2692;
Simran Ali, https://orcid.org/0009-0006-1450-3612; **Srinjoyee Bandyopadhyay,** https://orcid.org/0009-0003-1578-0951
Debamita Bhattacharya, https://orcid.org/0009-0008-3472-381X

REFERENCES

[1] S. Perlmutter, G. Aldering, M. D. Valle, S. Deustua, R. S. Ellis, S. Fabbro, A. Fruchter, G. Goldhaber, D. E. Groom, I. M. Hook, A. G. Kim, M. Y. Kim, R. A. Knop, C. Lidman, R. G. McMahon, P. Nugent, R. Pain, N. Panagia, C. R. Pennypacker, P. Ruiz-Lapuente, B. Schaefer, and N. Walton, "Discovery of a supernova explosion at half the age of the Universe," Nature, **391**(6662), 51–54 (1998). https://doi.org/10.1038/34124

[2] A. G. Riess, A. V. Filippenko, P. Challis, A. Clocchiatti, A. Diercks, P. M. Garnavich, R. L. Gilliland, C. J. Hogan, S. Jha, R. P. Kirshner, B. Leibundgut, M. M. Phillips, D. Reiss, B. P. Schmidt, R. A. Schommer, R. C. Smith, J. Spyromilio, C. Stubbs, N. B. Suntzeff, and J. Tonry, "Observational Evidence from Supernovae for an Accelerating Universe and a Cosmological Constant," Astron. J. **116**(3), 1009–1038 (1998). https://doi.org/10.1086/300499

[3] M. Kowalski, D. Rubin, G. Aldering, R. J. Agostinho, A. Amadon, R. Amanullah, C. Balland, K. Barbary, G. Blanc, P. J. Challis, A. Conley, N. V. Connolly, R. Covarrubias, K. S. Dawson, S. E. Deustua, R. Ellis, S. Fabbro, V. Fadeyev, X. Fan, B. Farris, G. Folatelli, B. L. Frye, G. Garavini, E. L. Gates, L. Germany, G. Goldhaber, B. Goldman, A. Goobar, D. E. Groom, J. Haissinski, D. Hardin, I. Hook, S. Kent, A. G. Kim, R. A. Knop, C. Lidman, E. V. Linder, J. Mendez, J. Meyers, G. J. Miller, M. Moniez, A. M. Mourão, H. Newberg, S. Nobili, P. E. Nugent, R. Pain, O. Perdereau, S. Perlmutter, M. M. Phillips, and J. L. Yun, "Improved Cosmological Constraints from New, Old, and Combined Supernova Data Sets," Astrophys. J. **686**(2), 749–778 (2008). https://doi.org/10.1086/589937

[4] J. Guy, M. Sullivan, A. Conley, N. Regnault, P. Astier, C. Balland, S. Basa, R. G. Carlberg, D. Fouchez, D. Hardin, I. M. Hook, D. A. Howell, R. Pain, N. Palanque-Delabrouille, K. M. Perrett, C. J. Pritchet, J. Rich, V. Ruhlmann-Kleider, D. Balam, S. Baumont, R. S. Ellis, S. Fabbro, H. K. Fakhouri, N. Fourmanoit, S. González-Gaitán, M. L. Graham, E. Hsiao, T. Kronborg, C. Lidman, A. M. Mourao, S. Perlmutter, P. Ripoche, N. Suzuki, and E. S. Walker, "The Supernova Legacy Survey 3-year sample: Type Ia supernovae photometric distances and cosmological constraints," Astron. & Astrophys. **523**, A7 (2010). https://doi.org/10.1051/0004-6361/201014468

[5] S. Perlmutter, G. Aldering, G. Goldhaber, R. A. Knop, P. Nugent, P. G. Castro, S. Deustua, S. Fabbro, A. Goobar, D. E. Groom, I. M. Hook, A. G. Kim, M. Y. Kim, J. C. Lee, N. J. Nunes, R. Pain, C. R. Pennypacker, R. Quimby, C. Lidman, R. S. Ellis, M. Irwin, R. G. McMahon, P. Ruiz-Lapuente, N. Walton, B. Schaefer, B. J. Boyle, A. V. Filippenko, T. Matheson, A. S. Fruchter, N. Panagia, H. J. M. Newberg, W. J. Couch, and T. S. C. Project, "Measurements of Ω and Λ from 42 High-Redshift Supernovae," Astrophys. J. **517**(2), 565–586 (1999). https://doi.org/10.1086/307221

[6] E. J. Copeland, M. Sami, and S. Tsujikawa, "Dynamics of dark energy," Int. J. Mod. Phys. D **15**(11), 1753–1935 (2006). https://doi.org/10.1142/s021827180600942x

[7] G. K. Goswami, A. Pradhan, M. Mishra, and A. Beesham, "FRW dark energy cosmological model with hybrid expansion law," New Astron. **73**, 101284 (2019). https://doi.org/10.1016/j.newast.2019.101284

[8] S. K. Tripathy, S. K. Pradhan, Z. Naik, D. Behera, and B. Mishra, "Unified dark fluid and cosmic transit models in Brans–Dicke theory," Phys. Dark Universe **30**, 100722 (2020). https://doi.org/10.1016/j.dark.2020.100722

[9] S. K. J. Pacif, "Dark energy models from a parametrization of H: a comprehensive analysis and observational constraints," Eur. Phys. J. Plus **135**(10) (2020). https://doi.org/10.1140/epjp/s13360-020-00769-y

[10] C. Brans and R. H. Dicke, "Mach's Principle and a Relativistic Theory of Gravitation," Phys. Rev. **124**(3), 925–935 (1961). https://doi.org/10.1103/physrev.124.925

[11] S. Capozziello, S. Carloni and A. Troisi, "Quintessence without scalar fields," arXiv preprint astro-ph/0303041. 2003 Mar 3. Available from: https://doi.org/10.48550/arXiv.astro-ph/0303041

[12] T. Harko, F. S. N. Lobo, S. Nojiri, and S. D. Odintsov, "f(R,T)gravity," Phys. Rev. D **84**(2) (2011). https://doi.org/10.1103/physrevd.84.024020

[13] S. Kalyana Rama and S. Ghosh, "Short distance repulsive gravity as a consequence of non-trivial PPN parameters β and γ," Phys. Lett. B **384**(1-4), 50–57 (1996). https://doi.org/10.1016/0370-2693(96)00818-0

[14] O. Bertolami and P. J. Martins, "Nonminimal coupling and quintessence," Phys. Rev. D **61**(6) (2000). https://doi.org/10.1103/physrevd.61.064007

[15] N. Banerjee and D. Pavón, "Cosmic acceleration without quintessence," Phys. Rev. D **63**(4) (2001). https://doi.org/10.1103/physrevd.63.043504

[16] D. R. K. Reddy and M. V. S. Rao, "Axially Symmetric String Cosmological Model In Brans-Dicke Theory of Gravitation," Astrophys. Space Sci. **305**(2), 183–186 (2006). https://doi.org/10.1007/s10509-006-9062-7

[17] R. K. Mishra and A. Chand, "Cosmological models in alternative theory of gravity with bilinear deceleration parameter," Astrophys. Space Sci. **361**(8) (2016). https://doi.org/10.1007/s10509-016-2837-6

[18] G. K. Goswami, "Cosmological parameters for spatially flat dust filled Universe in Brans-Dicke theory," Res. Astron. Astrophys. **17**(3), 27 (2017). https://doi.org/10.1088/1674-4527/17/3/27

[19] R. K. Mishra and H. Dua, "Evolution of FLRW universe in Brans-Dicke gravity theory," Astrophys. Space Sci. **366**(1) (2021). https://doi.org/10.1007/s10509-020-03908-0

[20] C. P. Singh and S. Kaur, "Probing bulk viscous matter-dominated model in Brans-Dicke theory," Astrophys. Space Sci. **365**(1) (2019). https://doi.org/10.1007/s10509-019-3713-y

[21] R. Prasad, A. K. Yadav, and A. K. Yadav, "Constraining Bianchi type V universe with recent H(z) and BAO observations in Brans–Dicke theory of gravitation," Eur. Phys. J. Plus **135**(3) (2020). https://doi.org/10.1140/epjp/s13360-020-00308-9

[22] S. K. Tripathy, S. K. Pradhan, Z. Naik, D. Behera, and B. Mishra, "Unified dark fluid and cosmic transit models in Brans–Dicke theory," Phys. Dark Universe **30**, 100722 (2020). https://doi.org/10.1016/j.dark.2020.100722

[23] M. Visser, "Cosmography: Cosmology without the Einstein equations," Gen Relativ Gravit **37**, 1541–1548 (2005). https://doi.org/10.1007/s10714-005-0134-8

[24] M. Visser, "Jerk, snap and the cosmological equation of state," Class. Quantum Gravity **21**(11), 2603–2615 (2004). https://doi.org/10.1088/0264-9381/21/11/006

[25] V. Sahni, T. D. Saini, A. A. Starobinsky, and U. Alam, "Statefinder—A new geometrical diagnostic of dark energy," J. Exp. Theor. Phys. Lett. **77**(5), 201–206 (2003). https://doi.org/10.1134/1.1574831

[26] V. Sahni, A. Shafieloo, and A. A. Starobinsky, "Two new diagnostics of dark energy," Phys. Rev. D **78**(10) (2008). https://doi.org/10.1103/physrevd.78.103502

[27] S. Ray, U. Mukhopadhyay, and S. B. D. Choudhury, "Dark Energy Models with a time-dependent gravitational constant," Int. J. Mod. Phys. D **16**(11), 1791–1802 (2007). https://doi.org/10.1142/s0218271807011097

[28] S. Ray, U. Mukhopadhyay, S. Ray, and A. Bhattacharjee, "Dirac's large number hypothesis: A journey from concept to implication," Int. J. Mod. Phys. D **28**(08), 1930014 (2019). https://doi.org/10.1142/s0218271819300143

[29] A. Pradhan, G. Goswami, and A. Beesham, "The reconstruction of constant jerk parameter with f(R,T) gravity," J. High Energy Astrophys. **2023**. https://doi.org/10.1016/j.jheap.2023.03.001

[30] C. R. Mahanta, S. Deka, and M. P. Das, "Bianchi Type V Universe with Time Varying Cosmological Constant and Quadratic Equation of State in f(R,T) Theory of Gravity," East Eur. J. Phys. **1**, 44-52 (2023). https://doi.org/10.26565/2312-4334-2023-1-04

[31] G. P. Singh, A. Y. Kale, and J. Tripathi, "Dynamic cosmological 'constant'in brans dicke theory," Romanian Journal of Physics **58**(1-2), 23-35 (2013). https://rjp.nipne.ro/2013_58_1-2/0023_0035.pdf

[32] M. Moksud Alam, "Kaluza-Klein Cosmological Models with Barotropic Fluid Distribution," Phys. & Astron. Int. J. **1**(3) (2017). https://doi.org/10.15406/paij.2017.01.00018

[33] G. P. Singh, B. K. Bishi, and P. K. Sahoo, "Scalar field and time varying cosmological constant in f (R , T) gravity for Bianchi type-I universe," Chin. J. Phys. **54**(2), 244–255 (2016). https://doi.org/10.1016/j.cjph.2016.04.010

[34] R. K. Tiwari, F. Rahaman, and S. Ray, "Five Dimensional Cosmological Models in General Relativity," Int. J. Theor. Phys. **49**(10), 2348–2357 (2010). https://doi.org/10.1007/s10773-010-0421-3

[35] M. Tegmark, M. R. Blanton, M. A. Strauss, F. Hoyle, D. Schlegel, R. Scoccimarro, M. S. Vogeley, D. H. Weinberg, I. Zehavi, A. Berlind, T. Budavari, A. Connolly, D. J. Eisenstein, D. Finkbeiner, J. A. Frieman, J. E. Gunn, A. J. S. Hamilton, L. Hui, B. Jain, D. Johnston, S. Kent, H. Lin, R. Nakajima, R. C. Nichol, J. P. Ostriker, A. Pope, R. Scranton, U. Seljak, R. K. Sheth, A. Stebbins, A. S. Szalay, I. Szapudi, L. Verde, Y. Xu, J. Annis, N. A. Bahcall, J. Brinkmann, S. Burles, F. J. Castander, I. Csabai, J. Loveday, M. Doi, M. Fukugita, J. R. Gott III, G. Hennessy, D. W. Hogg, Ž. Ivezić, G. R. Knapp, D. Q. Lamb, and D. G. York, "The Three-Dimensional Power Spectrum of Galaxies from the Sloan Digital Sky Survey," Astrophys. J. **606**(2), 702–740 (2004). https://doi.org/10.1086/382125

[36] A. Pradhan and H. Amirhashchi, "Dark energy model in anisotropic Bianchi type-III space-time with variable EoS parameter," Astrophys. Space Sci. **332**(2), 441–448 (2010). https://doi.org/10.1007/s10509-010-0539-z

[37] R. Chaubey and A. K. Shukla, "The anisotropic cosmological models in f(R, T) gravity with Λ(T)," Pramana **88**(4) (2017). https://doi.org/10.1007/s12043-017-1371-6

[38] D. M. Gusu and M. V. Santhi, "Analysis of Bianchi Type V Holographic Dark Energy Models in General Relativity and Lyra's Geometry," Adv. High Energy Phys. **2021**, 1–11 (2021). https://doi.org/10.1155/2021/8818590

[39] S. Arora and P. K. Sahoo, "Energy conditions in f(Q, T) gravity," Phys. Scr. **95**(9), 095003 (2020). https://doi.org/10.1088/1402-4896/abaddc

[40] Singh JK, Pradhan A, Beesham A. Power law cosmology in modified theory with higher order curvature term. arXiv preprint arXiv:2304.09917. 2023 Apr 19. Available from: https://doi.org/10.48550/arXiv.2304.09917

[41] J. K. Singh and R. Nagpal, "FLRW cosmology with EDSFD parametrization," Eur. Phys. J. C **80**(4) (2020). https://doi.org/10.1140/epjc/s10052-020-7827-8

A Study of Evolution of Cosmological Parameters Based on a Dark Energy...

107

EEJP. 3 (2023)

[42] J. K. Singh, A. Singh, G. K. Goswami, and J. Jena, "Dynamics of a parametrized dark energy model in f(R,T) gravity," Ann. Phys. **2022**, 168958. https://doi.org/10.1016/j.aop.2022.168958

ДОСЛІДЖЕННЯ ЕВОЛЮЦІЇ КОСМОЛОГІЧНИХ ПАРАМЕТРІВ НА ОСНОВІ МОДЕЛІ ТЕМНОЇ ЕНЕРГІЇ В РАМКАХ ГРАВІТАЦІЇ БРАНСА-ДІКЕ

Судіпто Рой[a], Ріву Кайал[b], Сімран Алі[b], Срінджої Бандіопадхай[b], Дебаміта Бхаттачар'я[b]

[a]Департамерт фізики, Коледж Св. Ксав'єра, Колката, Західна Бенгалія, Індія
[b]Коледж Св. Ксав'єра, магістр фізики (2021-2023), Колката, Індія

Мета цього дослідження полягає в тому, щоб знайти характеристики еволюції однорідного та ізотропного Всесвіту в рамках теорії гравітації Бренса-Дікке (BD). Для отримання рівнянь поля BD використовувався простір-час FLRW з нульовою просторовою кривизною. Масштабний коефіцієнт і параметр Хаббла були отримані з підходу для параметра уповільнення, прийнятого на основі його властивості перевороту знаку, що вказує на зміну фази від уповільнення до прискорення. Перевірка моделі була досягнута відповідною параметризацією цього підходу. Виведено та зображено графічно вирази для густини енергії, тиску, параметра рівняння стану (EoS), космологічної постійної, гравітаційної постійної. Встановлено, що гравітаційна стала зменшується з часом зі швидкістю, що поступово зменшується. Параметр Хаббла, параметр уповільнення та щільність енергії зменшуються з часом, що узгоджується з багатьма іншими дослідженнями. Значення параметра EoS в сучасну епоху від'ємне, а з часом воно стає ще від'ємнішим. Космологічна стала дуже швидко зростає в ранньому Всесвіті від негативних до менших негативних значень, стаючи врешті позитивною, з набагато повільнішими змінами після цього. Проведено космографічний та геометричний аналіз. Спостерігається поступовий перехід від режиму «квінтесенції» до фантомної темної енергії. Важливим висновком цього дослідження є те, що характерна зміна параметра уповільнення відбувається майже одночасно з характерною зміною космологічної постійної, що означає зв'язок між прискореним розширенням і темною енергією, яка тут представлена космологічною сталою. На відміну від загальноприйнятої практики використання довільних одиниць, для всіх вимірних величин використовуються правильні одиниці СІ. Це теоретичне дослідження надає читачеві простий метод формулювання моделей у рамках теорії BD.

Ключові слова: *гравітація Бранса-Дікке; темна енергія; гравітаційна стала; космологічна стала; космографічний аналіз; Ом діагностика; діагностика стану*

FIVE - DIMENSIONAL PLANE SYMMETRIC COSMOLOGICAL MODEL WITH QUADRATIC EQUATION OF STATE IN $f(R,T)$ THEORY OF GRAVITY†

V.A. Thakare[a], 🆔 **R.V. Mapari**[b], 🆔 **S.S. Thakre**[c,*]

[a] Department of Mathematics, Shivaji Science College, Amravati (M.S.) India
[b] Department of Mathematics, Government Vidarbha Institute of Science and Humanities, Amravati
[c] Department of mathematics, Independent junior college, Amravati (M.S.) -444604 India
[*] Corresponding Author e-mail: swati.thakre11@gmail.com

In this paper, we analysed the five-dimensional plane symmetric cosmological model containing perfect fluid in the context of $f(R,T)$ gravity. Field equations have solved for two class of $f(R,T)$ gravity i.e., $f(R,T) = R + f(T)$ and $f(R,T) = f_1(R)f_2(T)$ with the inclusion of cosmological constant Λ and quadratic equation of state parameters in the form $p = \alpha\rho^2 - \rho$, where α is a constant and strictly $\alpha \neq 0$. In order to derive the exact solutions, we utilize volumetric power law and exponential law of expansion. The physical and geometrical aspects of model have discussed.

Keywords: *Quadratic equation of state; $f(R,T)$ gravity; cosmological constant; five-dimensional plane symmetric cosmological model*

PACS: 04.20.-q; 04.20. Jb; 04.50. Kd, 98.80.-K, 98.80. Es

1. INTRODUCTION

Over a significant period of time, scientific understanding suggested that the expansion of the universe was decelerating. However, recent astrophysical observations have indicated that our universe is actually undergoing an accelerated expansion [1, 2, 3, 4, 5]. This phenomenon is attributed to the presence of a mysterious form of energy, known as dark energy, which possesses a negative pressure. Dark energy comprises approximately 69% of the total energy content of the universe, while dark matter constitutes about 26%, and baryonic matter (ordinary matter) makes up the remaining 5%. The precise nature of dark energy and dark matter remains largely unknown. Scientists have proposed various theoretical explanations to account for the accelerated expansion of the universe. One approach involves the consideration of dark energy candidates such as quintessence [6], phantom models [7, 8], polytropic gas models [9], k-essence [10], tachyons [11], chaplygin gas [12, 13], and the cosmological constant Λ. The cosmological constant Λ represents a straightforward and natural candidate for explaining the expansion of the universe. It is essentially a modification to Einstein's field equations, serving as a classical correction factor. Incorporating the cosmological constant into the field equations is an effective means of generating accelerated expansion. However, this approach faces significant challenges, including the fine-tuning problem and the cosmic coincidence problem in cosmology [14, 15]. An alternative avenue involves modifying the geometric component of Einstein's Hilbert action, leading to the formulation of modified theories of gravity, such as $f(R)$ [16], $f(T)$ [17], $f(G)$ [18], $f(R,T)$ [19] theories of gravity. These modified gravity theories play a crucial role in successfully explaining the motion of galaxy clusters and the rotation curves of galaxies within the universe. By altering the underlying gravitational framework, these theories provide alternative explanations for the observed accelerated expansion while addressing certain shortcomings associated with the cosmological constant approach.

Harko et al. [19] have developed a novel modified theory of gravity called $f(R,T)$ gravity, which extends the concept of $f(R)$ gravity. This theory introduces an arbitrary function within the gravitational Lagrangian, involving both the Ricci scalar R and the trace T of the energy-momentum tensor. By employing metric formalization, the researchers derived the dynamic field equations for various choices of the Lagrangian. Several investigations have focused on studying plane symmetric cosmological models within the framework of $f(R,T)$gravity. Chirde and Shekh [20] have explored plane symmetric models of dark energy represented as a wet dark fluid in the context of $f(R,T)$ gravity. Pawar and Agrawal [21] examined plane symmetric cosmological models incorporating quark and strange quark matter within the framework of $f(R,T)$ gravity. Shamir [22] have investigated exact static solutions for plane symmetric systems in $f(R,T)$gravity. Shaikh and Bhoyar [23] discussed a deterministic solution of field equation for plane symmetric cosmological model with Λ in modified theory of gravity. Mollah et al. [24] have explored Bianchi type-III universe with quadratic equation of state in

---

Lyra geometry and they found the shear free dark energy cosmological model universe for large values of cosmic time t. Katore et al. [25] explored plane symmetric cosmological models incorporating perfect fluid and dark energy within the framework of general relativity (GR). In summary, Harko et al. proposed the $f(R,T)$ gravity an extension of $f(R)$ gravity and various researchers have since investigated different aspects of plane symmetric cosmological models within this modified theory. These studies have examined dark energy models, quark matter, static solutions and perfect fluid dynamics within the context of $f(R,T)$ gravity, thereby contributing to our understanding of the universe's behaviour.

In recent times, several researchers have focused on investigating various cosmological models within the framework of modified $f(R,T)$ gravity, aiming to elucidate the evolution of the universe during both early and late times. Adhav [26] examined a locally-rotationally-symmetric (LRS) Bianchi-I spacetime model assuming a constant expansion rate in the $f(R,T) = R + 2\lambda T$ gravity theory and obtained a solution and they have studied physical behaviour of the universe. However, the solutions presented by the author were found to be mathematically and physically invalid due to an incorrect field equation. Singh and Beesham [27] on the other hand considered the correct field equations and extended the solutions to incorporate a scalar field model (quintessence or phantom). They thoroughly explored the geometrical and physical properties associated with the solutions. Nagpal and her co-authors [28, 29, 30] have also investigated various aspects of $f(R,T)$ gravity. Katore and Hatkar [31] studied Kantowski-Sachs and Bianchi type III models incorporating a domain wall within the $f(R,T)$ theory. Singh and Singh [32] examined the anisotropic LRS Bianchi type-I metric with dark energy within the framework of the modified $f(R,T)$ theory. Aditya et al. [33] analysed a plane-symmetric dark energy model incorporating a massive scalar field. Singh et al. [34] have studied a spherically symmetric spacetime in a 5D setting was explored within the framework of $f(R,T)$ gravity, where the $f(R,T)$ gravity theory itself behaves as a dark energy model. Biswal et al. [35] presented a five-dimensional Kaluza-Klein cosmological model within the $f(R,T)$ theory of gravity, considering the presence of domain walls and obtained the solutions using Berman's proposed special law of variation parameter leading to a constant deceleration parameter. Dasunaidu et al. [36] investigated non-static five-dimensional spherically symmetric cosmological models in the presence of massive strings within the framework of $f(R,T)$ gravity. Pawar et al. [37] have discussed Bianchi type-V model in presence of perfect fluid with heat conduction using modified theory of gravity.

In the realm of relativity and cosmology, the equation of state plays a significant role as it defines the relationship between combined matter, temperature, pressure, and energy density within any region of space. The quadratic equation of state holds particular importance in Brane world models and the study of dark energy and general relativistic dynamics in different models [38, 39]. Furthermore, the quadratic equation of state governs the evolution of the universe from the Planck epoch to the de-Sitter epoch, making it an increasingly relevant topic. Thus, exploring the quadratic equation of state becomes crucial. The general form of the quadratic equation of state can be expressed as

$$p = p_0 + \alpha\rho + B\rho^2 \qquad (1)$$

Where, α, β, p_0 are parameters. Equation (1) indicates the first terms of the Taylor expansion of any equation of state parameter of the form $p = p(\rho)$ about $\rho = 0$.

Ananda and Bruni [40] examined the Robertson-Walker cosmological model with a non-linear quadratic equation of state. Ananda and Bruni [41] also investigated the impact of the quadratic equation of state, described by the equation,

$$p = \alpha\rho + \frac{\rho^2}{\rho_c} \qquad (2)$$

on anisotropic homogeneous and inhomogeneous cosmological models in general relativity, aiming to achieve isotropization of the universe as the initial singularity is approached.

Nojiri and Odintsov [42] have discussed the modifications to the general equation of state, including inhomogeneous and Hubble parameter-dependent terms, in the late-time universe. Capozziello et al. [43] presented observational constraints on dark energy models with a quadratic equation of state. Nojiri and Odintsov [42] and Capozziello et al. [43] demonstrated that the quadratic equation of state can describe dark energy or unified dark matter. Mahanta et al. [44] have explored Bianchi type-V universe in the context of $f(R,T)$ gravity for time varying cosmological constant and quadratic equation of state. Aygün et al. [45] have studied Mader space-time in presence of perfect fluid for different quadratic equation of state models in modified $f(R,T)$ gravity. Rahman [46] discussed an electromagnetic mass model with a quadratic equation of state in the context of general relativity. Chavanis [47] proposed a cosmological model based on a quadratic equation of state, unifying vacuum, radiation, and dark energy. Additionally, Chavanis [48] investigated a cosmological model that describes early inflation, intermediate decelerating expansion, and late accelerating expansion using a quadratic equation of state. Feroze and Siddiqui [49] explored charged anisotropic matter models with a quadratic equation of state in general relativity. Malaver [50] studied strange quark star models with a quadratic equation of state, obtaining a class of models characterized by anisotropic compact spheres, where the gravitational potential Z

depends on an adjustable parameter n. Bhar et al. [51] investigated compact stellar models obeying a quadratic equation of state. Maharaj and Takisa [52] derived new exact solutions of the Einstein-Maxwell field equations by considering a static and spherically symmetric spacetime with charged anisotropic matter distribution and a quadratic equation of state. Sharma and Ratanpal [53] obtained a class of solutions describing the interior of a static spherically symmetric compact anisotropic star, demonstrating that the model admits a quadratic equation of state. Singh and Bishi [54] discussed the Bianchi type-I cosmological model containing perfect fluid with a quadratic equation of state and cosmological constant within the framework of $f(R,T)$ gravity. Singh and Bishi [55] analysed solutions with a quadratic equation of state in the context of $f(R,T)$ gravity, including a cosmological constant Λ, for the Bianchi I transit universe, as expressed by equation

$$p = \alpha\rho^2 - \rho \tag{3}$$

where $\alpha \neq 0$ is a constant.

In summary, various researchers have investigated different aspects of the quadratic equation of state in cosmological and stellar models considering its implications for the behaviour of the universe, dark energy, anisotropy, compact objects, and other phenomena in the framework of general relativity and modified gravity theories. Motivated by the previous studies in cosmology, this paper focuses on investigating a higher-dimensional plane symmetric cosmological model that involves a perfect fluid with a quadratic equation of state within the framework of $f(R,T)$ theory. The structure of the paper is outlined as follows:

Section 2 provides a concise overview of the gravitational field equations derived from the modified $f(R,T)$ gravity theory. In Section 3, the metric and field equations for the specific case of $f(R,T) = R + 2f(T)$ are discussed. Section 4 presents the solutions obtained for the metric and field equations using the volumetric power law and exponential expansion law. Section 5 explores the field equations for the case of $f(R,T) = f_1(R) + f_2(T)$, along with their corresponding solutions using power law and exponential expansion laws. Finally, in Section 6, concluding remarks are provided to summarize the findings and implications of the study. In essence, this paper delves into the analysis of a higher-dimensional plane symmetric cosmological model within the $f(R,T)$ theory, specifically focusing on the presence of a perfect fluid with a quadratic equation of state. The paper follows a structured format, presenting the theoretical background, field equations, solutions, and concluding remarks in a coherent manner.

2. GRAVITATIONAL FIELD EQUATIONS OF $f(R,T)$ GRAVITY

The $f(R,T)$ theory of gravity is the modification or generalization of general relativity which is proposed by Harko et al. (2011). The action principle is,

$$s = \frac{1}{16\pi G} \int f(R,T)\sqrt{-g}d^4x + \int L_m\sqrt{-g}d^4x \tag{4}$$

Where, $f(R,T)$ is an arbitrary function of Ricci scalar R and trace T of the energy momentum tensor of matter T_{ij}. L_m is the matter Lagrangian density. The energy momentum tensor of matter is defined as,

$$T_{\alpha\beta} = -\frac{2}{\sqrt{-g}}\frac{\delta(\sqrt{-g}L_m)}{\delta g^{\alpha\beta}} \tag{5}$$

on varying the action with respect to metric tensor $g_{\alpha\beta}$, the field equations of $f(R,T)$ gravity are obtained as $f_R(R,T)$ gravity are obtained as

$$f_R(R,T)R_{\alpha\beta} - \frac{1}{2}f(R,T)g_{\alpha\beta} - f_R(R,T)(\nabla_\alpha\nabla_\beta - g_{\alpha\beta}\Box) = 8\pi T_{\alpha\beta} - f_T(R,T)(T_{\alpha\beta} + \Theta_{\alpha\beta}) \tag{6}$$

where,

$$\Theta_{\alpha\beta} = -2T_{\alpha\beta} + g_{\alpha\beta}L_m - 2g^{lk}\frac{\partial^2 L_m}{\partial g_{\alpha\beta}\partial g^{lk}} \tag{7}$$

Here, $f_R(R,T) = \frac{\partial f(R,T)}{\partial R}$, $f_T(R,T) = \frac{\partial f(R,T)}{\partial T}$, $\Box = \nabla^\alpha\nabla_\alpha$ where ∇_α is the covariant derivative
Now contraction of equation (6) gives

$$f_R(R,T)R + 3f_R(R,T) - 2f(R,T) = 8\pi T - f_T(R,T)(T + \Theta) \tag{8}$$

where $\Theta = g^{\alpha\beta}\Theta_{\alpha\beta}$ eqn. (8) gives relation between Ricci scalar R and the trace T of energy momentum tensor. In the present study, we assume that the stress energy tensor of matter is given by,

$$T_{\alpha\beta} = (\rho + p)u_\alpha u_\beta - pg_{\alpha\beta} \tag{9}$$

Where, p and ρ indicates pressure and density of fluid. Here, $u^{\alpha} = (0, 0, 0, 0, 1)$ is the five-velocity vector in co-moving co-ordinate system and satisfies the conditions, $u_{\alpha} u^{\alpha} = 1$ and $u^{\alpha} \nabla_{\beta} u_{\alpha} = 0$. We choose matter Lagrangian as $L_m = -p$, which yields the

$$\theta_{\alpha\beta} = -pg_{\alpha\beta} - 2T_{\alpha\beta} \tag{10}$$

It may be mentioned that these field equations depend on physical nature of matter field. As $f(R, T)$ gravity depends on matter field, many theoretical models corresponding to different matter could be derived. The Three classes of three of these models are given as follow

$$f(R, T) = \begin{cases} R + 2f(T) \\ f_1(R) + f_2(T) \\ f_1(R) + f_2(R) f_3(T) \end{cases}$$

In this present work, we have focused on two classes of $f(R, T)$. i.e. first class $f(R, T) = R + 2f(T)$ and second class $f(R, T) = f_1(R) + f_2(T)$. for the choice of $f(R, T) = R + 2f(T)$ gravitational field equation of $f(R, T)$ modified gravity with the help of eqn. (8) and (9), eqn. (6) becomes

$$R_{\alpha\beta} - \frac{1}{2}g_{\alpha\beta}R = 8\pi T_{\alpha\beta} + 2f^{'}(T) T_{\alpha\beta} + \left[f(T) + 2Pf^{'(T)} \right] g_{\alpha\beta} \tag{11}$$

where, an overhead prime denotes differentiation with respect to the argument T.
for the choice of $f(R, T) = f_1(R) + f_2(T)$ gravitational field equation of $f(R, T)$ gravity with the help of eqn. (8) and (9), eqn. (6) becomes

$$f_1^{'}(R) R_{\alpha\beta} - \frac{1}{2}f_1(R) g_{\alpha\beta} + (g_{\alpha\beta\square} - \nabla_{\alpha}\nabla_{\beta}) f_1^{'}(R) = (8\pi + f_2'(T)) T_{\alpha\beta} + \left(f_2'(T) p + \frac{1}{2}f_2(T) \right) g_{\alpha\beta} \tag{12}$$

3. METRIC AND FIELD EQUATIONS FOR $f(R, T) = R + 2f(T)$

Higher dimensional plane symmetric cosmological model given by

$$ds^2 = dt^2 - R_1{}^2 \left(dx^2 + dy^2 \right) - R_2{}^2 dz^2 - R_3{}^2 d\omega^2 \tag{13}$$

here R_1, R_2, R_3 are matric potentials which are functions of cosmic time t.
Now using a co-moving coordinate system, the field equations (11) with the help of equation (9) for the metric (13) can be explicitly written as

$$\frac{\ddot{R}_1}{R_1} + \frac{\ddot{R}_2}{R_2} + \frac{\ddot{R}_3}{R_3} + \frac{\dot{R}_1\dot{R}_2}{R_1R_2} + \frac{\dot{R}_1\dot{R}_3}{R_1R_3} + \frac{\dot{R}_2\dot{R}_3}{R_2R_3} = (8\pi + 4\lambda)p - \lambda\rho - \Lambda \tag{14}$$

$$2\frac{\ddot{R}_1}{R_1} + 2\frac{\dot{R}_1\dot{R}_3}{R_1R_3} + \left(\frac{\dot{R}_1}{R_1}\right)^2 + \frac{\ddot{R}_3}{R_3} = (8\pi + 4\lambda)p - \lambda\rho - \Lambda \tag{15}$$

$$2\frac{\ddot{R}_1}{R_1} + \frac{\ddot{R}_2}{R_2} + \left(\frac{\dot{R}_1}{R_1}\right)^2 + 2\frac{\dot{R}_1\dot{R}_2}{R_1R_2} = (8\pi + 4\lambda)p - \lambda\rho - \Lambda \tag{16}$$

$$2\frac{\dot{R}_1\dot{R}_2}{R_1R_2} + 2\frac{\dot{R}_1\dot{R}_3}{R_1R_3} + \frac{\dot{R}_2\dot{R}_3}{R_2R_3} + \left(\frac{\dot{R}_1}{R_1}\right)^2 = -(8\pi + 3\lambda)\rho + 2p\lambda - \Lambda \tag{17}$$

Here overhead dot represents derivative with respect to t.
Dynamical parameters for five-dimensional plane symmetric cosmological model are defined as follows:
The spatial volume $V = a^4(t) = R_1{}^2 R_2 R_3$
The directional Hubble parameters

$$H_x = H_y = \frac{\dot{R}_1}{R_1} , \ H_z = \frac{\dot{R}_2}{R_2}, H_{\omega} = \frac{\dot{R}_3}{R_3}$$

The generalized mean Hubble's parameter H is given as

$$H = \frac{1}{4}\left(2\frac{\dot{R}_1}{R_1} + \frac{\dot{R}_2}{R_2} + \frac{\dot{R}_3}{R_3} \right) \tag{18}$$

The expansion Scalar θ is given by,

$$\theta = 4H = 2\frac{\dot{R_1}}{R_1} + \frac{\dot{R_2}}{R_2} + \frac{\dot{R_3}}{R_3} \tag{19}$$

The Shear Scalar and the mean anisotropic parameter are defined as

$$\sigma^2 = \frac{4}{2}\Delta H^2 \tag{20}$$

and

$$A_m = \frac{1}{4}\sum_{i=1}^{4}\left(\frac{H_i - H}{H}\right)^2 \tag{21}$$

4. SOLUTIONS OF FIELD EQUATIONS

After solving eqns. (14) – (17), we get

$$\frac{R_1}{R_2} = k_1 exp\left[x_1 \int \frac{dt}{V}\right] \tag{22}$$

$$\frac{R_2}{R_3} = k_2 exp\left[x_2 \int \frac{dt}{V}\right] \tag{23}$$

$$\frac{R_3}{R4} = k_3 exp\left[x_3 \int \frac{dt}{V}\right] \tag{24}$$

where k_1, k_2, k_3 and x_1, x_2, x_3 are constant of integration which satisfies the relation

$$k_3 = k_1 k_2 \ and \ x_3 = x_2 + x_1$$

Using above Eqns. (22) (23) and (24), we can write the metric functions A, B and C explicitly as

$$R_1 = K_1 V^{\frac{1}{4}} \ exp\left[X_1 \int \frac{dt}{V}\right] \tag{25}$$

$$R_2 = K_2 V^{\frac{1}{4}} exp\left[X_2 \int \frac{dt}{V}\right] \tag{26}$$

$$R_3 = K_3 V^{\frac{1}{4}} \ exp\left[X_3 \int \frac{dt}{V}\right] \tag{27}$$

where $K_1, \ K_2, \ K_3$ and $X_1, \ X_2, \ X_3$ are constant of integration which satisfies the relation
$K_1{}^2 K_2 K_3 = 1$ and $2X_1 + X_2 + X_3 = 0$
Now, using Eq. (14) and (17), we obtain

$$\rho^2 = \frac{1}{\alpha\left(8\pi + 2\lambda\right)}\left[\frac{\ddot{R_1}}{R_1} + \frac{\ddot{R_2}}{R_2} + \frac{\ddot{R_3}}{R_3} - \frac{\dot{R_1}\dot{R_3}}{R_1 R_3} - \left(\frac{\dot{R_1}}{R_1}\right)^2 - \frac{\dot{R_1}\dot{R_2}}{R_1 R_2}\right] \tag{28}$$

To solve the Einstein's modified field equations for the system having four equations and six unknowns (R_1, R_2, R_3, p, ρ, Λ). To obtain the complete solution, we need two more physically plausible relations.
1. Quadratic Equation of State
2. Expansion Law
Power Law

$$V = V_1 t^n \tag{29}$$

Exponential law

$$V = V_1 e^{4\beta t} \tag{30}$$

4.1. Power Law Model

$$V = V_1 t^n$$

where, V_1 and n are constant.
Then metric potential become

$$R_1 = K_1 V_1^{\frac{1}{4}} t^{\frac{n}{4}} exp\left[\frac{X_1}{V_1}\frac{t^{1-n}}{1-n}\right] \tag{31}$$

$$R_2 = K_2 V_1^{\frac{1}{4}} t^{\frac{n}{4}} exp\left[\frac{X_2}{V_1}\frac{t^{1-n}}{1-n}\right] \tag{32}$$

$$R_3 = K_3 V_1^{\frac{1}{4}} t^{\frac{n}{4}} exp\left[\frac{X_3}{V_1}\frac{t^{1-n}}{1-n}\right] \tag{33}$$

As the time t approaching zero, the analysis indicates that all the metric potentials become zero. As a result, the model exhibits an initial singularity.
The directional Hubble parameter $H_x = H_y, H_z, H_\omega$ are given as

$$H_x = H_y = \frac{n}{4t} + \frac{X_1}{V_1 t^n} \tag{34}$$

$$H_z = \frac{n}{4t} + \frac{X_2}{V_1 t^n} \tag{35}$$

$$H_\omega = \frac{n}{4t} + \frac{X_3}{V_1 t^n} \tag{36}$$

Mean Hubble parameter H is given by

$$H = \frac{n}{4t} \tag{37}$$

Anisotropy parameter of the expansion is

$$\Delta = \frac{4X^2}{n^2 V_1^2 t^{2(n-1)}} \tag{38}$$

where $2X_1^2 + X_2^2 + X_3^2 = X^2$
Dynamical scalar is given by

$$\theta = 4H = \frac{n}{t} \tag{39}$$

Deceleration parameter q is given by,

$$q = \frac{d}{dt}\left(\frac{1}{H}\right) - 1 = \frac{4}{n} - 1 \tag{40}$$

Shear scalar

$$\sigma^2 = \frac{4}{2}\Delta H^2 = \frac{X^2}{2V_1^2 t^{2n}} \tag{41}$$

Using equation (28)

$$\rho = \sqrt{\frac{1}{\alpha\,(8\pi + 2\lambda)}\left[\frac{X_2^2 + X_3^2 - X_1(X_2 + X_3)}{(V_1 t^n)^2} - \frac{3n}{t^2}\right]} \tag{42}$$

Using Eqn. (42) in Eqn. (3) pressure is obtained as

$$p = \frac{1}{8\pi + 2\lambda}\left[\frac{X_2^2 + X_3^2 - X_1(X_2 + X_3)}{(V_1 t^n)^2} - \frac{3n}{t^2}\right] - \sqrt{\frac{1}{\alpha\,(8\pi + 2\lambda)}\left[\frac{X_2^2 + X_3^2 - X_1(X_2 + X_3)}{(V_1 t^n)^2} - \frac{3n}{t^2}\right]} \tag{43}$$

With the help of Eqn. (15)

$$\Lambda = \frac{(4\pi + 2\lambda)}{(4\pi + \lambda)}\left[\frac{X_2^2 + X_3^2 - X_1(X_2 + X_3)}{(V_1 t^n)^2} - \frac{3n}{t^2}\right] - (8\pi + 5\lambda)\sqrt{\frac{1}{\alpha\,(8\pi + 2\lambda)}\left[\frac{X_2^2 + X_3^2 - X_1(X_2 + X_3)}{(V_1 t^n)^2} - \frac{3n}{t^2}\right]}$$

$$-6\left(\frac{n}{4t}\right)^2 - \frac{\left[3X_1{}^2 + X_3{}^2 + 2X_1X_3\right]}{\left(V_1t^n\right)^2} + \frac{2n}{t^2} \tag{44}$$
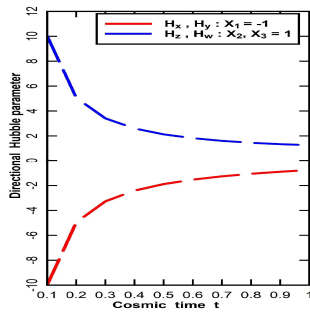
Figure 1.
Directional Hubble Parameter Vs Cosmic time t
for $n, V_1, n, X_2, X_3 = 1, X_1 = -1$.
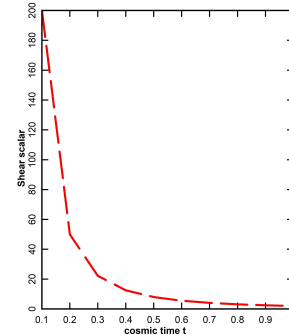
Figure 2.
Shear scalar Vs Cosmic time t for
$n, V_1, X_2, X_3 = 1, X_1 = -1$.
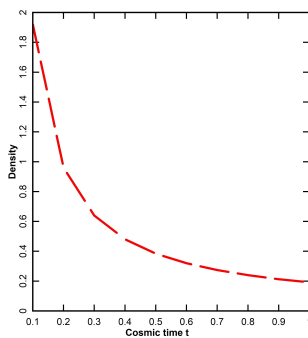
Figure 3.
Density Vs Cosmic time t for α,
$V_1, X_2, X_3, \lambda, n = 1, X_1 = -1$.
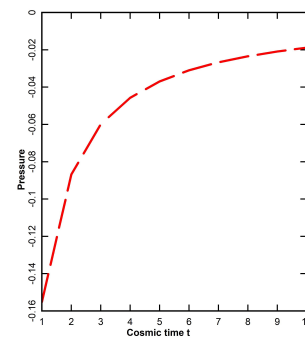
Figure 4.
Pressure Vs Cosmic time t for α,
$V_1, X_2, X_3, \lambda, n = 1, X_1 = -1$.

4.2. Exponential Law Model

We consider model for exponential expansion.

$$V = V_1 e^{4\beta t}$$

Then the scale factor can be obtained by using

$$R_1 = K_1 V_1{}^{\frac{1}{4}} e^{\beta t} \exp\left(\frac{-X_1}{4V_1\beta} e^{-4\beta t}\right) \tag{45}$$

$$R_2 = K_2 V_1{}^{\frac{1}{4}} e^{\beta t} \left(\frac{-X_2}{4V_1\beta} e^{-4\beta t}\right) \tag{46}$$

$$R_3 = K_3 V_1{}^{\frac{1}{4}} e^{\beta t} exp\left(\frac{-X_3}{4V_1\beta} e^{-4\beta t}\right) \tag{47}$$

Evidently, the metric potentials maintain constant values during the initial period and subsequently undergo time-dependent evolution without encountering any form of singularity. Eventually, they diverge towards infinity. This aligns with the concept of the big bang scenario, reminiscent of the findings presented in the Shaikh and Bhoyar [23].
The directional Hubble parameter are given as

$$H_x = \left(\frac{X_1}{V_1 e^{4\beta t}} + \beta\right) \tag{48}$$

$$H_Z = \left(\frac{X_2}{V_1 e^{4\beta t}} + \beta \right) \tag{49}$$

$$H_\omega = \left(\frac{X_3}{V_1 e^{4\beta t}} + \beta \right) \tag{50}$$

Mean Hubble parameter

$$H = \beta \tag{51}$$

At the time t equals zero, the directional Hubble parameters possess finite values. These parameters deviate from the average Hubble parameter due to the influence of factor β.

Anisotropy parameter

$$\Delta = \frac{X^2}{4\beta^2 (V_1 e^{4\beta t})^2} \tag{52}$$

where $2X_1{}^2 + X_2{}^2 + X_3{}^2 = X^2$

Dynamical scalar is given by

$$\sigma^2 = \frac{X^2}{2(V_1 e^{\beta t})^2} \tag{53}$$

Deceleration parameter is given by

$$q = -1 \tag{54}$$

With increasing time t, the expansion's anisotropy diminishes exponentially until it reaches null. As a result, the space converges towards isotropy in accordance with this model.

Using the values of metric potentials R_1, R_2, R_3 and substituting the quadratic equation of state in the form $p = \alpha \rho^2 - \rho$ we obtained the energy density ρ and Λ.

$$\rho = \sqrt{\frac{1}{\alpha (8\pi + 2\lambda)} \left[\frac{X_2{}^2 + X_3{}^2 - X_1(X_2 + X_3{}_)}{(V_1 e^{4\beta t})^2} \right]} \tag{55}$$

$$p = \frac{1}{(8\pi + 2\lambda)} \left[\frac{X_2{}^2 + X_3{}^2 - X_1(X_2 + X_3)}{(V_1 e^{4\beta t})^2} \right] - \sqrt{\frac{1}{\alpha (8\pi + 2\lambda)} \left[\frac{X_2{}^2 + X_3{}^2 - X_1(X_2 + X_3)}{(V_1 e^{4\beta t})^2} \right]} \tag{56}$$

$$\Lambda = \frac{(4\pi + 2\lambda)}{(4\pi + \lambda)} \left[\frac{X_2{}^2 + X_3{}^2 - X_1(X_2 + X_3{}_)}{(V_1 e^{4\beta t})^2} \right] - \frac{(8\pi + 5\lambda)}{V_1 e^{4\beta t}} \sqrt{\frac{1}{\alpha (8\pi + 2\lambda)} \left[X_2{}^2 + X_3{}^2 - X_1(X_2 + X_3{}) \right]}$$
$$- 6\beta^2 - \frac{\left[3X_1{}^2 + X_3{}^2 + 2X_1 X_3 \right]}{(V_1 e^{4\beta t})^2} \tag{57}$$
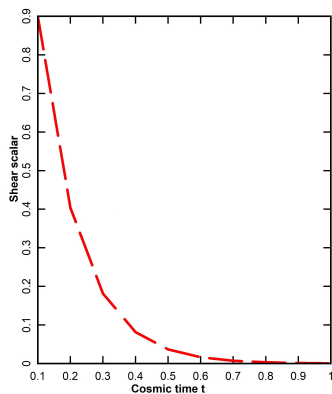
Figure 5.
Shear Scalar vs Cosmic time t for β,
$V_1, X_2, X_3 = 1, X_1 = -1$.
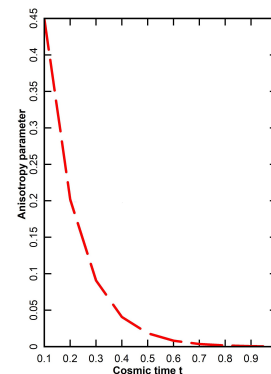
Figure 6.
Anisotropy Parameter vs Cosmic time t for β,
$V_1, X_2, X_3 = 1, X_1 = -1$.
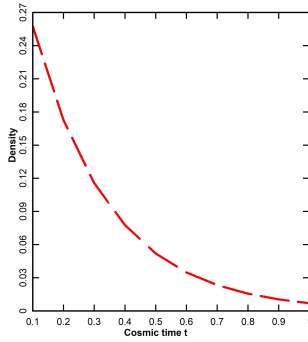
Figure 7.
Density vs Cosmic time t for β,
$V_1, X_2, X_3, \lambda, \alpha = 1, \pi = 3.14, X_1 = -1$.
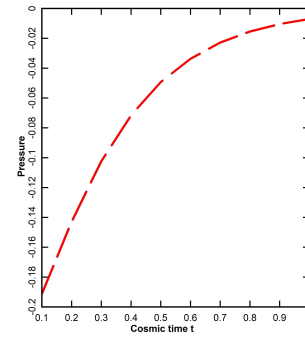
Figure 8.
Pressure vs Cosmic time t for β,
$V_1, X_2, X_3, \lambda = 1, \pi = 3.14, X_1 = -1$.

5. FIELD EQUATIONS FOR $f(R,T) = f_1(R) + f_2(R)$

In $f(R,T)$, with the choice of $f_1(R) = \lambda R, f_2(T) = \lambda T$ gravitational field equation (12) along with cosmological constant Λ appears as follows:

$$G_{ij} = \left(\frac{8\pi + \lambda}{\lambda}\right) T_{ij} + \left(\frac{\rho - p + 2\Lambda}{2}\right) g_{ij}$$

In this case, field equations are given by

$$\frac{\ddot{R}_1}{R_1} + \frac{\ddot{R}_2}{R_2} + \frac{\ddot{R}_3}{R_3} + \frac{\dot{R}_1\dot{R}_2}{R_1 R_2} + \frac{\dot{R}_1\dot{R}_3}{R_1 R_3} + \frac{\dot{R}_2\dot{R}_3}{R_2 R_3} = \frac{(8\pi + 2\lambda)}{\lambda} p - \frac{\rho}{2} - \Lambda \tag{58}$$

$$2\frac{\ddot{R}_1}{R_1} + 2\frac{\dot{R}_1\dot{R}_3}{R_1 R_3} + \left(\frac{\dot{R}_1}{R_1}\right)^2 + \frac{\ddot{R}_3}{R_3} = \frac{(8\pi + 2\lambda)}{\lambda} p - \frac{\rho}{2} - \Lambda \tag{59}$$

$$2\frac{\ddot{R}_1}{R_1} + \frac{\ddot{R}_2}{R_2} + \left(\frac{\dot{R}_1}{R_1}\right)^2 + 2\frac{\dot{R}_1\dot{R}_2}{R_1 R_2} = \frac{(8\pi + 2\lambda)}{\lambda} p - \frac{\rho}{2} - \Lambda \tag{60}$$

$$2\frac{\dot{R}_1\dot{R}_3}{R_1 R_3} + 2\frac{\dot{R}_1\dot{R}_2}{R_1 R_2} + \frac{\dot{R}_2\dot{R}_3}{R_2 R_3} + \left(\frac{\dot{R}_1}{R_1}\right)^2 = -\frac{(16\pi + 3\lambda)}{2\lambda} \rho + p - \Lambda \tag{61}$$

5.1. Power law Model

By adopting the same procedure as in subsection 4.1, we have obtained the same metric potential as in equation (31) (32) and (33). Using the values of metric potential R_1, R_2, R_3 and substituting the quadratic equation of state in the form $p = \alpha\rho^2 - \rho$, we obtained the energy density ρ, pressure p and cosmological constant Λ as follows:

$$\rho = \sqrt{\frac{\lambda}{\alpha(8\pi + \lambda)} \left[\frac{X_2{}^2 + X_3{}^2 - X_1(X_2 + X_3)}{(V_1 t^n)^2} - \frac{3n}{t^2}\right]} \tag{62}$$

$$p = \frac{\lambda}{8\pi + \lambda}\left[\frac{X_2{}^2 + X_3{}^2 - X_1(X_2 + X_3)}{(V_1 t^n)^2} - \frac{3n}{t^2}\right] - \sqrt{\frac{\lambda}{\alpha(8\pi + \lambda)}\left[\frac{X_2{}^2 + X_3{}^2 - X_1(X_2 + X_3)}{(V_1 t^n)^2} - \frac{3n}{t^2}\right]} \tag{63}$$

$$\Lambda = \frac{(8\pi + 2\lambda)\lambda}{(8\pi + \lambda)}\left[\frac{X_2{}^2 + X_3{}^2 - X_1(X_2 + X_3)}{(V_1 t^n)^2} - \frac{3n}{t^2}\right] - \left(\frac{16\pi + 5\lambda}{2\lambda}\right)\sqrt{\frac{\lambda}{\alpha(8\pi + \lambda)}\left[\frac{X_2{}^2 + X_3{}^2 - X_1(X_2 + X_3)}{(V_1 t^n)^2} - \frac{3n}{t^2}\right]}$$

$$-6\left(\frac{n}{4t}\right)^2 - \frac{[3X_1{}^2 + X_3{}^2 + 2X_1 X_3]}{(V_1 t^n)^2} + \frac{2n}{t^2} \tag{64}$$
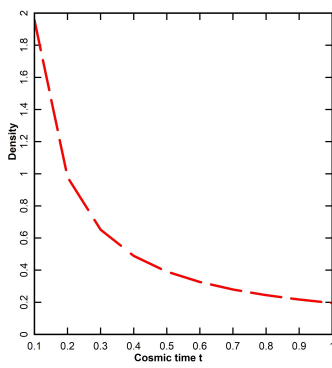
Figure 9.
Density vs Cosmic time t for β,
$V_1, X_2, X_3, \lambda, \alpha = 1, \pi = 3.14, X_1 = -1$.
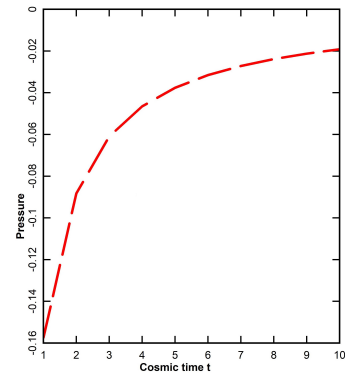
Figure 10.
Pressure vs Cosmic time t for β,
$V_1, X_2, X_3, \lambda, \alpha = 1, \pi = 3.14, , X_1 = -1$.

In this context, we have observed a comparable outcome similar to findings presented in section 4.1

5.2. Exponential Law Model

By adopting the same procedure as in subsection 4.2, we have obtained the same metric potential as in equation (45) (46) and (47). Using the values of metric potential R_1, R_2, R_3 and substituting the quadratic equation of state in the form $p = \alpha\rho^2 - \rho$, we obtained the energy density ρ, pressure p and cosmological constant Λ as follows:

$$\rho = \sqrt{\frac{\lambda}{\alpha\,(8\pi + \lambda)}\left[\frac{X_2{}^2 + X_3{}^2 - X_1(X_2 + X_{3\ })}{(V_1 e^{4\beta t})^2}\right]} \tag{65}$$

$$p = \frac{\lambda}{(8\pi + \lambda)}\left[\frac{X_2{}^2 + X_3{}^2 - X_1\,(X_2 + X_3)}{(V_1 e^{4\beta t})^2}\right] - \sqrt{\frac{\lambda}{\alpha\,(8\pi + \lambda)}\left[\frac{X_2{}^2 + X_3{}^2 - X_1(X_2 + X_{3\ })}{(V_1 e^{4\beta t})^2}\right]} \tag{66}$$

$$\Lambda = \frac{(8\pi + 2\lambda)}{(8\pi + \lambda)}\left[\frac{X_2{}^2 + X_3{}^2 - X_1(X_2 + X_{3\ })}{(V_1 e^{4\beta t})^2}\right] - \frac{(16\pi + 5\lambda)}{2\lambda}\sqrt{\frac{\lambda\,\left[X_2{}^2 + X_3{}^2 - X_1\,(X_2 + X_{3\ })\right]}{\alpha\,(8\pi + \lambda)\,(V_1 e^{4\beta t})^2}}$$
$$- 6\beta^2 - \frac{\left[3X_1{}^2 + X_3{}^2 + 2X_1 X_3\right]}{(V_1 e^{4\beta t})^3} \tag{67}$$
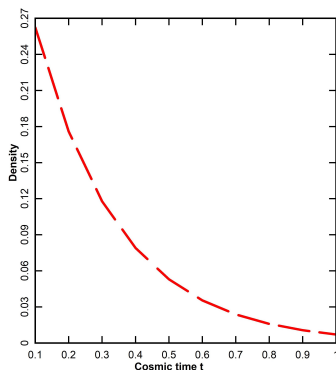
Figure 11.
Density vs Cosmic time t for β,
$V_1, X_2, X_3, \lambda, \alpha = 1, \pi = 3.14, X_1 = -1$.
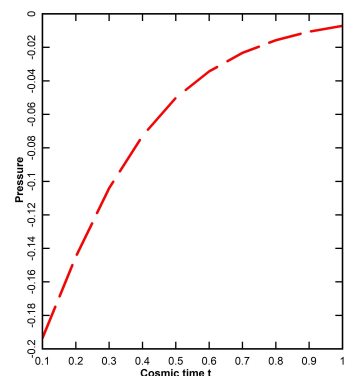
Figure 12.
Pressure vs Cosmic time t for β,
$V_1, X_2, X_3, \lambda, \alpha = 1, \pi = 3.14, , X_1 = -1$.

In this context, we have observed a comparable outcome similar to findings presented in section 4.2

6. OBSERVATION AND DISCUSSION

To decipher the exact solution of five- dimensional plane symmetric cosmological model we assumed power law expansion and exponential expansion law, in the previous section. We have found that

- In section 4.1, for Power Law Model.

  - Figure 1 represent that he directional Hubble parameter H_x and H_y in the direction x and y are increasing function of cosmic time t whereas directional Hubble parameter H_z , H_w in the direction z, w are decreasing function of cosmic time t.

  - Now from Figure 2 and equation (41), it is clear that the shear scalar is decreasing function of cosmic time t. At initial epoch, when time $t = 0$ shear scalar start with infinite value and vanishes as $t \rightarrow \infty$.

  - Figure 3 of equation (42), illustrate the variation of energy density ρ against time t . Here it is observed that energy density is positive function that decreases over time.

  - By analysing Figure 4 of equation (43), it is observed that pressure is increasing function of time. Initially, it begins from large negative value and gradually approaches to small negative value close to zero.

- In section 4.2, for exponential expansion model

  - From Figure 5 and 6, it is clear that shear scalar and anisotropy parameter are decreasing function of time t whereas for large time t universe approaches to isotropy.

  - The graph of energy density and pressure are shown in Figure 7 and Figure 8 respectively. Figure 7 shows that energy density is positive decreasing function over time t.

  - Figure 8 reveals that the pressure starts from significantly large negative value and approaches to small negative value close to zero. This result consistent with prior studies referenced in reference [23]

- In section 5

  - In this context, we have observed a comparable outcome similar to findings presented in section 4.1 and 4.2. for power law model we found that pressure Figure 10 and density Figure 9 exhibited identical graphs to pressure Figure 4 and density Figure 3

  - Similarly, for exponential expansion model, we found that density Figure 11 and pressure Figure 12 exhibited identical graphs to density Figure 7 and pressure Figure 8

7. CONCLUSION

We investigated the intricate details of a five-dimensional plane symmetric cosmological model governed by $f(R,T)$ gravity, taking into consideration the influence of a cosmological constant and employing a quadratic equation of state. The motivation for this inquiry originates from the desire to investigate modified gravity theories that go beyond the traditional general relativity framework, allowing for a more thorough understanding of the universe's behaviour and evolution. We studied two unique classes of functionals within the $f(R,T)$ gravity framework. The first is represented by $f(R,T) = R + f(T)$, and the second by $f(R,T) = f1(R) \, f2(T)$. To examine the model's behaviour, we used a quadratic equation of state and an expansion rule to find an exact solution to the field equations, yielding vital insights into the evolution of the cosmos within the considered framework. From both the models of $f(R,T)$ we have following findings.

In power law model, several intriguing findings emerge from our investigation. Because of the positive average Hubble parameter $(H > 0)$, we see an expanding cosmos. However, as time passes towards infinity, the expansion slows and eventually approaches zero. This behaviour is consistent with our assumptions and lends support to the idea of a universe approaching zero expansion asymptotically. Interestingly, we discover that the pace of expansion of the universe is extremely fast during the early stages of cosmic time $(0 < t < 1)$, followed by a slowing of the growth for $t > 1$. This behaviour implies a transition from a quick early phase to a more steady expansion over time. These findings are consistent with prior studies referenced in references [56, 57], which validates our methodology and increases the credibility of our findings. Furthermore, we have detected anisotropy and shearing in the cosmos throughout its whole existence. This implies that the universe has directional deviations and a lack of perfect symmetry, which could have serious ramifications for the distribution and evolution of matter on cosmic scales.

Additionally, our analysis indicates that the universe undergoes accelerated expansion for values of the parameter $n > 4$, as deduced from equation (40). This finding aligns with current observations [58], providing further support for the validity of the model and its ability to reproduce essential features of the real universe.

Examining the evolution of physical quantities, we find that the density of the cosmic fluid decreases as cosmic time progresses, as depicted in Figure 3. This decrease in density suggests that the universe becomes less dense as it expands, a result that is in line with our expectations and consistent with our understanding of cosmological expansion. Furthermore, our investigation reveals the presence of negative pressure, as illustrated in Figure 4. This negative pressure is a characteristic feature of dark energy. Its presence within the model lends support to the notion that dark energy plays a significant role in shaping the dynamics of our cosmos.

In exponential expansion model, we have obtained significant findings regarding this particular model including the deceleration parameter (q) and the rate of change of Hubble parameter $\left(\frac{dH}{dt}\right)$.These findings are indicative of the model's ability to provide highly accurate values for the Hubble parameter, while effectively representing both the inflationary era during the early stages of the universe and the late-time evolution. In this model, the directional Hubble parameters have finite values at both the beginning $t \to 0$ and the far future $t \to \infty$ while the mean Hubble parameter remains constant. The expansion scalar, which measures the rate of expansion of the universe remains constant throughout its evolution, indicating uniform exponential expansion.Anisotropic expansion of universe measures constant value at initial time t while it decreases as time progresses and finally tends to zero at infinite time.From Figure 5 the shear scalar is finite at initial epoch while the Shear Scalar approaches zero as time approaches infinity i.e. $\sigma \to 0$ as $t \to \infty$. This indicates that the anisotropy of the universe diminishes over time, eventually tending towards isotropy. The sign of the deceleration parameter q determines whether the universe is accelerating or decelerating. A positive value of q corresponds to the standard decelerating model while a negative value indicates acceleration. Current cosmological observations support the notion that the expansion of the universe is accelerating at present, whereas it was decelerating in the past. From the equation (54), we find that the deceleration parameter is negative aligning with the current observations of Type Ia supernovae and the cosmic microwave background (CMB). This result resembles with the Singh and Bishi [54].The expansion scalar, which measures the rate at which the universe expands remains constant throughout the entire evolution, thereby indicating a uniform exponential expansion.At the initial time the anisotropy parameter remains constant and diminishes as time advances.This implies that the universe was initially anisotropic but steadily moves towards isotropy as time elapses. This behavior is visually depicted in Figure5.

Overall, our study provides a comprehensive analysis of a five-dimensional plane symmetric cosmological model within the framework of $f(R,T)$ gravity. By incorporating a quadratic equation of state and exact solutions to the field equations, we have gained valuable insights into the nature of the universe, its expansion, anisotropy, and the presence of dark energy. Our findings not only contribute to the advancement of theoretical cosmology but also align with current observations, consolidating our understanding of the universe's behavior at both early and late cosmic timescales.

ORCID

⬤ **R.V. Mapari**, https://orcid.org/0000-0002-5724-9734
⬤ **S.S. Thakre**, https://orcid.org/0009-0009-9665-5530

REFERENCES

[1] A.G. Riess, A.V. Fillippenko, P. Cgallis, et al., "Observational evidence from supernovae for an accelerating universe and a cosmological constant," Astron J. **116**(3), 1009 (1998). https://doi.org/10.1086/300499

[2] S. Perlmutter, G. Aldering, G. Goldhaber, et al., "Measurement of Ω and Λ from 42 High – redshift Supernovae," Astrophys. J. **517**, 565 (1999). https://doi.org/10.1086/307221.

[3] W.J. Percival, "The build – up of haloes within Press – Schechter theory," Mon. Not. R. Astron. Soc. **327**, 1313(2001). https://doi.org/10.1046/j.1365-8711.2001.04837.x

[4] R. Jimenez, L. Verde, T. Tren, and D. Stern, "Constraint on the equation of state of dark energy and Hubble constant from stellar ages and the CMB," Astrophys. J. **593**, 622 (2003). https://doi.org/10.1086/376595

[5] D. Stern, R. Jimenez, L. Verde, M. Kamionkowski, and S.A. Stanford, "Cosmic chronometers: constraining the equation of state of dark energy. $I : H(z)$ measurements," J. Cosmolo. Astropart. Phys. **2**, 8 (2010). https://doi.org/10.48550/arXiv.0907.3149.

[6] J. Martin, "Quintessence: A Mini-Review," Mod. Phys. Lett. A, **23**, 1252 (2008). http://doi.org/10.1142/S0217732308027631

[7] S. Nojiri, S. D. Odintsov, and M. Sami, "Dark energy cosmology from higher – order, string-inspired gravity and its reconstruction," Phys. Rev. D, **74**, 046004 (2006). https://doi.org/10.1103/PhysRevD.74.046004

[8] N. Bilic¸ fortschritte der Physik, "Thermodynamics of dark energy," **56**, 363 (2008). https://doi.org/10.1002/prop.200710507

[9] K. Karami, S. Ghaffari, and J. Fehri, "Interacting polytropic gas model of phantom dark energy in non – flat universe," Eur. Phys. J. C, **64**(1), 85 (2009). https://doi.org/10.1140/epjc/s10052-009-1120-1

[10] T.Chiba, T. Okabe, and M. Yamaguchi, "Kinetically driven quintessence," Phys. Rev. D, **62**, 023511 (2000). https://doi.org/10.1103/PhysRevD.62.023511

[11] T. Padmanabhan, and T. R. Chaudhury, "Can the clustered dark matter and the smooth dark energy arise from the same scalar field?" Phys. Rev. D, **66**, 081301(2002). https://doi.org/10.1103/PhysRevD.62.023511

[12] M.C. Bento, O. Bertolami, and A.A. Sen, "Generalized Chaplygin gas, accelerated expansion and dark energy – matter unification," Phys. Rev. D, **66**, 043507 (2002). https://doi.org/10.1103/PhysRevD.66.043507.

[13] A. Kamenshchik, U. Moschella, and V. Pasquier," An alternative to quintessence," Phys. Lett. B, **511**, 265 (2001). https://doi.org/10.1016/S0370-2693(01)00571-8.

[14] P. J. E. Peebles, and B. Ratra, "The cosmological constant and dark energy," Rev. Mod. Phys. **75**, 559 (2003). https://doi.org/10.1103/RevModPhys.75.559.

[15] V. Sahni, and A. Starobinsky, "The Case for a Positive Cosmological Λ-Term," Int. J. Mod. Phy. D, **9**, 373 (2000). https://doi.org/10.1142/S0218271800000542

[16] R. Ferraro, and F. Fiorini, "Modified teleparallel gravity: inflation without an inflaton," Phys. Rev. D, **75**, 084031, (2007). https://doi.org/10.1103/PhysRevD.75.084031.

[17] G.R. Bengochea, and R. Ferraro, "Dark torsion as the cosmic speed-up," Phys. Rev. D, **79**, 124019 (2009). https://doi.org/10.1103/PhysRevD.79.124019

[18] A. De Felice, and S. Tsujikawa, "Construction of cosmologically viable $f(G)$ gravity models," Phys. Lett. B, **675**, 1 (2009). https://doi.org/10.48550/arXiv.0810.5712

[19] T. Harko, F.S.N. Lobo, S. Nojiri, and S.D. Odintsov, "$f(R,T)$gravity," Phys. Rev. D, **84**, 024020 (2011). https://doi.org/10.1103/PhysRevD.84.024020

[20] V.R. Chirde, and S.H. Shekh, "Plane Symmetric Dark Energy Models in the form of Wet Dark Fluid in $f(R,T)$ Gravity," J. Astrophys. Astr. **37**, 15 (2016). https://doi.org/10.1007/s12036-016-9391-z

[21] P.K. Agrawal, and D.D. Pawar, "Plane Symmetric Cosmological Model with Quark and Strange Quark Matter in $f(R,T)$ Theory of Gravity," J. Astrophys. Astr. **38**, 2, (2017). https://doi.org/10.1007/s12036-016-9420-y

[22] M. Farasat Shamir, "Plane Symmetric Solutions in $f(R,T)$ Gravity," Commun. Theor. Phys. **65**, 301–307, (2016). https://doi.org/10.1088/0253-6102/65/3/301

[23] A.Y. Shaikh, and S.R. Bhoyar, "Plane symmetric cosmological model with Λ in $f(R,T)$ Gravity," Prespacetime Journal, **6**, 11 (2015). https://www.prespacetime.com/index.php/pst/article/view/839/826

[24] M. Mollah, K. Singh, and P.S. Singh, "Bianchi type-III cosmological model with quadratic EoS in Lyra geometry," International Journal of Geometric Method in Modern physics, **15**(11), 1850194 (2018). 10.1142/S0219887818501943

[25] S. D. Katore, K. S. Adhav, A.Y. Shaikh, et al., "Plane symmetric cosmological models with dark energy," Astrophys. Space Sci. **333**, 333–341 (2011). https://doi.org/10.1007/s10509-011-0622-0

[26] K.S. Adhav, "LRS Bianchi type -I cosmological model in $f(R,T)$ theory of gravity," Astrophys. Space Sci. **339**, 365–369 (2012). https://doi.org/10.1007/s10509-011-0963-8.

[27] V. Singh, and A. Beesham, "LRS Bianchi I model with constant expansion rate in $f(R,T)$ gravity," Astrophys. Space Sci. **365**, 125 (2020). https://doi.org/10.1007/s10509-020-03839-w

[28] R. Nagpal, J.K. Singh, A. Beesham, and H. Shabani, "Cosmological aspects of a hyperbolic solution in in $f(R,T)$ gravity," Ann. Phys. **405**, 234 (2019). https://doi.org/10.1016/j.aop.2019.03.015

[29] R. Nagpal, S.K.J. Pacif, J K. Singh, K. Bamba, and A. Beesham, "Analysis with observational constraints in Λ – cosmology in $f(R,T)$ gravity," Eur. Phys. J. C, **78**, 946 (2018). https://doi.org/10.1140/epjc/s10052-018-6403-y

[30] J.K. Singh, K. Bamba, R. Nagpal, and S.K.J. Pacif, "Bouncing cosmology in $f(R,T)$ gravity," Phys. Rev. D,**97**, 123536 (2018). https://doi.org/10.1103/PhysRevD.97.123536

[31] S.D. Katore, and S.P. Hatkar, "Bianchi type – III and Kantowski – Sachs domain wall cosmological models in the $f(R,T)$ theory of gravitation," Prog. Theor. Exp. Phys. **216**, 033E01 (2016). https://doi.org/10.1093/ptep/ptw009

[32] M.S. Singh, and S.S. Singh, "Cosmological Dynamics of Anisotropic Dark Energy in $f(R,T)$ Gravity," New Astron. **72**, 36-41 (2019). https://doi.org/10.1016/j.newast.2019.03.007

[33] Y. Aditya, U.Y.D. Prasanthi, and D.R.K. Reddy, "Plane -symmetric dark energy model with a massive scalar field," New Astron. **84**, 101504 (2021). https://doi.org/10.1016/j.newast.2020.101504

[34] P.S. Singh, and K.P. Singh, "$f(R,T)$ Gravity model behaving as a dark energy source," New Astron. **84**, 101542 (2021). https://doi.org/10.1016/j.newast.2020.101542

[35] A.K. Biswal, K.L. Mahanta1, and P.K. Sahoo, "Kalunza – Klein cosmological model in $f(R,T)$ gravity with domain walls," Astrophys Space Sci.**359**, 42 (2015). https://doi.org/10.1007/s10509-015-2493-2

[36] K. Dasunaidu, Y. Aditya, and D.R.K. Reddy, "Cosmic strings in a five dimensional spherically symmetric background in $f(R,T)$ gravity," Astrophysical Space Science, **363**, 158 (2018). https://doi.org/10.1007/s10509-018-3380-4

[37] D.D. Pawar, R.V. Mapari, and J.L. Pawade, "Perfect fluid and heat flow in $f(R,T)$ theory," Pramana J. Phys. **95**, 10 (2021). https://doi.org/10.1007/s12043-020-02058-w

[38] P.H. Chavanis, "A cosmological model describing the early inflation, the intermediate decelerating expansion and late accelerating expansion of the universe by a quadratic equation of state," Universe, **1**(3), 357 (2015). https://doi.org/10.3390/universe1030357

[39] D.R.K. Reddy, K.S. Adhav, and M.A. Purandare, "Bianchi type – I cosmological model with quadratic equation of state," Astrophys. Space Sci. **357**(1), 20 (2015). https://doi.org/10.1007/s10509-015-2302-y

[40] K. Ananda, and M. Bruni, "Cosmo-dynamics and dark energy with non-linear equation of state: a quadratic model," (2005). https://doi.org/10.48550/arXiv.astro-ph/0512224

[41] K. Ananda, and M. Bruni, Phys. Rev. D, "Cosmological dynamics and dark energy with a quadratic equation of state: Anisotropic models, large – scale perturbations, and cosmological singularities," **74**, 023524 (2006). https://doi.org/10.1103/PhysRevD.74.023524

[42] S. Nojiri, and S.D. Odintsov, "Inhomogeneous equation of state of the universe: phantom era, future singularity and crossing the phantom barrier," Phys. Rev. D, **72**, 023003 (2005). https://doi.org/10.1103/PhysRevD.72.023003

[43] S. Capozziello et al., "Observational constraints on dark energy with generalized equation of state," Phys. Rev. D, **73**, 043512 (2006). https://doi.org/10.1103/PhysRevD.73.043512

[44] C.R. Mahanta, S. Deka, and M.P. Das, "Bianchi Type – V Universe with Time Varying Cosmological Constant and Quadratic Equation of State in $f(R,T)$ Theory of Gravity," East European Journal of Physics, **1**, 44 (2023). https://doi.org/10.26565/2312-4334-2023-1

[45] S. Ayug̈in, C. Aktas, B. Mishra, "Quadratic equation of state solutions with Λ in $f(R,T)$ gravitation theory," Indian j Phys. **93**, 407 (2019). https://doi.org/10.1007/s12648-018-1309-y

[46] F. Rahman, M. Jamil, and K. Chakraborty, "Construction of an electromagnetic mass model using quadratic equation of state," (2009). https://arxiv.org/abs/0904.0189v3

[47] P.H. Chavanis, "A cosmological model based on a quadratic equation of state unifying vacuum energy, radiation and dark energy," J. Gravity, **213**(1), 682451 (2013). https://doi.org/10.1155/2013/682451

[48] P.H. Chavanis, "A cosmological model describing the early inflation, the intermediate decelerating expansion, and the late accelerating expansion by a quadratic equation of state," (2013). http://arxiv.org/abs/1309.5784

[49] T. Feroze, and A.A. Siddiqui, "Charged anisotropic matter with quadratic equation of state," General Relativity and Gravitation, **43**(4), 1025-1035 (2011). https://doi.org/10.1007/s10714-010-1121-2

[50] M. Malaver, "Strange quark star model with quadratic equation of state," Frontiers of Mathematics and Its Applications, **1**(1), 9–15, (2014). https://arxiv.org/pdf/1407.0760

[51] P. Bhar, K.N. Singh, and N. Pant, "Compact stellar model obeying quadratic equation of state," Astrophysics Space Science, **361**(10), 343 (2016). https://doi.org/10.1007/s10509-016-2929-3

[52] S.D. Maharaj, and P.M. Takisa, "Regular models with quadratic equation of state," General Relativity and Gravitation, **44**(6), 1419–1432, (2012). (2013). https://doi.org/10.1007/s10714-012-1347-2

[53] R. Sharma, and B.S. Ratanpal, "Relativistic stellar model admitting a quadratic equation of state," Int. J. Mod. Phys. D, **22**(13), 1350074 (2013). https://doi.org/10.1142/S0218271813500740

[54] G.P. Singh, and B.K. Bishi, "Bianchi type – I Universe with cosmological constant and quadratic equation of state in $f(R,T)$ modified gravity," Advances in Higher Energy Physics, **2015**, (2015). https://doi.org/10.1155/2015/816826

[55] G.P. Singh, and B.K. Bishi, "Bianchi type – I transit Universe in $f(R,T)$ modified gravity with quadratic equation of state and Λ," Astrophys. Space Sci. **360**(1), 34 (2015). https://doi.org/10.1007/s10509-015-2495-0

[56] D.D. Pawar, R.V. Mapari, and P.K. Agrawal, "A modified holographic Ricci dark energy model in $f(R,T)$ theory of gravity," J. Astrophys. Astron. **40**, 13 (2019). https://doi.org/10.1007/s12036-019-9582-5

[57] D.D. Pawar, and R.V. Mapari, "Plane Symmetry Cosmology Model of Interacting Field in f(R, T) Theory," Journal of Dynamical Systems and Geometric Theories, **20**(1), 115-136 (2022). https://doi.org/10.1080/1726037X.2022.2079268

[58] D.D. Pawar, R.V. Mapari, and V.M. Raut, "Magnetized Strange Quark Matter in Lyra Geometry," Bulgarian Journal of Physics, **48**, 225–235 (2021). https://www.bjp-bg.com/papers/bjp2021_3_225-235.pdf

П'ЯТИВИМІРНА ПЛОСКА СИМЕТРИЧНА КОСМОЛОГІЧНА МОДЕЛЬ З КВАДРАТНИМ РІВНЯННЯМ СТАНУ В $f(R,T)$ ТЕОРІЇ ГРАВІТАЦІЇ

В.А. Такаре[a], **Р.В. Мапарі**[b], **С.С. Такре**[c]

[a] Факультет математики, Науковий коледж Шиваджі, Амраваті (М.С.), Індія

[b] Департамент математики, Урядовий Інститут науки та гуманітарних наук Відарбха, Амраваті

[c] Факультет математики, Незалежний молодший коледж, Амраваті (MS) -444604 Індія), Індія

У цій статті ми проаналізували п'ятивимірну плоску симетричну космологічну модель, що містить ідеальну рідину, у контексті $f(R,T)$ гравітації. Рівняння поля розв'язані для двох класів $f(R,T)$ гравітації, тобто $f(R,T) = R + f(T)$ і $f(R,T) = f_1(R)f_2(T)$ із включенням космологічної сталої Λ і квадратного рівняння параметрів стану у вигляді $p = \alpha\rho^2 - \rho$, де α — константа і строго $\alpha \neq 0$. Щоб отримати точні рішення, ми використовуємо об'ємний степеневий закон і експоненціальний закон розширення. Розглянуто фізичні та геометричні аспекти моделі.

Ключові слова: *Квадратне рівняння стану; $f(R,T)$ гравітація; космологічна стала; п'ятивимірна плоска симетрична космологічна модель*

GENERATION OF O-MODE IN THE PRESENCE OF ION-CYCLOTRON DRIFT WAVE TURBULENCE IN A NONUNIFORM PLASMA[†]

Banashree Saikia*, P.N. Deka

Department of Mathematics, Dibrugarh University, Dibrugarh, 786004, Assam, India
*Corresponding Author e-mail: banashreesaikia18@gmail.com, e-mail: pndeka@dibru.ac.in
Received May 21, 2023; revised June 23, 2023; in final form July 31, 2023; accepted August 1, 2023

This study aims to investigate the effect of ion-cyclotron drift wave turbulence on the generation of ordinary mode (O-mode) in the presence of density and temperature gradients. For this, a Vlasov plasma is considered where a resonant, and non-resonant modes are considered to be present in the system. Here, the non-resonant mode is a perturbation caused by O-mode in a quasi-steady state of plasma, which is characterised by the presence of low frequency ion-cyclotron resonant mode waves. The interaction between these waves is studied by the Vlasov-Maxwell set of equations and a modified Maxwellian-type distribution function for particles that includes the external force field $\vec{F}$ and associated density and temperature gradient parameters λ_j. The study analyses the growth rate of electromagnetic O-mode at the expense of ion-cyclotron drift wave energy and the associated impact of the density and temperature gradient. This model uses the linear response theory on weakly turbulent plasma, evaluates the responses due to turbulent and perturbed fields, and obtains the nonlinear dispersion relation for O-mode.

Keywords: *Ordinary mode; Density and temperature gradients; Drift wave turbulence; Wave-particle interaction*
PACS: 52.35.Hr, 52.35.Kt, 52.35.Fp

INTRODUCTION

Ordinary mode (O-mode) waves are high-frequency electromagnetic plasma waves that are observed in magnetospheric plasma, as reported by satellite observations. [1] This enhanced O-mode phenomenon is a subject of interest to many plasma physicists for the explanation of many radiation phenomena in the magnetosphere and the ionosphere, including radiation phenomena in the auroral zone. O-mode instability is a purely growing mode that was first discussed by Davidson and Wu [2] in high beta plasmas. They found that the O-mode waves propagated in the perpendicular direction of the ambient magnetic field, which could become unstable in high beta plasmas and temperature anisotropic when $T_{\parallel} > T_{\perp}$ in bi-Maxwellian distribution functions.

The generation of unstable O-mode waves in the auroral region of the Earth's magnetosphere was considered by Gurnett [3] and also by Hayes & Melrose [4]. In their study, they thoroughly considered the enhanced electromagnetic radiation in the top ionospheric regions and characterised such radiation as Auroral Kilometric Radiation (AKR). Later, in the investigations done by Mellott et al. [5], it was confirmed that the AKR is composed of X and O-mode radiations. Later, it received renewed attention owing to its potential applicability to the solar wind plasma. Ibscher, Schlickeiser, and their co-authors [6-9] examined the O-mode instability and expanded it to the low-beta plasma domain by studying a counter-streaming bi-Maxwellian model. Temperature anisotropic effects on O-mode and its instability have been reviewed [10] in magnetised non-relativistic bi-Maxwellian plasma. Based on a numerical approach [11], it has been confirmed that the unstable O-mode is possible at low beta plasma in the presence of a finite counter-stream. So, further, the authors in Ref. [12] have derived an accurate analytical marginal instability condition for O-mode, where they identified that though it has large enough counter-stream parameters, the O-mode must operate for temperature anisotropy $T_{\perp}/T_{\parallel} > 1$ even larger than unity.

In our manuscript, we have considered the nonlinear wave-particle interaction process in the presence of ion-cyclotron drift wave turbulence based on the plasma turbulence theory proposed by Nambu [13] and Tystovich [14]. Based on the non-linear wave-particle interaction mechanism known as the plasma maser effect [13,15-16], it may be possible to transfer wave energy from the low-frequency mode to the high-frequency mode. The Plasma maser effect occurs in the presence of both resonant and non-resonant modes. The resonant modes are those for which the Cherenkov resonance condition $\omega - \vec{k} \cdot \vec{v} = 0$ is satisfied, while the non-resonant waves are those for which the Cherenkov condition and the nonlinear scattering conditions are not satisfied, i.e., $\Omega - \vec{k} \cdot \vec{v} \neq 0$ and $(\Omega - \omega) - (\vec{K} - \vec{k}) \cdot \vec{v} \neq 0$. Here, ω is the frequency of the resonant wave, Ω is the frequency of the non-resonant wave, and $\vec{k}$ and $\vec{K}$ are the corresponding wave vectors. Though most of the studies on the plasma maser effect have been carried out considering the plasma system as homogeneous [17-19], many attempts have been made to investigate the role of the density gradient parameter in the energy up-conversion process through the plasma maser effect in inhomogeneous plasma [20, 21]. Applying the plasma-maser theory, Deka and Borgohain [1] studied the amplification of O-mode through non-linear wave-particle interaction

---

in the presence of drift wave turbulence in an inhomogeneous plasma. In their study, they found that the amplification process of electromagnetic radiation is possible at the expense of drift wave turbulence in space plasma. The generation of high-frequency electromagnetic O-mode waves and low-frequency ion sound waves in the upper ionosphere region has been mentioned in several studies [5, 22, 23]. Several studies have mentioned the generation of high-frequency electromagnetic O-mode waves and low-frequency ion sound waves in the upper ionosphere region. Previous works have mostly focused on investigating the impact of density gradients on wave amplification through the nonlinear wave-particle interaction associated with drift waves. However, Gogoi [24] discussed the generation of wave energy up-conversion of electromagnetic O-mode waves through plasma maser instability in inhomogeneous ionospheric plasma in the presence of electrostatic ion sound waves. In practical situations like tokamak plasmas [25-27], particle drift is often caused by temperature gradients, which may lead to the creation of drift wave turbulence [28-30].

Motley and D'Angelo first discovered electrostatic ion cyclotron waves in a Q-machine, which spread outward across the magnetic field and were stimulated by a current drawn to a small auxiliary electrode. The solar wind has been observed by spacecraft to contain ion-cyclotron waves (ICWs) at various distances (0.3 - 1 AU) from the Sun [31].

Our investigation focused on the generation of ordinary mode waves in the presence of density and temperature gradients. We studied the plasma maser effect in the presence of an ion cyclotron drift wave and analysed the energy exchange process between waves. In this case, the resonant wave is the ion cyclotron drift wave, while the non-resonant wave is the ordinary mode wave. Through resonant interaction, plasma particles can transfer their energy to non-resonant waves via a modulated field, resulting in energy up-conversion from resonant mode to non-resonant mode. In our study, we have also considered a nonlinear process that enables the exchange of wave energy among participating waves, even with significant frequency differences [15, 31, 32].

Plasma nonuniformity, associated with gradients in density and temperature, generates drift motions and supports ion cyclotron drift wave turbulence. To investigate the instability of the O-mode, we employed the Vlasov-Maxwell system of equations and a modified Maxwellian-type particle distribution function. From the nonlinear dispersion relation of the O-mode, the expression of the growth rate is obtained, and by using satellite observational data [33], we have estimated the impact of gradient parameters on the growth of the O-mode.

The paper is organised as follows: In Section 2, the geometrical and mathematical formulations are given. In Section 3, the nonlinear dispersion relation of the ordinary mode wave is discussed. In Section 4, the growth rate of the electromagnetic O-mode is presented, and in Section 5, the discussions of the work along with the conclusion are given.

MATHEMATICAL FORMULATION

We consider an inhomogeneous plasma in the presence of drift wave turbulence. In order to describe this system, we use a particle distribution function [32] involving density and temperature gradients caused by an external force in a uniform magnetic field $\vec{B}_0$ along the z-axis. There exists a turbulence field characterised by a wave vector $\vec{k} = \left(0, 0, k_\parallel\right)$.

We introduce an electromagnetic ordinary mode as a perturbation to the system with a propagation vector $\vec{K} = \left(K_\perp, 0, 0\right)$.

The density gradient $\vec{\nabla} n(y)$ and temperature gradient $\vec{\nabla} T(y)$ are along the y-direction, which is also the direction of the uniform effective force field $\vec{F}$. This force supports $\vec{F} \times \vec{B}$ drift and is perpendicular to the embedded magnetic field $\vec{B}_0$. The geometry of the model is depicted in Figure 1.
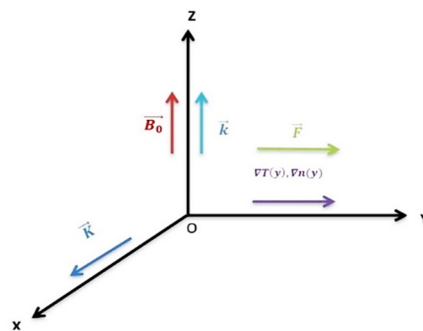
Figure 1. Geometry of the Model

In the absence of collisions, the distribution function for particles is considered Maxwellian.

$$f_j\left(\vec{v}\right) = \left(\frac{m_j}{2\pi T_j}\right)^{3/2} \exp\left(-\frac{m_j \vec{v}^2}{2T_j}\right), \qquad (j = e, i).$$

Here, we use the subscript $j = e$ for the electrons and $j = i$ for the ion.

In our system, field $\vec{B}$ and $\vec{F}$ are time invariant, so the Hamiltonian H is a constant of motion given by

$$H = \frac{1}{2} m_j \vec{v}^2 - Fy.$$

The system is translationally invariant in the x and z directions, so canonical momentum

$$p_x = m_j v_x + \frac{e_j}{c} yB,$$

$$p_z = m_j v_z.$$

where e_j is the charge of the plasma particle.

The quasi Maxwellian distribution will be

$$f_{0j}\left(Y', H\right) = \frac{N\left(Y'\right)}{\left(\dfrac{2\pi T_j\left(Y'\right)}{m_j}\right)^{3/2}} \exp\left(-\frac{H}{T_j\left(Y'\right)}\right), \tag{1}$$

where $Y' = y + \dfrac{v_x}{\Omega}$.

For $\lambda_L / L \ll 1$, where L is the characteristic length and λ_L is the Larmor radius, we can expand (1) to the first order in the Larmor radius as

$$f_{0j}\left(Y, H\right) = f_{0j}\left(y, H\right) + \left(y + \frac{v_x}{\Omega_j}\right)\frac{\partial f_{0j}\left(x, H\right)}{\partial x},$$

where $\dfrac{\partial f_{0j}\left(x, H\right)}{\partial x} = \left[\dfrac{1}{N}\dfrac{dN}{dy} + \dfrac{dT_j}{dy}\dfrac{\partial}{\partial T_j} - \dfrac{F}{T_{0j}}\right] f_{0j}$,

and we can have a particle distribution function [32] for (1) as

$$f_{0j}\left(T_j, y, \vec{v}\right) = \left(\frac{m_j}{2\pi T_j}\right)^{3/2}\left[1 + \lambda_j\left(y + \frac{v_x}{\Omega_j}\right)\right]\exp\left[-\left(\frac{m_j \vec{v}^2}{2T_j} - \frac{Fy}{T_j}\right)\right]. \tag{2}$$

The distribution function for the guiding centre is denoted by f_{0j}. $\Omega_j = e_j B_0 / m_j c$ denotes the cyclotron frequency of the plasma particles. The parameter λ_j is associated with gradients in density and temperature. At y = 0, the value of λ_j can be computed using Eq. (2).

$$\lambda_j = \left[\left(\frac{\partial}{\partial T_j}\frac{dT_j}{dy}\right) + \left(\frac{1}{f_j}\frac{df_j}{dy}\right)\right]_{y=0} - \frac{F}{T_{0j}}. \tag{3}$$

$\vec{K} = \left(K_\perp, 0, 0\right)$ is the propagation vector of the ordinary mode wave; $\vec{k} = \left(0, 0, k_\parallel\right)$ is the propagation vector of the ion-cyclotron drift wave; $\vec{B}_0$ is the magnetic field along the positive z-axes; $\vec{\nabla} n(y)$ is the density gradient along the y-direction; $\vec{\nabla} T(y)$ is the temperature gradient along the y-direction; F is the uniform effective force field along the y-direction.

The interaction of high-frequency electromagnetic ordinary mode with low-frequency ion-cyclotron drift wave turbulence is governed by the Vlasov-Maxwell system of equations.

$$\left[\frac{\partial}{\partial t} + \vec{v}\frac{\partial}{\partial \vec{r}} + \left\{\frac{e_j}{m_j}\left(\vec{E} + \frac{\vec{v}\times\vec{B}}{c}\right) - \frac{\vec{F}}{m_j}\right\}\frac{\partial}{\partial \vec{v}}\right]F_{0j}\left(\vec{r}, \vec{v}, t\right) = 0, \tag{4}$$

$$\nabla \times \vec{E} = -\frac{1}{c}\frac{\partial \vec{B}}{\partial t}, \tag{5}$$

$$\nabla \times \vec{B} = \frac{1}{c}\frac{\partial \vec{E}}{\partial t} + \frac{4\pi}{c}\vec{J}, \tag{6}$$

$$\vec{J} = \sum_{j=e,i} e_j n_j \int \vec{v} f_{0j}\left(\vec{r},\vec{v},t\right) d\vec{v}, \tag{7}$$

$$\nabla.\vec{E} = \sum_{j=e,i} 4\pi e_j n_j \int f_{0j}\left(\vec{r},\vec{v},t\right) d\vec{v}. \tag{8}$$

The unperturbed particle distribution function and fields are described by the linear response theory of a turbulent plasma [32].

$$F_{0j} = f_{0j} + \varepsilon f_{1j} + \varepsilon^2 f_{2j}, \tag{9}$$

and

$$\vec{E}_{0l} = \varepsilon \vec{E}_l + \varepsilon^2 \vec{E}_2, \tag{10}$$

where ε is a small parameter associated with the ion cyclotron drift wave turbulent field $\vec{E}_l = \left(0,0,E_{l\parallel}\right)$, f_{0j} is the space and time averaged parts, f_{1j} and f_{2j} are fluctuating parts of the distribution function, $\vec{E}_2$ is the second order electric field. On putting these in Eq. (4)

$$\left[\frac{\partial}{\partial t} + \vec{v}\frac{\partial}{\partial \vec{r}} + \left\{\frac{e_j}{m_j}\left(\varepsilon\vec{E}_l + \varepsilon^2\vec{E}_2 + \frac{\vec{v}\times\vec{B}}{c}\right) - \frac{\vec{F}}{m_j}\right\}\frac{\partial}{\partial \vec{v}}\right]\left[f_{0j} + \varepsilon f_{1j} + \varepsilon^2 f_{2j}\right] = 0.$$

Now to the order of ε ,

$$\left[\frac{\partial}{\partial t} + \vec{v}\frac{\partial}{\partial \vec{r}} + \left\{\frac{e_j}{m_j}\left(\varepsilon\vec{E}_l + \varepsilon^2\vec{E}_2 + \frac{\vec{v}\times\vec{B}}{c}\right) - \frac{\vec{F}}{m_j}\right\}\frac{\partial}{\partial \vec{v}}\right]f_{1j}\left(\vec{r},\vec{v},t\right) = \frac{e_j}{m_j}\left(\vec{E}_l\frac{\partial}{\partial \vec{v}}f_{0j}\right). \tag{11}$$

Using the Fourier transform of the form

$$A\left(\vec{r},\vec{v},t\right) = \sum_{\vec{k},\omega} A\left(\vec{k},\omega,\vec{v}\right)\exp\left[i\left(\vec{k}\cdot\vec{r} - \omega t\right)\right], \tag{12}$$

and integrating along the unperturbed orbit, the fluctuating part of the distribution function due to the low-frequency turbulence field f_{1j} , is obtained from Eq. (11).

$$f_{1j}\left(\vec{k},\omega\right) = \int_{-\infty}^{0} \frac{e_j}{m_j}\vec{E}_l\frac{\partial}{\partial \vec{v}}f_{0j}\exp\left[i\left\{\vec{k}\left(\vec{r}' - \vec{r}\right) - \omega\tau\right\}\right]d\tau, \tag{13}$$

$$f_{1j}\left(\vec{k},\omega\right) = \frac{ie_j}{m_j}\frac{E_{l\parallel}}{\omega - k_\parallel v_\parallel + i\cdot 0^+}\frac{\partial}{\partial v_\parallel}f_{0j};$$

In order to attain a quasi-steady state, we introduce a perturbation to the test high-frequency ordinary mode by applying an electric field $\delta\vec{E}_{hj} = \left(0,0,\delta E_{hj}\right)$ with a propagating vector $\vec{K} = \left(K_\perp,0,0\right)$, a magnetic field $\delta\vec{B}_{hj} = \left(0,\delta B_{hj},0\right)$, and a frequency Ω_j . This results in a perturbed electric field, magnetic field, and particle distribution function, given by

$$\delta\vec{E} = \mu\delta\vec{E}_{hj} + \mu\varepsilon\delta\vec{E}_{lhj} + \mu\varepsilon^2\Delta\vec{E},$$

$$\delta\vec{B} = \mu\delta\vec{B}_{hj} + \mu\varepsilon\delta\vec{B}_{lhj} + \mu\varepsilon^2\Delta\vec{B},$$

$$\delta f = \mu\delta f_{hj} + \mu\varepsilon\delta f_{lhj} + \mu\varepsilon^2\Delta f_j.$$

where the variables $\delta\vec{E}_{lhj}, \Delta\vec{E}, \delta\vec{B}_{lhj}, \Delta\vec{B}, \delta f_{lhj}$, and Δf_j represent modulation fields, while δf_{hj} is the fluctuating part caused by the high-frequency ordinary mode. δf_{lhj} and Δf_j refer to the particle distribution function associated with the modulation field, and μ is the smallness parameter for the perturbed field, which is much smaller than ε .

Then, putting these in Vlasov Eq. (4), resulting in an expression up to the order of $\mu, \mu\varepsilon$, $\mu\varepsilon^2$, we get,

$$P\delta f_{hj} = \frac{e_j}{m_j}\left(\delta\vec{E}_{hj} + \frac{\vec{v}\times\delta\vec{B}_{hj}}{c}\right)\cdot\frac{\partial f_{0j}}{\partial \vec{v}}, \tag{14}$$

$$P\delta f_{lhj} = \frac{e_j}{m_j}\delta\vec{E}_{hj}\frac{\partial f_{1j}}{\partial \vec{v}} + \frac{e_j}{m_j}\frac{\vec{v}\times\delta\vec{B}_{hj}}{c}\cdot\frac{\partial f_{1j}}{\partial \vec{v}} + \frac{e_j}{m_j}\delta\vec{E}_{lhj}\frac{\partial f_{0j}}{\partial \vec{v}}$$

$$+ \frac{e_j}{m_j}\vec{E}_l\frac{\partial}{\partial \vec{v}}\delta f_{hj} + \frac{e_j}{m_j}\frac{\vec{v}\times\vec{B}_l}{c}\cdot\frac{\partial}{\partial \vec{v}}\delta f_{hj} + \frac{e_j}{m_j}\frac{\vec{v}\times\delta\vec{B}_{lhj}}{c}\cdot\frac{\partial f_{0j}}{\partial \vec{v}}, \tag{15}$$

$$P\Delta f_j = \frac{e_j}{m_j}\left[\delta\vec{E}_{lhj}\frac{\partial f_{1j}}{\partial \vec{v}} + \frac{\vec{v}\times\delta\vec{B}_{lhj}}{c}\cdot\frac{\partial f_{1j}}{\partial \vec{v}} + \vec{E}_l\frac{\partial}{\partial\vec{v}}\delta f_{lhj} + \frac{\vec{v}\times\vec{B}_l}{c}\cdot\frac{\partial}{\partial\vec{v}}\delta f_{lhj} \right],\tag{16}$$

where $P = \left[\dfrac{\partial}{\partial t} + \vec{v}\dfrac{\partial}{\partial\vec{r}} - \left\{ \dfrac{e_j}{m_j}\left(\vec{E} + \dfrac{\vec{v}\times\vec{B}}{c} \right) - \dfrac{\vec{F}}{m_j} \right\}\dfrac{\partial}{\partial\vec{v}} \right]$.

We solve this differential equation for the fluctuating parts of the equation $\delta f_{hj}, \delta f_{lhj}, \Delta f_j$ over the electron trajectories using the method of characteristics, commonly known as "integration over an unperturbed orbit" [34]. Using the Fourier transform of Eq. (12) and integrating along the unperturbed orbits, we evaluate the various perturbed distribution functions from Eqs. (14) to (16) to obtain the nonlinear dielectric function of the electromagnetic ordinary mode wave of frequency Ω_j in the presence of ion-cyclotron drift wave turbulence.

Now, we calculate the modulated field $\delta E_{lhj}(\vec{K}-\vec{k}, \Omega-\omega)$ using Maxwell's equation.

$$\nabla\times\delta\vec{B}_{lhj} = \frac{1}{c}\frac{\partial}{\partial t}\delta\vec{E}_{lhj} + \frac{4\pi i}{c}\vec{J},\tag{17}$$

$$\vec{J} = \sum_{j=e,i} e_j n_j \int \vec{v}\delta f_{lhj}d\vec{v}.\tag{18}$$

Therefore, we have

$$\nabla\times\delta\vec{B}_{lhj} = \frac{1}{c}\frac{\partial}{\partial t}\delta\vec{E}_{lhj} + \frac{4\pi i}{c}\sum_{j=e,i} e_j n_j \int \vec{v}\delta f_{lhj}d\vec{v},\tag{19}$$

$$\delta\vec{E}_{lhj}\times\frac{c^2\left|\vec{K}-\vec{k}\right|^2 - (\Omega-\omega)^2}{(\Omega-\omega)c} = \frac{4\pi i e_j n_j}{c}\int \vec{v}\delta f_{lhj}d\vec{v},\tag{20}$$

$$\delta E_{lhj} = \frac{4\pi i e_j n_j (\Omega-\omega)}{c^2\left|\vec{K}-\vec{k}\right|^2 - (\Omega-\omega)^2}\int v_{\parallel}\delta f_{lhj}d\vec{v},\tag{21}$$

$$\delta E_{lhj} = -\frac{i\omega_{pj}^2(\Omega-\omega)}{R\left\{c^2\left|\vec{K}-\vec{k}\right|^2 - (\Omega-\omega)^2\right\}}\left(\frac{e_j}{m_j}\right)E_l\delta E_{hj}\times\int v_{\parallel}\left[\left[\left(1-\frac{k_{\parallel}v_{\parallel}}{\omega}\right)\frac{\partial}{\partial v_{\perp}} + \frac{k_{\parallel}v_{\perp}}{\omega}\frac{\partial}{\partial v_{\parallel}}\right]\times\right.$$
$$\left[\frac{K_{\perp}}{\Omega}\frac{m_j}{T_j K_{\perp}}\left\{1+\left(\Omega-\frac{\lambda_j T_j K_{\perp}}{m_j\Omega_j}\right)Q_{s,t}\right\}f_{0j} - \left(1-\frac{K_{\perp}v_{\perp}}{\Omega}\cos\theta\right)\frac{\partial f_{0j}}{\partial v_{\parallel}}Q_{s,t}\right]T_{p,q}$$
$$\left.-\left[\frac{K_{\perp}}{\Omega}\frac{m_j}{T_j K_{\perp}}\left\{1+\left(\Omega-\omega+k_{\parallel}v_{\parallel}-\frac{\lambda_j T_j K_{\perp}}{m\Omega_j}\right)T_{p,q}\right\}+\frac{K_{\perp}v_{\perp}}{\Omega}\cos\theta\frac{\partial}{\partial v_{\parallel}}\left(T_{p,q}\right)\right]\right]d\vec{v},\tag{22}$$

where

$$R = 1 + \frac{\omega_{pj}^2(\Omega-\omega)}{\left\{c^2\left|\vec{K}-\vec{k}\right|^2 - (\Omega-\omega)^2\right\}}\int v_{\parallel}\left[\left(\frac{K_{\perp}}{\left|\vec{K}-\vec{k}\right|} - \frac{\left|\vec{K}-\vec{k}\right|}{\Omega-\omega}v_{\parallel}\right)\frac{m_j}{T_j K_{\perp}}\right.$$
$$\left.\left\{1+\left(\Omega+k_{\parallel}v_{\parallel}-\omega-\frac{\lambda_j T_j K_{\perp}}{m\Omega_j}\right)\times T_{p,q}\right\}f_{0j} - \left(\frac{\left|\vec{K}-\vec{k}\right|}{\Omega-\omega}v_{\perp}\cos\theta + \frac{k_{\parallel}}{\left|\vec{K}-\vec{k}\right|}\right)\times\frac{\partial f_{0j}}{\partial v_{\parallel}}T_{p,q}\right]d\vec{v},\tag{23}$$

$$Q_{s,t} = \sum_{s,t}\frac{J_s(\alpha)J_t(\alpha)\exp\left[i(t-s)\right]}{s\Omega_j - \Omega + K_{\perp}v_F + \omega - k_{\parallel}v_{\parallel}},\quad \alpha = \frac{K_{\perp}v_F}{\Omega_j},$$

and

$$T_{p,q} = \sum_{p,q}\frac{J_p(\alpha)J_q(\alpha)\exp\left[i(q-p)\right]}{p\Omega_j - \Omega + K_{\perp}v_F + \omega - k_{\parallel}v_{\parallel}},\quad \alpha = \frac{K_{\perp}v_F}{\Omega_j}.$$

Non-linear Dispersion Relation of Ordinary Mode Wave

The nonlinear dispersion relation for electromagnetic ordinary mode waves can be obtained from Maxwell's equations.

$$\nabla \times \delta \vec{B}_{hj} = \frac{1}{c} \frac{\partial}{\partial t} \delta \vec{E}_{hj} + \frac{4\pi}{c} \vec{J}. \tag{24}$$

$$J = \sum_{j=e,i} e_j n_j \int v_{\parallel} \left(\delta f_{hj} + \Delta f_j \right) d\vec{v}. \tag{25}$$

$$\delta E_{hj} = \sum_{j=e,i} \frac{4\pi e_j n_j \left(\Omega - \omega \right)}{c^2 K_{\perp}^2 - \Omega^2} \int v_{\parallel} \left(\delta f_{hj} + \Delta f_j \right) d\vec{v}. \tag{26}$$

After simplification, we get,

$$\delta E_{hj} \varepsilon_h \left(\vec{K}, \Omega \right) = 0. \tag{27}$$

Here, $\varepsilon_h \left(\vec{K}, \Omega \right)$ represents the nonlinear dispersion relation of the ordinary mode wave, which is described by

$$\varepsilon_h \left(\vec{K}, \Omega \right) = \varepsilon_0 \left(\vec{K}, \Omega \right) + \varepsilon_d \left(\vec{K}, \Omega \right) + \varepsilon_p \left(\vec{K}, \Omega \right). \tag{28}$$

where $\varepsilon_0 \left(\vec{K}, \Omega \right)$ is the linear part, $\varepsilon_d \left(\vec{K}, \Omega \right)$ is the direct coupling part, and $\varepsilon_p \left(\vec{K}, \Omega \right)$ is the polarisation coupling part. The expressions of these parts are given by,

$$\varepsilon_0 \left(\vec{K}, \Omega \right) = 1 + \frac{\omega_{pj}^2 \left(\Omega - \omega \right)}{c^2 K_{\perp}^2 - \Omega^2} \int v_{\parallel} \left[\frac{cK_{\perp}}{\Omega} \frac{m_j}{T_j K_{\perp}} \left\{ 1 + \left(\Omega - \frac{\lambda_j T_j K_{\perp}}{m_j \Omega_j \Omega} \right) Q_{s,t} \right\} f_{0j} - \left(1 - \frac{K_{\perp} v_{\perp}}{\Omega_j} \cos\theta \right) \frac{\partial f_{0j}}{\partial v_{\parallel}} Q_{s,t} \right] d\vec{v}. \tag{29}$$

$$\varepsilon_d \left(\vec{K}, \Omega \right) = \frac{\omega_{pj}^2 \left(\Omega - \omega \right)}{c^2 K_{\perp}^2 - \Omega^2} \left(\frac{e_j}{m_j} \right)^2 |E_l|^2 \int v_{\parallel} \left[\left[\left(1 - \frac{k_{\parallel} v_{\parallel}}{\omega} \right) \frac{\partial}{\partial v_{\perp}} + \frac{k_{\parallel} v_{\perp}}{\omega} Q_{s,t} \right] \times \left[\frac{K_{\perp}}{\Omega} \frac{m_j}{T_j K_{\perp}} \left\{ 1 + \left(\Omega - \frac{\lambda_j T_j K_{\perp}}{m_j \Omega_j \Omega} \right) Q_{s,t} \right\} f_{0j} - \right. \right.$$
$$\left(1 - \frac{K_{\perp} v_{\perp}}{\Omega} \cos\theta \right) \frac{\partial f_{0j}}{\partial v_{\parallel}} Q_{s,t} \right] T_{p,q} - \left[\frac{K_{\perp}}{\Omega} \frac{m_j}{T_j K_{\perp}} \left\{ 1 + \left(\Omega - \omega + k_{\parallel} v_{\parallel} - \frac{\lambda_j T_j K_{\perp}}{m_j \Omega_j \Omega} \right) T_{p,q} \right\}$$
$$\left. + \frac{K_{\perp} v_{\perp}}{\Omega} \cos\theta \frac{\partial}{\partial v_{\parallel}} \left(T_{p,q} \right) \left(\frac{1}{\left(k_{\parallel} v_{\parallel} - \omega + i.0 \right)} \right) \left[\left(1 - \frac{k_{\parallel} v_{\parallel}}{\omega} \right) \frac{\partial f_{0j}}{\partial v_{\perp}} + \frac{k_{\parallel} v_{\perp}}{\omega} \frac{\partial f_{0j}}{\partial v_{\parallel}} \right] \right] d\vec{v}. \tag{30}$$

Since, the expression $\varepsilon_p \left(\vec{K}, \Omega \right)$ is very lengthy, we may write it as follows:

$$\varepsilon_p \left(\vec{K}, \Omega \right) = \frac{\omega_{pj}^4 \left(\Omega - \omega \right)^2}{R \left(c^2 K_{\perp}^2 - \Omega^2 \right) \left\{ c^2 \left| \vec{K} - \vec{k} \right|^2 - \left(\Omega - \omega \right)^2 \right\}} \left(\frac{e_j}{m_j} \right)^2 |E_l|^2 \left(A + B \right) \left(C + D \right). \tag{31}$$

where A, B, C, and D are obtained as:

$$A = \int v_{\parallel} \left[\left[\left(1 - \frac{k_{\parallel} v_{\parallel}}{\omega} \right) \frac{\partial}{\partial v_{\parallel}} + \frac{k_{\parallel} v_{\perp}}{\omega} \frac{\partial}{\partial v_{\parallel}} \right] Q_{s,t} \times \left[\left(\frac{K_{\perp}}{\left| \vec{K} - \vec{k} \right|} - \frac{\vec{K} - \vec{k}}{\Omega - \omega} v_{\parallel} \right) \frac{m_j}{T_j K_{\perp}} \left\{ 1 + \left(\Omega + k_{\parallel} v_{\parallel} - \omega - \frac{\lambda_j T_j K_{\perp}}{m_j \Omega_j \Omega} \right) \times T_{p,q} \right\} f_{0j} - \right. \right.$$
$$\left. \left(\frac{\left| \vec{K} - \vec{k} \right|}{\Omega - \omega} v_{\perp} \cos\theta + \frac{k_{\parallel}}{\left| \vec{K} - \vec{k} \right|} \right) \times \frac{\partial f_{0j}}{\partial v_{\parallel}} T_{p,q} \right] d\vec{v}. \tag{32}$$

$$B = -\int v_{\parallel} \left[\left[\left(\frac{K_{\perp}}{\left| \vec{K} - \vec{k} \right|} - \frac{\left| \vec{K} - \vec{k} \right|}{\Omega - \omega} v_{\parallel} \right) \frac{m_j}{T_j K_{\perp}} \left\{ 1 + \left(\Omega - \frac{\lambda_j T_j K_{\perp}}{m_j \Omega_j \Omega} \right) Q_{s,t} \right\} \times \left[\left(\frac{1}{k_{\parallel} v_{\parallel} - \omega + i.0} \right) \times \left[\left(1 - \frac{k_{\parallel} v_{\parallel}}{\omega} \right) \frac{\partial f_{0j}}{\partial v_{\perp}} + \frac{k_{\parallel} v_{\perp}}{\omega} \frac{\partial f_{0j}}{\partial v_{\parallel}} \right] \right] \right.$$
$$\left. + \left(\frac{\left| \vec{K} - \vec{k} \right|}{\Omega - \omega} v_{\perp} \cos\theta + \frac{k_{\parallel}}{\left| \vec{K} - \vec{k} \right|} \right) \times \frac{\partial}{\partial v_{\parallel}} \left[\left(\frac{1}{k_{\parallel} v_{\parallel} - \omega + i.0} \right) \times \left[\left(1 - \frac{k_{\parallel} v_{\parallel}}{\omega} \right) \frac{\partial f_{0j}}{\partial v_{\perp}} + \frac{k_{\parallel} v_{\perp}}{\omega} \frac{\partial f_{0j}}{\partial v_{\parallel}} \right] Q_{s,t} \right] d\vec{v} \right]. \tag{33}$$

$$C = \int v_{\parallel} \left[\left[\left(1 - \frac{k_{\parallel} v_{\parallel}}{\omega}\right)\frac{\partial}{\partial v_{\parallel}} + \frac{k_{\parallel} v_{\perp}}{\omega}\frac{\partial}{\partial v_{\parallel}} \right] \times \left[\frac{Ck_{\perp}}{\Omega}\frac{m_j}{T_j K_{\perp}} \left\{ 1 + \left(\Omega - \frac{\lambda_j T_j K_{\perp}}{m_j \Omega_j \Omega}\right) \times Q_{p,q} \right\} f_{0j} - \left(1 - \frac{K_{\perp} v_{\perp}}{\Omega}\cos\theta\right)\frac{\partial f_{0j}}{\partial v_{\parallel}} Q_{s,t} \right] T_{p,q} \right] d\vec{v}. \quad (34)$$

$$D = -\int v_{\parallel} \left[\left[\left(1 - \frac{k_{\parallel} v_{\parallel}}{\omega}\right)\frac{\partial f_{0j}}{\partial v_{\perp}} + \frac{k_{\parallel} v_{\perp}}{\omega}\frac{\partial f_{0j}}{\partial v_{\parallel}} \right] \times \left(\frac{1}{k_{\parallel} v_{\parallel} - \omega + i.0}\right) \times \left[\frac{Ck_{\perp}}{\Omega} \cdot \frac{m_j}{T_j K_{\perp}} \left\{ 1 + \left(\Omega - \omega + k_{\parallel} v_{\parallel} - \frac{\lambda_j T_j K_{\perp}}{m_j \Omega_j \Omega}\right) \times T_{p,q} \right\} \right. \right.$$

$$\left. \left. + \frac{K_{\perp} v_{\perp}}{\Omega}\cos\theta\frac{\partial}{\partial v_{\parallel}} T_{p,q} \right] \right] d\vec{v}. \quad (35)$$

Instabilities

The growth rate of the ordinary mode wave is computed using the formula:

$$\frac{\gamma_h}{\Omega} = -\left[\frac{Im\,\epsilon_d + Im\,\epsilon_h + \frac{1}{2}\left(\frac{\partial^2 \epsilon_0}{\partial\Omega\partial t}\right)}{\Omega\left(\frac{\partial\epsilon_0}{\partial\Omega}\right)} \right]_{\Omega=\Omega_j}. \quad (36)$$

As a result of the reverse absorption effect, the second term of the growth rate expression in Eq. (36) reduces to zero. Now, from Eq. (29), we estimate the linear term of the dielectric function for the ordinary mode wave, considering that the term s = t = p = q = 1 contributes the most to Bessel's sum for the ordinary mode wave.

$$\varepsilon_0\left(\vec{K},\Omega\right) = 1 + \frac{\omega_{pj}^2\left(\Omega - \omega\right)\int_0^\infty J_1^2\left(\frac{K_{\perp} v_{\perp}}{\Omega_j}\right)2\pi v_{\perp}dv_{\perp}f_{0j}\left(v_{\perp}\right)}{\left(c^2 K_{\perp}^2 - \Omega^2\right)\left(\Omega_j - \Omega + K_{\perp} v_F\right)} - \frac{\omega_{pj}^2\left(\Omega - \omega\right)K_{\perp}\cos\theta\int_0^\infty J_1^2\left(\frac{K_{\perp} v_{\perp}}{\Omega_j}\right)2\pi v_{\perp}^2 f_{0j}\left(v_{\perp}\right)dv_{\perp}}{\Omega\left(c^2 K_{\perp}^2 - \Omega^2\right)\left(\Omega_j - \Omega + K_{\perp} v_F\right)}. \quad (37)$$

where v_F is the particle drift velocity defined by $v_F = -\dfrac{F}{m_j \Omega_j}$.

From equation (37), we obtain,

$$\Omega\frac{\partial\varepsilon_0}{\partial\Omega}\left(\vec{K},\Omega\right) = \frac{\Omega}{\left(c^2 K_{\perp}^2 - \Omega^2\right)}\left(\frac{\omega_{pj}^2\int_0^\infty J_1^2\left(\frac{K_{\perp} v_{\perp}}{\Omega_j}\right)2\pi v_{\perp}f_{0j}\left(v_{\perp}\right)}{\left(\Omega_j - \Omega + \omega_F\right)} + \frac{\omega_{pj}^2\Omega\left(\Omega - \omega\right)\int_0^\infty J_1^2\left(\frac{K_{\perp} v_{\perp}}{\Omega_j}\right)2\pi v_{\perp}dv_{\perp}f_{0j}\left(v_{\perp}\right)}{\left(\Omega_j - \Omega + \omega_F\right)^2} \right.$$

$$\left. + \frac{2\omega_{pj}^2\Omega\left(\Omega - \omega\right)\int_0^\infty J_1^2\left(\frac{K_{\perp} v_{\perp}}{\Omega_j}\right)2\pi v_{\perp}dv_{\perp}f_{0j}\left(v_{\perp}\right)}{\left(c^2 K_{\perp}^2 - \Omega^2\right)\left(\Omega_j - \Omega + \omega_F\right)} \right) + \left(1 - \frac{K_{\perp}\cos\theta}{2\Omega}\int_0^\infty J_1^2\left(\frac{K_{\perp} v_{\perp}}{\Omega_j}\right)2\pi v_{\perp}dv_{\perp}f_{0j}\left(v_{\perp}\right)\right) + \quad (38)$$

$$\frac{\omega_{pj}^2\int_0^\infty J_1^2\left(\frac{K_{\perp} v_{\perp}}{\Omega_j}\right)2\pi v_{\perp}dv_{\perp}f_{0j}\left(v_{\perp}\right)\int_0^\infty J_1^2\left(\frac{K_{\perp} v_{\perp}}{\Omega_j}\right)2\pi v_{\perp}^2 dv_{\perp}f_{0j}\left(v_{\perp}\right)K_{\perp}\cos\theta\left(\Omega - \omega\right)}{\Omega^2\left(\Omega_j - \Omega + \omega_F\right)}.$$

where $\omega_F = K_{\perp} v_F$.

The imaginary component of the dispersion relation contributes to the growth rate. Here, we consider the contribution of polarisation coupling to the growth rate, which is the dominant contribution of the plasma maser effect. Now, we compute $Im\,\varepsilon_p\left(\vec{K},\Omega\right)$ from Eq. (31).

$$Im\,\varepsilon_p\left(\vec{K},\Omega\right) = \frac{\omega_{pj}^4\left(\Omega - \omega\right)^2}{R\left(c^2 K_{\perp}^2 - \Omega^2\right)c^2 K^2 - \left(\Omega - \omega\right)^2}\left(\frac{e_j}{m_j}\right)^2 |E_l|^2\left(A\times Im\,D + C\times Im\,B\right). \quad (39)$$

where $K = \left|\vec{K} - \vec{k}\right|$.

Hence, the dominant portion comes from $A \times \text{Im} D$.

$$A = \frac{\int_0^\infty J_1^2\left(\frac{K_\perp v_\perp}{\Omega_j}\right) 2\pi v_\perp^2 f_{0j}(v_\perp) dv_\perp}{v_d v_j^2 \left|\vec{K} - \vec{k}\right| (\Omega_j + K_\perp v_F - \Omega)} - \frac{\int_0^\infty J_1^4\left(\frac{K_\perp v_\perp}{\Omega_j}\right) 2\pi v_\perp^2 f_{0j}(v_\perp) dv_\perp (\Omega - \lambda_j v_{0j} \alpha)}{v_d v_j^2 \left|\vec{K} - \vec{k}\right| (\Omega_j - \Omega + \omega_F)(\Omega_j - \Omega - \omega + \omega_F)} + \frac{1}{v_j^2}\left(\frac{1}{v_d \left|\vec{K} - \vec{k}\right|} + \frac{\left|\vec{K} - \vec{k}\right|}{(\Omega - \omega) K_\perp}\right) \times$$

$$\left[\frac{\int_0^\infty J_1^2\left(\frac{K_\perp v_\perp}{\Omega_j}\right) 2\pi v_\perp^2 f_{0j}(v_\perp) dv_\perp}{(\Omega_j - \Omega + \omega_F)} + \frac{\int_0^\infty J_1^4\left(\frac{K_\perp v_\perp}{\Omega_j}\right) 2\pi v_\perp^2 f_{0j}(v_\perp) dv_\perp (\Omega - \lambda_j v_{0j} \alpha)}{(\Omega_j - \Omega + \omega_F)^2}\right] - \qquad (40)$$

$$\frac{2\left|\vec{K} - \vec{k}\right| \cos\theta \int_0^\infty J_1^4\left(\frac{K_\perp v_\perp}{\Omega_j}\right) 2\pi v_\perp^3 f_{0j}(v_\perp) dv_\perp}{v_j^2 (\Omega - \omega)(\Omega_j - \Omega + \omega_F)^2} - \frac{k_\parallel \int_0^\infty J_1^4\left(\frac{K_\perp v_\perp}{\Omega_j}\right) 2\pi v_\perp^2 f_{0j}(v_\perp) dv_\perp}{v_j^2 \left|\vec{K} - \vec{k}\right| (\Omega_j - \Omega + \omega_F)^2}.$$

$$\text{Im}\,\varepsilon_p(\vec{K}, \Omega) = \left(\frac{\omega_{pj}}{\Omega_j}\right)^2 \left(\frac{\Omega_j - \omega}{ck_\parallel}\right)^2 \left(\frac{e_j}{m_j}\right)^2 |E_l|^2 \times \frac{\int_0^\infty J_1^2\left(\frac{K_\perp v_\perp}{\Omega_j}\right) 2\pi v_\perp^2 f_{0j}(v_\perp) dv_\perp}{v_d v_j^2 \left|\vec{K} - \vec{k}\right| \omega_F} - \frac{\int_0^\infty J_1^4\left(\frac{K_\perp v_\perp}{\Omega_j}\right) 2\pi v_\perp^2 f_{0j}(v_\perp) dv_\perp (\Omega - \lambda_j v_{0j} \alpha)}{v_d v_j^2 \left|\vec{K} - \vec{k}\right| \omega_F(\omega_F - \omega)}$$

$$+ \frac{1}{v_j^2}\left(\frac{1}{v_d \left|\vec{K} - \vec{k}\right|} + \frac{\left|\vec{K} - \vec{k}\right|}{(\Omega_j - \omega) K_\perp}\right) \times \left(\frac{\int_0^\infty J_1^2\left(\frac{K_\perp v_\perp}{\Omega_j}\right) 2\pi v_\perp^2 f_{0j}(v_\perp) dv_\perp}{\omega_F} + \frac{\int_0^\infty J_1^4\left(\frac{K_\perp v_\perp}{\Omega_j}\right) 2\pi v_\perp^2 f_{0j}(v_\perp) dv_\perp (\Omega - \lambda_j v_{0j} \alpha)}{\omega_F^2}\right) -$$

$$\frac{2\left|\vec{K} - \vec{k}\right| \int_0^\infty J_1^4\left(\frac{K_\perp v_\perp}{\Omega_j}\right) 2\pi v_\perp^3 f_{0j}(v_\perp) dv_\perp}{v_j^2 (\Omega_j - \omega) \omega_F^2} - \frac{k_\parallel \int_0^\infty J_1^4\left(\frac{K_\perp v_\perp}{\Omega_j}\right) 2\pi v_\perp^2 f_{0j}(v_\perp) dv_\perp}{v_j^2 \left|\vec{K} - \vec{k}\right| \omega_F^2} \times$$

$$\frac{\sqrt{\pi} K_\perp v_d c}{v_j^5 \Omega |k_\parallel|}\left[\frac{\sqrt{\pi} v_j}{4} + \frac{(\Omega - \lambda_j v_{0j} \alpha)}{\omega_F} \int_0^\infty J_1^2\left(\frac{K_\perp v_\perp}{\Omega_j}\right) 2\pi v_\perp^2 f_{0j}(v_\perp) dv_\perp - \frac{4\sqrt{\pi} K_\perp v_d \int_0^\infty J_1^4\left(\frac{K_\perp v_\perp}{\Omega_j}\right) 2\pi v_\perp^3 f_{0j}(v_\perp) dv_\perp}{v_j^2 |k_\parallel| \Omega_j \omega_F}\right] \exp\left[-\frac{v_d^2}{v_j^2}\right]. \qquad (41)$$

where $\alpha = \frac{K_\perp v_F}{\Omega_j}$.

Using Eqs. (29), (39), (40), and (41) in Eq. (36), we obtain the growth of ordinary mode waves due to the polarisation coupling term as

$$\frac{\gamma_p}{\Omega} = \pi \left(\frac{\omega_{pj}}{\Omega_j}\right)^2 \left(\frac{e_j}{m_j}\right)^2 \frac{c^2 k_\parallel^2}{c^2 K_\perp^2 - \Omega^2}\left(1 - \frac{\lambda_j T_j K_\perp}{m_j \Omega_j \Omega}\right) \frac{E_l^2}{|k_\parallel| v_j^3} \exp\left\{-\left(\frac{v_d}{v_j}\right)^2\right\}. \qquad (42)$$

DISCUSSIONS AND CONCLUSIONS

Drift waves are the characteristic feature of inhomogeneous plasma and are observed in magnetosphere and ionospheric plasma as well as in fusion devices. Drift waves are in phase with plasma particles, and energy transfer through wave particle interaction is possible in such a case. This study on nonlinear energy exchange among drift wave and O-mode through wave particle interaction is called the plasma maser effect, which may help in understanding electromagnetic instabilities in fusion plasma and in the magnetosphere in inhomogeneous regions. Such a nonlinear process may be useful in developing methods to control and minimise the effect of gradient features on plasma confinement and stability.

Temperature gradients in ionospheric plasma are responsible for the drift motion of plasma particles and associated drift wave turbulence phenomena. We have considered drift ion-cyclotron waves in the magnetospheric region and in the upper ionospheric plasma [1]. The low-frequency ion-cyclotron wave energy is taking part in the growth of the O-mode,

as shown in Eq. (42). The external force involved in the drift motion of particles is also contributing to the growth of the O-mode. The role of gradient parameters 'λ_j' in the amplification process for O-mode may also be analysed from Eq. (42).

In earlier work on the growth of O-mode through nonlinear wave-particle interaction [1, 26], analysis of the effect of external force and gradient parameters for density and temperature was not included.
By using the following satellite observational data from magnetospheric plasma [33],
$\Omega = 2.804 \times 10^6 \, Hz, \Omega_j = 2.8 \times 10^6 \, Hz, K_\perp = 10^{-3} \, m^{-1}, \omega_{pj} = 2.84 \times 10^8 \, Hz, v_j = 4.19 \times 10^5 \, ms^{-1}, k_\parallel \sim 10^{-5} \, m^{-1}, E_l \sim 10^{-4} \, Vm^{-1},$

$E_l \sim 10^{-4} \, Vm^{-1},$ we have

To demonstrate the influence of gradient parameters, we express the growth rate of Eq. (42) as a function of λ_j,

$$\frac{\gamma_p}{\Omega} = \pi \left(\frac{\omega_{pj}}{\Omega_j}\right)^2 \left(\frac{e_j}{m_j}\right)^2 \frac{c^2 k_\parallel^2}{c^2 K_\perp^2 - \Omega^2} \left(1 - \frac{\lambda_j T_j K_\perp}{m_j \Omega_j \Omega}\right) \frac{E_l^2}{|k_\parallel| v_j^3} \exp\left\{-\left(\frac{v_d}{v_j}\right)^2\right\},$$

$$\Rightarrow \frac{\gamma_p}{\Omega} = M \times R(\lambda_j),$$

where $M = \pi \left(\frac{\omega_{pj}}{\Omega_j}\right)^2 \left(\frac{e_j}{m_j}\right)^2 \frac{c^2 k_\parallel^2}{c^2 K_\perp^2 - \Omega^2} \frac{E_l^2}{|k_\parallel| v_j^3} \exp\left\{-\left(\frac{v_d}{v_j}\right)^2\right\},$

and $R(\lambda_j) = \left(1 - \frac{\lambda_j T_j K_\perp}{m_j \Omega_j \Omega}\right).$

Case 1: When both temperature and density gradients are not present, i.e., plasma is homogeneous,
then $R(\lambda_j) = 1.$

$$\Rightarrow \frac{\gamma_p}{\Omega} = M \times 1,$$

$$\Rightarrow \frac{\gamma_p}{\Omega} = \pi \left(\frac{\omega_{pj}}{\Omega_j}\right)^2 \left(\frac{e_j}{m_j}\right)^2 \frac{c^2 k_\parallel^2}{c^2 K_\perp^2 - \Omega^2} \frac{E_l^2}{|k_\parallel| v_j^3} \exp\left\{-\left(\frac{v_d}{v_j}\right)^2\right\},$$

$$\Rightarrow \frac{\gamma_p}{\Omega} = 10^{-2},$$

$$\Rightarrow \gamma_p = 10^{-2} \Omega.$$

Case 2: When the temperature gradient is ignored,

$$R(\lambda_j) = \left(1 - \frac{\lambda_{2j} T_j K_\perp}{m_j \Omega_j \Omega}\right),$$

where $\lambda_{2j} = \frac{1}{f_j} \frac{df_j}{dy} - \frac{F}{T_{0j}},$

$$\Rightarrow \frac{\gamma_p}{\Omega} = M \times R(\lambda_{2j}),$$

$$\Rightarrow \frac{\gamma_p}{\Omega} = 10^{-3} \lambda_{2j},$$

$$\Rightarrow \gamma_p = \Omega 10^{-3} \lambda_{2j}.$$

Case 3: When the density gradient is ignored,

$$R(\lambda_j) = \left(1 - \frac{\lambda_{1j} T_j K_\perp}{m_j \Omega_j \Omega}\right),$$

where $\lambda_{1j} = \frac{\partial}{\partial T_j} \frac{dT_j}{dy} - \frac{F}{T_{0j}},$

$$\Rightarrow \frac{\gamma_p}{\Omega} = M \times R(\lambda_{1j}),$$

$$\Rightarrow \frac{\gamma_p}{\Omega} = 10^{-3} \lambda_{1j},$$

$$\Rightarrow \gamma_p = \Omega 10^{-3} \lambda_{1j}.$$

Case 4: When all the gradients are present,

$$\frac{\gamma_p}{\Omega} = M \times R\left(\lambda_j\right),$$

$$\Rightarrow \frac{\gamma_p}{\Omega} = 10^{-5},$$

$$\Rightarrow \gamma_p = 10^{-5}\,\Omega.$$

As a result, we have observed that the gradients in density and temperature, along with the frequency related to particle pressure, may influence the amplification process of electromagnetic O-mode instability through electrostatic ion cyclotron drift wave turbulence.

Data Availability Statement
Data sharing is not applicable to this article as no datasets were generated or analysed during the current study.

ORCID
Banashree Saikia, https://orcid.org/0000-0002-3816-5949; **P.N. Deka**, https://orcid.org/0000-0001-9485-9294

REFERENCES
[1] P.N. Deka, and A. Borgohain, "On unstable electromagnetic radiation through nonlinear wave–particle interactions in presence of drift wave turbulence," Journal of Plasma Physics, **78**(5), 515-524 (2012). https://doi.org/10.1017/S0022377812000207
[2] R.C. Davidson, and C.S. Wu, "Ordinary-mode electromagnetic instability in high- plasmas," The Physics of Fluids, **13**(5), 1407-1409 (1970). https://doi.org/10.1063/1.1693082
[3] D.A. Gurnett, "The Earth as a radio source: Terrestrial kilometric radiation," Journal of Geophysical Research, **79**(28), 4227-4238 (1974). https://doi.org/10.1029/JA079i028p04227
[4] L.M. Hayes, and D.B. Melrose, "Generation of ordinary mode auroral kilometric radiation from extraordinary mode waves," Journal of Geophysical Research: Space Physics, **91**(A1), 211-217 (1986). https://doi.org/10.1029/JA091iA01p00211
[5] M.M. Mellott, W. Calvert, R.L. Huff, D.A. Gurnett, and S.D. Shawhan, "DE-1 observations of ordinary mode and extraordinary mode auroral kilometric radiation," Geophysical research letters, **11**(12), 1188-1191 (1984). https://doi.org/10.1029/GL011i012p01188
[6] D. Ibscher, M. Lazar, and R. Schlickeiser, "On the existence of Weibel instability in a magnetized plasma. II. Perpendicular wave propagation: The ordinary mode," Physics of Plasmas, **19**(7), 072116 (2012). https://doi.org/10.1063/1.4736992
[7] D. Ibscher, M. Lazar, M.J. Michno, and R. Schlickeiser, "Towards a complete parametrization of the ordinarymode electromagnetic instability in counterstreaming plasmas. I. Minimizing ion dynamics," Physics of Plasmas, **20**(1), 012103 (2013). https://doi.org/10.1063/1.4774066
[8] D. Ibscher, R. Schlickeiser, "Towards a complete parametrization of the ordinary-mode electromagnetic instability in counterstreaming plasmas. II. Ion effects," Physics of Plasmas, **20**(4), 042121 (2013). https://doi.org/10.1063/1.4802929
[9] D. Ibscher, and R. Schlickeiser, "Solar wind kinetic instabilities at small plasma betas," Physics of Plasmas, **21**(2), 022110 (2014). https://doi.org/10.1063/1.4863497
[10] M.F. Bashir, and G. Murtaza, "Effect of temperature anisotropy on various modes and instabilities for a magnetized non-relativistic bi-Maxwellian plasma," Brazilian Journal of Physics, **42**(5), 487-504 (2012). https://doi.org/10.1007/s13538-012-0087-9
[11] F. Hadi, M.F. Bashir, A. Qamar, P.H. Yoon, and R. Schlickeiser, "On the ordinary mode instability for low beta plasmas," Physics of Plasmas, **21**(5), 052111 (2014). https://doi.org/10.1063/1.4879823
[12] R. Schlickeiser, and P.H. Yoon, "On the marginal instability threshold condition of the aperiodic ordinary mode," Physics of Plasmas, **21**(7), 072119 (2014). https://doi.org/10.1063/1.4890463
[13] M. Nambu, "A new maser effect in plasma turbulence," Laser and Particle Beams, **1**, 427-454 (1983). https://doi.org/10.1017/S0263034600000513
[14] V.N. Tsytovich, L. Stenflo, and H. Wilhelmsson, "Current flow in ion-acoustic and Langmuir turbulence plasma interaction," Physica Scripta, **11**(5), 251 (1975). https://doi.org/10.1088/0031-8949/11/5/001
[15] M. Nambu, "Plasma-maser effects in plasma astrophysics," Space science reviews, **44**(3), 357-391 (1986). https://doi.org/10.1007/BF00200820
[16] S.V. Vladimirov, and M.Y. Yu, "Brief review of the turbulent bremsstrahlung (plasma-maser) effect," Physica Scripta, **2004**(T113), 32 (2004). https://doi.org/10.1238/Physica.Topical.113a00032
[17] P.N. Deka, K.S. Goswami, and S. Bujarbarua, "Plasma maser effect in magnetosphere plasma associated with MHD turbulence," Planetary and space science, **45**(11), 1443-1447 (1997). https://doi.org/10.1016/S0032-0633(97)00055-X
[18] B.J. Saikia, P.N. Deka, and S. Bujarbarua, "Plasma-Maser Instability of Bernstein Mode in Presence of Magnetohydrodynamic Turbulence," Contributions to Plasma Physics, **35**(3), 263-271 (1995). https://doi.org/10.1002/ctpp.2150350308
[19] P.N. Deka, "Orthogonal interaction of Bernstein mode with ion-acoustic wave through plasma maser effect," Pramana, **50**, 345-354 (1998). https://doi.org/10.1007/BF02845556
[20] M. Singh, and P.N. Deka, Pramana, **66**, 547 (2006). https://doi.org/10.1007/BF02704498
[21] M. Singh, and P.N. Deka, "Plasma-maser effect in inhomogeneous plasma in the presence of drift wave turbulence," Physics of plasmas, **12**(10), 102304 (2005). https://doi.org/10.1063/1.2087587

[22] R.N. Khound, S.N. Sarma, and S. Bujarbarua, "Plasma maser theory of ordinary mode radiation," Indian Journal of Radio and Space Physics, **18**, 90-94 (1989). https://nopr.niscpr.res.in/handle/123456789/36391

[23] J. D. Huba, G. Joyce, and J.A. Fedder, Ion sound waves in the topside low latitude ionosphere. Geophysical research letters, **27**(19), 3181-3184 (2000). https://doi.org/10.1029/2000GL003808

[24] S.J. Gogoi, P.N. Deka, "Estimation of Growth Rate of Electromagnetic Plasma Wave through Vlasov-Maxwell Mathematical Frame in Ionospheric Plasma," Physical Science International Journal, **23**(3), 1-10 (2019). https://doi.org/10.9734/psij/2019/v23i330155

[25] J. Zielinski, A.I. Smolyakov, P. Beyer, and S. Benkadda, Electromagnetic electron temperature gradient driven instability in toroidal plasmas. Physics of Plasmas, **24**(2), 024501 (2017). https://doi.org/10.1063/1.4975189

[26] P. Senapati, and P.N. Deka, "Instability of Electron Bernstein Mode in Presence of Drift Wave Turbulence Associated with Density and Temperature Gradients," Journal of Fusion Energy, **39**(6), 477-490 (2020). https://doi.org/10.1007/s10894-020-00269-y

[27] V. Tangri, R. Singh, and P. Kaw, "Effects of impurity seeding and charge non-neutrality on electromagnetic electron temperature gradient modes in a tokamak," Physics of plasmas, **12**(7), 072506 (2005). https://doi.org/10.1063/1.1938975

[28] H. Du, H. Jhang, T.S. Hahm, J.Q. Dong, and Z.X. Wang, Properties of ion temperature gradient and trapped electron modes in tokamak plasmas with inverted density profiles. Physics of Plasmas, **24**(12), 122501 (2017). https://doi.org/10.1063/1.5000125

[29] H. Du, Z.X. Wang, J.Q. Dong, and S.F. Liu, "Coupling of ion temperature gradient and trapped electron modes in the presence of impurities in tokamak plasmas," Physics of Plasmas, **21**(5), 052101 (2014). https://doi.org/10.1063/1.4875342

[30] A. Hirose, and M. Elia, "Electron temperature gradient driven skin size drift mode in tokamaks," Plasma physics and controlled fusion, 45(1), L1 (2002). https://doi.org/10.1088/0741-3335/45/1/101

[31] J.J. Podesta, and S.P. Gary, "Magnetic helicity spectrum of solar wind fluctuations as a function of the angle with respect to the local mean magnetic field," The Astrophysical Journal, **734**(1), 15 (2011). https://doi.org/10.1088/0004-637X/734/1/15

[32] S. Ichimaru, *Statistical plasma physics: basic principles*, (CRC Press, 2018).

[33] N.F. Blagovecshchenskaya, T.D. Borisova, A.S. Kalishin, V.N. Kayatkin, T.K. Yeoman, and I. Haggstron, "Comparison of the effects induced by the ordinary (O-mode) and extraordinary (X-mode) polarized powerful HF radio waves in the high-latitude ionospheric *F* region," Cosmic Research, **56**(1), 11-25 (2018). https://doi.org/10.1134/S0010952518010045

[34] S.P. Gary, *Theory of space plasma microinstabilities*, no. 7, (Cambridge university press, 1993).

[35] A.B. Mikhailovskii, "Oscillations of an Inhomogeneous Plasma," In: Leontovich, M.A. editors, *Reviews of Plasma Physics*, (Springer, Boston, MA, 1967). https://doi.org/10.1007/978-1-4615-7799-7_2

[36] P.N. Deka, Ph.D. Thesis, Guwahati University, Assam, India, 1999.

ГЕНЕРАЦІЯ О-МОДИ ЗА НАЯВНОСТІ ІОННО-ЦИКЛОТРОННОЇ ТУРБУЛЕНТНОСТІ ДРЕЙФОВОЇ ХВИЛІ В НЕОДНОРІДНІЙ ПЛАЗМІ

Банашрі Сайк'я, П.Н. Дека
Факультет математики, Університет Дібругарх, Дібругарх, 786004, Ассам, Індія

Це дослідження має на меті дослідити вплив турбулентності іонно-циклотронної дрейфової хвилі на генерацію звичайної моди (О-моди) за наявності градієнтів густини та температури. Для цього розглядається плазма Власова, де в системі присутні як резонансні, так і нерезонансні моди. Тут нерезонансний режим – це збурення, викликане О-модою в квазістаціонарному стані плазми, яке характеризується наявністю низькочастотних хвиль іонно-циклотронного резонансного режиму. Взаємодія між цими хвилями вивчається системою рівнянь Власова-Максвелла та модифікованою функцією розподілу максвеллівського типу для частинок, яка включає зовнішнє силове поле та пов'язані параметри градієнта густини та температури. У дослідженні аналізується швидкість зростання електромагнітної О-моди за рахунок енергії іонно-циклотронного дрейфу хвилі та пов'язаного з цим впливу градієнта густини та температури. Ця модель використовує теорію лінійного відгуку на слабко турбулентну плазму, оцінює відгуки через турбулентні та збурені поля та отримує нелінійне співвідношення дисперсії для О-моди.

Ключові слова: *звичайний режим; градієнти густини і температури; турбулентність дрейфової хвилі; взаємодія хвиля-частинка*

DETERMINATION OF THE DEPENDENCE OF THE OSCILLATION OF TRANSVERSE ELECTRICAL CONDUCTIVITY AND MAGNETORESISTANCE ON TEMPERATURE IN HETEROSTRUCTURES BASED ON QUANTUM WELLS†

Ulugbek I. Erkaboev*, Rustamjon G. Rakhimov§

Namangan Institute of Engineering and Technology,160115 Namangan, Uzbekistan
*Corresponding Author e-mail: erkaboev1983@gmail.com, §Corresponding author: rgrakhimov@gmail.com

In this work, the influence of two-dimensional state density on oscillations of transverse electrical conductivity in heterostructures with rectangular quantum wells is investigated. A new analytical expression is derived for calculating the temperature dependence of the transverse electrical conductivity oscillation and the magnetoresistance of a quantum well. For the first time, a mechanism has been developed for oscillating the transverse electrical conductivity and magnetoresistance of a quantum well from the first-order derivative of the magnetic field (differential) $\partial\left(\rho_\perp^{2d}\left(E,B,T,d\right)\right)\big/\partial B$ at low temperatures and weak magnetic fields. The oscillations of electrical conductivity and magnetoresistance of a narrow-band quantum well with a non-parabolic dispersion law are investigated. The proposed theory explored the results of experiments with a narrow-band quantum well ($In_xGa_{1-x}Sb$).

Keywords: *semiconductor; conductivity; quantum well; magnetoresistance; magnetic field*
PACS: 73.63.Hs, 73.21.Fg, 73.21.−b

INTRODUCTION

In the presence of a quantizing magnetic field in nanoscale semiconductor structures, not only the optical or magnetic, but also the kinetic properties of free electrons or holes change significantly. The study of the oscillation of longitudinal and transverse magnetoresistance in heterostructures based on quantum wells, along with the Hall measurements, can provide important information about its characteristics, such as the effective masses of free electrons and holes [1,2], the number of occupied zones, spin degeneration, quantum relaxation time and other kinetic parameters [3]. In a series of experiments conducted in the last decade, it was discovered that the kinetic properties of a quantum well subjected to deformation, temperature, ultra-high frequency electromagnetic field, deformation and light in the applied magnetic field provide even richer information for the theory of quantum physics. In particular, in the works [4,5], in the quantum well GaAs, the semiclassical theory of magnetoresistance oscillation during irradiation with microwaves is analyzed. In a quantizing magnetic field, the specific magnetoresistance of the system demonstrates Shubnikov-de Haase oscillations at low temperatures. And also, experimental values were established for the quantum pit GaAs, under the illumination of microwave radiation. In the works [6-23] various experimental techniques have been developed for determining the temperature dependence of the Shubnikov-de Haase oscillation in heterostructures with quantum wells with parabolic and non-parabolic laws of dispersion. For example, in the work [6], quantum oscillation phenomena were observed in heterostructures with quantum wells $Ga_{1-x}In_xN_yAs_{1-y}$ using magnetotransport measurements. Shubnikov-de Haase oscillations are obtained at magnetic fields up to 3 T and temperatures up to 20 K, which are used to determine the effective mass, two-dimensional density of charge and Fermi energy carriers. In the work [7], measurements of magnetic conductivity during compression of quantum wells $In_XGa_{1-X}Sb$ and GaSb are presented. Hall and Van de Pau structures were manufactured and Shubnikov–de Haase oscillations in the temperature range T=2–300 K at magnetic fields B=0–9 T were measured. In these samples, the high mobility of the charge carriers makes it possible to observe the Shubnikov-de Haase oscillation.

And also, in work [8], in the heterostructures of GaInNAs/GaAs with quantum wells doped with modulation of n- and p- type, magnetoresistance measurements were made, both in weak (B < 0.08 T) and in a strong magnetic field (up to 18 T) at temperatures of 75 mK and 6 K. It is shown that quantum oscillations in ρ_{xx} and the quantum Hall effect in ρ_{xy} are affected by the presence of nitrogen in the lattice of $A_{III}B_V$. For such materials, in weak magnetic fields, Shubnikov-de-Haas oscillations develop with higher mobility at a temperature of 6 K, and with an increase in the composition of nitrogen, the amplitude of the Shubnikov-de Haas oscillation decreases.

From the above literature it can be seen that a full-fledged theory has not been built in the heterostructures of quantum wells.

As can be seen from the literature analyzed above, there is no clear and complete theory of the dependence of quantum oscillations on the temperature and magnetic field found in experiments in heterostructures with a quantum well. A new mathematical model has not been developed to determine the temperature dependence of Shubnikov-de Haase oscillations in heterostructural semiconductors with a quantum well through the density of energy states of two-dimensional materials.

The purpose of this work is to simulate the temperature dependence of magnetoresistance oscillation in heterostructures based on quantum wells, taking into account the thermal widening of the two-dimensional density of states.

MODEL

Kinetic equation of charge carriers in nanoscale semiconductor structures in the absence of a quantizing magnetic field

In nanoscale semiconductor structures, the analysis of the electrical conductivity of electrons or holes is carried out using the Boltzmann distribution function $f_n(k)$ and in a homogeneous electric field F, this distribution function satisfies the solutions of the following kinetic equation in the absence of a magnetic field [24,25]:

$$\frac{q}{\hbar} F \nabla_k f_n(k) = \sum_{n`k`} w_{nn`}(k,k`)(f_{n`}(k`) - f_n(k)) \tag{1}$$

Here, q is the charge of the charge carriers, $w_{nn`}(k,k`)$ is probability of scattering per unit time from the $|nk\rangle в |n`k`\rangle$ state, n and n' are the subzone or minizone numbers.

In the case of classical electric fields, when the deviation of the distribution function $\varphi(k)$ from the equilibrium Fermi-Dirac function $f_0(E)$ can be considered small, in the one-minizone approximation the kinetic equation (1) is described as follows:

$$qFv(k)\frac{\partial f_0(E)}{\partial E} = \sum_{k`} w(k,k`)(\varphi(k`) - \varphi(k)) \tag{2}$$

Here, $\varphi(k) = f_1(k) - f_0(E)$; $E = E_1(k)$ is the energy of a free electron or hole in a main subzone or minizone; $v(k)$ is the velocity of a free electron or hole.

To solve equation (2), we can use the approximation of the relaxation time tensor taking into account the anisotropic nature of nanoscale semiconductors and obtain the following expression, in this approximation, to solve equation (2):

$$\varphi(k) = q\left(-\frac{\partial f_0(E)}{\partial E}\right)\sum_i \tau_i(E)F_i v_i(k) \tag{3}$$

In here

$$\frac{1}{\tau_i} = \sum_{k`} w(k,k`)\left(1 - \frac{v_i(k`)}{v_i(k)}\right) \tag{4}$$

The relaxation time tensor component in the principal axes of the tensor is inverse of the effective mass.

Influence of two-dimensional state density on temperature dependence of electrical conductivity oscillation in heterostructures with quantum wells at quantizing magnetic field

Now let's calculate the temperature dependence of the oscillation of longitudinal electrical conductivity in a quantum well when exposed to a quantizing magnetic field. In heterostructures with quantum wells for a two-dimensional free electron or hole, the addition to the distribution function (3), taking into account the symmetry, is written as:

$$\varphi(k) = q\left(-\frac{\partial f_0(E)}{\partial E}\right)\tau_\perp(E)Fv(k) \tag{5}$$

Here, $\tau_\perp = \tau_x = \tau_y$.

In this problem, the induction of the magnetic field is directed along the thickness of the quantum plate and is calculated perpendicular to the plane of the quantum plate (plane XY). Hence, when carrying out theoretical calculations, we introduce transverse electrical conductivity ($\sigma_\perp(E,B)$) perpendicular to the thickness of the quantum well (along the plane XY), one of the kinetic quantities calculated from the thickness of the quantum well is defined as longitudinal electrical conductivity ($\sigma_\parallel(E,B)$).

Using the expression (5) quantizing magnetic field, we can obtain the expression of the transverse electrical conductivity of $\sigma_\perp(E,B)$:

$$\sigma_\perp(E,B) = \sigma_{xx}(E,B) = \sigma_{yy}(E,B) = qn_s\mu_\perp(E,B) = \frac{e^2 n_s \langle \tau_\perp(E,B) \rangle}{m*} \tag{6}$$

Here, the n_s is concentration of charge carriers for a two-dimensional electron gas; $\mu_\perp$ mobility; m^* is effective mass of the charge carriers in a quantum well. $\langle \tau_\perp(E,B) \rangle$ is the energy-averaged relaxation time of a free electron when exposed to a quantizing magnetic field, and is calculated by the following expression [24,25]:

$$\langle \tau_\perp(E,B) \rangle = \frac{\int\limits_0^\infty N_s^{2d}(E,B)\left(\frac{\partial f_0}{\partial E}\right)\tau_\perp(E)E\,dE}{n_s} \tag{7}$$

Where, $N_s^{2d}(E,B)$ is the two-dimensional density of energy states in a quantizing magnetic field.

In a quantizing magnetic field, the two-dimensional density of energy states in the conduction zone of the quantum well is taken as the sum of Gaussian peaks [26]:

$$N_s^{2d}\left(E,B,d,n_Z\right) = \frac{eH}{2\pi c}\sum_{n_L}\sqrt{\frac{2}{\pi}}\frac{1}{G}\exp\left[-2\left(\frac{E-\left[\hbar\omega_c\left(n_L+\frac{1}{2}\right)+\frac{\pi^2\hbar^2}{2m^*d^2}n_Z^2\right]}{G}\right)^2\right] \tag{8}$$

Where, n_L is the number of Landau levels. $\omega_c = \dfrac{eH}{mc}$ is a cyclotron frequency. G is a widening parameter that is assumed to be constant.

In a strong magnetic field, two-dimensional electron systems of non-interacting electrons are considered according to the parabolic law of dispersion at low temperature T. In addition to the Gaussian peak of state density, at each Landau level there is a common multiplier of the magnetic field B before the total density of energy states. This means that as magnetic field B increases, each Landau level can contain more and more electrons. According to (8), there is no density of states between Landau levels if their distance $h\omega_c$ is noticeably greater than G.

Calculation of the temperature dependence of transverse electrical conductivity in quantum wells when exposed to a quantizing magnetic field

For the basic mechanisms, in massive semiconductors in the approximation of elastic scattering, the dependence of $\tau_3(E,T)$ relaxation time on energy and temperature is of a power nature [27]:

$$\tau_3(E,T) = \gamma_3(k_0 T)^\beta E^\alpha \tag{9}$$

For free electrons in a quantum well, the change in the density of states and the energy spectrum, taking into account dimensional quantization, leads to the following equation [28]:

$$\tau_\perp/\tau_3 = \gamma dk_\perp = \gamma d\sqrt{\frac{2m^*E}{\hbar^2}} \sim E^{\frac{1}{2}} \tag{10}$$

From (10), we get:

$$\tau_\perp = \gamma_\perp(k_0 T)^\beta E^{\alpha+\frac{1}{2}} \tag{11}$$

Here, d is the thickness of the quantum well. Taking into account (7), (8) and (11), the dependence of transverse electrical conductivity on the quantizing magnetic field and temperature in heterostructures with quantum wells takes the following form:

$$\sigma_\perp^{2d}(E,B,T,d) = \frac{e^3 B}{2\pi m^* c}\sqrt{\frac{2}{\pi}}\frac{1}{G}\int_0^\infty \sum_{n_L}\exp\left[-2\left(\frac{E-\left[\hbar\omega_c\left(n_L+\frac{1}{2}\right)+\frac{\pi^2\hbar^2}{2m^*d^2}n_Z^2\right]}{G}\right)^2\right]\gamma_\perp(k_0 T)^\beta E^{\alpha+\frac{3}{2}}\left(\frac{\partial f_0(E,T)}{\partial E}\right)dE \tag{12}$$

Thus, we can determine the temperature dependence of the oscillation of electrical conductivity in a quantum well when exposed to a quantizing magnetic field. And so, a new analytical expression was derived for calculating the oscillation of electrical conductivity in heterostructures with quantum wells in the presence of temperature and a magnetic field, based on the equation (12). Using equation (12), it is possible to analyze some experimental results at different temperatures and magnetic fields. In addition, using the equation (12), it is possible to calculate the temperature dependence of the oscillation of transverse magnetoresistance in the conduction zone of the quantum well in the presence of a quantizing magnetic field. Then, for a heterostructure based on a quantum well, the change in the oscillation of the

transverse magnetoresistance $\rho_\perp^{2d}(E,B,T,d)$ with respect to temperature and quantizing magnetic field is determined in the following new analytical expression:

$$\rho_\perp^{2d}(E,B,T,d) = 1/\sigma_\perp^{2d}(E,B,T,d)$$

$$\rho_\perp^{2d}(E,B,T,d) = \cfrac{1}{\left[\begin{array}{c} \cfrac{e^3 B}{2\pi m^* c}\sqrt{\cfrac{2}{\pi}}\cfrac{1}{G}\cdot \\ \int\limits_0^\infty \sum\limits_{n_L} \exp\left[-2\left(\cfrac{E-\left[\hbar\omega_c\left(n_L+\cfrac{1}{2}\right)+\cfrac{\pi^2\hbar^2}{2m^* d^2}n_z^2\right]}{G}\right)^2\right]\gamma_\perp(k_0 T)^\beta E^{\alpha+\frac{3}{2}}\left(\cfrac{\partial f_0(E,T)}{\partial E}\right)dE \end{array}\right]} \tag{13}$$

RESULTS AND DISCUSSION

Now, based on equations (12) and (13), let's consider the dependences $\sigma_\perp^{2d}(E,B,T,d)$ and $\rho_\perp^{2d}(E,B,T,d)$ on the graph. As can be seen from the new analytical expressions obtained, the term under the integral is a very complex function with respect to the energy E. That is, it is impossible to obtain an exact result by integrating it, and we will use a computer program to obtain $\sigma_\perp^{2d}(E,B,T,d)$ and $\rho_\perp^{2d}(E,B,T,d)$.

Figure 1 shows the dependence of the oscillation of the transverse electrical conductivity on the magnetic field (Figure 1a) and the reverse induction of the magnetic field (Figure 1b) in heterostructures based on the quantum well $In_{0.52}Al_{0.48}As/In_{0.53}Ga_{0.47}As/ In_{0.52}Al_{0.48}As$ at constant low temperatures. Here, the parameters of the quantum well $In_{0.53}Ga_{0.47}As$ are equal to the following value: the thickness of the quantum well $d = 16.8\ nm$, the effective mass of electrons in the conduction band of the quantum well $m_n = 0.059m_0$, the widening parameter $G = 0.5\ meV$ and the temperature $T = 4.2K$ [27].
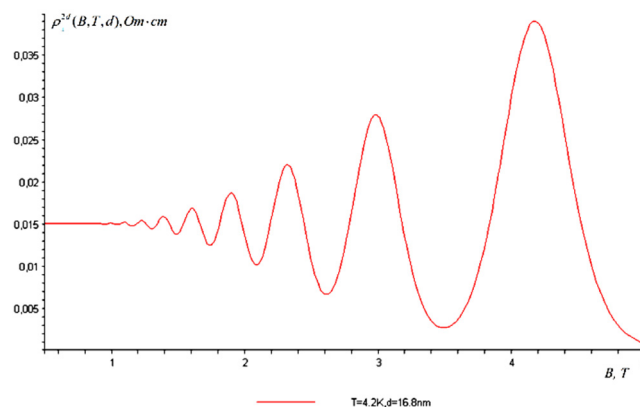
Figure 1a. Dependence of the oscillations of the transverse electrical conductivity on the magnetic field in heterostructures based on the $In_{0.52}Al_{0.48}As/In_{0.53}Ga_{0.47}As/ In_{0.52}Al_{0.48}As$ quantum well at temperatures T=4.2 K.
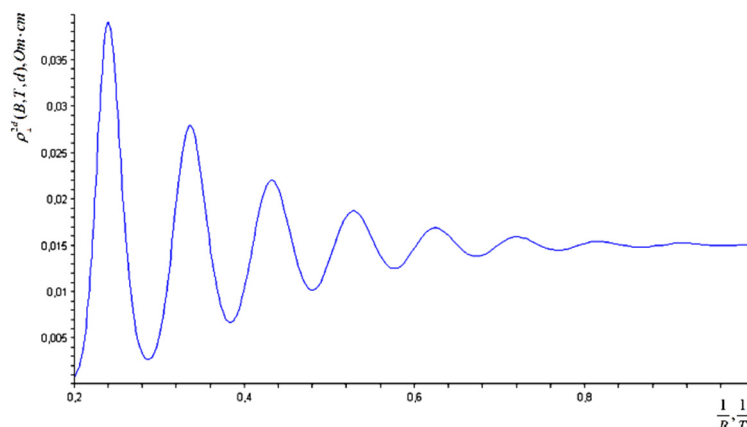
Figure 1b. Dependence of the oscillations of the transverse electrical conductivity on the reverse magnetic field induction in heterostructures based on the $In_{0.52}Al_{0.48}As/In_{0.53}Ga_{0.47}As/ In_{0.52}Al_{0.48}As$ quantum well at temperatures T=4.2 K.

In this case, when constructing the $\sigma_{\perp}^{2d}(E,B,T,d)$ graph, the number of Landau levels was taken as $n_L = 8$, and the number of dimensional quanta (the number of dimensional quanta) as $n_Z = 1$. In the figures, there is a sharp increase in the amplitude of fluctuations in electrical conductivity in the conductivity zone of the quantum well $In_{0.53}Ga_{0.47}As$ at magnetic field induction values of 1.5 T and above. Figure 2 shows the effect of temperature on the dependence of the oscillation of transverse electrical conductivity on the induction of the magnetic field (Figure 2a) and the reverse induction of the magnetic field (Figure 2b) in heterostructures based on the quantum well $In_{0.52}Al_{0.48}As/In_{0.53}Ga_{0.47}As/In_{0.52}Al_{0.48}As$ with a parabolic law of dispersion. As can be seen from these figures, with increasing temperature, the amplitude of the oscillation of electrical conductivity in the conduction band of the quantum well $In_{0.53}Ga_{0.47}As$ decreases. At sufficiently high temperatures, for example, at T = 40 K, magnetoresistance oscillations do not feel the quantizing magnetic field and do not observe oscillations of kinetic parameters. Because in nanoscale semiconductor materials to observe the effects of quantum oscillations, the thermal energy of the free charge carriers must be much smaller than the difference between two adjacent discrete energy levels.
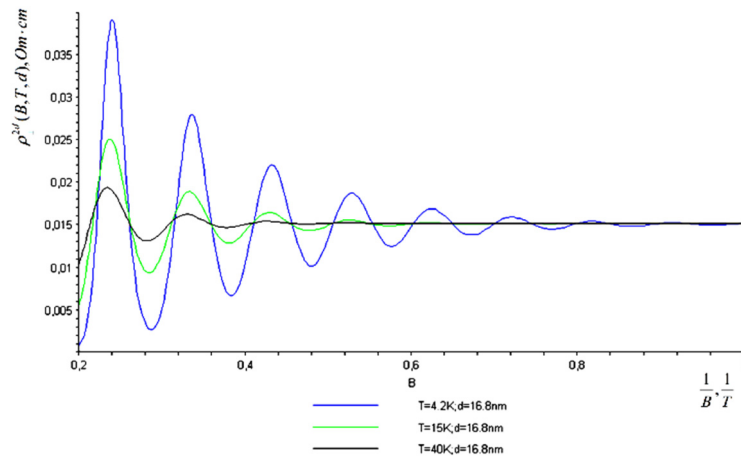
Figure 2a. Influence of temperature on the dependence of transverse electrical conductivity oscillations on magnetic field induction in heterostructures based on quantum well $In_{0.52}Al_{0.48}As/In_{0.53}Ga_{0.47}As/In_{0.52}Al_{0.48}As$
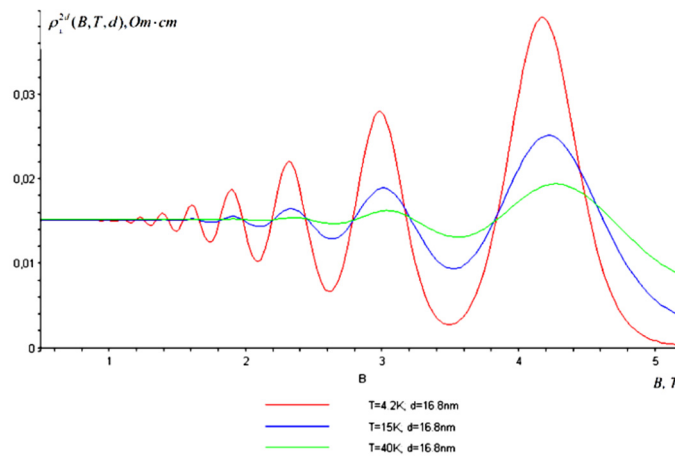
Figure 2b. Influence of temperature on the dependence of the oscillation of transverse electrical conductivity on the reverse induction of the magnetic field in heterostructures based on the quantum well $In_{0.52}Al_{0.48}As/In_{0.53}Ga_{0.47}As/In_{0.52}Al_{0.48}As$

Figure 3a shows the oscillations of the transverse magnetoresistance $\rho_{\perp}^{2d}(E,B,T,d)$ in the conduction band of the $In_{0.53}Ga_{0.47}As$ quantum well at low constant temperatures T=4.2K. This $\rho_{\perp}^{2d}(E,B,T,d)$ graph is obtained using equation(11). If we observe fluctuations in the induction of the quantizing magnetic field in the range from 0.5 T to 3.5 T, then the maximum value of the amplitude of the magnetic resistance of the quantum coil is about 1000 Om. With increasing temperature, a decrease in the amplitude of oscillations of the transverse conductivity is observed (Figure 3b). When the temperature reaches 40K, when the magnitude of the quantizing magnetic field reaches almost 3 T, the $\rho_{\perp}^{2d}(E,B,T,d)$ oscillations begin to disappear, that is, the influence of the quantizing magnetic field becomes not noticeable. However, as the temperature decreases, the quantizing magnetic field begins to increase its effect. In a simplified way, this can be explained as follows: statistical physics is applied to these quantum effects, i.e. the temperature dependence of $\rho_{\perp}^{2d}(E,B,T,d)$ oscillations is studied by thermal smearing (or thermal broadening).
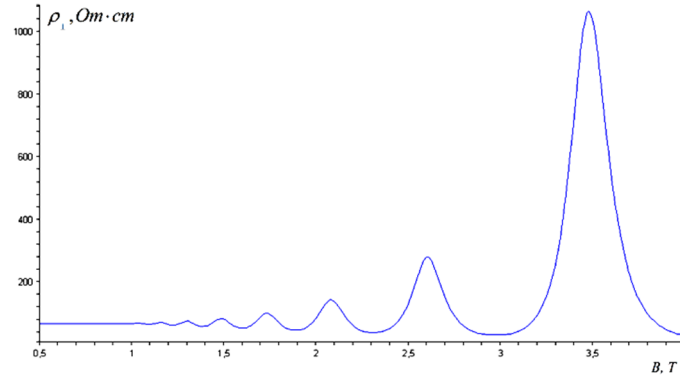
Figure 3a. Oscillations of transverse magnetoresistance $\rho_{\perp}^{2d}(E,B,T,d)$ in the conduction zone of the quantum well In$_{0.53}$Ga$_{0.47}$As at temperatures T = 4.2 K.
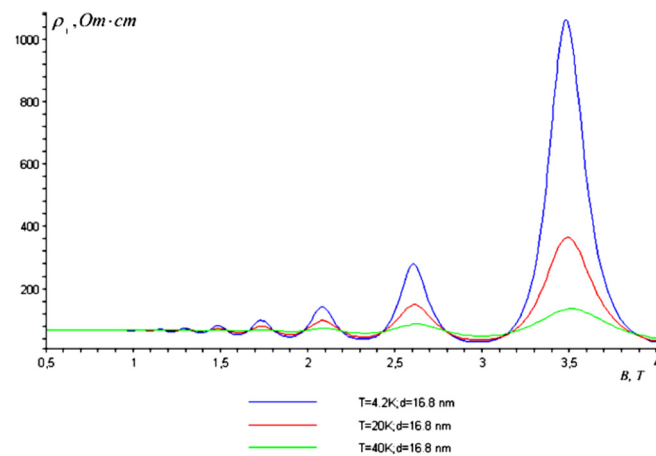
Figure 3b. Effect of temperature on oscillations of transverse magnetoresistance $\rho_{\perp}^{2d}(E,B,T,d)$ in the conduction zone of the quantum well In$_{0.53}$Ga$_{0.47}$As

It is known that the temperature dependence of oscillations of the density of energy states in two-dimensional and three-dimensional semiconductor materials has been studied in detail from a theoretical point of view in works [27, 28]. At the same time, a new mathematical model was developed. The equation (8) for constantly low temperatures shows the dependence of the energy density oscillations of the $N_s^{2d}(E,B,n_L,d,n_Z)$ states in two-dimensional semiconductor materials on the energy and magnetic field. The energy derivative of the Fermi-Dirac distribution function gives the delta function of $\left(\dfrac{\partial f_0(E,T)}{\partial E}\right)$ at very low temperatures, with the height of $\left(\dfrac{\partial f_0(E,T)}{\partial E}\right)$ decreasing and the width increasing with increasing temperature. Hence, the thermal widening of Landau levels is determined with the help of the $\left(\dfrac{\partial f_0(E,T)}{\partial E}\right)$ function. However, as can be seen from the work [27,28], the oscillation of the quantum effect is carried out by observing $N_s^{2d}(E,B,n_L,d,n_Z)$. Therefore, by decomposing $N_s^{2d}(E,B,n_L,d,n_Z)$ into a series of $\left(\dfrac{\partial f_0(E,T)}{\partial E}\right)$, oscillations of the transverse magnetoresistance of $\rho_{\perp}^{2d}(E,B,T,d)$ heterostructural semiconductors with a quantum well depending on temperature are determined.

In addition, using the analytical expression (13), one can analyze the dependence of the $\rho_{\perp}^{2d}(E,B,T,d)$ oscillations of the transverse magnetoresistance of heterostructural semiconductors with quantum wells. Figure 4 shows the dependence of the oscillations of the transverse magnetoresistance of the In$_{0.52}$Al$_{0.48}$As/In$_{0.53}$Ga$_{0.47}$As/In$_{0.52}$Al$_{0.48}$As heterostructure on the thickness of the In$_{0.53}$Ga$_{0.47}$As quantum well with a parabolic dispersion law. Here, $\rho_{\perp}^{2d}(E,B,T,d)$ at a quantizing magnetic field B = 3.5 T:

$$\rho_{\perp}^{2d}(T=3K,d=16,8nm)=1000\,Om; \quad \rho_{\perp}^{2d}(T=3K,d=14,8nm)=1100\,Om;$$

$$\rho_{\perp}^{2d}(T=3K,d=12,8nm)=1200\,Om$$

Thus, with a decrease in the thickness of the quantum well, the amplitude of the oscillations of the transverse magnetoresistance increases. Hence, we can conclude that the height of discrete Landau levels in two-dimensional semiconductor materials depends both on the temperature and on the thickness of the quantum well. In order to observe oscillations of the quantum effect even at higher temperatures, it is proposed that the thickness of the quantum well be as close as possible to the de Broglie length.
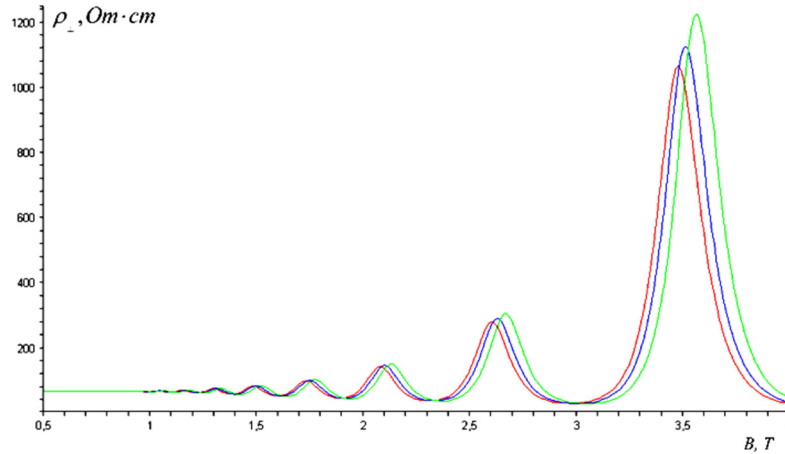
Figure 4. Dependence of the oscillation of transverse magnetoresistance of the heterostructure $In_{0.52}Al_{0.48}As/In_{0.53}Ga_{0.47}As/In_{0.52}Al_{0.48}As$ on the thickness of the quantum well $In_{0.53}Ga_{0.47}As$ with a parabolic law of dispersion.

Calculation of the temperature dependence of differential oscillations of magnetoresistance $\dfrac{\partial\left(\rho_{\perp}^{2d}(E,B,T,d)\right)}{\partial B}$ heterostructure with quantum well

As mentioned above, to observe the oscillation of the quantum effect in bulk and two-dimensional semiconductor materials, it is necessary to meet the conditions of a strong magnetic field and a very low temperature. Let's estimate the discrete quantum energy of a quantizing magnetic field and a quantum well at very low temperatures and the thermal energy of an electron corresponding to this energy level. In Figure 3a, the value of the induction of the magnetic field oscillations $\rho_{\perp}^{2d}(E,B,T,d)$ is calculated from 0.5 T to 4 T and at a temperature of 3 K. Temperature at T= 3 K $\dfrac{k}{e}T = 2,6\cdot10^{-4}\,eV$. At a magnetic field B= 1, $\hbar\dfrac{eB}{m}\Big/e = 12.4\cdot10^{-3}\,eV$.

Hence, $\dfrac{\hbar\dfrac{eB}{m}}{kT} \approx 48$, i.e. $\hbar\dfrac{eB}{m} \gg kT$. Although this estimate is completely subject to the conditions for the formation of quantum oscillatory effects in heterostructures with quantum wells, however, as can be seen from Figure 3a, oscillatory processes are clearly observed starting from 1.5 T. Why is this happening? With a magnetic field of 0.6 T, 1 T or 1.2 T, oscillations of the transverse magnetoresistance are not formed in the conduction field of the quantum coil, or does it seem that the obtained analytical expression (13) is not fully satisfied? This process is explained as follows. The value of the transverse magnetoresistance of a quantum well semiconductor varies greatly due to the magnetic field induction. From here, according to the differential law of resistance, the first derivative of the magnetic field induction is obtained according to the equation (13).

That is:

$$\frac{\partial\left(\rho_{\perp}^{2d}(E,B,T,d)\right)}{\partial B} = \frac{e^3}{2\pi m^* c}\sqrt{\frac{2}{\pi}}\frac{1}{G} = \frac{\partial\left[B\int_0^\infty\sum_{n_L}\exp\left[-2\left(\frac{E-\left[\hbar\frac{eB}{m_n^*}\left(n_L+\frac{1}{2}\right)+\frac{\pi^2\hbar^2}{2m^*d^2}n_Z^2\right]}{G}\right)^2\right]\gamma_{\perp}(k_0T)^\beta E^{\alpha+\frac{3}{2}}\left(\frac{\partial f_0(E,T)}{\partial E}\right)dE\right]^{-1}}{\partial B}$$

(14)

From a theoretical point of view, taking the derivative of the magnetic field induction from equation (14) and obtaining its graph is a very difficult task. However, implementation using computer programs allows you to evaluate both accuracy and quality. To compare the graphical results obtained by equations (13) and (14), we consider them in the same coordinate system.

In Figure 5 shows the dependence of $\rho_{\perp}^{2d}(E,B,T,d)$ and $\dfrac{\partial\left(\rho_{\perp}^{2d}(E,B,T,d)\right)}{\partial B}$ on the weak induction of the magnetic

field at T=3 K in the heterostructure In$_{0.52}$Al$_{0.48}$As / In$_{0.53}$Ga$_{0.47}$As / In$_{0.52}$Al$_{0.48}$As with a quantum well In$_{0.53}$Ga$_{0.47}$As. In this case, the number of Landau levels is n_L=7, and the dimensional quantum number is n_Z=1. Magnetic field induction was obtained in the range from 0.6 T to 1.22 T.
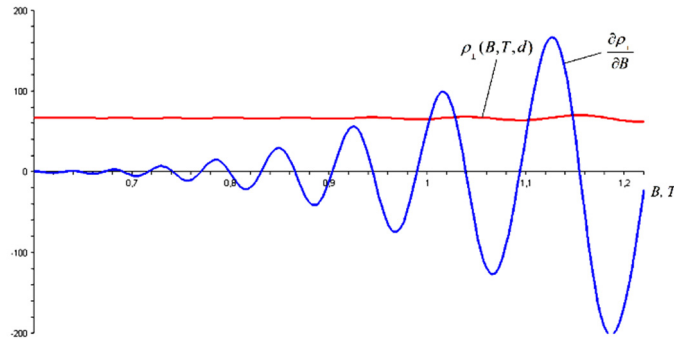
Figure 5. Dependence of $\rho_{\perp}^{2d}(E,B,T,d)$ and $\dfrac{\partial\left(\rho_{\perp}^{2d}(E,B,T,d)\right)}{\partial B}$ on weak induction of the magnetic field at T = 3 K in

heterostructures In$_{0.52}$Al$_{0.48}$As/In$_{0.53}$Ga$_{0.47}$As/In$_{0.52}$Al$_{0.48}$As with a quantum well In$_{0.53}$Ga$_{0.47}$As.

As in Figure 3a, $\rho_{\perp}^{2d}(E,B,T,d)$ oscillations at 0.6÷1.22 T are practically not formed due to a too low magnetic field.

However, the graph of its first order derivative with respect to the magnetic field $\dfrac{\partial\left(\rho_{\perp}^{2d}(E,B,T,d)\right)}{\partial B}$ is completely

different from $\rho_{\perp}^{2d}(E,B,T,d)$. That is, this indicates the presence of quantum effects, that is, Landau levels, even at low temperatures and weak magnetic fields. In fact, the purpose of taking the derivative of the magnetoresistance with respect to B was the same, that is, it was necessary to feel the magnetic field increased by one standard. At the same time, both

positive and negative magnetoresistances can be observed on the $\dfrac{\partial\left(\rho_{\perp}^{2d}(E,B,T,d)\right)}{\partial B}$ graph. In conclusion, we can say

that the differential magnetoresistance of an $\dfrac{\partial\left(\rho_{\perp}^{2d}(E,B,T,d)\right)}{\partial B}$ heterostructure with a quantum well makes it possible

not only to study the sensitivity to the influence of a magnetic field in weak magnetic fields using equation (13), but also to visually observe the number of discrete Landau levels using equation (14).

Now consider how the oscillations of the differential magnetoresistance of $\dfrac{\partial\left(\rho_{\perp}^{2d}(E,B,T,d)\right)}{\partial B}$ depend on temperature.

As in Figure 3b, we will change the value of the induction of the magnetic field by 4 T and the temperature from 4.2 K to 40 K. As a result, a graph of the temperature dependence of fluctuations according to the equation (14) is obtained (Figure 6).
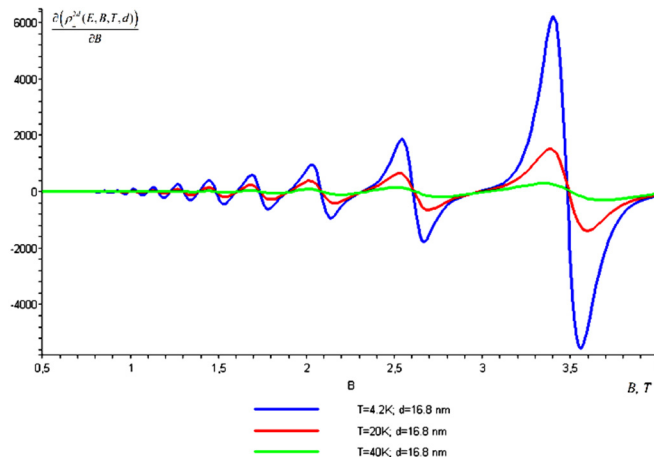
Figure 6. Influence of temperature on differential magnetoresistance $\dfrac{\partial\left(\rho_{\perp}^{2d}(E,B,T,d)\right)}{\partial B}$ in quantum well In$_{0.53}$Ga$_{0.47}$As.

As can be seen from Figure 6, there is a decrease in the amplitude of oscillations of the differential magnetoresistance of $\dfrac{\partial\left(\rho_\perp^{2d}(E,B,T,d)\right)}{\partial B}$ with increasing temperature. This leads to a decrease in the height of the discrete landau peaks and an increase in their width due to thermal expansion. In general, this leads to the fact that the effect of temperature on the differential oscillations of the magnetoresistance of $\dfrac{\partial\left(\rho_\perp^{2d}(E,B,T,d)\right)}{\partial B}$ coincides with the above theoretical base.

Determination of transverse magnetoresistance oscillation in heterostructures based on narrow-band quantum wells with nonparabolic dispersion law

Let's analyze quantum oscillation phenomena for electrons and light holes in heterostructures based on narrow-band quantum wells when exposed to a strong magnetic field, with a non-parabolic law of dispersion. For the parabolic law of dispersion, the effective mass of charge carriers does not depend on its energy, but if the law of dispersion is non-quadratic, then the effective masses of charge carriers vary greatly in energy in the permitted zone of the quantum well.

The energy of charge carriers in the conduction band under the action of a quantizing magnetic field for a non-parabolic dispersion law in bulk semiconductor materials with a narrow band is calculated by the following expression [29]:

$$E_{N\pm}^{3d}(B)=-\frac{E_g^{3d}}{2}+\frac{1}{2}\sqrt{\left(E_g^{3d}\right)^2+4E_g^{3d}\left[\left(N+\frac{1}{2}\right)\hbar\omega_c+\frac{\hbar^2k_z^2}{2m_n}\pm\frac{g_0\mu_B H}{2}\right]}. \tag{15}$$

Here E_g^{3d} is the band gap of the bulk semiconductor material; $g_0\mu_B H$ - spin energy of charge carriers.

If the induction of the quantizing magnetic field is applied along the quantum well thickness (parallel to the Z axis) and perpendicular to the XY quantum well plane, assume that the band gap depends on the quantum well thickness, and take into account that the value of the spin energy is much less than the sum of the quantum and the magnetic field energy, then expression (13) takes the form:

$$E_N^{2d}(B,d)=-\frac{E_g^{2d}}{2}+\frac{1}{2}\sqrt{\left(E_g^{2d}\right)^2+4\left(E_g^{2d}\right)\left[\left(n_L+\frac{1}{2}\right)\hbar\omega_c+\frac{\pi^2\hbar^2}{2m_n d^2}n_z^2\right]}. \tag{16}$$

Here, $\dfrac{1}{\mu_n}=\dfrac{1}{m_n}+\dfrac{1}{m_p}$; $E_g^{2d}=E_g^{3d}+\dfrac{\pi^2\hbar^2}{2\mu_n d^2}n_z^2$

Equation (16) expresses the dependence of the narrow-field quantum well on the magnetic field, which quantizes the energy of free electrons in the conduction field for the nonparabolic dispersion law. It can be seen that the energy of free electrons in the conduction region of a narrow-gap quantum well under the action of a quantizing magnetic field strongly varies non-squarely with the band gap and quantum well thickness. This relation certainly strongly affects the two-dimensional energy density of states (8). Hence it follows that the oscillations of the magnetoresistance of a quantum well with a nonparabolic dispersion law differ significantly from the parabolic law. Consequently, the $\left[\hbar\omega_c\left(n_L+\dfrac{1}{2}\right)+\dfrac{\pi^2\hbar^2}{2m^*d^2}n_Z^2\right]$ term in expression (8) is the total energy of free electrons in the conduction field of a quantum well in a quantizing magnetic field for the parabolic dispersion law. In the non-parabolic dispersion law, the total energy is determined by expression (16). Then, substituting (16) into (8), we obtain an expression for the two-dimensional energy density of states in a quantizing magnetic field for the nonparabolic dispersion law:

$$N_{s,noparabolic}^{2d}\left(E,B,E_g^{2d},n_L,d,n_Z\right)=\frac{eH}{2\pi c}\sqrt{\frac{2}{\pi}}\frac{1}{G}\sum_{n_L}\exp\left[-2\left(\frac{E-\left[-\frac{E_g^{2d}}{2}+\frac{1}{2}\sqrt{\left(E_g^{2d}\right)^2+4\left(E_g^{2d}\right)\left[\left(n_L+\frac{1}{2}\right)\hbar\omega_c+\frac{\pi^2\hbar^2}{2m_n d^2}n_z^2\right]}\right]}{G}\right)^2\right] \tag{17}$$

It follows from this equation that, for a nonparabolic dispersion law, the quantum field depends on the magnetic field, which quantizes the density of energy states in the conduction region. It can be seen that equations (8) and (17) are fundamentally different from a mathematical point of view. In this case, if the band gap is narrow, then it is recommended to use equation (17), otherwise equation (8), i.e. if the semiconductor is wide-gap. We can also understand this by substituting (17) into (13) to get the following new analytic expression:

$$\rho_{\perp noparabolic}^{2d}\left(E,B,T,d,E_g^{2d}\right)=\left[\frac{e^3B}{2\pi m*c}\sqrt{\frac{2}{\pi}}\frac{1}{G}\gamma_\perp(k_0T)^\beta\cdot\int_0^\infty N_{s,noparabolic}^{2d}\left(E,B,E_g^{2d},n_L,d,n_Z\right)E^{\alpha+\frac{3}{2}}\left(\frac{\partial f_0(E,T)}{\partial E}\right)dE\right]^{-1} \quad (18)$$

Analytical expression (18) is suitable mainly for heterostructural materials with narrow-field quantum wells, since the energy spectrum of narrow-gap semiconductors mainly obeys the non-parabolic dispersion law.

Now let's compare $\rho_{\perp noparabolic}^{2d}(E,B,T,d,E_g^{2d})$ and $\rho_{\perp parabolic}^{2d}(E,B,T,d,E_g^{2d})$ for two dispersion laws and look at their fluctuations at different magnetic fields and temperatures. The thickness of the InAs/GaInSb/InAs semiconductor heterostructure with a narrow-gap quantum well (InAs - quantum well) is 3.36 nm [30], the volume band gap is 0.426 eV at T=0 K [31], the effective mass of a free electron in the conduction field m_n=0.026m_0. Substituting these experimental values into the proposed analytical expressions (13) and (18), we calculate the oscillations of the transverse magnetoresistance of the InAs/GaInSb/InAs quantum well at T=4 K and obtain graphical results for $\rho_{\perp noparabolic}^{2d}(E,B,T,d,E_g^{2d})$ and $\rho_{\perp parabolic}^{2d}(E,B,T,d,E_g^{2d})$ (Figure 7). As can be seen from this figure, one can observe that the oscillations of the transverse magnetoresistance of the quantum well obtained for the parabolic and nonparabolic dispersion laws are fundamentally different. In conclusion, we can say that if the quantum well consists of a narrow-gap semiconductor, it is proposed to calculate the oscillations of the transverse magnetoresistance by expression (18), and if the material of the quantum well is classical and wide-gap, then it is proposed to calculate by equation (13).
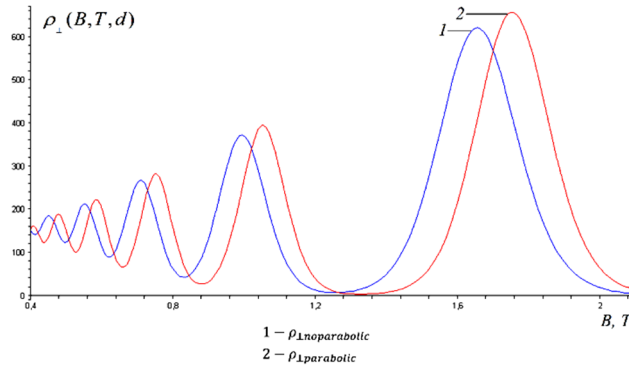
Figure 7. Comparison of transverse magnetoresistance oscillation for $\rho_{\perp noparabolic}^{2d}(E,B,T,d,E_g^{2d})$ and $\rho_{\perp parabolic}^{2d}(E,B,T,d,E_g^{2d})$ in the quantum well InAs/GaInSb/InAs at T=4 K

Comparison of experimental results with theory and their discussion

This work mainly presents the results of a comparison of experimental and theoretical studies of the oscillations of the transverse magnetoresistance on the example of a heterostructure with narrow quantum wells $In_xGa_{1-x}Sb$ [7]. The band gap and thickness of the quantum well of this material is $E_g^{3d}=0,49\,eV$ [32] and d=7.5 nm, and the effective mass of charge carriers is m_n=0.06m_0 [7]. In this work, oscillations of the transverse magnetoresistance of $In_xGa_{1-x}Sb$ are observed at a temperature of 2 K and at quantizing magnetic fields from 3 T to 9 T (Figure 8). Since this material is a narrow gap semiconductor with quantum wells, it obeys a non-parabolic dispersion law. From here, using the above experimental physical parameters, the oscillations of the transverse magnetoresistance of the $In_xGa_{1-x}Sb$ quantum well at a temperature of 2 K are theoretically calculated using equation (18). In Figure 9 shows the $\rho_{\perp noparabolic}^{2d}(E,B,T,d,E_g^{2d})$ graph of the theoretically calculated $In_xGa_{1-x}Sb$ quantum well. It can be seen that the experimental (Figure 8) and theoretical (Figure 9) results are very close to each other in terms of quality. If we look at the experimental results, then the oscillations of the $In_xGa_{1-x}Sb$ quantum well practically do not appear in the range of magnetic field induction values from 1 T to 2.9 T.

As if, at a temperature of 2 K and a magnetic field of 2.5 T, Landau levels are not visible, there is no quantization process. Although, on the graph obtained from a theoretical point of view, the amplitude of the magnetoresistance is formed precisely in this magnetic field, since the condition kT<<ħωc is satisfied. Even at such a very low temperature, the induction of the magnetic field must already be a quantization process at 1.5 T. This can also be observed on the $\dfrac{\partial\left(\rho_{\perp nonparabolic}^{2d}(E,B,T,d)\right)}{\partial B}$ plot using equations (14) for the non-parabolic dispersion law, i.e. differentiating equation (18) with respect to the magnetic field (Figure 10). Therefore, one should not rush to draw conclusions on the basis of oscillation amplitudes not seen in the experiment, i.e. it is necessary to rework it from a theoretical point of view, check it through quantization conditions, and in the process, it is necessary to study the state of charge carriers in perfection. This can be seen by comparing the experimental (Figure 8) and theoretical (Figure 10) results. Let us analyze the experimental oscillations of the transverse magnetoresistance according to the equation (18) using the dynamics of the temperature increase (Figure 11). On Figure 11 shows a three-dimensional graph of the oscillations of the transverse magnetoresistance of the $In_xGa_{1-x}Sb$ quantum well as a function of temperature and magnetic field. This three-dimensional

graph is obtained from a theoretical point of view by substituting experimental values into equation (18). As can be seen from Figure 11, with increasing temperature, the amplitude of oscillations of the transverse magnetoresistance of the quantum coil decreases, and a broadening of the peak is observed. This is called thermal blur. This means that, due to thermal smearing, as the temperature rises from 40 K, the discrete Landau levels are transformed into continuous energy spectra. At the same time, it is possible to analyze the dependence of this experimental graph on the thickness of the quantum well using equations obtained from the theoretical side. In addition, with the help of the proposed new theory or the obtained new equation, it becomes possible to determine the dependence of external factors on experimental oscillations of the transverse magnetoresistance in bulk heterostructures with quantum wells.
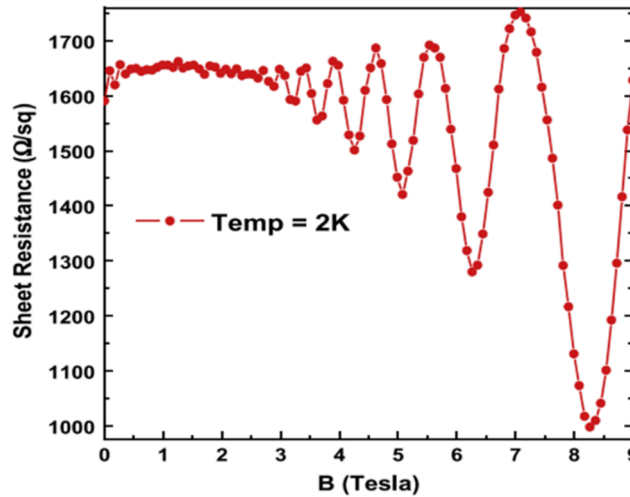
Figure 8. Oscillations of transverse magnetoresistance of the quantum well $In_xGa_{1-x}Sb$ at a temperature of 2 K [7].
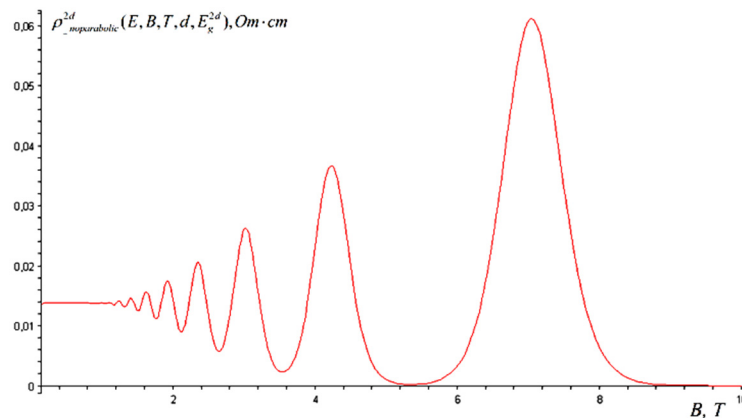
Figure 9. Oscillations of transverse magnetoresistance of the quantum well $In_xGa_{1-x}Sb$ at a temperature of 2 K, our results
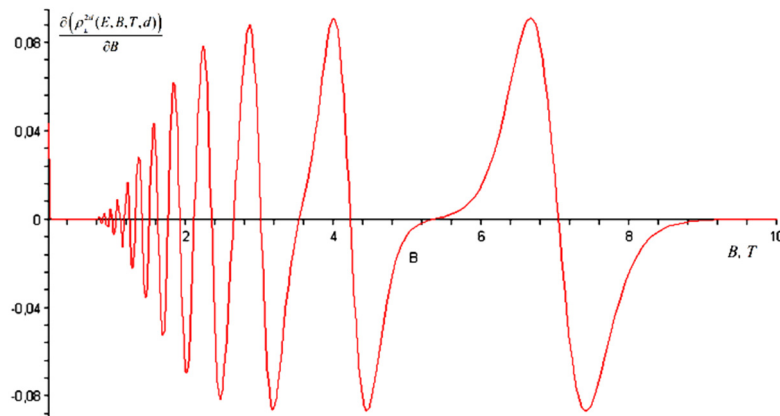
Figure 10. Dependence of $\dfrac{\partial\left(\rho^{2d}_{\perp nonparabolic}(E,B,T,d)\right)}{\partial B}$ on the magnetic field for narrow-band quantum wells $In_xGa_{1-x}Sb$

at a temperature of T = 2 K.
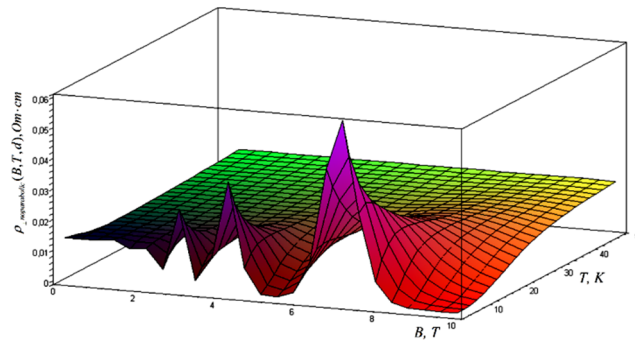
Figure 11. View of a three-dimensional graph of the oscillation of the transverse magnetoresistance
of the quantum well $In_xGa_{1-x}Sb$

CONCLUSIONS.

Based on the study, the following conclusions can be drawn: A new analytical expression is derived for calculating the temperature dependence of the oscillations of the transverse electrical conductivity and magnetoresistance of a quantum well. A mechanism has been developed for the oscillation of the transverse electrical conductivity and magnetoresistance of a quantum well from the first-order derivative of the magnetic field (differential) $\frac{\partial\left(\rho_{\perp}^{2d}(E,B,T,d)\right)}{\partial B}$ at low temperatures and weak magnetic fields. Oscillations of the electrical conductivity and magnetoresistance of a narrow-window quantum well with a nonparabolic dispersion law are studied. The proposed theory was used to study the results of experiments on a narrow-gap quantum well ($In_xGa_{1-x}Sb$). The Landau levels of the $In_xGa_{1-x}Sb$ quantum well in weak magnetic fields, which were not observed in the experiment, oscillate. This has been proven through the $\frac{\partial\left(\rho_{\perp}^{2d}(E,B,T,d)\right)}{\partial B}$ theory of magnetoresistance. The experiment shows that the oscillations of the transverse magnetoresistance of the $In_xGa_{1-x}Sb$ quantum filament, measured at a temperature of 2 K, transform into a continuous energy spectrum due to thermal washing under the influence of the temperature growth dynamics.

ORCID

Ulugbek I. Erkaboev, https://orcid.org/0000-0002-6841-8214; **Rustamjon G. Rakhimov,** https://orcid.org/0000-0003-0850-1398

REFERENCES

[1] N.A. Yuzeeva, G.B. Galiev, E.A. Klimova, L.N. Oveshnikov, R.A. Lunin, and V.A. Kulbachinskii, Phys. Procedia, **72**, 425 (2015). https://doi.org/10.1016/j.phpro.2015.09.087
[2] V. Tarquini, T. Knighton, Zh. Wu, J. Huang, L. Pfeiffer, and K. West, Appl. Phys. Lett. **104**, 092102 (2014). https://doi.org/10.1063/1.4867086
[3] I.B. Berkutov, V.V. Andrievskii, Yu.F. Komnik, Yu.A. Kolesnichenko, R.J.H. Morris, and D.R. Leadley, Low Temp. Phys. **38**, 1145 (2012). https://doi.org/10.1063/1.4770520
[4] Y. Abdullah, and S. Kashif, J. Phys. Condens. Matter, **27**, 435007, (2015). https://doi.org/10.1088/0953-8984/27/43/435007
[5] A. Bogan, A.T. Hatke, S.A. Studenikin, A. Sachrajda, M.A. Zudov, L.N. Pfeiffer, and K.W. West, J. Phys. Conf. Ser. **456**, 012004 (2013). https://doi.org/10.1088/1742-6596/456/1/012004
[6] B.T. Abdulazizov, Eurasian J. Phys. Funct. Mater. **6**, 32 (2022). https://doi.org/10.32523/ejpfm.2022060103
[7] F. Sarcan, A. Erol, M. Gunes, M.Ç. Arikan, J. Puustinen, and M. Guina, Nanoscale Res. Lett. **9**, 141 (2014). https://doi.org/10.1186/1556-276X-9-141
[8] G. Gulyamov, U.I. Erkaboev, R.G. Rakhimov, J.I. Mirzaev, and N.A. Sayidov, Mod Phys Lett B. **37**, 2350015 (2023). https://doi.org/10.1142/S021798492350015X
[9] B.T. Abdulazizov, G. Gulyamov, P.J. Baymatov, Sh.T. Inoyatov, M.S. Tokhirjonov, and Kh.N. Juraev, SPIN. **12**, 2250002 (2022). https://doi.org/10.1142/S2010324722500023
[10] F. Nutku, O. Donmez, F. Kuruoglu, S. Mutlu, A. Erol, S. Yildirim, and M.C. Arikan, J. Phys. D: Appl. Phys. **48**, 305108 (2015). https://doi.org/10.1088/0022-3727/48/30/305108
[11] P.J. Baymatov, A.G. Gulyamov, B.T. Abdulazizov, Kh.Yu. Mavlyanov, and M.S. Tokhirjonov, Int. J. Mod. Phys. B, **35**, 2150070 (2021). https://doi.org/10.1142/S0217979221500703
[12] G. Gulyamov, U.I. Erkaboev, R.G. Rakhimov, and J.I. Mirzaev, J. Nano- Electron. Phys. **12**, 03012 (2020). https://doi.org/10.1142/S0217979220500526
[13] U.I. Erkaboev, G. Gulyamov, J.I. Mirzaev, and R.G. Rakhimov, Int. J. Mod. Phys. B, **34**, 2050052 (2020). https://doi.org/10.1142/S0217979220500526
[14] G. Gulyamov, B.T. Abdulazizov, and P.J. Baymatov, J. Nanomater. **2021,** 5542559 (2021). https://doi.org/10.1155/2021/5542559
[15] G. Gulyamov, U.I. Erkaboev, N.A. Sayidov, and R.G. Rakhimov, J. Appl. Sci. Eng. **23**, 453 (2020). https://doi.org/10.6180/jase.202009_23(3).0009
[16] Ch.T. Tai, P.Y. Chiu, Ch.Y. Liu, H.Sh. Kao, C.Th. Harris, T.M. Lu, Ch.T. Hsieh, Sh.W. Chang, and J.Y. Li, Adv. Mater. **33**, 2007862 (2021). https://doi.org/10.1002/adma.202007862

[17] F.S. Pena, S. Wiedmann, E. Abramof, D.A.W. Soares, P.H.O. Rappl, S. Castro, and M.L. Peres, Phys. Rev. B, **103**, 205305 (2021.) https://doi.org/10.1103/PhysRevB.103.205305

[18] U.I. Erkaboev, G. Gulyamov, J.I. Mirzaev, R.G. Rakhimov, and N.A. Sayidov, Nano, **16**, 2150102 (2021). https://doi.org/10.1142/S0217984921502936

[19] U.I. Erkaboev, R.G. Rakhimov, and N.A. Sayidov, Mod. Phys. Lett. B, **35**, 2150293 (2021). https://doi.org/10.1142/S0217984921502936

[20] P.J. Baymatov, A.G. Gulyamov, and B.T. Abdulazizov, Adv. Condens. Matter Phys. **2019**, 8317278 (2019). https://doi.org/10.1155/2019/8317278

[21] N.Q. Bau, and B.D. Hoi, Int. J. Mod. Phys. B, **28**, 1450001 (2014). https://doi.org/10.1142/S0217979214500015

[22] U.I. Erkaboev, R.G. Rakhimov, N.A. Sayidov, and J.I. Mirzaev, Indian J. Phys. **97**, 1601 (2023). https://doi.org/10.1007/s12648-022-02435-8

[23] U.I. Erkaboev, U.M. Negmatov, R.G. Rakhimov, J.I. Mirzaev, and N.A. Sayidov, Int. J. Appl. Sci. Eng. **19**, 2021123(2022). https://doi.org/10.6703/IJASE.202206_19(2).004

[24] I.B. Berkutov, V.V. Andrievskii, Yu.F. Komnik, and O.A. Mironov, Low Temp. Phys. **36**(12), 1076 (2010). https://doi.org/10.1063/1.3536348

[25] A.Ya. Shik, L.G. Bakueva, S.F. Musikhin, and S.A. Rykov, *Physics of low-dimensional system*, (Press "Science", Saint Petersburg, 2001).

[26] U.I. Erkaboev, G. Gulyamov, and R.G. Rakhimov, Indian J. Phys. **96**, 2359 (2022). https://doi.org/10.1007/s12648-021-02180-4

[27] W. Zawadzki, A. Raymond, and M. Kubisa, Phys. Status Solidi B, **251**(2), 247 (2013). https://doi.org/10.1002/pssb.201349251

[28] A.I. Anselm, Phys.-Uspekhi. **85**(1), 183 (1965). https://doi.org/0.3367/UFNr.0085.196501f.0183

[29] G. Gulyamov, U.I. Erkaboev, and P.J. Baymatov, Adv. Condens. Matter Phys. **2016**, 5434717 (2016). https://doi.org/10.1155/2016/5434717

[30] P.J. Baymatov, and B.T. Abdulazizov, Ukr. J. Phys. **62**(1), 46 (2017). https://doi.org/10.15407/ujpe62.01.0046

[31] V.N. Brudnyi, N.G. Kolin, and A.I. Potapov, Semiconductors, **37**(4), 390 (2003). https://doi.org/10.1134/1.1568456

[32] R. Magno, E.R. Glaser, B.P. Tinkham, J.G. Champlain, J.B. Boos, M.G. Ancona, and P.M. Campbell, J. Vac. Sci. Technol. B: Nanotechnol. Microelectron. **24**(3), 1622 (2006). https://doi.org/10.1116/1.2201448

ВИЗНАЧЕННЯ ЗАЛЕЖНОСТІ ОСЦИЛЯЦІЇ ПОПЕРЕЧНОЇ ЕЛЕКТРОПРОВІДНОСТІ ТА МАГНІТООПОРУ ВІД ТЕМПЕРАТУРИ В ГЕТЕРОСТРУКТУРАХ НА ОСНОВІ КВАНТОВИХ ЯМ

Улугбек І. Еркабоєв, Рустамжон Г. Рахімов

Наманганський інженерно-технологічний інститут, 160115 Наманган, Узбекистан

У даній роботі досліджено вплив густини двовимірного стану на осциляції поперечної електропровідності в гетероструктурах з прямокутними квантовими ямами. Отримано новий аналітичний вираз для розрахунку температурної залежності осциляцій поперечної електропровідності та магнітоопору квантової ями. Вперше розроблено механізм осциляції поперечної електропровідності та магнітоопору квантової ями від похідної першого порядку магнітного поля (диференціала) $\partial\left(\rho_\perp^{2d}(E,B,T,d)\right)\big/\partial B$ при низьких температурах і слабких магнітних полях. Досліджено осциляції електропровідності та магнітоопору вузькосмугової квантової ями з непараболічним законом дисперсії. Із запропонованою теорією досліджено результати експериментів з вузькосмугою квантовою ямою ($In_xGa_{1-x}Sb$).

Ключові слова: *напівпровідник; провідність; квантова яма; магнітоопір; магнітне поле*

COMPARATIVE STUDY OF THE MASS SPECTRA OF HEAVY QUARKONIUM SYSTEM WITH AN INTERACTING POTENTIAL MODEL[†]

Joseph A. Obu[b], Etido P. Inyang[a]*, Eddy S. William[c], Donatus E. Bassey[b], Ephraim P. Inyang[b]

[a]Department of Physics, National Open University of Nigeria, Jabi, Abuja, Nigeria
[b]Department of Physics, University of Calabar, PMB 1115, Calabar, Nigeria
[c]Department of Physics, School of Pure and Applied Sciences, Federal University of Technology, Ikot Abasi, Nigeria
*Corresponding author email: etidophysics@gmail.com, OR einyang@noun.edu.ng
Received February 22, 2023; revised March 13, 2023; accepted June 21, 2023

In this work, the comparison of the mass spectra of heavy quarkonium system with an interacting potential (class of Yukawa potential) was studied. The Schrodinger equation is analytically solved using the Nikiforov-Uvarov (NU) method and the series expansion method (SEM). The approximate solutions of the eigen energy equation and corresponding eigenfunction in terms of Laguerre polynomials were obtained using the NU method and the solutions of the eigen energy equation were also obtained with the SEM. The mass spectra for heavy quarkonium system (HQS) for the potential under study were obtained for bottomonium $b\bar{b}$ and charmonium $c\bar{c}$. We compared the results obtained between the NU and the SEM. It was noticed that SEM solutions yield mass spectra very close to experimental data compared to solutions with the NU method. The obtained results were also compared with works by some other authors and were found to be improved. This study can be extended by using other exponential-type potential models with other analytical approach and a different approximation scheme to obtain the mass spectra of heavy quarkonium system. The relativistic properties using Klein-Gordon or Dirac equations can be explored to obtain the mass spectra of light quarkonia. Finally, the information entailed in the normalized wave-functions can also be studied.

Keywords: *Schrödinger equation; Nikiforov-Uvarov method; Class of Yukawa potential; Mass Spectra; Series expansion method*
PACS: 12.39.Jh

1. INTRODUCTION

The study of the fundamental or constituent blocks of matter has been for long time a fascinating field in Physics. In the nineteenth century, the atom was considered to be the fundamental particles from which all matters were composed. This idea was used to explain the basic structure of all elements. Experiments performed at the end of the nineteenth century and beginning of the twentieth century provided evidence for the structure of an atom [1].

The conclusions were that all atoms have a nucleus containing protons which is surrounded by elements and that the nucleus was very small compared with the size of the atom. The neutron was introduced to explain the discrepancy between the mass of the atom and the mass from the number of protons. In 1932, Chadwick discovered the neutron and the fundamental particles were considered to be proton, the neutron and the electron. The discovery of antimatter in cosmic radiation supported the theory developed from the special theory of relativity and quantum theory that all fundamental particles have corresponding antimatter particles. The matter and antimatter particles have the same mass but opposite charge. The problem of what were considered to be fundamental particles was resolved by the quarks. Quarks are the basic building blocks of hadrons, particles interacting with each other through strong interaction [2,3]. In nuclear physics, we are mostly concerned with the lightest members of the hadron's family; nucleons, which make up all the nuclei and pions which constitute the main carriers of nuclear force. Since their discoveries, investigation of heavy quarkonium system (HQS) provides us with great tools for quantitative tests of quantum chromodynamics (QCD) [4]. Because of the heavy masses of the constituent quarks, a good description of many features of these systems can be obtained using non-relativistic models, where one assumes that the motion of constituent quarks is non-relativistic, so that the quark-antiquark strong interaction is described by a phenomenological potential [5,6]. Heavy quarkonium system have turned out to provide extremely useful probes for the deconfined state of matter because the force between a heavy quark and anti-quark is weakened due to the presence of gluons which lead to the dissociation of quarkonium bound states [7]. The quarkonia with heavy quark and antiquark and their interaction are well described by the Schrodinger equation (SE). The solution of the Schrodinger equation with spherically symmetric potential is of major concern in describing the mass spectra (MS) of quarkonium system [8,9]. In simulating the interaction potentials for these systems, confining-type potentials are generally used. The holding potentials can be of any form. For instance, a variety of this type of potential is the Cornell potential (CP) with two terms one of which is responsible for the Coulomb interaction of the quarks and the other correspond to a confining term [10,11]. Researchers have studied the MS of heavy and heavy-light quarkonia using the CP and its extended form [12-14]. For studying the behavior of several physical problems in Physics, we require to solve the Schrodinger equation. The solutions to the Schrodinger equation can be established with analytical methods such as the Nikiforov-Uvarov (NU) method [15-24], the asymptotic iterative method (AIM) [25], the extended NU method [26], the Nikiforov-Uvarov functional analysis (NUFA) method [27-30], the series expansion

method [30-34], the WKB approximation [35-37], and so on [38]. Recently, the study of MS of HQS with exponential-type potentials has attracted the attention of most researchers. For example, Inyang et al. [39] studied the MS of HQS with Yukawa potential using the NU method. Also, Akpan et al. [40], presented the mass spectra of HQS using Hulthen and Hellmann potential model through the solutions of the Schrodinger equation. Furthermore, Ibekwe et al. [41] studied the mass spectra of HQS using the NU with the combination of screened Coulomb and Kratzer potential. Abu-Shady and Inyang [42], suggested trigonometric Rosen-Morse potential as the quark-antiquark interaction potential for studying the masses of heavy and heavy-light mesons. In the present research, our interest is to compare the mass spectra of HQS with the class of Yukawa potential (CYP) using the Nikiforov-Uvarov and the series expansion methods. The CYP is a combination of Yukawa potential [43], Hellmann potential [44] and inverse quadratic Yukawa potential [45]. The CYP applications cut across other fields of physics such has atomic, nuclear and condensed matter physics, among others. The CYP takes the form [46],

$$V(r) = -\frac{a}{r} + \frac{be^{-\alpha_I r}}{r} - \frac{ce^{-2\alpha_I r}}{r^2} , \qquad (1)$$

where a, b and c are potential strengths, α_I is the screening parameter.

The exponential terms in Eq. (1) are expanded with Taylor series up to order three, so that the potential can interact in the quark-antiquark system, and Eq. (2) is obtained.

$$V(r) = -\frac{\alpha_0}{r} + \alpha_1 r + \alpha_2 r^2 + \frac{\alpha_3}{r^2} + \alpha_4 \qquad (2)$$

where

$$\left. \begin{array}{l} -\alpha_0 = b - a + 2c\alpha_I, \ \alpha_1 = \frac{b\alpha_I^2}{2} - 1.33\alpha_I^3 \\[2mm] \alpha_2 = -\frac{b\alpha_I^3}{6}, \ \alpha_3 = -c, \ \alpha_4 = -b\alpha_I - 2c\alpha_I^2 \end{array} \right\} \qquad (3)$$

2. REVIEW OF THE METHODS
2.1. The Nikiforov- Uvarov method

The Nikiforov-Uvarov (NU) method is based on solving the hypergeometric-type second-order differential equations by means of the special orthogonal functions [47]. For a given potential, the Schrodinger-like equations in spherical coordinates are reduced to a generalized equation of hypergeometric-type with an appropriate coordinate transformation $r \rightarrow x$ and then they can be solved systematically to find the exact solutions. The main equation which is closely associated with the method is given in the following form [48].

$$\psi''(x) + \frac{\tilde{\tau}(x)}{\sigma(x)}\psi'(s) + \frac{\tilde{\sigma}(x)}{\sigma^2(x)}\psi(x) = 0 \qquad (4)$$

where $\sigma(x)$ and $\tilde{\sigma}(x)$ are polynomials at most second- degree, $\tilde{\tau}(x)$ is a first- degree polynomial and $\psi(x)$ is a function of the hypergeometric-type.
By taking $\psi(x) = \phi(x)y(x)$ and choosing an appropriate function $\phi(x)$, Eq. (4) is reduced to a comprehensible form;

$$y''(x) + \left(2\frac{\phi'(x)}{\phi(x)} + \frac{\tilde{\tau}(x)}{\sigma(x)}\right)y'(x) + \left(\frac{\phi''(x)}{\phi(x)} + \frac{\phi'(x)}{\phi(x)}\frac{\tilde{\tau}(x)}{\sigma(x)} + \frac{\tilde{\sigma}(x)}{\sigma^2(x)}\right)y(x) = 0 \qquad (5)$$

The coefficient of $y'(x)$ is taken in the form $\tau(x)/\sigma(x)$, where $\tau(x)$ is a polynomial of degree at most one, i.e.,

$$2\frac{\phi'(x)}{\phi(x)} + \frac{\tilde{\tau}(x)}{\sigma(x)} = \frac{\tau(x)}{\sigma(x)} . \qquad (6)$$

And hence the most regular form is obtained as follows,

$$\frac{\phi'(x)}{\phi(x)} = \frac{\pi(x)}{\sigma(x)} \qquad (7)$$

where

$$\pi(x) = \frac{1}{2}[\tau(x) - \tilde{\tau}(x)] \qquad (8)$$

The most useful demonstration of Eq. (8) is

$$\tau(x) = \tilde{\tau}(x) + 2\pi(x) \tag{9}$$

The new parameter π(x) is a polynomial of degree at most one. In addition, the term $\phi''(x)/\phi(x)$ which appears in the coefficient of $y(x)$ in Eq. (5) is arranged as follows,

$$\frac{\phi''(x)}{\phi(x)} = \left(\frac{\phi'(x)}{\phi(x)}\right)' + \left(\frac{\phi'(x)}{\phi(x)}\right)^2 = \left(\frac{\pi(x)}{\sigma(x)}\right)' + \left(\frac{\pi(x)}{\sigma(x)}\right)^2 \tag{10}$$

In this case, the coefficient of $y(x)$ is transformed into a more suitable form by taking the equality given in Eq.(31);

$$\frac{\phi''(x)}{\phi(x)} + \frac{\phi'(x)}{\phi(x)}\frac{\tilde{\tau}(x)}{\sigma(x)} + \frac{\tilde{\sigma}(x)}{\sigma^2(x)} = \frac{\bar{\sigma}(x)}{\sigma^2(x)} \tag{11}$$

where

$$\bar{\sigma}(x) = \tilde{\sigma}(x) + \pi^2(x) + \pi(x)\left[\tilde{\tau}(x) - \sigma'(x)\right] + \pi'(x)\sigma(x) \tag{12}$$

Substituting the right-hand sides of Eq. (6) and Eq. (11) into Eq. (5), an equation of hypergeometric-type is obtained as follows;

$$y''(x) + \frac{\tau(x)}{\sigma(x)}y'(x) + \frac{\bar{\sigma}(x)}{\sigma^2(x)}y(x) = 0 \tag{13}$$

As a consequence of the algebraic transformations mentioned above, the functional form of Eq. (4) is protected in a systematic way. If the polynomial $\bar{\sigma}(x)$ in Eq. (13) is divisible by $\sigma(x)$, i.e.,

$$\bar{\sigma}(x) = \lambda\sigma(x) \tag{14}$$

where λ is a constant, Eq. (13) is reduced to an equation of hypergeometric-type

$$\sigma(x)y''(x) + \tau(x)y'(x) + \lambda y(x) = 0 \tag{15}$$

And so its solution is given as a function of hypergeometric-type. To determine the polynomial $\pi(x)$, Eq. (12) is compared with Eq. (14) and then a quadratic equation for $\pi(x)$ is obtained as follows,

$$\pi^2(x) + \pi(x)\left[\tilde{\tau}(x) - \sigma'(x)\right] + \tilde{\sigma}(x) - k\sigma(x) = 0 \tag{16}$$

where

$$k = \lambda - \pi'_-(x) \tag{17}$$

The solution of this quadratic equation for π(x) yields the following equality

$$\pi(x) = \frac{\sigma'(x) - \tilde{\tau}(x)}{2} \pm \sqrt{\left(\frac{\sigma'(x) - \tilde{\tau}(x)}{2}\right)^2 - \tilde{\sigma}(x) + k\sigma(x)} \tag{18}$$

In order to obtain the possible solutions according to plus and minus of Eq. (18), the parameter k within the square root sign must be known explicitly. To provide this requirement, the expression under the square root sign has to be the square of a polynomial, since $\pi(x)$ is a polynomial of degree at most one. In this case, an equation of the quadratic form is available for the constant k. Setting the discriminant of this quadratic equal to zero, the constant k is determined clearly. After determining k, the polynomial $\pi(x)$ is obtained from Eq. (18), and then $\tau(x)$ and λ are also obtained by using Eq.(8) and Eq.(17), respectively.

A common trend that has been followed to generalize the solutions of Eq. (15) is to show that all the derivatives of hypergeometric-type functions are also of the hypergeometric-type. Equation (15) is differentiated by using the representation $v_1(x) = y'(x)$.

$$\sigma(x)v_1''(x) + \tau_1(x)v_1'(x) + \mu_1 v_1(x) = 0 \tag{19}$$

where $\tau_1(x) = \tau(x) + \sigma'(x)$ and $\mu_1 = \lambda + \tau'(x)$. $\tau_1(x)$ is a polynomial of degree at most one and μ_1 is a parameter that is independent of the variables. It is clear that Eq. (19) is an equation of hypergeometric- type. By taking $v_2(x) = y''(x)$ as a new representation, the second derivative of Eq. (15) becomes

$$\sigma(x) v_2''(x) + \tau_2(x) v_2'(x) + \mu_2 v_2(x) = 0 \qquad (20)$$

where

$$\tau_2(x) = \tau_1(x) + \sigma'(x) = \tau(x) + 2\sigma'(x) \qquad (21)$$

$$\mu_2 = \mu_1 + \tau_1'(x) = \lambda + 2\tau'(x) + \sigma''(x) \qquad (22)$$

In a similar way, an equation of hypergeometric–type can be constructed as a family of particular solutions of Eq. (15) by taking $v_n(x) = y''(x)$;

$$\sigma(x) v_n''(x) + \tau_n(x) v_n'(x) + \mu_n v_n(x) = 0 \qquad (23)$$

And here the general recurrence relations for $\tau_n(x)$ and μ_n are found as follows, respectively,

$$\tau_n(x) = \tau(x) + n\sigma'(x) \qquad (24)$$

$$\mu_n = \lambda + n\tau'(x) + \frac{n(n-1)}{2}\sigma''(x). \qquad (25)$$

When $\mu_n = 0$, Eq. (25) becomes as follows

$$\lambda_n = -n\tau'(x) - \frac{n(n-1)}{2}\sigma''(x), (n = 0,1,2,3,...). \qquad (26)$$

And then Eq. (23) has a particular solution of the form $y(x) = y_n(x)$ which is a polynomial of degree n. To obtain an eigenvalue solution through the NU method, the relationship between λ and λ_n must be set up by means of Eq.(17) and Eq.(26). $y_n(x)$ is the hypergeometric –type function whose polynomial solutions are given by the Rodrigues relation

$$y_n(x) = \frac{B_n}{\rho(x)} \frac{d^n}{dx^n} \left[\sigma^n(x)\rho(x) \right] \qquad (27)$$

where B_n is a normalization constant and the weight function $\rho(x)$ must satisfy the condition below

$$\left(\sigma(x)\rho(x) \right)' = \tau(x)\rho(x). \qquad (28)$$

2.2 The series expansion method

The series expansion method is based on solving the hypergeometric-type second-order differential equations. For a given potential the wave function of SE is chosen in the form.

$$R(r) = e^{-\alpha r^2 - \beta r} F(r) \qquad (29)$$

where α and β are parameters whose values are to be determined in terms of potential strength parameters. The functional series for $F(r)$ is taken to be

$$F(r) = \sum_{n=0}^{\infty} a_n r^{2n+L} \qquad (30)$$

where a_n is an expansion coefficient [48].

By substituting $F(r), F'(r)$ and $F''(r)$ into the SE, rearranging and equating coefficients of the corresponding powers of r to zero. The eigen-values are subsequently obtained.

3. APPROXIMATE SOLUTIONS OF THE SCHRODINGER EQUATION WITH CLASS OF YUKAWA POTENTIAL USING THE NU METHOD

The Schrodinger equation takes the form [49]

$$\frac{d^2 U(r)}{dr^2} + \left[\frac{2\mu}{\hbar^2} \left(E_{nl} - V(r) \right) - \frac{l(l+1)}{r^2} \right] U(r) = 0 \qquad (31)$$

where l, is the angular momentum quantum number, μ, is the reduced mass for the quark-antiquark particle, r is the inter-particle distance and $\hbar$ is reduced plank constant respectively.

Substituting Eq.(2) into Eq.(31) gives,

$$\frac{d^2R(r)}{dr^2}+\left[\frac{2\mu E}{\hbar^2}+\frac{2\mu\alpha_0}{\hbar^2 r}-\frac{2\mu\alpha_1 r}{\hbar^2}-\frac{2\mu\alpha_2 r^2}{\hbar^2}-\frac{2\mu\alpha_3}{\hbar^2 r^2}-\frac{2\mu\alpha_4}{\hbar^2}-\frac{l(l+1)}{r^2}\right]R(r)=0 \tag{32}$$

Transforming the coordinate of Eq.(32) we set

$$x=\frac{1}{r} \tag{33}$$

Using Eqs. (32) and (33) we have

$$\frac{d^2R(x)}{dx^2}+\frac{2}{x}\frac{dR}{dx}+\frac{1}{x^4}\left[\begin{array}{c}\dfrac{2\mu E}{\hbar^2}+\dfrac{2\mu\alpha_0 x}{\hbar^2}-\dfrac{2\mu\alpha_1}{\hbar^2 x}\\[2mm]-\dfrac{2\mu\alpha_2}{\hbar^2 x^2}-\dfrac{2\mu\alpha_3 x^2}{\hbar^2}-\dfrac{2\mu\alpha_4}{\hbar^2}-l(l+1)x^2\end{array}\right]R(r)=0 \tag{34}$$

Next, we propose the following approximation scheme on the term $\dfrac{\alpha_1}{x}$ and $\dfrac{\alpha_2}{x^2}$.

Let us assume that there is a characteristic radius r_0 of the meson. Then the scheme is based on the expansion of $\dfrac{\alpha_1}{x}$ and

$\dfrac{\alpha_2}{x^2}$. in a power series around r_0 ; i.e. around $\delta\equiv\dfrac{1}{r_0}$, in the x-space up to the second order. This is similar to Pekeris approximation, which helps to deform the centrifugal term such that the modified potential can be solved by the NU method [12].

Setting $y=x-\delta$ and around $y=0$ it can be expanded into a series of powers we obtain;

$$\frac{\alpha_1}{x}=\alpha_1\left(\frac{3}{\delta}-\frac{3x}{\delta^2}+\frac{x^2}{\delta^3}\right) \tag{35}$$

and

$$\frac{\alpha_2}{x^2}=\alpha_2\left(\frac{6}{\delta^2}-\frac{8x}{\delta^3}+\frac{3x^2}{\delta^4}\right) \tag{36}$$

Putting Eqs. (35) and (36) into Eq. (34) and simplifying gives

$$\frac{d^2R(x)}{dx^2}+\frac{2x}{x^2}\frac{dR(x)}{dx}+\frac{1}{x^4}\left[-\varepsilon+\alpha x-\beta x^2\right]R(x)=0 \tag{37}$$

where

$$\left.\begin{array}{c}-\varepsilon=\left(\dfrac{2\mu E}{\hbar^2}-\dfrac{6\mu\alpha_1}{\hbar^2\delta}-\dfrac{12\mu\alpha_2}{\hbar^2\delta^2}-\dfrac{2\mu\alpha_4}{\hbar^2}\right)\\[3mm]\alpha_{II}=\left(\dfrac{2\mu\alpha_0}{\hbar^2}+\dfrac{6\mu\alpha_1}{\hbar^2\delta^2}+\dfrac{16\mu\alpha_2}{\hbar^2\delta^3}\right)\\[3mm]\beta_{II}=\left(\dfrac{2\mu\alpha_1}{\hbar^2\delta^2}+\dfrac{6\mu\alpha_2}{\hbar^2\delta^4}+\dfrac{2\mu\alpha_3}{\hbar^2}+\gamma\right)\\[3mm]\gamma=l(l+1)\end{array}\right\} \tag{38}$$

Comparing Eq. (37) and Eq. (4) we obtain

$$\left.\begin{array}{c}\tilde{\tau}(x)=2x,\sigma(x)=x^2,\tilde{\sigma}(x)=-\varepsilon+\alpha x-\beta x^2\\[2mm]\sigma'(x)=2x,\sigma''(x)=2\end{array}\right\} \tag{39}$$

Substituting Eq. (39) into Eq. (18) gives

$$\pi(x)=\pm\sqrt{\varepsilon-\alpha_{II}x+\left(\beta_{II}+k\right)x^2} \tag{40}$$

To determine k, we take the discriminant of the function under the square root.

$$k=\frac{\alpha_{II}{}^2-4\beta_{II}\varepsilon}{4\varepsilon} \tag{41}$$

We substitute Eq. (41) into Eq. (40) and have

$$\pi(x) = \pm\left(\frac{\alpha_{II}x}{2\sqrt{\varepsilon}} - \frac{\varepsilon}{\sqrt{\varepsilon}}\right) \tag{42}$$

Taking the negative part of Eq. (48), gives

$$\pi'_-(x) = -\frac{\alpha_{II}}{2\sqrt{\varepsilon}} \tag{43}$$

Substituting Eqs.(39) and (43) into Eq.(9) we have

$$\tau(x) = 2x - \frac{\alpha_{II}x}{\sqrt{\varepsilon}} + \frac{2\varepsilon}{\sqrt{\varepsilon}} \tag{44}$$

From Eq. (44) we have

$$\tau'(x) = 2 - \frac{\alpha_{II}}{\sqrt{\varepsilon}} \tag{45}$$

Substituting Eqs. (41) and (43) into Eq.(17) we have

$$\lambda = \frac{\alpha_{II}^2 - 4\beta_{II}\varepsilon}{4\varepsilon} - \frac{\alpha_{II}}{2\sqrt{\varepsilon}} \tag{46}$$

We substitute Eqs. (39) and (45) into Eq.(26) and obtain

$$\lambda_n = \frac{n\alpha_{II}}{\sqrt{\varepsilon}} - n^2 - n \tag{47}$$

To obtain the energy equation, we equate Eqs. (46) and (47) and then substitute Eqs. (3) and (38)

$$E_{nl} = \frac{3}{\delta}\left(\frac{b\alpha_I^2}{2} - 1.33\alpha_I^3\right) - \frac{b\alpha_I^3}{\delta^2} - b\alpha_I - 2c\alpha_I^2$$

$$-\frac{\hbar^2}{8\mu}\left[\frac{\frac{6\mu}{\hbar^2\delta^2}\left(\frac{b\alpha_I^2}{2} - 1.33\alpha_I^3\right) + \frac{2\mu}{\hbar^2}(a - b - 2c\alpha_I) - \frac{8\mu b\alpha_I^3}{3\hbar^2\delta^3}}{n + \frac{1}{2} + \sqrt{\left(l + \frac{1}{2}\right)^2 + \frac{2\mu}{\hbar^2\delta^3}\left(\frac{b\alpha_I^2}{2} - 1.33\alpha_I^3\right) - \frac{\mu b\alpha_I^3}{\hbar^2\delta^4} - \frac{2\mu c}{\hbar^2}}}\right]^2 \tag{48}$$

The wave function in terms of Laguerre polynomials is

$$\psi(x) = N_{nl}x^{-\frac{\alpha_I}{2\sqrt{\varepsilon}}}e^{-\frac{\varepsilon}{x\sqrt{\varepsilon}}}L_n^{\frac{\alpha_I}{\sqrt{\varepsilon}}}\left(\frac{2\varepsilon}{x\sqrt{\varepsilon}}\right) \tag{49}$$

where N_{nl} is normalization constant, which can be obtain from

$$\int_0^\infty |N_{nl}(r)|^2 dr = 1 \tag{50}$$

4. EXACT SOLUTIONS OF THE SCHRODINGER EQUATION WITH CLASS OF YUKAWA POTENTIAL USING THE SEM

We consider the radial Schrodinger equation of the form [50]

$$\frac{d^2R(r)}{dr^2} + \frac{2}{r}\frac{dR(r)}{dr} + \left[\frac{2\mu}{\hbar^2}(E - V(r)) - \frac{l(l+1)}{r^2}\right]R(r) = 0 \tag{51}$$

where l is angular quantum number taking the values 0,1,2,3,4…, μ is the reduced mass for the quarkonium particle, and r is the internuclear separation.
Putting Eq. (2) into Eq. (51) gives

$$\frac{d^2R(r)}{dr^2} + \frac{2}{r}\frac{dR(r)}{dr} + \left[\varepsilon + \frac{A}{r} - Br - Cr^2 - \frac{L(L+1)}{r^2}\right]R(r) = 0 \tag{52}$$

where

$$\varepsilon = \frac{2\mu}{\hbar^2}(E - \alpha_4), A = \frac{2\mu\alpha_0}{\hbar^2}, B = \frac{2\mu\alpha_1}{\hbar^2}, C = \frac{2\mu\alpha_2}{\hbar^2}\Big\} \tag{53}$$

$$L(L+1) = \frac{2\mu\alpha_3}{\hbar^2} + l(l+1) \tag{54}$$

From Eq. (54) we have

$$L = -\frac{1}{2} + \frac{1}{2}\sqrt{(2l+1)^2 + \frac{8\mu\alpha_3}{\hbar^2}} \tag{55}$$

From Eq. (29), Eqs.(56) and (57) are obtained

$$R'(\mathrm{r}) = F'(\mathrm{r})e^{-\alpha r^2 - \beta r} + F(r)(-2\alpha r - \beta)e^{-\alpha r^2 - \beta r} \tag{56}$$

$$\begin{aligned} R''(\mathrm{r}) = F''(\mathrm{r})e^{-\alpha r^2 - \beta r} + F'(\mathrm{r})(-2\alpha r - \beta)e^{-\alpha r^2 - \beta r} \\ + \left[(-2\alpha) + (-2\alpha r - \beta)(-2\alpha r - \beta)\right]F(r)e^{-\alpha r^2 - \beta r} \end{aligned} \tag{57}$$

Substituting Eqs. (29), (56) and (57) into Eq. (51) and divide through by $e^{-\alpha r^2 - \beta r}$ we obtain

$$F''(\mathrm{r}) + \left[-4\alpha r - 2\beta + \frac{2}{r}\right]F'(\mathrm{r}) + \left| \begin{array}{l} (4\alpha^2 - C)r^2 + (4\alpha\beta - B)r \\ + (A - 2\beta)\frac{1}{r} - \frac{L(L+1)}{r^2} + (\varepsilon + \beta^2 - 6\alpha) \end{array} \right| F(r) = 0 \tag{58}$$

Also, from Eq. (30), we obtain the following

$$F'(r) = \sum_{n=0}^{\infty}(2n+L)a_n r^{2n+L-1} \tag{59}$$

$$F''(r) = \sum_{n=0}^{\infty}(2n+L)(2n+L-1)a_n r^{2n+L-2} \tag{60}$$

We substitute Eqs. (30),(59) and (60) into Eq.(58) and obtain

$$\begin{aligned} \sum_{n=0}^{\infty}(2n+L)(2n+L-1)a_n r^{2n+L-2} + \left[-4\alpha r - 2\beta + \frac{2}{r}\right]\sum_{n=0}^{\infty}(2n+L)a_n r^{2n+L-1} \\ + \left[(4\alpha^2 - C)r^2 + (4\alpha\beta - B)r + \frac{(A-2\beta)}{r} - \frac{L(L+1)}{r^2} + (\varepsilon + \beta^2 - 6\alpha)\right]\sum_{n=0}^{\infty}a_n r^{2n+L} = 0 \end{aligned} \tag{61}$$

By collecting powers of r in Eq. (61) we have

$$\sum_{n=0}^{\infty}a_n \left\{ \begin{array}{l} \left[(2n+L)(2n+L-1) + 2(2n+L) - L(L+1)\right]r^{2n+L-2} \\ + \left[-2\beta(2n+L) + (A-2\beta)\right]r^{2n+L-1} \\ + \left[-4\alpha(2n+L) + \varepsilon + \beta^2 - 6\alpha\right]r^{2n+L} \\ + [4\alpha\beta - B]r^{2n+L+1} + \left[4\alpha^2 - C\right]r^{2n+L+2} \end{array} \right\} = 0 \tag{62}$$

Equation (62) is linearly independent implying that each of the terms is separately equal to Zero, noting that r is a non-zero function; therefore, it is the coefficient of r that is zero. With this in mind, we obtain the relation for each of the terms.

$$(2n+L)(2n+L-1) + 2(2n+L) - L(L+1) = 0 \tag{63}$$

$$-2\beta(2n+L) + A - 2\beta = 0 \tag{64}$$

$$-4\alpha(2n+L) + \varepsilon + \beta^2 - 6\alpha = 0 \tag{65}$$

$$4\alpha\beta - B = 0 \tag{66}$$

$$4\alpha^2 - C = 0 \tag{67}$$

From Eq. (64) we have

$$\beta = \frac{A}{4n + 2L + 2} \tag{68}$$

From Eq. (67) we have

$$\alpha = \frac{\sqrt{C}}{2} \tag{69}$$

The energy equation of the CYP is obtain by substituting Eqs. (53), (55), (68) and (69) into Eq. (65) and simplifying we have

$$
E_{nl} = \sqrt{\frac{-\hbar^2 b \alpha_I{}^3}{12\mu} \left(4n + 2 + \sqrt{(2l+1)^2 - \frac{8\mu c}{\hbar^2}} \right)}
$$
$$
- \frac{2\mu}{\hbar^2}(a - b - 2c\alpha_I)^2 \left(4n + 1 + \sqrt{(2l+1)^2 - \frac{8\mu c}{\hbar^2}} \right)^{-2} - b\alpha_I - 2c\alpha_I{}^2 \tag{70}
$$

4. RESULTS AND DISCUSSION
4.1 Results

We calculate mass spectra of the heavy quarkonium system such as charmonium and bottomonium that have the quark and antiquark flavor, and apply the following relation [51-53]

$$M = 2m + E_{nl} \tag{71}$$

where

M = Mass spectra of the heavy quarkonium,

m = Quarkonium bare mass,

E_{nl} = Energy eigenvalue.

By substituting Eq. (48) into Eq. (71) we obtain the mass spectra for class of Yukawa potential using the NU method as,

$$
M = 2m + \frac{3}{\delta} \left(\frac{b\alpha_I{}^2}{2} - 1.33\alpha_I{}^3 \right) - \frac{b\alpha_I{}^3}{\delta^2} - b\alpha_I - 2c\alpha_I{}^2
$$
$$
- \frac{\hbar^2}{8\mu} \left[\frac{\frac{6\mu}{\hbar^2\delta^2}\left(\frac{b\alpha_I{}^2}{2} - 1.33\alpha_I{}^3 \right) + \frac{2\mu}{\hbar^2}(a - b - 2c\alpha_I) - \frac{8\mu b\alpha_I{}^3}{3\hbar^2\delta^3}}{n + \frac{1}{2} + \sqrt{\left(l + \frac{1}{2} \right)^2 + \frac{2\mu}{\hbar^2\delta^3}\left(\frac{b\alpha_I{}^2}{2} - 1.33\alpha_I{}^3 \right) - \frac{\mu b\alpha_I{}^3}{\hbar^2\delta^4} - \frac{2\mu c}{\hbar^2}}} \right]^2 \tag{72}
$$

By substituting Eq. (70) into Eq.(71) we obtain the MS for CYP using the SEM as,

$$
M = 2m + \sqrt{\frac{-\hbar^2 b \alpha_I{}^3}{12\mu} \left(4n + 2 + \sqrt{(2l+1)^2 - \frac{8\mu c}{\hbar^2}} \right)}
$$
$$
- \frac{2\mu}{\hbar^2}(a - b - 2c\alpha_I)^2 \left(4n + 1 + \sqrt{(2l+1)^2 - \frac{8\mu c}{\hbar^2}} \right)^{-2} - b\alpha_I - 2c\alpha_I{}^2 \tag{73}
$$

4.2. Determination of the potential strength parameters

The reduced mass μ is defined in the standard way as $\mu = \frac{m}{2}$, where m = mass of the constituent quarks and antiquarks. For bottomonium $b\bar{b}$ and charmonium $c\bar{c}$ systems we adopt the numerical values of these masses as m_b = 4.823 GeV for bottomonium and m_c = 1.209 GeV for charmonium [54]. Then, the corresponding reduced mass are μ_b = 2.4115 GeV and μ_c = 0.6045 GeV. The potential parameters of Eqs. (72) and (73) are fitted with experimental data. Experimental data are taken from [55]. The parameters for charmonium and bottomonium of the Eq. (72) are

$$
\begin{pmatrix}
m_c = 1.209\ GeV, \mu = 0.6045\ GeV,\ a = -19.045\ GeV,\ b = 5.885\ GeV, \\
c = -1.188\ GeV, \delta = 0.23\ GeV, \alpha_i = 1.52\ GeV, \hbar = 1
\end{pmatrix}
$$

and

$$\begin{pmatrix} m_b = 4.823 \ GeV, \mu = 2.4115 \ GeV, \ a = -1.591 \ GeV, \ b = 8.875 \ GeV, \\ c = -11.153 \ GeV, \delta = 0.23 \ GeV, \alpha_l = 1.52 \ GeV, \hbar = 1 \end{pmatrix}$$

respectively. In the same vain, the parameters for charmonium and bottomonium of the Eq. (73) are

$$\begin{pmatrix} m_c = 1.209 \ GeV, \mu = 0.6045 \ GeV, \ \hbar = 1, \alpha_l = 1.52 \ GeV \\ a = 0.489 \ GeV, \ b = -0.695 \ GeV, \ c = 5.679 \ GeV \end{pmatrix}$$

and

$$\begin{pmatrix} m_b = 4.823 \ GeV, \mu = 2.4115 \ GeV, \ a = 1.192 \ GeV, \\ c = -13.876 \ GeV, \alpha_l = 1.52 \ GeV, \hbar = 1, \ b = 0.998 \ GeV \end{pmatrix}$$

respectively.

4.3. Discussion of results

The mass spectra of charmonium and bottomonium for class of Yukawa potential for the NU and the SEM were calculated as shown in Tables 1and 2 respectively using Eqs. (72) and (73).

Table 1. Comparison of mass spectra of charmonium in (GeV) for the class of Yukawa potential $M_{n,l}^{CYP}$, between the NU, SEM, some authors and experimental data

State	$M_{n,l}^{CYP}$ with the NU	$M_{n,l}^{CYP}$ with the SEM	[12]	[13]	Experiment [55]
1s	3.096	3.096	3.096	3.095	3.096
2s	3.686	3.686	3.686	3.685	3.686
1p	3.493	3.524	3.255	3.258	3.525
2p	3.772	3.773	3.779	3.779	3.773
3s	4.040	4.040	4.040	4.040	4.040
4s	4.267	4.263	4.269	4.262	4.263
1d	3.763	3.769	3.504	3.510	3.770
2d	4.146	4.156	-	3.928	4.159
1f	3.962	4.081	-	-	-

The free parameters are fitted with experimental data. In addition, quark masses are obtained from Ref. [55]. We note the spectra masses of charmonium from states 1s,2s, 3s and 2p from both the NU and the series expansion methods agree with experimental data and 1s,2s,3s and 4s states for bottomonium agree with experimental data for both methods as shown in Tables 1 and 2. Other states appear to be close with experimental data, but the SEM solutions appear to be very close to experimental data for charmonium and bottomonium compared to the NU method. It was noticed that in the 1f state for charmonium and 2d and 1f states for bottomonium the values of the experimental data are not available. The mass spectra obtained agree with Ref. [12]. Our results are improved in comparison with works of other researcher like Ref. [12] as shown in the Tables in which the author investigated the N-radial SE analytically. The Cornell potential was extended to finite temperature. The energy eigenvalue and the wave functions were calculated in the N-dimensional form using the NU method. Also, the mass spectra obtained using Eqs. (72) and (73) are improved in comparison with the works of Ref. [13] in which they studied the N-dimensional radial Schrodinger equation using the analytical exact iteration method, in which the Cornell potential is generalized to finite temperature and chemical potential.

Table 2. Comparison of mass spectra of bottomonium in (GeV) for the class of Yukawa potential $M_{n,l}^{CYP}$, between the NU, SEM, some authors and experimental data

State	$M_{n,l}^{CYP}$ with the NU	$M_{n,l}^{CYP}$ with the SEM	[12]	[13]	Experiment [55]
1s	9.460	9.460	9.460	9.460	9.460
2s	10.023	10.023	10.023	10.022	10.023
1p	9.761	9.889	9.619	9.609	9.899
2p	10.258	10.260	10.114	10.109	10.260
3s	10.355	10.355	10.355	10.360	10.355
4s	10.577	10.579	10.567	10.580	10.580
1d	9.989	10.164	9.864	9.846	10.164
2d	10.336	10.575	_	_	_
1f	10.279	10.299	_	_	_

CONCLUSION

In this work, the Schrodinger equation is analytically solved using the Nikiforov- Uvarov and series expansion methods with the class of Yukawa potential. The approximate solutions of the eigen energy equation and corresponding eigenfunction in terms of Laguerre polynomials were obtained using the NU method. The solutions of the eigen energy equation were also obtained with the SEM. The mass spectra for heavy quarkonium system for the potential under study

were obtained for bottomonium $b\bar{b}$ and charmonium $c\bar{c}$. We adopted the numerical values of these masses as $m_b = 4.823\ GeV$ for bottomonium and $m_c = 1.209\ GeV$ for charmonium. We compared the results obtained between the Nikiforov- Uvarov and series expansion methods. It was noticed that SEM solutions yield mass spectra very close to experimental data compared to solutions with the NU method. The obtained results were also compared with works by some other authors [12,13] with different analytical methods. The values obtained are improved in comparison with their works. This work can be extended by using other exponential-type potential models with other analytical approach and a different approximation scheme to obtain the mass spectra of heavy quarkonium system. The relativistic properties using Klein-Gordon or Dirac equations can be explored to obtain the mass spectra of light quarkonia. Finally, the information entailed in the normalized wave-functions can also be studied.

ORCID IDs
Joseph A. Obu, https://orcid.org/0000-0001-9633-4045; **Etido P. Inyang**, https://orcid.org/0000-0002-5031-3297
Eddy S. William, https://orcid.org/0000-0002-5247-5281; **Donatus E. Bassey**, https://orcid.org/0000-0002-0296-7878

REFERENCES
[1] C. Mike, G. Geoff, and M. Chris, *Advanced Level Physics* (2nd ed.), (Hodder Education, Hachette UK company, 2014). pp. 243-248.
[2] K.S. Krane, *Introductory Nuclear Physics*, (John Wiley & Sons,1987). pp. 1123-1213.
[3] E.P. Inyang, E.P. Inyang, I.O. Akpan, J.E. Ntibi, and E.S. William, Masses and thermodynamic properties of a Quarkonium system. *Canadian Journal of Physics.* 99(11),982-990 (2021). https://doi.org/10.1139/cjp-2020-0578
[4] P. Amore et al., Analytical approximations to the spectra of quark–antiquark potentials, J. Phys. G: Nucl. Part. Phys. 32, 1061 (2006). https://doi.org/10.1088/0954-3899/32/7/014
[5] A. Mocsy, "Can quarkonia survive deconfinement?", Phys. Rev. D, **77**, 45-55 (2008). https://doi.org/10.1103/PhysRevD.77.014501
[6] E.P. Inyang, E.P. Inyang, E.S. William, and E.E. Ibekwe, "Study on the applicability of Varshni potential to predict the mass-spectra of the Quark-Antiquark systems in a non-relativistic framework," Jord. J. Phys. **14**, 339-345 (2021). https://doi.org/10.47011/14.4.8
[7] T. Matsui, and H. Satz, "J/φ suppression by quark-gluon plasma formation," Physics Letters B, **178**(4), 416-422 (1986). https://doi.org/10.1016/0370-2693(86)91404-8
[8] A. Mira-Cristiana, "Yukawa: The man and the potential," Didactica Mathematica, **33**, 1-9 (2015). https://www.researchgate.net/profile/Mira-Cristiana-Anisiu/publication/309807406_Yukawa_the_man_and_the_potential/links/582439cc08aeebc4f898aaf6/Yukawa-the-man-and-the-potential.pdf
[9] E.P. Inyang, E.O. Obisung, P.C. Iwuji, J.E. Ntibi, J. Amajama, and E.S. William, "Masses and thermal properties of a charmonium and Bottomonium mesons", J. Nig. Soc. Phys. Sci. **4**, 884 (2022). https://doi.org/10.46481/jnsps.2022.884
[10] A. Mocsy, "Potential models for quarkonia," The European Physical Journal, **61**, 705-710 (2009). https://doi.org/10.1140/epjc/s10052-008-0847-4
[11] E.P. Inyang, P.C. Iwuji, J.E. Ntibi, E. Omugbe, E.A. Ibanga, and E.S. William, "Quark-antiquark study with inversely quadratic Yukawa potential using Nikiforov-Uvarov-Functional analysis method", East European Journal of Physics, **2**, 51 (2022). https://doi.org/10.26565/2312-4334-2022-2-05
[12] M. Abu-Shady, "N-dimensional Schrodinger equation at finite temperature using the Nikiforov-Uvarov method," J. Egypt. Math. Soc. **23**, 1-4 (2016). https://doi.org/10.1016/j.joems.2016.06.006
[13] M. Abu-Shady, and H.M. Fath-Allah, "The effect of extended Cornell potential on heavy and heavy-light meson masses using series method," Journal of the Egyptian mathematical society, **23**(2), 156-165 (2019). https://arxiv.org/abs/1908.09131
[14] E.P. Inyang, F.O. Faithpraise, J. Amajama, E.S. William, E.O. Obisung, J.E. Ntibi, "Theoretical Investigation Of Meson Spectrum Using Exact Quantization Rule Technique," East European Journal of Physics, **1**, 53-62 (2023). https://doi.org/10.26565/2312-4334-2023-1-05
[15] P.O. Okoi, C.O. Edet, T.O. Magu, and E.P. Inyang, "Eigensolution and Expectation values of the Hulthén and Generalized Inverse Quadratic Yukawa potential," Jordan Journal of Physics, **15**, 137-148 (2022). https://doi.org/10.47011/15.2.4
[16] E.S. William, E.P. Inyang, and E.A. Thompson, "Arbitrary ℓ -solutions of the Schrödinger equation interacting with Hulthén-Hellmann potential model," Rev. Mex. Fis. **66**, 730 (2020). https://doi.org/10.31349/RevMexFis.66.730
[17] E.E. Ibekwe, E.P. Inyang, J.B. Emah, J.B. Akpan, and O.J. Yawo, "Mass spectra and thermal properties of deformed Schrödinger Equation for pseudoharmonic potential," Sri Lankan Journal of Physics, **23**(2), 63–76 (2022). https://doi.org/10.4038/sljp.v23i2.8119
[18] E.P. Inyang, E.S. William, and J.A. Obu, "Eigensolutions of the N-dimensional Schrödinger equation` interacting with Varshni-Hulthen potential model," Rev. Mexi. Fis. **67**, 193 (2021). https://doi.org/10.31349/RevMexFis.67.193

[19] E.S. William, E.P. Inyang, I.O. Akpan, J.A. Obu, A.N. Nwachukwu, and E.P. Inyang, "Ro-vibrational energies and expectation values of selected diatomic molecules via Varshni plus modified Kratzer potential model," Indian Journal of Physics, **96**, 3461-3476 (2022). https://doi.org/10.1007/s12648-022-02308-0

[20] E.P. Inyang, A.N. Ikot, E.P. Inyang, I.O. Akpan, J.E. Ntibi, E. Omugbe, and E.S. William, "Analytic study of thermal properties and masses of heavy mesons with quarkonium potential", Result in Physics, **39**, 105754 (2022). https://doi.org/10.1016/j.rinp.2022.105754

[21] E.P. Inyang, and E.O. Obisung, "The study of electronic states of NI and ScI molecules with screened Kratzer Potential," East Eur. J. Phys. **3**, 32 (2022). https://doi.org/10.26565/2312-4334-2022-3-04

[22] E.P. Inyang, E.S. William, J.O. Obu, B.I. Ita, E.P. Inyang, and I.O. Akpan, "Energy spectra and expectation values of selected diatomic molecules through the solutions of Klein-Gordon equation with Eckart-Hellmann potential model," Molecular Physics, **119**(23), e1956615 (2021). https://doi.org/10.1080/00268976.2021.1956615

[23] E.S. William, E.P. Inyang, J.E. Ntibi, J.A. Obu, and E.P. Inyang, "Solutions of the Non-relativistic Equation Interacting with the Varshni-Hellmann potential model with some selected Diatomic molecules," Jordan Journal of Physics, **15**, 179-193 (2022). https://doi.org/10.47011/15.2.8

[24] E.P. Inyang, F. Ayedun, E.A. Ibanga, K.M. Lawal, I.B. Okon, E.S. William, O. Ekwevugbe, C.A. Onate, A.D. Antia, and E.O. Obisung, "Analytical Solutions of the N-Dimensional Schrödinger equation with modified screened Kratzer plus Inversely Quadratic Yukawa potential and Thermodynamic Properties of selected Diatomic Molecules," Results in Physics, **43**, 106075 (2022). https://doi.org/10.1016/j.rinp.2022.106075

[25] C.O. Edet, S. Mahmoud, E.P. Inyang, N. Ali, S.A. Aljunid, R. Endut, A.N. Ikot, and M. Asjad, "Non-Relativistic Treatment of the 2D Electron System Interacting via Varshni-Shukla Potential Using the Asymptoptic Iteration Method," Mathematics, **10**, 2824 (2022). https://doi.org/10.3390/math10152824

[26] A.N. Ikot, L.F. Obagboye, U.S. Okorie, E.P. Inyang, P.O. Amadi, and A. Abdel-Aty, Solutions of Schrodinger equation with generalized Cornell potential (GCP) and its applications to diatomic molecular systems in D-dimensions using Extended Nikiforov–Uvarov (ENU) formalism," The European Physical Journal Plus, **137**, 1370 (2022). https://doi.org/10.1140/epjp/s13360-022-03590-x

[27] A.N. Ikot, U.S. Okorie, P.O. Amadi, C.O. Edet, G.J. Rampho, and R. Sever, "The Nikiforov-Uvarov –Functional Analysis (NUFA) Method: A new approach for solving exponential – Type potentials," Few-Body System, **62,** 9 (2021). https://doi.org/10.1007/s00601-021-021-01593-5

[28] E.P. Inyang, E.S. William, J.E. Ntibi, J.A. Obu, P.C. Iwuji, and E.P. Inyang, "Approximate solutions of the Schrödinger equation with Hulthén plus screened Kratzer Potential using the Nikiforov–Uvarov – functional analysis (NUFA) method: an application to diatomic molecules," Can. J. Phys. **100**(10), 473 (2022). https://doi.org/10.1139/cjp-2022-003

[29] E.P. Inyang, E.P. Inyang, E.S. William, J.E. Ntibi, and E.A. Ibanga, "Bound State Solutions of the Schrödinger equation with Frost-Musulin potential using the Nikiforov-Uvarov-Functional Analysis (NUFA) method," Bulg. J. Phys. **49**(4), 329-339 (2022). https://doi.org/10.55318/bgjp.2022.49.4.329

[30] E.P. Inyang, E.S. William, E. Omugbe, E.P. Inyang, E.A. Ibanga, F. Ayedun, I.O. Akpan, and J.E. Ntibi, "Application of Eckart-Hellmann potential to study selected diatomic molecules using Nikiforov-Uvarov-Functional analysis method", Rev. Mex. Fis. **68**, 020401 (2022). https://doi.org/10.31349/RevMexFis.68.020401

[31] E.P. Inyang, E.P. Inyang, I.O. Akpan, J.E. Ntibi, and E.S. William, "Analytical solutions of the Schrödinger equation with class of Yukawa potential for a quarkonium system via series expansion method", European Journal of Applied Physics, **2**, 26 (2020). http://dx.doi.org/10.24018/ejphysics.2020.2.6.26

[32] E.P. Inyang, P.C. Iwuji, J.E. Ntibi, E.S. William, and E.A. Ibanga, "Solutions of the Schrodinger equation with Hulthén-screened Kratzer potential: Application to diatomic molecules," East European Journal of Physics, **1**, 12-22 (2022). https://doi.org/10.26565/2312-4334-2022-2-02

[33] E.P. Inyang, J.E. Ntibi, O.O. Akintola, E.A. Ibanga, F. Ayedun, and E.S. William, "Analytical solutions to the Schrödinger Equation with a Combined Potential using the Series Expansion Method to Study Selected Diatomic Molecules," Communication in Physical Science, **8**(2), 258-276 (2022). https://journalcps.com/index.php/volumes/article/view/279/244

[34] E.P. Inyang, E.P. Inyang, J.E. Ntibi, and E.S. William, "Analytical solutions of Schrodinger equation with Kratzer-screened Coulomb potential for a Quarkonium system. Bulletin of Pure and Applied Sciences," **40**, 24 (2021). https://doi.org/10.5958/2320-3218.2021.0002.6

[35] E. Omugbe, "Non-relativistic energy spectrum of the Deng-Fan Oscillator via the WKB Approximation method", Asian Journal of Physics and Chemistry, **8**(1), 26-36 (2020). https://doi.org/10.9734/ajopacs/2020/v8i130107

[36] E. Omugbe, O.E. Osafile, E.P. Inyang, and A. Jahanshir, "Bound state solutions of the hyper-radial Klein-Gordon equation under the Deng-Fan potential by WKB and SWKB methods," Phys. Scr. **96**(12), 125408 (2021). https://doi.org/10.1088/1402-4896/ac38d4

[37] E. Omugbe, O.E. Osafile, I.B. Okon, E.P. Inyang, E.S. William, and A. Jahanshir, "Any l - state Energy of the Spinless Salpter Equation under the Cornell potential by the WKB Approximation method: An Application to mass Spectra of Mesons," Few-Body Systems, **63**(1), 1-7 (2022). https://doi.org/10.1007/s00601-021-01705-1

[38] M. Abu-Shady, and E.P. Inyang, "The fractional Schrödinger equation with the generalized Woods-Saxon potential," East European Journal of Physics, **1**, 63-68 (2023). https://doi.org/10.26565/2312-4334-2023-1-06

[39] E.P. Inyang, E.P. Inyang, J.E. Ntibi, E.E. Ibekwe, and E.S. William, "Approximate solutions of D-dimensional Klein-Gordon equation with Yukawa potential via Nikiforov-Uvarov method," Ind. J. Phys. 95, 2733–2739 (2021). https://doi.org/10.1007/s12648-020-01933-x

[40] I.O. Akpan, E.P. Inyang, E.P. Inyang, and E.S. William, "Approximate solutions of the Schrödinger equation with Hulthen-Hellmann Potentials for a Quarkonium system," Rev. Mex. Fis. **67**, 482-490 (2021). https://doi.org/10.31349/revmexfis.67.482

[41] E.E. Ibekwe, J.B. Emah, E.P. Inyang, and A.O. Akpan, "MASS Spectrum of Heavy Quarkonium for Combined Potentials (Modified Kratzer Plus Screened Coulomb Potential)," Iran J. Sci. Technol. Trans. Sci. **46**, 1741-1748 (2022). https://doi.org/10.1007/s40995-022-01377-4

[42] M. Abu-Shady, and E.P. Inyang, "Heavy-Light Meson masses in the Framework of Trigonometric Rosen-Morse Potential using the Generalized Fractional Derivative," East Eur. J. Phys. **4**, 80-87 (2022). https://doi.org/10.26565/2312-4334-2022-4-06

[43] H.M. Yukawa, "On the Interaction of Elementary Particles." Proc. Phys. Math. Soc. Jap. **17**, 48-57 (1935). https://doi.org/10.11429/ppmsj1919.17.0_48

[44] H. Hellmann, "A New Approximation Method in the Problem of Many Electrons," J. Chem. Phys. 3, 61 (1935). https://doi.org/10.1063/1.1749559

[45] B.I. Ita, and A.I. Ikeuba, "Solution to the Schrodinger equation with inversely quadratic Yukawa plus inversely quadratic Hellmann potential using Nikiforov-Uvarov method", Journal of Atomic and Molecular Physics, **2013**, 582610 (2013). http://dx.doi.org/10.1155/2013/582610

[46] C.A. Onate, and J.O. Ojonubah, "Eigensolutions of the Schrodinger equation with a class of Yukawa Potentials via supersymmetric approach," Journal of theoretical and applied Physics, **19**, 679-685 (2016). https://doi.org/10.1007/s40094-015-0196-2

[47] G. Sezgo, *Orthogonal Polynomials*, (American Mathematical Society, New York, 1934), pp. 345-346.

[48] S.K. Nikiforov, and V.B. Uvarov, *Special functions of mathematical Physics*, (Birkhauser, Basel, 1988).

[49] R. Rani, S.B. Bhardwaj, and F. Chand, "Bound state solutions to the Schrodinger equation for some diatomic molecules," Pramana Journal of Physics, **91**, 1602-1615 (2018). https://doi.org/10.1007/s12043-018-1622-1

[50] F. Ayedun, E.P. Inyang, E.A. Ibanga, and K.M. Lawal, "Analytical Solutions to The Schrödinger Equation with Collective Potential Models: Application to Quantum Information Theory," East Eur. J. Phys. **4**, 87-98 (2022). https://doi.org/10.26565/2312-4334-2022-4-06

[51] E.E. Ibekwe, U.S. Okorie, J.B. Emah, E.P. Inyang and S.A. Ekong, "Mass spectrum of heavy quarkonium for screened Kratzer potential (SKP) using series expansion method," European Physical Journal Plus, **87**, 11 (2021). https://doi.org/10.1140/epjp/s13360-021-01090-y

[52] E.P. Inyang, J. Ntibi, E.A. Ibanga, F. Ayedun, E.P. Inyang, and E.S. William, "Thermal Properties, Mass Spectra and Root Mean Square Radii of Heavy Quarkonium System with Class of Inversely Quadratic Yukawa Potential," AIP Conference Proceedings **2679**, 030003 (2023). https://doi.org/10.1063/5.0112829

[53] E.P. Inyang, E.O .Obisung, J. Amajama, E.S William, and I.B. Okon, "The Effect of Topological Defect on the Mass Spectra of Heavy and Heavy-Light Quarkonia," Eurasian Physical Technical Journal, **19**(4), 78-87 (2022). https://doi.org/10.31489/2022No4/78-87

[54] E.P. Inyang, E.O. Obisung, E.S. William and I.B. Okon, Non-Relativistic study of mass spectra and thermal properties of a quarkonium system with Eckart-Hellmann potential. East European Journal of Physics, **3**, 104-114 (2022). https://doi.org/10.26565/2312-4334-2022-3-14

[55] R. Olive, D.E. Groom, and T.G. Trippe, Particle Data Group, Chin. Phys. C, **38**, 60 (2014).

[56] M. Tanabashi, C.D. Carone, T.G. Trippe, and C.G. Wohl, Particle Data Group, Phys. Rev. D, **98**, 546 (2018).

ПОРІВНЯЛЬНЕ ДОСЛІДЖЕННЯ СПЕКТРІВ МАСИ ВАЖКОЇ КВАРКОНІЄВОЇ СИСТЕМИ З МОДЕЛЛЮ ПОТЕНЦІАЛУ ВЗАЄМОДІЇ

Джозеф А. Обу[b]**, Етідо П. Іньянг**[a]**, Едді С. Вільям**[c]**, Донатус Е. Бассей**[b]**, Ефраїм П. Іньянг**[b]

[a]Департамент фізики, Національний відкритий університет Нігерії, Джабі, Абуджа, Нігерія
[b]Департамент фізики, Університет Калабара, PMB 1115, Калабар, Нігерія
[c]Департамент фізики, школа чистих і прикладних наук, Федеральний технологічний університет, Ікот Абасі, Нігерія

У цій роботі досліджено порівняння мас-спектрів важкої кварконієвої системи з потенціалом взаємодії (клас потенціалу Юкави). Рівняння Шредінгера аналітично розв'язується за допомогою методу Нікіфорова-Уварова (NU) і методу розкладання в ряд (SEM). Наближені розв'язки рівняння власної енергії та відповідної власної функції через поліноми Лагерра були отримані за допомогою методу NU, також за допомогою SEM були отримані розв'язки рівняння власної енергії. Мас-спектри важкої кварконієвої системи (ВСК) для досліджуваного потенціалу отримано для боттонієвої та чармонієвої ВСК. Ми порівняли результати, отримані між NU та SEM. Було помічено, що SEM-рішення дають мас-спектри, дуже близькі до експериментальних даних, порівняно з розв'язанням методом NU. Отримані результати також порівнювали з роботами деяких інших авторів і визнали їх покращеними. Це дослідження можна розширити, використовуючи інші потенційні моделі експоненціального типу з іншим аналітичним підходом і іншою схемою наближення для отримання мас-спектрів важкої кварконієвої системи. Релятивістські властивості за допомогою рівнянь Клейна-Гордона або Дірака можна досліджувати для отримання мас-спектрів легких кварконіїв. Нарешті, також можна вивчати інформацію, що міститься в нормалізованих хвильових функціях.

Ключові слова: *рівняння Шредінгера; метод Нікіфорова-Уварова; клас Юкава-потенціалу; мас-спектри; метод серійного розширення*

BOUND STATE AND RO-VIBRATIONAL ENERGIES EIGENVALUES OF SELECTED DIATOMIC MOLECULES WITH A CLASS OF INVERSELY QUADRATIC YUKAWA PLUS HULTHÉN POTENTIAL MODEL[†]

Fina O. Faithpraise[a], Etido P. Inyang[b]*

[a]Department of Physics, University of Calabar, PMB 1115, Calabar, Nigeria
[b]Department of Physics, National Open University of Nigeria, Jabi, Abuja, Nigeria
Corresponding author email: etidophysics@gmail.com OR einyang@noun.edu.ng
Received July 7, 2023; revised July 17, 2023; accepted July 18, 2023

The Nikiforov-Uvarov approach is used in this study to solve the Schrödinger equation utilizing a class of inversely quadratic Yukawa plus Hulthén potential model with an approximation to the centrifugal term. The normalized wave function and energy eigenvalue equation were obtained. The numerical bound state for a few diatomic molecules (N_2, O_2, NO, and CO) for various rotational and vibrational quantum numbers was calculated using the energy equation and the related spectroscopic data. Our results show that, with no divergence between the s-wave and l-wave, the energy eigenvalues are very sensitive to the potential and diatomic molecule properties, suggesting that the approximation approach is appropriate for this set of potentials. The results are consistent with earlier studies in the literature, and we also found four special cases of this potential.
Keywords: *Schrödinger equation; Nikiforov-Uvarov method; Class of inversely quadratic plus Hulthén potential; Diatomic molecules; Bound state*
PACS: 31.15.-p

INTRODUCTION

The time-independent Schrödinger wave equation can be used to study the dynamics and interactions of quantum mechanical processes and non-relativistic spinless particles [1-4]. Because the eigenvalues and eigenfunctions associated with quantum problems include essential information regarding the quantum system. The analytical solutions to this equation with physical potentials are likely to play an important role in our understanding of the underlying principles of a quantum system [5, 6]. The bound state solutions of the Schrödinger equation for a few of these potentials, such as the Coulomb potential (CP) [7], Woods-Saxon [8], Hulthén [9], Manning-Rosen [10], and so on, are possible in some situations. A suitable approximation scheme can also be used to solve the Schrödinger equation approximately when the arbitrary rotational momentum quantum number is available [11]. The approximation scheme proposed by Greene and Aldrich [11], the improved approximation scheme by Jia et al. [12], the approximation scheme by Hill [13], the Pekeris approximation [14], the approximation scheme by Yazarloo et al. [15], and the improved approximation scheme in Ref. [16] are a few examples of these approximations.

To find the exact and approximate solutions to the Schrödinger equation, quantum mechanical techniques have been extensively used over time by scholars [17–27]. Inversely quadratic Hellmann potential (IQHP) has been used by numerous authors in different areas of physics [28-31]. Another intriguing potential is inversely quadratic potential (IQP). The inversely quadratic potential has been used by Oyewumi and Bangudu [32] and several authors in the literature [33-35].

In order to investigate the interaction that exists between two particles, the Hulthén potential (HP) [36] is essential. It is utilized in the study of atomic, condensed matter, nuclear, and molecular physics as well as chemical physics [37,38]. Another potential of interest is a newly proposed potential by Inyang et al. [39] called the class of inversely quadratic Yukawa potential. This work aims to use the class of inversely quadratic Yukawa plus Hulthén potential (CIQYHP) to obtain bound state approximate solutions to the Schrödinger equation. The obtain energy equation will be used to investigate the ro-vibrational energies of some selected diatomic molecules and the bound state energies. The potential model under study is of the form:

$$V(r) = -\frac{V_{01}}{r} + \frac{V_{21}e^{-\delta_0 r}}{r^2} - \frac{V_{11}}{r^2} - \frac{V_{31}e^{-\delta_0 r}}{1-e^{-\delta_0 r}}, \tag{1}$$

where V_{01}, V_{11}, V_{21}, and V_{31} are potential strength and δ_0 is the screening parameter.

The shape of this potential as a function of the screening parameter is given in Fig. 1. The following is how the paper is set up: The energy eigenvalues and normalized eigenfunctions are obtained by solving the Schrödinger equation with the class of inversely quadratic Yukawa plus Hulthén potential using the Nikiforov-Uvarov method in Section 2. The resulting energy equation will be applied in Section 3 to compute numerically the energy eigenvalues at various states of the chosen diatomic molecules and the discussion. In Section 4, conclusions are provided.
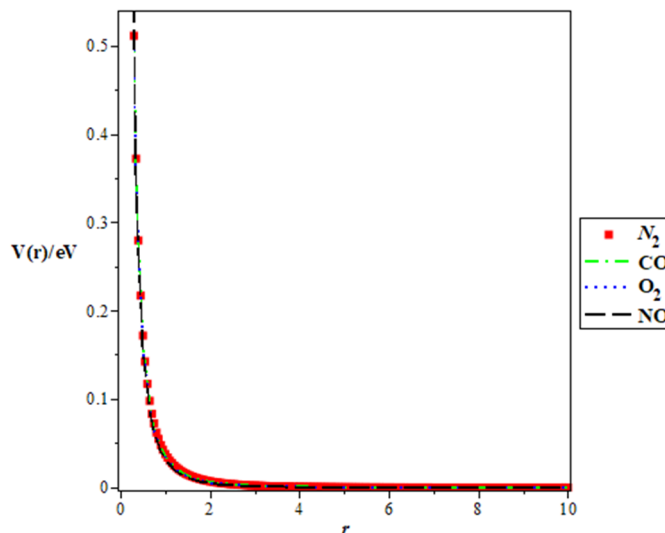
Figure 1. Variation of the potential $V(r)$ against internuclear distance r for the N$_2$, O$_2$, NO and CO diatomic molecules

2. APPROXIMATE SOLUTION OF SCHRÖDINGER EQUATION WITH THE CLASS OF INVERSELY QUADRATIC YUKAWA PLUS HULTHÉN POTENTIAL

In this study, the second-order differential equation of the hypergeometric type is solved using the Nikiforov-Uvarov method. The specifics are provided in Reference [17]. The Schrödinger equation reads [40]

$$\left(-\frac{\hbar^2}{2\mu}\nabla^2 + V(r)\right)\psi_{nl}(r) = E_{nl}\psi_{nl}(r), \tag{2}$$

where $\psi_{nl}(r)$ is the wavefunctions, E_{nl} is the eigenvalues of the quantum system, r is the radial distance from the origin, $\hbar$ is the reduced Planck's constant and μ is the reduced mass. Replacing Eq. (1) into Eq. (2) gives

$$\frac{d^2\psi_{nl}(r)}{dr^2} + \left[\frac{2\mu E_{nl}}{\hbar^2} + \frac{2\mu V_{01}}{\hbar^2 r} - \frac{2\mu V_{11}e^{-\delta_0 r}}{\hbar^2 r^2} + \frac{2\mu V_{21}}{\hbar^2 r^2} + \frac{2\mu V_{31}e^{-\delta_0 r}}{\hbar^2(1-e^{-\delta_0 r})} - \frac{l(l+1)}{r^2}\right]\psi_{nl}(r) = 0 \tag{3}$$

Equation (3) cannot be solved with the proposed potential because of the inverse square term. We then introduce the Greene-Aldrich approximation scheme [11] to deal with the inverse square term. This approximation scheme is a good approximation and is valid for $\delta_0 \ll 1$, and it becomes

$$\frac{1}{r^2} \approx \frac{\delta_0^2}{\left(1-e^{-\delta_0 r}\right)^2}. \tag{4}$$

Applying Eq. (5), we have

$$\frac{d^2\psi_{nl}(r)}{dr^2} + \left[\frac{2\mu E_{nl}}{\hbar^2} + \frac{2\mu V_{01}\delta_0}{\hbar^2(1-e^{-\delta_0 r})} - \frac{2\mu V_{11}\delta_0^2 e^{-\delta_0 r}}{\hbar^2(1-e^{-\delta_0 r})^2} + \frac{2\mu V_{21}\delta_0^2}{\hbar^2(1-e^{-\delta_0 r})^2} + \frac{2\mu V_{31}e^{-\delta_0 r}}{\hbar^2(1-e^{-\delta_0 r})} - \frac{\delta_0^2 l(l+1)}{(1-e^{-\delta_0 r})^2}\right]\psi_n(r) = 0. \tag{5}$$

By using the change of variable from $r \to x_b$, new coordinate is

$$x_b = e^{-\delta_0 r}. \tag{6}$$

We put Eq. (6) into Eq. (5) and simplify to get,

$$\frac{d^2\psi(x_b)}{dx_b^2} + \frac{1-x_b}{x_b(1-x_b)}\frac{d\psi(x_b)}{dx_b} + \frac{1}{\left[x_b(1-x_b)\right]^2}\left[\begin{array}{c}-(\varepsilon+\beta_{30})x_b^2 + (2\varepsilon+\beta_{00}-\beta_{10}+\beta_{30})x_b \\ -(\varepsilon-\beta_{00}-\beta_{20}+\gamma)\end{array}\right]\psi(x_b) = 0, \tag{7}$$

where

$$-\varepsilon = \frac{2\mu E_{nl}}{\delta_0^2 \hbar^2}, \quad \beta_{00} = \frac{2\mu V_{01}}{\delta_0 \hbar^2}, \quad \beta_{10} = \frac{2\mu V_{11}}{\hbar^2}, \quad \beta_{20} = \frac{2\mu V_{21}}{\hbar^2}, \quad \beta_{30} = \frac{2\mu V_{31}}{\delta_0^2 \hbar^2}, \quad \gamma = l(l+1) \Big\}. \tag{8}$$

Linking Eq. (7) and Eq. (1) of Ref. [17], we obtain the polynomials:

$$\tilde{\tau}(x_b) = 1 - x_b; \quad \sigma(x_b) = x_b(1 - x_b); \quad \sigma'(x_b) = 1 - 2x_b, \quad \sigma''(x_b) = -2; \Big\}$$
$$\tilde{\sigma}(x_b) = -(\varepsilon + \beta_{30})x_b^2 + (2\varepsilon + \beta_{00} - \beta_{10} + \beta_{30})x_b - (\varepsilon - \beta_{00} - \beta_{20} + \gamma) \Big] \tag{9}$$

Inserting Eq. (9) into Eq. (11) of Ref. [17], gives;

$$\pi(x_b) = -\frac{x_b}{2} \pm \sqrt{(\eta_{01} - K_0)x_b^2 + (K_0 + \eta_{02})x_b + \eta_{03}}, \tag{10}$$

where

$$\eta_{01} = \left(\frac{1}{4} + \varepsilon + \beta_{30}\right), \quad \eta_{02} = -(2\varepsilon - \beta_{00} - \beta_{10} + \beta_{30}), \quad \eta_{03} = (\varepsilon - \beta_{00} - \beta_{20} + \gamma) \Big\}. \tag{11}$$

The NU approach states that the discriminant of this quadratic equation must be set to zero in order to solve the quadratic form of Eq. (10) under the square root sign. A new quadratic equation is generated by this discriminant, which can be solved for the constant K_0 to obtain the two roots:

$$K_0 = -(\eta_{02} + 2\eta_{03}) - 2\sqrt{\eta_{03}}\sqrt{\eta_{03} + \eta_{02} + \eta_{01}}. \tag{12}$$

Replacing Eq. (12) into Eq. (10), $\pi(x_b)$ has the expression given as

$$\pi(x_b) = -\frac{x_b}{2} - \left[\left(\sqrt{\eta_{03}} + \sqrt{\eta_{03} + \eta_{02} + \eta_{01}}\right)x_b - \sqrt{\eta_{03}}\right], \tag{13}$$

with Eq. (9) and Eq. (13). Therefore, we obtain

$$\tau(x_b) = 1 - 2x_b - 2\sqrt{\eta_{03}}\,x_b - 2\sqrt{\eta_{03} + \eta_{02} + \eta_{01}}\,x_b + 2\sqrt{\eta_{03}}, \tag{14}$$

$$\tau'(x_b) = -2\left[1 + \sqrt{\eta_{03}} + \sqrt{\eta_{03} + \eta_{02} + \eta_{01}}\right], \tag{15}$$

Referring to Eq. (10) and Eq. (13) of Ref. [17], we have the following equations:

$$\lambda_n = n^2 + \left[1 + 2\sqrt{\eta_{03}} + 2\sqrt{\eta_{03} + \eta_{02} + \eta_{01}}\right]n, \tag{16}$$

$$\lambda = -\frac{1}{2} - \sqrt{\eta_{03}} - \sqrt{\eta_{03} + \eta_{02} + \eta_{01}} - (\eta_{02} + 2\eta_{03}) - 2\sqrt{\eta_{03}}\sqrt{\eta_{03} + \eta_{02} + \eta_{01}}, \tag{17}$$

With the aid of Eq. (8), we can compare Eqs. (16) and (17) and get the bound state energy eigenvalues of the Schrödinger equation with the class of inversely quadratic Yukawa plus Hulthén potential as follows:

$$E_{nl} = V_{21}\delta_0^2 - V_{01}\delta_0 - \frac{\delta_0^2 \hbar^2 l(l+1)}{2\mu} - \frac{\delta_0^2 \hbar^2}{8\mu}\left[\frac{\left(n + \frac{1}{2} + \sqrt{\frac{1}{4} + l(l+1) + \frac{2\mu V_{11}}{\hbar^2} - \frac{2\mu V_{21}}{\hbar^2}}\right)^2}{n + \frac{1}{2} + \sqrt{\frac{1}{4} + l(l+1) + \frac{2\mu V_{11}}{\hbar^2} - \frac{2\mu V_{21}}{\hbar^2}}}\right]^2. \tag{18}$$

Therefore, the complete eigenfunction can be express as:

$$\psi_{nl}(x_b) = \left[\frac{n!2\sqrt{\eta_{03}} \ \delta_0 \ \Gamma\left(2\sqrt{\eta_{03}} + \sqrt{4\eta_{03} + 4\eta_{02} + 4\eta_{01}} + n + 2\right)}{2\Gamma\left(2\sqrt{\eta_{03}} + n + 1\right)\Gamma\left(\sqrt{4\eta_{03} + 4\eta_{02} + 4\eta_{01}} + n + 2\right)} \right]^{\frac{1}{2}}$$
$$x_b^{\sqrt{\eta_{03}}} (1-x_b)^{\left(\frac{1}{2} + \sqrt{\eta_{03}+\eta_{02}+\eta_{01}}\right)} P_n^{\left(2\sqrt{\eta_{03}}, 2\sqrt{\eta_{03}+\eta_{02}+\eta_{01}}\right)} (1-2x_b) \tag{19}$$

Special cases
1. Setting $V_{01} = V_{11} = V_{21} = 0$ in Eq. (18), we obtain the energy equation for the Hulthén potential,

$$E_{nl} = -\frac{\delta_0^2 \hbar^2 l(l+1)}{2\mu} - \frac{\delta_0^2 \hbar^2}{8\mu} \left[\frac{(n+l+1)^2 + l(l+1) - \frac{2\mu V_{31}}{\delta_0^2 \hbar^2}}{(n+l+1)} \right]^2 . \tag{20}$$

Equation (20) is in agreement with Eq. (32) of [41] and Eq. (37) of [42].
2. Setting $V_{01} = V_{11} = V_{31} = 0$ in Eq. (18), we obtain the energy equation for the inversely quadratic potential

$$E_{nl} = V_{21}\delta_0^2 - \frac{\delta_0^2 \hbar^2 l(l+1)}{2\mu} - \frac{\delta_0^2 \hbar^2}{8\mu} \left[\frac{\left(n + \frac{1}{2} + \sqrt{\frac{1}{4} + l(l+1) - \frac{2\mu V_{21}}{\hbar^2}}\right)^2 - \frac{4\mu V_{21}}{\hbar^2} + l(l+1)}{n + \frac{1}{2} + \sqrt{\frac{1}{4} + l(l+1) - \frac{2\mu V_{21}}{\hbar^2}}} \right]^2 . \tag{21}$$

3. Setting $V_{01} = V_{11} = V_{21} = V_{31} = \delta_0 = 0$ in Eq. (18), we obtain the energy equation for Coulomb potential,

$$E_{nl} = \frac{Z^2 e^4 \mu}{2\hbar^2 (n+l+1)^2}, \tag{22}$$

where $V_{01} = Ze^2$ is the nuclear charge. Equation (22) agrees with Eq. (24) of [46].
4. Setting $V_{21} = V_{31} = 0$ in Eq. (18), we obtain the energy equation for IQHP,

$$E_{nl} = -V_{01}\delta_0 - \frac{\delta_0^2 \hbar^2 l(l+1)}{2\mu} - \frac{\delta_0^2 \hbar^2}{8\mu} \left[\frac{\left(n + \frac{1}{2} + \sqrt{\frac{1}{4} + l(l+1) + \frac{2\mu V_{11}}{\hbar^2}}\right)^2 - \frac{2\mu V_{01}}{\delta_0 \hbar^2} + \frac{2\mu V_{11}}{\hbar^2} + l(l+1)}{n + \frac{1}{2} + \sqrt{\frac{1}{4} + l(l+1) + \frac{2\mu V_{11}}{\hbar^2}}} \right]^2 . \tag{23}$$

Equation (23) agrees with Eq. (29) of [46].

3. Results and Discussion
We numerically computed the energy eigenvalues for the class of inversely quadratic Yukawa plus Hulthén potential in Table 1 through adjusting the principal quantum number at a fixed orbital angular momentum quantum number with the potential strength $(V_{01} = 1, V_{11} = -1, V_{21} = -1, V_{31} = 0.025, V_{01} = 2, V_{11} = -3, V_{21} = -3, V_{31} = 0.05)$ for $\delta_0 = 0.025$. For a fixed value of angular momentum quantum l, the energy spectrum increases as the principal quantum number n increases for this range of potential strength as the screening parameter is not varied.

Table 1. Energy bound states (eV) for the class of inversely quadratic Yukawa plus Hulthén potential with $\hbar = 2\mu = 1, \delta_0 = 0.025$

n	l	$V_{01} = 1, V_{11} = -1,$ $V_{21} = -1, V_{31} = 0.025$	$V_{01} = 2, V_{11} = -2,$ $V_{21} = -2, V_{31} = 0.05$	$V_{01} = 4, V_{11} = -4,$ $V_{21} = -4, V_{31} = 0.1$
0	0	-1.012851562	-4.000625000	-15.90140625
1		-0.2726660156	-1.038476562	-4.051406250
2		-0.1362890625	-0.4906250000	-1.857656250
3		-0.08937744140	-0.2996972656	-1.090664062
4		-0.06856406250	-0.2122250000	-0.7365562500

n	l	$V_{01}=1, V_{11}=-1,$ $V_{21}=-1, V_{31}=0.025$	$V_{01}=2, V_{11}=-2,$ $V_{21}=-2, V_{31}=0.05$	$V_{01}=4, V_{11}=-4,$ $V_{21}=-4, V_{31}=0.1$
0	1	-0.2622753906	-1.015664062	-4.003750000
1		-0.1327126736	-0.4815277778	-1.837517361
2		-0.08818603515	-0.2954003906	-1.080156250
3		-0.06847656250	-0.2101500000	-0.7305062500
4		-0.05872504340	-0.1647960070	-0.5415277778
0	2	-0.1259765625	-0.4637500000	-1.797656250
1		-0.08603759765	-0.2870410156	-1.059375000
2		-0.06845156250	-0.206150000	-0.7185562500
3		-0.05985351562	-0.1631640625	-0.5343750000
4		-0.05566406250	-0.1382397959	-0.4243144132
0	3	-0.08340087890	-0.2750878906	-1.028789062
1		-0.06878906250	-0.2005250000	-0.7010062500
2		-0.06180664062	-0.1609765625	-0.5239062500
3		-0.05859135842	-0.1381250000	-0.4181154336
4		-0.05752990723	-0.1243188476	-0.3504785156
0	4	-0.06993906250	-0.1937250000	-0.6783062500
1		-0.06489691840	-0.1585460070	-0.5104340278
2		-0.06285156250	-0.1383290816	-0.4102072704
3		-0.06254943848	-0.1262329102	-0.3461816406
4		-0.06339168596	-0.1189891975	-0.3033352624

In Table 2, we numerically show the energy eigenvalues of this potential at a fixed n by varying l for various screening parameters, $\delta_0 = 0.05, 0.075,$ and 0.1. As the screening parameter and angular momentum quantum l increases for a fixed value of principal quantum number n, the energy spectrum increases.

Table 2. Energy bound states (eV) for the class of inversely quadratic Yukawa plus Hulthén potential with $\hbar = \mu = 1$ $V_{01}=2, V_{11}=-3, V_{21}=-3, V_{31}=0.05$

n	l	$\delta_0 = 0.05$	$\delta_0 = 0.075$	$\delta_0 = 0.1$
0	0	-4.455000000	-3.541805556	-3.145000000
	1	-1.215078125	-1.058752170	-1.035312500
	2	-0.6187500000	-0.6122492285	-0.6722222222
	3	-0.4197070312	-0.4794536676	-0.5882031250
	4	-0.3398000000	-0.44627222222	-0.6002000000
1	0	-1.247578125	-1.0975021700	-1.0778125000
	1	-0.6426388889	-0.6354436729	-0.6900000000
	2	-0.4337695312	-0.4853130426	-0.5788281250
	3	-0.3450000000	-0.4359722222	-0.5650000000
	4	-0.3073003472	-0.4341148245	-0.6028125000
2	0	-0.6550000000	-0.6479783951	-0.7005555555
	1	-0.4439257812	-0.4909771051	-0.5757031250
	2	-0.3499500000	-0.4306097222	-0.5428000000
	3	-0.3063281250	-0.4166495467	-0.5600347222
	4	-0.2896938776	-0.4312613379	-0.6123469388
3	0	-0.4492382812	-0.4943364801	-0.5750781250
	1	-0.3537500000	-0.4281597222	-0.5300000000
	2	-0.3063281250	-0.4051912134	-0.5308680556
	3	-0.2850000000	-0.4094756236	-0.5650000000
	4	-0.2803173828	-0.4340235731	-0.6267382812
4	0	-0.3558000000	-0.4272722222	-0.5242000000
	1	-0.3066753472	-0.3983335745	-0.5128125000
	2	-0.2820153061	-0.3943416950	-0.5316326531
	3	-0.2732080078	-0.4094337294	-0.5764257812
	4	-0.2759876543	-0.4406395748	-0.6450000000

In Table 3, we numerically present energy eigenvalues of Hulthén potential at 2p, 3p, 3d, 4p. As the screening parameter increases, the energy eigenvalues increase with increase in the quantum numbers. We compared our result for the Hulthén potential with the results from three other methods.

Using the energy equation found in Eq. (18), we quantitatively presented the eigenvalues for four diatomic molecules in Tables 4. The model parameters for each molecule listed in Table 4 were entered to do this. These diatomic molecules were chosen due to their significance in chemical physics and chemistry. In addition, we have also used the following

transformations: $1\ amu = 931.494028\ \text{MeV}/c^2$ and $\hbar c = 1973.29\ \text{eV Å}$ [47-49]. The results show that the bound state energy spectra of these diatomic molecules increase as various quantum numbers n and l increases. Our newly developed potential models reduce to special cases by applying certain boundary conditions to validate the mathematical accuracy of our analytical calculations.

Table 3. Energy bound states (eV) of the Hulthén potential as a function of the screening parameters δ_0 for 2p, 3p, 3d, and 4p states and for $Z = 1$ in atomic units $(\hbar = \mu = e = 1)$.

State	δ_0	Present (NU)	AIM [43]	EQR [44]	SUSY [45]
2p	0.025	-0.1128125000	-0.1128125	-0.1128125	-0.1127605
	0.050	-0.1012500000	-0.1012500	-0.1012500	-0.1010425
	0.075	-0.09031249994	-0.0903125	-0.0903125	-0.0898478
	0.10	-0.08000000000	-0.0800000	-0.0800000	-0.0791794
	0.15	-0.06124999998	-0.0612500	-0.0612500	-0.0594415
3p	0.025	-0.04070312500	-0.0437590	-0.0437590	-0.0437068
	0.050	-0.03336810000	-0.0333681	-0.0333681	-0.0331632
	0.075	-0.02438370000	-0.0243837	-0.0243837	-0.0239331
	0.10	-0.01680560000	-0.0168056	-0.0168056	-0.0160326
	0.15	-0.00586810000	-0.0058681	-0.0058681	-0.0043599
3d	0.025	-0.04360440000	-0.0437587	-0.0437587	-0.0436030
	0.050	-0.03275080000	-0.0333681	-0.0333681	-0.0327532
	0.075	-0.02299480000	-0.0243837	-0.0243837	-0.0230306
	0.10	-0.01433640000	-0.0162600	-0.0162600	-0.0144832
	0.15	-0.00031240000	-0.0058681	-0.0058681	-0.0132820
4p	0.025	-0.01994860000	-0.0200000	-0.0200000	-0.0199480
	0.050	-0.01104420000	-0.0112500	-0.0112500	-0.0110430
	0.075	-0.00453700000	-0.0050000	-0.0050000	-0.0045385
	0.10	-0.00042690000	-0.0012500	-0.0012500	-0.0004434

Table 4. Spectroscopic parameters of the diatomic molecules used in this work [50,51]

Molecule	$\delta_0 = \left(\text{Å}\right)^{-1}$	$\mu\,(amu)$	$\mu\,(eV)$
N_2	2.69860	7.0033500000	0.6523578701
O_2	1.295515	7.9974575040	0.74495839042
NO	2.75340	7.4684410000	0.69568081900
CO	2.29940	6.8605860000	0.63905948876

Table 5. Energy spectra $(in\ eV)$ of class of inversely quadratic Yukawa plus Hulthén potential $(V_{01} = 1,\ V_{11} = V_{21} = -1, V_{31} = 0.025$) for N_2, O_2, NO and CO diatomic molecules

n	l	N_2	O_2	NO	CO
0	0	-102.7119268	-23.19497264	-126.7384336	-20.57424584
	1	-30.30849598	-9.453142109	-36.45622154	-8.798919265
	2	-16.95021661	-6.930212578	-19.79018435	-6.641819365
	3	-12.30628452	-6.063890161	-13.98924338	-5.905643942
	4	-10.18475382	-5.679164767	-11.33218294	-5.583549884
	5	-9.059727937	-5.486789797	-9.915958908	-5.427786332
1	0	-30.07202715	-9.368846178	-36.19627464	-8.713879144
	1	-16.73132841	-6.849755612	-19.55063368	-6.559784975
	2	-12.11100219	-5.989268264	-13.77677931	-5.828574813
	3	-10.00628951	-5.607970361	-11.13933831	-5.509021515
	4	-8.892132746	-5.416928527	-9.736182578	-5.353695279
	5	-8.247963204	-5.317833657	-8.917746069	-5.278508861
2	0	-16.62260878	-6.809987732	-36.19627464	-6.519304712
	1	-11.98217237	-5.940383964	-19.55063368	-5.778202139
	2	-9.874266958	-5.555735276	-13.77677931	-5.454478305
	3	-8.760230009	-5.362421323	-11.13933831	-5.296033229
	4	-8.116182734	-5.261007963	-9.736182578	-5.217664321
	5	-7.724662434	-5.210441659	-8.917746069	-5.184264747
3	0	-11.91816497	-5.916200905	-13.56670214	-5.753317826
	1	-9.787121287	-5.521464611	-10.90210156	-5.418760482
	2	-8.662570784	-5.322346977	-9.489446311	-5.253726320

n	l	N_2	O_2	NO	CO
	3	-8.012355153	-5.216562617	-8.666361658	-5.170172128
	4	-7.616127092	-5.162076555	-8.158300703	-5.132017704
	5	-7.369538341	-5.139134138	-7.835113863	-5.122355833
4	0	-9.743809264	-5.504495097	-10.85516342	-5.401094865
	1	-8.598068359	-5.296014583	-9.420011074	-5.225969157
	2	-7.935415930	-5.183820812	-8.584125641	-5.135243324
	3	-7.530521367	-5.124161742	-8.067455968	-5.091126140
	4	-7.276939786	-5.096569587	-7.737532584	-5.076003205
	5	-7.119236710	-5.090491185	-7.525275330	-5.080827207

4. CONCLUSION

The Greene-Aldrich approximation scheme has been used to study the bound state solutions to the Schrödinger equation with the newly proposed potential of a class of inversely quadratic Yukawa plus Hulthén potential model. Using the NU technique, the eigenvalues and normalized eigenfunctions are determined. After that, we impute the experimental values for each molecular parameter and apply the solution for four diatomic molecules. The findings demonstrate that these diatomic molecules' bound state energy spectrum increases as various quantum numbers increase. These findings can be applied in Molecular and Chemical Physics.

ORCID
Fina O. Faithpraise, https://orcid.org/0000-0001-8222-2034; **Etido P. Inyang**, https://orcid.org/0000-0002-5031-3297

REFERENCES
[1] E.P. Inyang, E.O. Obisung, J. Amajama, E.S William, and I.B. Okon, "The Effect of Topological Defect on the Mass Spectra of Heavy and Heavy-Light Quarkonia," Eurasian Physical Technical Journal, **19**(4), 78-87 (2022). https://doi.org/10.31489/2022No4/78-87

[2] E.S. William, E.P. Inyang, I.O. Akpan, J.A. Obu, A.N. Nwachukwu, and E.P. Inyang, "Ro-vibrational energies and expectation values of selected diatomic molecules via Varshni plus modified Kratzer potential model," Indian Journal of Physics, **96**, 34613476 (2022). https://doi.org/10.1007/s12648-022-02308-0

[3] E.P. Inyang, E.P. Inyang, I.O. Akpan, J.E. Ntibi, and E.S. William, Masses and thermodynamic properties of a Quarkonium system. Canadian Journal of Physics. 99(11), 982-990 (2021). https://doi.org/10.1139/cjp-2020-0578

[4] I.B. Okon, C.A. Onate, R. Horchani, O.O. Popoola, E. Omugbe, E.S. William, U.S. Okorie, *et al.*, "Thermomagnetic properties and its effects on Fisher entropy with Schioberg plus Manning-Rosen potential (SPMRP) using Nikiforov-Uvarov functional analysis (NUFA) and supersymmetric quantum mechanics (SUSYQM) methods," Scientifc Reports, 13, 8193 (2023). https://doi.org/10.1038/s41598-023-34521-0

[5] F. Ayedun, E.P. Inyang, E.A. Ibanga, and K.M. Lawal, "Analytical Solutions to The Schrödinger Equation with Collective Potential Models: Application to Quantum Information Theory," East Eur. J. Phys. **4**, 87-98 (2022). https://doi.org/10.26565/2312-4334-2022-4-06

[6] E.S. William, S.C. Onye, A.N. Ikot, A.N. Nwachukwu, E.P. Inyang, I.B. Okon, I.O. Akpan and B. I. Ita, "Magnetic susceptibility and Magnetocaloric effect of Frost-Musulin potential subjected to Magnetic and Aharonov-Bohm(Flux)for CO and NO diatomic molecules", Journal of Theoretical and Applied Physics, **17**, 1-12 (2023). https://doi.org/10.30495/JTAP.172318

[7] C. Berkdermir, A. Berkdemir, and R. Sever, "Polynomial solutions of the Schrodinger equation for the generalized Woods-Saxon potential," Phys. Rev. C, **72**, 027001 (2008). http://dx.doi.org/10.1103/PhysRevC.72.027001

[8] M. Abu-Shady, and E.P. Inyang, "The Fractional Schrödinger Equation with The Generalized Woods-Saxon Potential," East European Journal of Physics, **1**. 63-68 (2023). https://doi.org/10.26565/2312-4334-2023-1-06

[9] S.M. Ikhdair, "The bound state solutions of the Manning-Rosen potential including an improved approximation to the orbital centrifugal term," Phys. Scr. **83**, 015010 (2011). https://doi.org/10.1088/0031-8949/83/01/015010

[10] J. Lu, "Approximate spin and pseudospin solutions of the Dirac equation," Physica Scripta, **72**, 349 (2005). https://doi.org/10.1238/Physica.Regular.072a00349

[11] R.L. Greene, and C. Aldrich, "Variational wave functions for a screened Coulomb potential," Phys. Rev. A, **14**, 2363 (1976). https://doi.org/10.1103/PhysRevA.14.2363

[12] C.S. Jia, T. Chen, and L.G. Cui, "Approximate analytical solutions of the Dirac equation with the generalized Pöschl-Teller potential including the pseudo-centrifugal term," Phys. Lett. A, **373**, 1621-1626 (2009). https://doi.org/10.1016/j.physleta.2009.03.006

[13] E.L. Hill, "The Theory of Vector Spherical Harmonics," Am. J. Phys. **22**, 211-214 (1954). https://doi.org/10.1119/1.1933682

[14] C.L. Pekeris, "The Rotation-Vibration Coupling in Diatomic Molecules," Phys. Rev. **45**, 98 (1934). https://doi.org/10.1103/PhysRev.45.98

[15] B.H. Yazarloo, H. Hassanabadi, and S. Zarrinkamar, "Oscillator strengths based on the Mobius square potential under Schrodinger equation," Eur. Phys. J. Plus, **127**, 51 (2012). https://doi.org/10.1140/epjp/i2012-12051-9

[16] S.H. Dong, W.C. Qiang, G.H. Sun, and V.B. Bezerra, "Analytical approximations to the *l*-wave solutions of the Schrödinger equation with the Eckart potential," J. Phys. A, **40**, 10535 (2007). https://doi.org/10.1088/1751-8113/40/34/010

[17] S.K. Nikiforov, and V.B. Uvarov, *Special functions of Mathematical Physics*, (Birkhauser, Basel, 1988).

[18] E.S. William, E.P. Inyang, and E.A. Thompson, "Arbitrary ℓ -solutions of the Schrödinger equation interacting with Hulthén-Hellmann potential model," Rev. Mex. Fis. **66**, 730 (2020). https://doi.org/10.31349/RevMexFis.66.730

[19] I.O. Akpan, E.P. Inyang, E.P. Inyang, and E.S. William, "Approximate solutions of the Schrödinger equation with Hulthen-Hellmann Potentials for a Quarkonium system," Rev. Mex. Fis. **67**, 482-490 (2021). https://doi.org/10.31349/revmexfis.67.482

[20] E.P. Inyang, E.O. Obisung, E.S. William, and I.B. Okon, "Non-Relativistic study of mass spectra and thermal properties of a quarkonium system with Eckart-Hellmann potential," East European Journal of Physics, **3**, 104-114 (2022). https://doi.org/10.26565/2312-4334-2022-3-14

[21] E.P. Inyang, F.O. Faithpraise, J. Amajama, E.S. William, E.O. Obisung, and J.E. Ntibi, "Theoretical Investigation of Meson Spectrum using Exact Quantization Rule Technique," East European Journal of Physics, **1**, 53-62 (2023). https://doi.org/10.26565/2312-4334-2023-1-05

[22] A.N. Ikot, U.S. Okorie, P.O. Amadi, C.O. Edet, G.J. Rampho, and R. Sever, "The Nikiforov-Uvarov Functional Analysis (NUFA) Method: A new approach for solving exponential-Type potentials," Few-Body System, **62**, 9 (2021). https://doi.org/10.1007/s00601-021-021-01593-5

[23] C.O. Edet, S. Mahmoud, E.P. Inyang, N. Ali, S.A. Aljunid, R. Endut, A.N. Ikot, and M. Asjad, "Non-Relativistic Treatment of the 2D Electron System Interacting via Varshni-Shukla Potential Using the Asymptoptic Iteration Method," Mathematics, **10**, 2824 (2022). https://doi.org/10.3390/math10152824

[24] A.N. Ikot, L.F. Obagboye, U.S. Okorie, E.P. Inyang, P.O. Amadi, and A. Abdel-Aty, Solutions of Schrodinger equation with generalized Cornell potential (GCP) and its applications to diatomic molecular systems in D-dimensions using Extended Nikiforov–Uvarov (ENU) formalism," The European Physical Journal Plus, 137, 1370 (2022). https://doi.org/10.1140/epjp/s13360-022-03590-x

[25] E.O. Omugbe, E. Osafile, E.P. Inyang, and A. Jahanshir, "Bound state solutions of the hyper-radial Klein-Gordon equation under the Deng-Fan potential by WKB and SWKB methods," Physica Scripta, **96**, 125408 (2021). https://doi.org/10.1088/1402-4896/ac38d4

[26] E.S. William, E.P. Inyang, J.E. Ntibi, J.A. Obu, and E.P. Inyang, "Solutions of the Non-relativistic Equation Interacting with the Varshni-Hellmann potential model with some selected Diatomic molecules," Jordan Journal of Physics, **15**, 179-193 (2022). https://doi.org/10.47011/15.2.8

[27] M. Abu-Shady, and E.P. Inyang, "Heavy-Light Meson masses in the Framework of Trigonometric Rosen-Morse Potential using the Generalized Fractional Derivative," East Eur. J. Phys. **4**, 80-87 (2022). https://doi.org/10.26565/2312-4334-2022-4-06

[28] B.I. Ita, "Solutions of the Schrödinger equation with inversely quadratic Hellmann plus Mie-type potential using Nikiforov-Uvarov method," International Journal of Recent Advances in Physics. **2**(4), 25 (2013). https://wireilla.com/physics/ijrap/papers/2413ijrap02.pdf

[29] B.I. Ita, and A.I. Ikeuba, "Solutions to the Schrödinger Equation with Inversely Quadratic Yukawa Plus Inversely Quadratic Hellmann Potential Using Nikiforov-Uvarov Method," Phys. Journal of Atomic and Molecular Physics, 582610 (2013). https://doi.org/10.1155/2013/582610

[30] E.P. Inyang, E.S. William, J.O. Obu, B.I. Ita, E.P. Inyang, and I.O. Akpan, "Energy spectra and expectation values of selected diatomic molecules through the solutions of Klein-Gordon equation with Eckart-Hellmann potential model," Molecular Physics, **119**(23), e1956615 (2021). https://doi.org/10.1080/00268976.2021.1956615

[31] B.I. Ita, C.O. Ehi-Eromosele, A. Edobor-Osoh, and A.I. Ikeuba, "Solutions of the Schrödinger equation with inversely quadratic Hellmann plus inversely quadratic potential using Nikiforov-Uvarov method," AIP Conf. Proc. **1629**, 360 (2014). https://doi.org/10.1063/1.4902294

[32] K.J. Oyewumi, and E.A. Bangudu, "Isotropic harmonic oscillator plus inverse quadratic potential in N-dimensional spaces," Arab. J. Sci. Eng. **28**, 173-182 (2003).

[33] R.H. Parmar, K.R. Purohit, and A.K. Rai, "Approximaate analytical solution of the extended Hulthen-Yukawa with inverse square and Coulombic term plus ring shape potential," AIP Conf. Proc. **2220**, 140071 (2020). https://doi.org/10.1063/5.0001432

[34] B.I. Ita, N. Nzeata-Ibe, T.O. Magu, and L. Hitler, "Bound-State Solutions of the Schrödinger Equation with Woods–Saxon Plus Attractive Inversely Quadratic Potential via Parametric Nikiforov-Uvarov Method," Manila Journal of Science, **11**, 58-67 (2018). https://www.dlsu.edu.ph/wp-content/uploads/pdf/research/journals/mjs/MJS11-2018/volume-1/MJS11-6-Ita-et-al.pdf

[35] A. Maireche, "New Exact Non-Relativistic Energy Eigen Values for Modified Inversely Quadratic Hellmann Plus Inversely Quadratic Potential," J. Nanosci. Curr. Res. **2**, 1000115 (2017). https://doi.org/10.4172/2572-0813.1000115

[36] L. Hulthen, "Über die eigenlosunger der Schrödinger-Gleichung des deuterons," Ark. Mat. Astron. Fys. A, **28**, 5 (1942).

[37] E.P. Inyang, E.S. William, E. Omugbe, and F. Ayedun, "The study of H_2 and N_2 Diatomic Molecules in Arbitrary Dimensions with Collective Potential Model," Bulgarian Journal of Physics, **50**, 1-15 (2023). https://www.bjp-bg.com/papers/bjp1578.pdf

[38] I.B. Okon, O. Popoola, and E.E. Ituen, "Bound state solution to Schrödinger equation with Hulthen plus exponential Coulombic potential with centrifugal potential barrier using parametric Nikiforov Uvarov method," Intl. J. Rec. adv. Phys. **5**, 5101 (2016). https://doi.org/10.14810/ijrap.2016.5101

[39] E.P. Inyang, J. Ntibi, E.A. Ibanga, F. Ayedun, E.P. Inyang, and E.S. William, "Thermal Properties, Mass Spectra and Root Mean Square Radii of Heavy Quarkonium System with Class of Inversely Quadratic Yukawa Potential," AIP Conference Proceedings 2679, 030003 (2023). https://doi.org/10.1063/5.0112829

[40] E.S. William, I.B. Okon, O.O. Ekerenam, I.O. Akpan, B.I. Ita, E.P. Inyang, I.P. Etim, and I.F. Umoh, "Analyzing the effects of magnetic and Aharonov-Bohm (AB) flux fields on the energy spectra and thermal properties of N_2, NO, CO, and H_2 diatomic molecules," International Journal of Quantum Chemistry, (2022). https://doi.org/10.1002/qua.26925

[41] O. Bayrak, G. Kocak, and I. Boztosun, "Any l-state solutions of the Hulth´en potential by the asymptotic iteration method, J. Phys. A, **39**, 11521 (2006). https://doi.org/10.1088/0305-4470/39/37/012

[42] I.B. Okon, and O. Popoola, "Bound-State solution of Schrodinger equation with Hulthen plus generalized exponential Coulomb potential using Nikiforov-Uvarov method," Intl. J. Rec. Adv. Phys. **4**(3), 1-12 (2015). https://doi.org/10.14810/ijrap.2015.4301

[43] K.J. Oyewumi, and O.J. Oluwadare, "The scattering phase shifts of the Hulthen-type potential plus Yukawa potential," Eur. Phys. J. Plus, **131**, 295 (2016). https://doi.org/10.1140/epjp/i2016-16295-y

[44] W.C. Qiang, Y. Gao, and R. Zhou, "Arbitrary *l*-state approximate solutions of the Hulthen potential through the exact quantization rule," Cen. Eur. Phys. J. Phys. **6**, 356 (2008). https://doi.org/10.2478/s11534-008-0041-1

[45] S.M. Ikhdair, "An improved approximation scheme for the centrifugal term and the Hulth´en potential, The Eur. Phys. J. A, **39**, 307 (2009). https://doi.org/10.1140/epja/i2008-10715-2

[46] L. Hitler, B.I. Ita, P.A. Isa, N. Nzeata-Ibe, I. Joseph, O. Ivan, and T.O. Magu, "Wkb Solutions for Inversely Quadratic Yukawa plus Inversely Quadratic Hellmann Potential," World Journal of Applied Physics, **2**, 4 (2017). https://article.sciencepublishinggroup.com/pdf/10.11648.j.wjap.20170204.13.pdf

[47] E.P. Inyang, E.S. William, J.E. Ntibi, J.A. Obu, P.C. Iwuji, and E.P. Inyang, "Approximate solutions of the Schrödinger equation with Hulthén plus screened Kratzer Potential using the Nikiforov-Uvarov – functional analysis (NUFA) method: an application to diatomic molecules," Can. J. Phys. **100**(10), 473 (2022). https://doi.org/10.1139/cjp-2022-003

[48] E.P. Inyang, I.B. Okon, F.O. Faithpraise, E.S. William, P.O. Okoi, and E.A. Ibanga, "Quantum mechanical treatment of Shannon entropy measure and energy spectra of selected diatomic molecules with the modified Kratzer plus generalized inverse quadratic Yukawa potential model," Journal of Theoretical and Applied Physics, **17**(4), (2023). https://doi.org/10.57647/J.JTAP.2023.1704.40

[49] E.P. Inyang, F. Ayedun, E.A. Ibanga, K.M. Lawal, I.B. Okon, E.S. William, O. Ekwevugbe, *et al*., "Analytical Solutions of the N-Dimensional Schrödinger equation with modified screened Kratzer plus Inversely Quadratic Yukawa potential and Thermodynamic Properties of selected Diatomic Molecules," Results in Physics, **43**, 106075 (2022). https://doi.org/10.1016/j.rinp.2022.106075

[50] E.P. Inyang, E.S. William, J.E. Ntibi, J.A. Obu, P.C. Iwuji, and E.P. Inyang, "Approximate solutions of the Schrodinger equation with Hulthen plus screened Kratzer potential using the Nikiforov-Uvarov-Functional analysis method: An Application to diatomic molecules," Canadian Journal of Physics, **100**(10), 463-473 (2022). https://doi.org/10.1139/cjp-2022-0030

[51] K.J. Oyewumi, and K.D. Sen, "Exact solutions of the Schrödinger equation for the pseudoharmonic potential: an application to some diatomic molecules," J. Math. Chem. **50**, 1039-1059 (2012). https://doi.org/10.1007/s10910-011-9967-4

ВЛАСНІ ЗНАЧЕННЯ ЗВ'ЯЗАНОГО СТАНУ ТА КОЛИВАЛЬНОЇ ЕНЕРГІЇ ВИБРАНИХ ДВОХАТОМНИХ МОЛЕКУЛ З КЛАСОМ ОБЕРНЕНО КВАДРАТИЧНОЇ МОДЕЛІ ЮКАВИ ПЛЮС ПОТЕНЦІАЛ ХУЛЬТХЕНА

Фіна О. Фейтпрайз[a], Етідо П. Іньянг[b]
[a]Кафедра фізики, Університет Калабара, РМВ 1115, Калабар, Нігерія
[b]Кафедра фізики, Національний відкритий університет Нігерії, Джабі, Абуджа, Нігерія

В цьому дослідженні для розв'язання рівняння Шредінгера використовується підхід Нікіфорова-Уварова з використанням класу оберено квадратичної моделі Юкави плюс потенціалу Хультена з наближенням до відцентрового члена. Отримано нормовану хвильову функцію та рівняння власних значень енергії. Чисельний зв'язаний стан для кількох двоатомних молекул (N₂, O₂, NO та CO) для різних обертальних і вібраційних квантових чисел було розраховано за допомогою енергетичного рівняння та відповідних спектроскопічних даних. Наші результати показують, що за відсутності розбіжності між s-хвилею та *l*-хвилею власні значення енергії дуже чутливі до потенціалу та властивостей двоатомної молекули, що свідчить про те, що підхід наближення підходить для цього набору потенціалів. Результати узгоджуються з попередніми дослідженнями в літературі, і ми також знайшли чотири особливі випадки цього потенціалу.
Ключові слова: *рівняння Шредінгера; метод Нікіфорова-Уварова; клас оберено квадратичного плюс потенціал Хюльтена; двохатомні молекули; зв'язаний стан*

DEFORMATION OF ODD NUCLEI ^{27}Al, ^{31}P AND ^{35}Cl IN SINGLE-PARTICLE STATES[†]

Volodymyr Yu. Korda[a,*], Larisa P. Korda[b], Vyacheslav F. Klepikov[a], Iryna S. Timchenko[b]

[a]Institute of Electrophysics and Radiation Technologies, National Academy of Sciences, Kharkiv 61002, Ukraine
[b]National Science Center "Kharkiv Institute of Physics and Technology", National Academy of Sciences, Kharkiv 61108, Ukraine
*Corresponding Author e-mail: kvyu@kipt.kharkov.ua
Received May 18, 2023; revised June 5, 2023 accepted June 6, 2023

Using the evolutionary approach recently developed by us, the shapes of odd s-d-shell ^{27}Al, ^{31}P and ^{35}Cl nuclei in the ground and single-particle excited states have been extracted from the experimental data on the energies, spins, and parities of these states, as well as the measured probabilities of electromagnetic transitions between them. The key ingredient of our procedure is the evolutionary algorithm that evolves the population of the bad-quality data-fitting nuclear shapes to the high-quality data-fitting nuclear shapes. We have found that the studied nuclei in the ground states are abnormally weakly deformed, which is not expected for the nuclei in the shell middle. Even in their low-laying single-particle excited states, the nuclei ^{27}Al and ^{31}P are found to be weakly deformed, too. With the increase of the single-particle excitation energy, the change of the state of the only one nucleon – the valence proton the spin and parity of which determine the spin and parity of the ^{35}Cl nucleus – causes the shape phase transition from the high-symmetry phase – spherical ground state – to the low-symmetry phase – deformed excited states. The angular part of the ^{27}Al and ^{31}P nuclei shape is described by two harmonics – quadrupole and hexadecapole. The angular part of the ^{35}Cl nucleus shape is described by three harmonics – quadrupole, hexadecapole, and hexacontatetrapole, but the contribution of hexadecapole deformation is not independent. At present, there are no fundamental nuclear models that account for or predict the dominant hexacontatetrapole deformation, especially for light and medium nuclei. We have found that the spin and parity of the ^{27}Al, ^{31}P and ^{35}Cl nuclei are determined by the spin and parity of the last odd (valence) proton. At the same time, some of the nucleons of the nucleus core change their characteristics, too. Thus, the electromagnetic transitions between the single-particle states of the ^{27}Al, ^{31}P and ^{35}Cl nuclei are the multi-particle processes.
Keywords: *Nuclear deformation; Deformed shell model; Single-particle state; s-d-shell nuclei; Evolutionary algorithm; Shape phase transition*
PACS: 21.60.−n, 21.60.Cs, 21.60.Ev, 27.30.+t

1. INTRODUCTION

Complex, multi-particle nature of nuclear forces makes nuclear physics a largely eclectic science: to understand different observable properties of nuclei, it is often necessary to use different concepts from different areas of physics (see, e.g., Refs. [1,2] or any textbook on nuclear physics). And any new idea is always welcome.

So, to understand the origin of nuclear deformation, the concept of phase transitions and the Landau theory of phase transitions, proposed and well developed for condensed matter physics [3], turned out to be useful (see, e.g., review [4] and references therein). Indeed, the very fact of the appearance of a deformation of the nucleus shape caused by a change in, say, the number of nucleons in the nucleus can be considered as a result of phase transition from a high-symmetry (spherical) phase to a low-symmetry (deformed) phase of a nucleus. Thus, spontaneous breaking of rotational symmetry of a spherical nucleus can be accepted as an origin of nuclear deformation. The Landau theory of phase transitions is well suited for describing such shape phase transitions in a phenomenological language.

Currently known applications of the Landau theory to shape phase transitions suggest that the potential energy of the nucleus (in the form of thermodynamic potentials, Helmholtz free energy, Gibbs free energy, etc.) has the form of a polynomial from rotationally invariant combinations of quadrupole deformation parameters introduced by Bohr and Mottelson [5]. Such a polynomial is either the by-product of microscopic or semi-microscopic calculations (as, e.g., in the interacting boson and boson-fermion models), or is parameterized directly (as, e.g., in geometric collective models) [4]. The coefficients of the polynomial depend on the control parameter associated with the number of nucleons in the nucleus. Equilibrium deformation parameters minimize potential energy. A change in the control parameter leads to a transition from a spherical phase, for which the equilibrium deformation parameters are zero, to deformed phases, for which the equilibrium deformation parameters differ from zero. Following this recipe, interesting data were described and phase transitions of the first and second order were identified (see, e.g., reviews [6–8] and references therein).

Presently, the dynamics of nuclear shape caused by a change in the number of nucleons in the nucleus is mainly studied (see, e.g., [4,9,10]). However, the same nucleus in different single-particle states can have different shapes too and, in principle, the shape phase transition can be caused not only by changing the number of nucleons in the nucleus, but also by changing the states of nucleons in the nucleus. Regardless of the method of calculation, the shape of the nucleus in the single-particle state strongly influences its wave function. The wave functions of the initial and final states of the nucleus largely determine the probability of electromagnetic transition between them. Therefore, the experimentally observed probabilities of electromagnetic transitions are a valuable source of information about the shape of the nucleus in various single-particle states.

The generalized nucleus model (in the form of Nilsson model [5,11]) allows, in principle, to calculate the equilibrium deformation of the nucleus in any single-particle state. In fact, Nilsson model with spin-orbit coupling describes the sequence of shape phase transitions because it predicts spherically symmetric equilibrium shape of the equipotential surface of a nucleus if all states with the shell number N and the total momentum I are occupied. However, the probabilities of electromagnetic transitions can only be calculated between single-particle states with the same deformation. In a number of works [12–18], the modification of Nilsson model was proposed, in which the deformation of the nucleus was considered as a dynamic parameter. That is, the initial and final states are assumed to have different deformations. Thus, during the transition, the states of all nucleons can change.

The modified Nilsson model enabled to calculate the probabilities of electromagnetic transitions between single-particle states, taking into account their different deformations [12–18]. The assumption of the dynamic nature of the deformation of single-particle states of odd s-d-shell nuclei significantly reduced the discrepancy between the measured and calculated probabilities of some $E2$-transitions. However, it appeared impossible to adequately describe the entire set of experimental data, including energies, spins and parities of the ground and single-particle excited states, as well as the probabilities of both E- and M-transitions between them.

That is why it would be highly desirable to have a procedure that could extract the angular dependence (deformation) of the potential of the self-consistent field of the nucleus in the ground and single-particle excited states directly from the experimental data on the energies, spins, and parities of the states of nuclei, as well as the measured probabilities of electromagnetic transitions between these states [19]. The goal that this procedure could be aimed at is the study of the shape of odd s-d-shell nuclei, both in the ground and low-laying single-particle excited states and the search for possible phase transitions from spherical to deformed states of the nucleus.

2. DEFORMED-SHELL-MODEL SINGLE-PARTICLE HAMILTONIAN

We restrict ourselves to the case of an axially symmetric nucleus with an additional symmetry plane perpendicular to the symmetry axis. We chose a single-particle harmonic-oscillator potential with the spin-orbit interaction (see, e.g., Refs. [5,11]). Making a direct generalization, we write the single-particle Hamiltonian in the form:

$$H = \hbar\omega(H_0 + H_1), \ H_0 = \left(-\Delta + r^2\right)/2, \ H_1 = -r^2\varphi(\theta)/2 - 2\kappa(\mathbf{l}\cdot\mathbf{s})[1 - \varphi(\theta)], \tag{1}$$

where r is the reduced coordinate; $1/\sqrt{1-\varphi(\theta)}$ is the reduced radius of the equipotential surface of the nuclear potential; θ is the polar angle, $\theta \in [0; \pi/2]$; $\varphi(\theta)$ is the function that describes the shape of the equipotential surface, $\varphi(\pi - \theta) \equiv \varphi(\theta)$, $d\varphi/d\theta \equiv 0$ at the points $\theta = 0$ and $\theta = \pi/2$; $r^2\varphi(\theta)$ is the coupling of the particle with the symmetry axis; $(\mathbf{l}\cdot\mathbf{s})$ is the spin-orbit interaction; $(\mathbf{l}\cdot\mathbf{s})\varphi(\theta)$ is the coupling of the spin-orbit interaction with the symmetry axis; $\hbar\omega = 41A^{-1/3}(1+\varepsilon)$ MeV is the energy scale; $A = N + Z$ is the nucleus mass number; N and Z are the numbers of neutrons and protons in the nucleus; ε takes into account the deviation of the energy scale from its simple estimate. We do not expect the nucleus volume to conserve because we are aimed at extracting the nucleus shape (including its radius) directly from the available data.

In our approach, by definition, the function $\varphi(\theta)$ contains all information on the nuclear shape. Initially, no deformation parameters are needed to determine it. The function $\varphi(\theta)$ directly and explicitly enters in the total Hamiltonian H (1) (generally, as a numerical array). Using as a basis the eigenfunctions of the spherical harmonic oscillator Hamiltonian H_0 from Eq. (1), the matrix of the total Hamiltonian H is numerically diagonalized (see Ref. [11] for details). As a result, the eigenfunctions of the Hamiltonian H appear as a finite mixture of the eigenfunctions of the Hamiltonian H_0. The coefficients of the mixture are calculated numerically and, in this way, contain information on the nuclear shape. The single-particle wave function of the nucleus in a certain state is the Slater determinant constructed from the occupied single-particle states calculated using the Hamiltonian H (1). We emphasize that this wave function directly and explicitly depends on the mixture coefficients but not on any deformation parameters.

3. PROBABILITIES OF ELECTROMAGNETIC TRANSITIONS BETWEEN SINGLE-PARTICLE STATES WITH DIFFERENT DEFORMATIONS

To determine the matrix element of the single-particle multipole operator

$$\mathsf{M} = \sum_{s=1}^{A} \hat{t}_s, \tag{2}$$

we consider two sets of occupied single-particle states

$$\begin{aligned} \{u_j\}, j = 1,...,N, N+1,...,N+Z \\ \{v_i\}, i = 1,...,N, N+1,...,N+Z \end{aligned} \tag{3}$$

calculated using the Hamiltonian (1) with two different functions $\varphi(\theta)$, which form two Slater determinants $\Psi\{u_j\}$ and $\Psi'\{v_i\}$. The matrix element of M, taken between $\Psi\{u_j\}$ and $\Psi'\{v_i\}$, is equal to (see, e.g., [20])

$$(\Psi', \mathrm{M}\Psi) = \sum_{s=1}^{A} \left| \mathbf{M}^s \right|,$$ (4)

where the elements of determinants $\left| \mathbf{M}^s \right|$ are as follows

$$\mathbf{M}_{ij}^s = \begin{cases} \left(v_i, \hat{t}_s u_j \right), & i = s, \\ \left(v_i, \quad u_j \right), & i \neq s. \end{cases}$$ (5)

The reduced electric and magnetic multipole transition probabilities between the initial and final states with IK and $I'K'$, where I and K are the total momentum and its projection take the form ($\lambda < K + K'$) [12–14]:

$$B(E\lambda; IK \to I'K') = e^2 \left[1 + (-1)^\lambda \frac{Z}{A^\lambda} \right] \left(\frac{\hbar}{m\omega} \right)^\lambda \frac{2\lambda + 1}{4\pi} \left| \langle I\lambda KK' - K \mid I'K' \rangle \right|^2 \left| \mathbf{N} \right| \left| \sum_{s=N+1}^{N+Z} \left| \mathbf{z}_E^s \right| \right|^2$$ (6)

$$B(M\lambda; IK \to I'K') = \left(\frac{e\hbar}{2mc} \right)^2 \left(\frac{\hbar}{m\omega} \right)^{\lambda-1} \frac{2\lambda + 1}{16\pi} \left| \langle I\lambda KK' - K \mid I'K' \rangle \right|^2 \left| |\mathbf{z}| \sum_{s=1}^{N} \left| \mathbf{N}^s \right| + |\mathbf{N}| \sum_{s=N+1}^{N+Z} \left| \mathbf{z}_M^s \right| \right|^2$$ (7)

$$\mathbf{N}_{ij} = \left(v_i, u_j \right) = \delta_{N_i N_j} \sum_{l\Lambda} a_{l\Lambda}^i a_{l\Lambda}^j, \mathbf{N}_{ij}^s = \begin{cases} G_{M\lambda}^{ij}, & i = s, \\ \mathbf{N}_{ij}, & i \neq s. \end{cases}, i, j = 1, \ldots,$$ (8)

$$\mathbf{Z}_{ij} = \left(v_i, u_j \right) = \delta_{N_i N_j} \sum_{l\Lambda} a_{l\Lambda}^i a_{l\Lambda}^j, \mathbf{z}_{E(M)ij}^s = \begin{cases} G_{E(M)\lambda}^{ij}, & i = s, \\ \mathbf{Z}_{ij}, & i \neq s. \end{cases}, i, j = N+1, \ldots, N+Z$$ (9)

where $a_{l\Lambda}^i$ and $a_{l\Lambda}^j$ are the coefficients of decomposition of the functions v_i and u_j in the basis of the spherical harmonic oscillator [11]; N_i and N_j are the principal quantum numbers of states i and j; l and Λ are the angular momentum and its projection; $G_{E(M)\lambda}^{ij}$ correspond to the quantities $G_{E(M)\lambda}$ calculated in Ref. [11].

Note that the matrix element of the single-particle multipole operator is taken between two determinant wave functions. That is why the transition probabilities depend on the mixture coefficients $a_{l\Lambda}^i$ [Eqs. (8) and (9)] but not on any deformation parameters. Because the mixture coefficients are calculated numerically, it is not possible to derive analytical dependence of the transition probabilities on the deformation in the form of deformation parameters.

The case $\lambda \geq K + K'$ was studied in Ref. [15]. The influence of different deformations of the initial and final states of odd s-d-shell nuclei on the probabilities of $E2$-transitions was analyzed in Ref. [16]. The role of Coriolis interaction in calculations of the probabilities of electromagnetic transitions between states with different deformations was accounted for in Ref. [17]. The experimentally measured probabilities of $M1$-transitions between analogue and anti-analogue states with different deformations in odd s-d-shell nuclei were examined in Ref. [18].

Note that the authors of Refs. [12–18] restricted themselves to the case of quadrupole deformations. Using two different deformation parameters they plotted the area where the discrepancy between the measured and calculated probabilities of some $E2$-transitions for odd s-d-shell nuclei significantly reduced. But this was done numerically.

4. EVOLVING NUCLEAR SHAPES VIA EVOLUTIONARY ALGORITHM

We chose the function that describes the shape of the equipotential surface of the nuclear potential in the i-th single-particle state of the nucleus in the following form:

$$\varphi^{(i)}(\theta) = \sum_{k=0}^{\infty} \varphi_{2k}^{(i)} \cos(2k\theta).$$ (10)

The values of the weight parameters $\left\{ \varphi_{2k}^{(i)} \right\}$ ($i=0$ marks the ground state and $i=1, \ldots, n$ mark the single-particle excited states) are determined independently for each level of the nucleus. Additional requirements imposed on the

weight parameters $\left\{\varphi_{2k}^{(i)}\right\}$ are their minimum number for each level and their minimum value that ensures a good description of experimental data. Note that both ε and $\left\{\varphi_0^{(i)}\right\}$ affect the radius of spherical equipotential surface of the potential in the Hamiltonian (1). Thus, to avoid overestimation, we set $\left\{\varphi_0^{(0)}\right\}= 0$.

To determine the number and values of the weight parameters $\left\{\varphi_{2k}^{(i)}\right\}$, an approach based on the use of an evolutionary algorithm [21,22] to fit the calculated observables to the measured ones was developed.

Our evolutionary approach operates on a population of N individuals. Each individual is a set of parameters $\left(\varepsilon, \kappa, \left\{\varphi_{2k}^{(i)}\right\}\right)$, i=0, ..., n, k=0, ..., m. Fitness of each individual reflects the quality of data fitting provided by the individual's parameters. Using the mutation operation, the algorithm evolves the initial population of poorly fitted individuals to the final population of the well fitted ones.

Every iteration, the so-called generation, of our procedure contains the following steps.

1. Generating the initial population of N individuals. For each individual, the values of all parameters $\left(\varepsilon, \kappa, \left\{\varphi_{2k}^{(i)}\right\}\right)$ are set to zero.

2. Evaluating fitness of each individual in the population. The fitness function accounts for the quality of data fitting, which is estimated using the standard χ^2 magnitude per datum.

3. Letting each individual in the population produce $M>>1$ offspring. Replication of each parameter x_j from the set $\left(\varepsilon, \kappa, \left\{\varphi_{2k}^{(i)}\right\}\right)$ is performed according to the transformation:

$$x_j' = x_j + A_j C_j , \tag{11}$$

$$A_j' = A_j \exp\left(L N_j(0,1)\right), \tag{12}$$

where x_j and x_j' are the parent's and the offspring's parameters from the set $\left(\varepsilon, \kappa, \left\{\varphi_{2k}^{(i)}\right\}\right)$, $A_j > 0$ and $A_j' > 0$ are the parent's and the offspring's mutation amplitudes, $A_j \in [A_{\min}; A_{\max}]$, C_j is a Cauchy random variable with the scale parameter set to unity, $N_j(0,1)$ denotes a normally distributed one-dimensional random number with mean zero and one standard deviation, and $L > 0$ is the learning parameter that controls the adaptation speed.

4. Evaluating fitness values of all offspring. Sort offspring in descending order according to their fitness. Select N best offspring to form the new population.

5. Going to step 3 or stop if the best fitness in the population is sufficiently high (the χ^2 value is small enough).

The evolutionary process should produce the best possible solution with respect to the fitness function. To achieve this goal and avoid premature convergence in a local optimum, the lower limit of the mutation amplitude $A_{\min}$ behaves as a smooth oscillatory function of generation, while the upper limit $A_{\max}$ remains constant [remember that the real value of A is adapted according to Eq.(12)]. If the value of $A_{\min}$ increases and the rms deviation from the mean value of the fitness function in the population exceeds some upper level (the diversity in the population is too high) then $A_{\min}$ starts to slowly decrease. And vice versa, if the value of $A_{\min}$ decreases and the rms deviation of the fitness function becomes less than some lower level (the diversity is too low) then $A_{\min}$ starts to slowly increase. However, before that, the best fitted individual is saved out of the converged population to preserve the globally best individual. Then, all individuals in the population jump to the new point in the parameter space according to the transformation:

$$x_j^* = x_j + a|x_j|C_j , \tag{13}$$

where x_j and x_j^* are the individual's parameters from the set $\left(\varepsilon, \kappa, \left\{\varphi_{2k}^{(i)}\right\}\right)$ before and after the jump, C_j is a Cauchy random variable with the scale parameter set to unity, and $a \in [0;1]$ is the jump amplitude. Being transposed to the new point in the parameter space, the population starts to explore the vicinity of this point by increasing and decreasing $A_{\min}$ as described above. After finishing another cycle of evolution, the globally best individual is refreshed. Then the population is filled with the current globally best individual, next jump is performed, and new cycle of evolution begins.

Evolutionary algorithms make up, generally, the global optimization technique that, however, cannot guarantee that the optimum found is the global one (see, e.g., Refs. [23–25] or any textbook on evolutionary computations). Therefore, it is necessary to run the procedure several times. Besides, there is no way to know in advance what the minimum value of the χ^2 magnitude will be. Thus, it is instructive to monitor the dynamics of the best, worst, and mean fitness values and the rms deviation from the mean fitness in the population during those several runs of the procedure in order to localize the region of the lowest χ^2 values.

Analysis of experimental data begins with the assumption of the quadrupole deformation of the shapes of nucleus in the ground and single-particle excited states [the terms with k=0, 1 are left in Eq.(10)]. If the desired quality of data fitting is not

achieved within this assumption, then the hexadecapole deformation comes into play [the term with k=2 is added in Eq.(10)], and so forth. After the number of terms in Eq.(10) is determined, the contribution of the first term found (the term with k=0 that violates the volume conservation) is smoothly consistently reduced, preserving the desired quality of data fitting with that. If this procedure produces rather different solutions that are similar in fitness, the contribution of the term next to the previous one (say, k=1) is gradually reduced, and so forth. Following the described prescription, it appears possible to substantially reduce the parameter space of the problem under study and localize the region of the similar solutions.

The reason for the choice of deformation parameterization (10) is, to some extent, technological. The Hamiltonian (1) linearly depends on the function $\varphi(\theta)$. The radius of equipotential surface of the potential is $1/\sqrt{1-\varphi(\theta)}$. Thus, direct parameterization of the radius brings additional computational difficulties.

The decomposition (10) is analytically equivalent to the widely used decomposition of the radius of an axially symmetric nucleus into a series of spherical harmonics (see, e.g., Ref.[5]). Note that, e.g., the Legendre polynomial $P_4(\cos\theta)$ contains not only the term $\cos(4\theta)$, but also the term $\cos(2\theta)$ that is the kernel of the polynomial $P_2(\cos\theta)$. Thus, the decomposition of the function $\varphi(\theta)$ into the series of even Legendre polynomials gives, in fact, the term $\cos(2\theta)$ with two different free weight parameters. This makes additional difficulty for the search algorithm to determine these parameters. In other words, the decomposition (10) substantially simplifies the search for the solution of our problem. Besides, the decomposition (10) gives extremely concise description of the topological features of the nuclear shape.

After the parameters $\varphi_{2k}^{(i)}$ are determined, the values of conventional deformation parameters $\alpha_{2k}^{(i)}$ can be estimated using the following approximate correlation:

$$\frac{1}{\sqrt{1-\varphi^{(i)}(\theta)}} \approx 1 + \frac{1}{2}\varphi^{(i)}(\theta) = 1 + \frac{1}{2}\sum_{k=0}^{m}\varphi_{2k}^{(i)}\cos(2k\theta) = 1 + \sum_{k=0}^{m}\alpha_{2k}^{(i)}P_{2k}(\cos\theta) \ . \tag{14}$$

5. ^{27}Al NUCLEUS SHAPES IN LOW-LAYING SINGLE-PARTICLE STATES

Good quality of fit was achieved when the terms with k=0, 1, 2 were left in Eq.(10). The schemes of occupation of single-particle states by protons (proton configurations) in the ground (g.s.) and first three single-particle excited states (1–3 e.s.) of the ^{27}Al nucleus were chosen as follows:

$$\begin{array}{lccccccccccc}
\text{g.s.} & 2 & 2 & 2 & 2 & 2 & 2 & 1 & 0 & 0 & 0 & 0 \\
\text{1 e.s.} & 2 & 2 & 2 & 2 & 2 & 2 & 0 & 1 & 0 & 0 & 0 \\
\text{2 e.s.} & 2 & 2 & 2 & 2 & 2 & 2 & 0 & 0 & 0 & 1 & 0 \\
\text{3 e.s.} & 2 & 2 & 2 & 2 & 2 & 2 & 0 & 0 & 1 & 0 & 0 \\
\end{array}$$

The schemes of occupation of single-particle states by neutrons (neutron configurations) were chosen to be independent of the nucleus state:

$$2 \quad 2 \quad 2 \quad 2 \quad 2 \quad 2 \quad 2 \quad 0 \quad 0 \quad 0 \quad 0$$

Figure 1 and Tables 1–4 present the best fitted result. Experimental data were taken from Refs. [26,27].
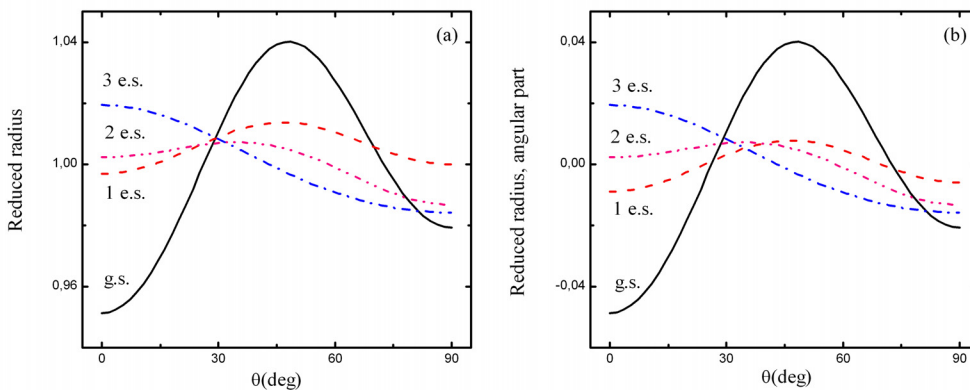
Figure 1. Shapes for four single-particle states of ^{27}Al nucleus, calculated by our procedure. (a) Reduced radii $1/\sqrt{1-\varphi(\theta)}$ of the equipotential surface of the nuclear potential for four single-particle states of ^{27}Al nucleus. (b) The same as Fig. 1(a) but only for angular part of $1/\sqrt{1-\varphi(\theta)}$. Curve marked as g.s. corresponds to the ground state. Curves marked as 1–3 e.s. present three low-laying excited states.

Table 1. Experimentally measured $E_{exper}(2J^\pi)$ and calculated $E_{theor}(2J^\pi)$ energies (MeV), spins $2J$, and parities π of the ground and first three low-laying single-particle excited states of ^{27}Al nuclei.

$E_{exper}(2J^\pi)$	$E_{theor}(2J^\pi)$
0.0000 (5$^+$)	0.0000 (5$^+$)
0.8438 (1$^+$)	0.8438 (1$^+$)
2.9820 (3$^+$)	2.9820 (3$^+$)
3.6804 (1$^+$)	3.6804 (1$^+$)

We are aware that the dynamics of nuclear deformation with the increase of excitation energy is better analyzed looking at the plot of the nuclear radius as function of the angle. Therefore, instead of the function $\varphi(\theta)$, we show the reduced radius of equipotential surface of the potential $1/\sqrt{1-\varphi(\theta)}$ [Fig. 1(a)] and its angular part $1/\sqrt{1-\varphi(\theta)}-1/\sqrt{1-\varphi_0}$ [Fig. 1(b)] as functions of the angle. Besides, Table 4 contains the values of conventional deformation parameters estimated with help of Eq. (14).

Table 2. Experimentally measured $\Gamma_{\gamma i}(E2)_{exper}$ and calculated $\Gamma_{\gamma i}(E2)_{theor}$ partial gamma widths (eV) for ^{27}Al nuclei. $E_i(2J^\pi)$ and $E_f(2J^\pi)$ denote energies (MeV), spins 2J, and parities π of initial and final states.

$E_i(2J^\pi) \rightarrow E_f(2J^\pi)$	$\Gamma_{\gamma i}(E2)_{exper}$	$\Gamma_{\gamma i}(E2)_{theor}$
0.8438 (1$^+$) $\rightarrow$ 0.0000 (5$^+$)	$(1.30\pm0.20)\times10^{-5}$	1.30×10^{-5}
2.9820 (3$^+$) $\rightarrow$ 0.0000 (5$^+$)	$<4.55\times10^{-5}$	2.60×10^{-5}
3.6804 (1$^+$) $\rightarrow$ 0.0000 (5$^+$)	$(1.00\pm0.30)\times10^{-3}$	1.00×10^{-3}

Table 3. Experimentally measured $\Gamma_{\gamma i}(M1)_{exper}$ and calculated $\Gamma_{\gamma i}(M1)_{theor}$ partial gamma widths (eV) for ^{27}Al nuclei. $E_i(2J^\pi)$ and $E_f(2J^\pi)$ denote energies (MeV), spins $2J$, and parities π of initial and final states.

$E_i(2J^\pi) \rightarrow E_f(2J^\pi)$	$\Gamma_{\gamma i}(M1)_{exper}$	$\Gamma_{\gamma i}(M1)_{theor}$
2.9820 (3$^+$) $\rightarrow$ 0.0000 (5$^+$)	$(1.14\pm0.03)\times10^{-1}$	1.14×10^{-1}
2.9820 (3$^+$) $\rightarrow$ 0.8438 (1$^+$)	$(1.20\pm0.40)\times10^{-3}$	1.20×10^{-3}
3.6804 (1$^+$) $\rightarrow$ 0.8438 (1$^+$)	$(5.20\pm0.20)\times10^{-2}$	5.20×10^{-2}

Table 4. Deformation parameters α_{2k}, k=0, 1, 2, of the shape of ^{27}Al nucleus in its ground (g.s.) and first three low-laying single-particle excited states (1–3 e.s.), estimated according to Eq. (14).

	g.s.	1 e.s.	2 e.s.	3 e.s.
α_0	7.6×10^{-3}	6.8×10^{-3}	-2.2×10^{-3}	-5.9×10^{-3}
α_2	7.4×10^{-3}	3.6×10^{-3}	1.4×10^{-2}	2.2×10^{-2}
α_4	-6.7×10^{-2}	-1.3×10^{-2}	-1.0×10^{-2}	2.3×10^{-3}

Figure 1 and Table 4 show that the angular part of the ^{27}Al nucleus shape is described by two harmonics – quadrupole [$\cos(2\theta)$ or $P_2(\cos\theta)$] and hexadecapole [$\cos(4\theta)$ or $P_4(\cos\theta)$]. In its ground and first three low-laying single-particle excited states the ^{27}Al nucleus is abnormally weakly deformed. The hexadecapole deformation dominates in the ground state of the ^{27}Al nucleus. Then, with the increase of the excitation energy, its contribution decreases and almost vanishes for the third excited state. The contribution of the quadrupole deformation is small for the ground and first excited states, but it increases with the increase of the excitation energy and becomes dominant for the third excited state of the ^{27}Al nucleus.

6. ^{31}P NUCLEUS SHAPES IN LOW-LAYING SINGLE-PARTICLE STATES

Good quality of fit was achieved when the terms with k=0, 1, 2 were left in Eq.(10). The schemes of occupation of single-particle states by protons (proton configurations) in the ground (g.s.) and first three single-particle excited states (1–3 e.s.) of the ^{31}P nucleus were chosen as follows:

```
g.s.    2 2 2 2 2 2 2 1 0 0 0 0 0 0
1 e.s.  2 2 2 2 2 2 2 0 1 0 0 0 0 0
2 e.s.  2 2 2 2 2 2 1 2 0 0 0 0 0 0
3 e.s.  2 2 2 2 2 2 2 0 0 0 0 0 0 1
```

The schemes of occupation of single-particle states by neutrons (neutron configurations) were chosen to be independent of the nucleus state:

```
2 2 2 2 2 2 2 2 0 0 0
```

Figure 2 and Tables 5-9 present the best result. Experimental data were taken from Refs. [26,28].

As in Fig. 1, we show the reduced radius of equipotential surface of the potential [Fig. 2(a)] and its angular part [Fig. 2(b)] as function of the angle, while Table 9 contains the values of conventional deformation parameters estimated with help of Eq. (14).

Table 5. Experimentally measured $E_{\text{exper}}(2J^\pi)$ and calculated $E_{\text{theor}}(2J^\pi)$ energies (MeV), spins $2J$, and parities π of the ground and first three low-laying single-particle excited states of ^{31}P nuclei.

$E_{\text{exper}}(2J^\pi)$	$E_{\text{theor}}(2J^\pi)$
0.0000 (1$^+$)	0.0000 (1$^+$)
3.1343 (1$^+$)	3.1343 (1$^+$)
3.2950 (5$^+$)	3.2950 (5$^+$)
4.4312 (7$^-$)	4.4312 (7$^-$)

Table 6. Experimentally measured $\Gamma_{\gamma i}(E2)_{\text{exper}}$ and calculated $\Gamma_{\gamma i}(E2)_{\text{theor}}$ partial gamma widths (eV) for ^{31}P nuclei. $E_i(2J^\pi)$ and $E_f(2J^\pi)$ denote energies (MeV), spins $2J$, and parities π of initial and final states.

$E_i(2J^\pi) \rightarrow E_f(2J^\pi)$	$\Gamma_{\gamma i}(E2)_{\text{exper}}$	$\Gamma_{\gamma i}(E2)_{\text{theor}}$
3.2950 (5$^+$) $\rightarrow$ 0.0000 (1$^+$)	$(4.35\pm0.5)\times10^{-5}$	4.35×10^{-5}

Table 7. Experimentally measured $\Gamma_{\gamma i}(M1)_{\text{exper}}$ and calculated $\Gamma_{\gamma i}(M1)_{\text{theor}}$ partial gamma widths (eV) for ^{31}P nuclei. $E_i(2J^\pi)$ and $E_f(2J^\pi)$ denote energies (MeV), spins $2J$, and parities π of initial and final states.

$E_i(2J^\pi) \rightarrow E_f(2J^\pi)$	$\Gamma_{\gamma i}(M1)_{\text{exper}}$	$\Gamma_{\gamma i}(M1)_{\text{theor}}$
3.1343 (1$^+$) $\rightarrow$ 0.0000 (1$^+$)	$(6.2\pm0.5)\times10^{-2}$	6.2×10^{-2}
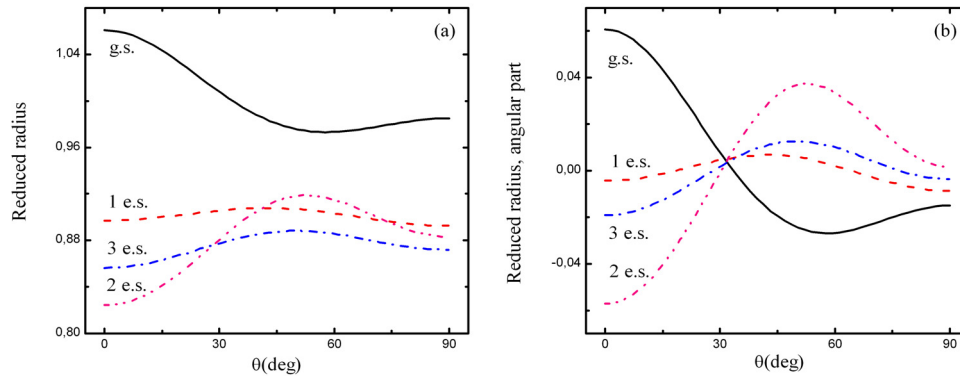
Figure 2. Shapes for four single-particle states of ^{31}P nucleus, calculated by our procedure. (a) Reduced radii $1/\sqrt{1-\varphi(\theta)}$ of the equipotential surface of the nuclear potential for four single-particle states of ^{31}P nucleus. (b) The same as Fig. 2(a) but only for angular part of $1/\sqrt{1-\varphi(\theta)}$. Curve marked as g.s. corresponds to the ground state. Curves marked as 1–3 e.s. present three low-laying excited states.

Table 8. Experimentally measured $\Gamma_{\gamma i}(E3)_{\text{exper}}$ and calculated $\Gamma_{\gamma i}(E3)_{\text{theor}}$ partial gamma widths (eV) for ^{31}P nuclei. $E_i(2J^\pi)$ and $E_f(2J^\pi)$ denote energies (MeV), spins $2J$, and parities π of initial and final states.

$E_i(2J^\pi) \rightarrow E_f(2J^\pi)$	$\Gamma_{\gamma i}(E3)_{\text{exper}}$	$\Gamma_{\gamma i}(E3)_{\text{theor}}$
4.4312 (7$^-$) $\rightarrow$ 0.0000 (1$^+$)	$(9.80\pm2.1)\times10^{-6}$	9.80×10^{-6}
4.4312 (7$^-$) $\rightarrow$ 3.1343 (1$^+$)	$<1.10\times10^{-6}$	1.10×10^{-6}

Table 9. Deformation parameters α_{2k}, $k = 0, 1, 2$, of the shape of ^{31}P nucleus in its ground (g.s.) and first three low-laying single-particle excited states (1–3 e.s.), estimated according to Eq. (14).

	g.s.	1 e.s.	2 e.s.	3 e.s.
α_0	-1.3×10^{-2}	-1.1×10^{-1}	-1.2×10^{-1}	-1.4×10^{-1}
α_2	3.1×10^{-2}	1.0×10^{-2}	-2.9×10^{-2}	-2.6×10^{-3}
α_4	3.6×10^{-2}	-1.6×10^{-2}	-8.2×10^{-2}	-3.1×10^{-2}

Figure 2 and Table 9 show that, as in case of ^{27}Al nucleus, the angular part of the ^{31}P nucleus shape is described by two harmonics – quadrupole and hexadecapole. In its ground and first three low-laying single-particle excited states the ^{31}P nucleus is abnormally weakly deformed. The ground and first excited states of the ^{31}P nucleus are characterized by the mixture of the quadrupole and hexadecapole deformations. Then, with the increase of the excitation energy, the hexadecapole deformation becomes dominant in the second and third excited states.

7. ^{35}Cl NUCLEUS SHAPES IN LOW-LAYING SINGLE-PARTICLE STATES

Good quality of fit was achieved when the terms with $k=0, 1, 3$ were left in Eq.(10). The term $\cos(4\theta)$ ($k=2$) did not influence the quality of fit. The schemes of occupation of single-particle states by protons (proton

configurations) in the ground (g.s.) and first three single-particle excited states (1–3 e.s.) of the ^{35}Cl nucleus were chosen as follows:

$$
\begin{array}{llcccccccccccc}
\text{g.s.} & 2 & 2 & 2 & 2 & 2 & 2 & 2 & 2 & 1 & 0 & 0 & 0 & 0 & 0 \\
\text{1 e.s.} & 2 & 2 & 2 & 2 & 2 & 2 & 2 & 2 & 0 & 1 & 0 & 0 & 0 & 0 \\
\text{2 e.s.} & 2 & 2 & 2 & 2 & 2 & 2 & 2 & 2 & 0 & 0 & 0 & 0 & 0 & 1 \\
\text{3 e.s.} & 2 & 2 & 2 & 2 & 2 & 2 & 1 & 2 & 2 & 0 & 0 & 0 & 0 & 0 \\
\end{array}
$$

The schemes of occupation of single-particle states by neutrons (neutron configurations) were chosen to be independent of the nucleus state:

$$2\quad 2\quad 2\quad 2\quad 2\quad 2\quad 2\quad 2\quad 2\quad 0\quad 0$$

Figure 3 and Tables 10-15 present the best result. Experimental data were taken from Refs. [26,29].

As in Figs. 1 and 2, we show the reduced radius of equipotential surface of the potential [Fig. 3(a)] and its angular part [Fig. 3(b)] as function of the angle, while Table 15 contains the values of conventional deformation parameters estimated with help of Eq. (14). We emphasized that in order to replicate well the experimental data on ^{35}Cl nucleus it was not necessary to account for the contribution of the basis function $\cos(4\theta)$ in the decomposition (10). Thus, the values of the parameters $\varphi_4^{(i)}$ were set to zero and, consequently, the values of the deformation parameters $\alpha_4^{(i)}$ appeared to be linearly dependent on the values of the parameters $\alpha_6^{(i)}$ (Table 15).
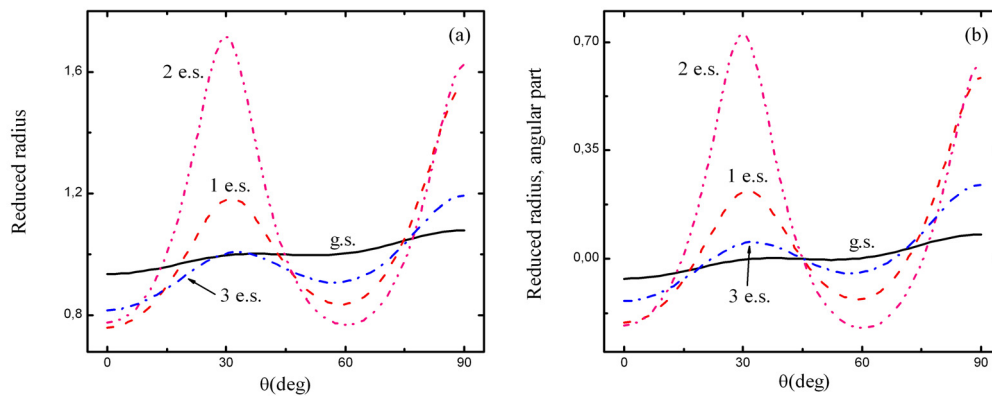
Figure 3. Shapes for four single-particle states of ^{35}Cl nucleus, calculated by our procedure. (a) Reduced radii $1/\sqrt{1-\varphi(\theta)}$ of the equipotential surface of the nuclear potential for four single-particle states of ^{35}Cl nucleus. (b) The same as Fig. 3(a) but only for angular part of $1/\sqrt{1-\varphi(\theta)}$. Curve marked as g.s. corresponds to the ground state. Curves marked as 1–3 e.s. present three low-laying excited states.

Table 10. Experimentally measured $E_{\text{exper}}(2J^\pi)$ and calculated $E_{\text{theor}}(2J^\pi)$ energies (MeV), spins $2J$, and parities π of the ground and first three low-laying single-particle excited states of ^{35}Cl nuclei.

$E_{\text{exper}}(2J^\pi)$	$E_{\text{theor}}(2J^\pi)$
0.0000 (3$^+$)	0.0000 (3$^+$)
1.2193 (1$^+$)	1.2193 (1$^+$)
3.1628 (7$^-$)	3.1628 (7$^-$)
3.9185 (3$^+$)	3.9185 (3$^+$)

Table 11. Experimentally measured $\Gamma_{\gamma i}(E2)_{\text{exper}}$ and calculated $\Gamma_{\gamma i}(E2)_{\text{theor}}$ partial gamma widths (eV) for ^{35}Cl nuclei. $E_i(2J^\pi)$ and $E_f(2J^\pi)$ denote energies (MeV), spins $2J$, and parities π of initial and final states.

$E_i(2J^\pi) \rightarrow E_f(2J^\pi)$	$\Gamma_{\gamma i}(E2)_{\text{exper}}$	$\Gamma_{\gamma i}(E2)_{\text{theor}}$
1.2193 (1$^+$) → 0.0000 (3$^+$)	(4.0±0.44)×10^{-5}	4.0×10^{-5}
3.9185 (3$^+$) → 0.0000 (3$^+$)	(3.1±0.89)×10^{-3}	3.1×10^{-3}

Table 12. Experimentally measured $\Gamma_{\gamma i}(M1)_{\text{exper}}$ and calculated $\Gamma_{\gamma i}(M1)_{\text{theor}}$ partial gamma widths (eV) for ^{35}Cl nuclei. $E_i(2J^\pi)$ and $E_f(2J^\pi)$ denote energies (MeV), spins $2J$, and parities π of initial and final states.

$E_i(2J^\pi) \rightarrow E_f(2J^\pi)$	$\Gamma_{\gamma i}(M1)_{\text{exper}}$	$\Gamma_{\gamma i}(M1)_{\text{theor}}$
1.2193 (1$^+$) → 0.0000 (3$^+$)	(3.6 ±0.4)×10^{-3}	3.6×10^{-3}
3.9185 (3$^+$) → 0.0000 (3$^+$)	(7.1 ±2.0)×10^{-2}	7.1×10^{-2}
3.9185 (3$^+$) → 1.2193 (1$^+$)	<5.0×10^{-4}	5.0×10^{-4}

Table 13. Experimentally measured $\Gamma_{\gamma i}(M2)_{\text{exper}}$ and calculated $\Gamma_{\gamma i}(M2)_{\text{theor}}$ partial gamma widths (eV) for ^{35}Cl nuclei. $E_i(2J^\pi)$ and $E_f(2J^\pi)$ denote energies (MeV), spins $2J$, and parities π of initial and final states.

$E_i(2J^\pi) \rightarrow E_f(2J^\pi)$	$\Gamma_{\gamma i}(M2)_{\text{exper}}$	$\Gamma_{\gamma i}(M2)_{\text{theor}}$
3.1628 (7$^-$) → 0.0000 (3$^+$)	(1.3 ±0.03)×10^{-5}	1.3×10^{-5}

Table 14. Experimentally measured $\Gamma_{\gamma i}(E3)_{\text{exper}}$ and calculated $\Gamma_{\gamma i}(E3)_{\text{theor}}$ partial gamma widths (eV) for ^{35}Cl nuclei. $E_i(2J^\pi)$ and $E_f(2J^\pi)$ denote energies (MeV), spins $2J$, and parities π of initial and final states.

$E_i(2J^\pi) \rightarrow E_f(2J^\pi)$	$\Gamma_{\gamma i}(E3)_{\text{exper}}$	$\Gamma_{\gamma i}(E3)_{\text{theor}}$
3.1628 (7$^-$) → 0.0000 (3$^+$)	(3.3±0.075)×10^{-7}	3.3×10^{-7}
3.1628 (7$^-$) → 1.2193 (1$^+$)	<3.0×10^{-8}	3.0×10^{-8}

Table 15. Deformation parameters α_{2k}, k=0, 1, 2, 3, of the shape of ^{35}Cl nucleus in its ground (g.s.) and first three low-laying single-particle excited states (1–3 e.s.), estimated according to Eq. (14). The values of the parameter α_4 linearly depend on the values of the parameter α_6.

	g.s.	1 e.s.	2 e.s.	3 e.s.
α_0	1.6×10^{-2}	3.5×10^{-3}	-4.4×10^{-3}	-1.4×10^{-2}
α_2	-6.1×10^{-2}	-9.0×10^{-2}	8.1×10^{-2}	-1.0×10^{-1}
α_4	2.1×10^{-2}	2.2×10^{-1}	3.3×10^{-1}	1.0×10^{-1}
α_6	-4.8×10^{-2}	-5.0×10^{-1}	-7.3×10^{-1}	-2.2×10^{-1}

Figure 3 and Table 15 show that the angular part of the ^{35}Cl nucleus shape is described by three harmonics – quadrupole [$P_2(\cos\theta)$], hexadecapole [$P_4(\cos\theta)$], and hexacontatetrapole [$P_6(\cos\theta)$]. Note again that, in case of ^{35}Cl nucleus, the contribution of hexadecapole deformation is not independent. In its ground state the ^{35}Cl nucleus is abnormally weakly deformed. With the increase of excitation energy, the contribution of hexacontatetrapole deformation sharply (by an order of magnitude) increases and becomes dominant for the first and third excited states, and especially for the second excited state. This observation indicates that the change of the state of the only one nucleon – the valence proton the spin and parity of which determine the spin and parity of the ^{35}Cl nucleus – causes the shape phase transition from the high-symmetry phase – spherical ground state – to the low-symmetry phase – deformed excited states.

8. DISCUSSION

The evolutionary procedure of determining the shape of a nucleus in single-particle states presented in this article is aimed at searching for the globally optimal solution. However, being aware of the complexity of the problem under study and the fact that the actual number of fitting parameters is substantially greater than the actual number of data points, we do not expect to achieve it. Therefore, we consider the obtained results (Figs.1–3, and Tables 1–15) as very promising.

The shapes of the nuclei studied in the ground and low-laying single-particle excited states obtained in different runs of the procedure go rather close to each other. Besides, the variations of the parameter that takes into account the deviation of the energy scale from its simple estimate ε and of the spin-orbit interaction strength κ from run to run of the optimization procedure are found to be insignificant. This result is a consequence of application of the requirements imposed on the weight parameters $\left\{\varphi_{2k}^{(i)}\right\}$ from the decomposition (10). Namely, the number of these parameters must be the smallest possible for each level and the values of these parameters must be the smallest possible, ensuring a good description of experimental data along with that. From the formally mathematical viewpoint, these requirements are equivalent to the numerous constraints imposed on the variables $\left\{\varphi_{2k}^{(i)}\right\}$, which leads to the substantial reduction of the parameter space of the problem (the "effective" number of free parameters is much smaller than the "actual" one). One should also bear in mind that the measured probabilities of electromagnetic transitions between single-particle states of nuclei are the highly correlated data that are difficult to analyze. Thus, in this case, the belief that "anything can be fitted with a sufficient number of parameters", is a substantial oversimplification (see, e.g., Ref. [2]).

From the computational viewpoint, in general, the parameter space of our problem is highly dimensional, highly nonlinear, and has unknown and unpredictable topography. This makes the choice of an appropriate search method crucial. Evolutionary (or genetic) algorithms have many times proved very efficient in dealing with very difficult physical problems (see, e.g., Refs. [30–35]), so we have chosen it as a key element of our procedure. Usually, in evolutionary computations, the mutation amplitude is either constant, or decreases across the run of the evolutionary procedure. Often this leads the search algorithm in a local optimum in the parameter space. To avoid premature convergence in a local optimum, we have devised the special schedule of tuning the mutation amplitude, in which the latter behaves as a smooth oscillatory function of generation. This mechanism resembles, in part, the so-called "simulated annealing" approach to solve the optimization problems of combinatorial complexity. Due to the consecutive cycles of increasing and decreasing of the mutation amplitude, the population hops from the less fitted optimum to the more fitted one situated in the close vicinity. To have an opportunity to explore the parameter space much further, we

have allowed the population as a whole to periodically jump to the new point in the parameter space. As a consequence, we have managed to localize the region of the nuclear shapes that give the lowest values to the χ^2 magnitude: Tables 1–15 show very good agreement between the calculated and measured observables.

In principle, our algorithm could treat $\varphi(\theta)$ as a numerical array and evolve it as a whole quantity with help of the diffused mutation operator devised in Refs. [21,22]. We emphasize that the devised approach of extracting nuclear shapes from the data does not depend on the particular nuclear data and the particular analytical tools (nuclear models) to analyze it. For instance, our approach, with minor changes, could be used to extract the matter-density distributions in nuclei [36], the radial dependence of the nuclear potentials [37], etc. from the suitable data. Our preliminary investigations show that our method enables to extract the radial dependence of the nuclear potentials from the set of energy levels. Thus, our method could be applied to the wide set of nuclear problems in wide mass region.

From the physics viewpoint, our analysis of experimental data on the energies, spins, and parities of the low-laying single-particle states and the probabilities of electromagnetic transitions between them in ^{27}Al, ^{31}P and ^{35}Cl nuclei shows the following.

We have found that the studied nuclei in the ground states are abnormally weakly deformed, which is not expected for the nuclei in the shell middle. Even in their low-laying single-particle excited states, the nuclei ^{27}Al and ^{31}P are found to be weakly deformed, too. The change of the state of the only one nucleon – the valence proton the spin and parity of which determine the spin and parity of the ^{35}Cl nucleus – causes the shape phase transition from the high-symmetry phase – spherical ground state – to the low-symmetry phase – deformed excited states. Hence, in case of ^{27}Al, ^{31}P and ^{35}Cl nuclei, we are dealing with manifestation of the forces that are not related to the formation of nuclear shells.

The angular part of the ^{27}Al and ^{31}P nuclei shape is described by two harmonics – quadrupole and hexadecapole. The angular part of the ^{35}Cl nucleus shape is described by three harmonics – quadrupole, hexadecapole, and hexacontatetrapole, but the contribution of hexadecapole deformation is not independent. It is usually assumed that quadrupole deformations are of the most importance, while hexadecapole deformations are good but rather small corrections to quadrupole deformations and may be important for describing the ground states of heavy nuclei (see, e.g., Refs. [1,2] or any textbook on nuclear physics). As for the higher multipolarity deformations, they are not considered to have much physical significance. At present, there are no fundamental nuclear models that account for or predict the dominant hexacontatetrapole deformation, especially for light and medium nuclei.

Analyzing quantum characteristics of the single nucleons that form the ^{27}Al, ^{31}P and ^{35}Cl nuclei, we find that the spin and parity of these nuclei are determined by the spin and parity of the last odd (valence) proton. At the same time, some of the nucleons of the nucleus core change their characteristics, too. This means that the electromagnetic transitions between the single-particle states of the ^{27}Al, ^{31}P and ^{35}Cl nuclei are the multi-particle processes.

Applications of the Landau theory of phase transitions, briefly mentioned in the Introduction, are based on the decomposition of the radius of a nucleus, which depends on spherical angles, into a series of spherical functions [5]. Thus, the potential energy of the nucleus contains collective forces that act on the deformation parameters, but not on the angular variables. Strictly speaking, to predict the equilibrium shape of the nucleus, the theory must contain angular derivatives of various orders.

Spatial derivatives naturally arise in the Landau-type theory of phase transitions with a spatially inhomogeneous order parameter (see, e.g., Ref. [38] or any textbook on phase transitions). This theory turned out to be very effective in describing phase transitions in ferroelectrics and magnetics with incommensurate phases (see, e.g., Refs. [39–42] and also Ref. [33]). These phases are states in which the period of spatial modulation of the order parameter is not commensurate with (or does not depend on) the period of the crystal lattice. In this case, the Landau-type potential is a functional of the order parameter and its derivatives. The competition and compromise of different powers of the order parameter and its derivatives lead to the appearance of various stable spatially inhomogeneous states of the system.

Assuming that the characteristic size at which the angular function describing the deviation of the nucleus shape from sphericity changes significantly is not commensurate with both the size of the nucleon and the distance between the nucleons, the deformed nucleus can be considered as an incommensurate phase. Therefore, the Landau-type theory of phase transitions with a spatially inhomogeneous order parameter could be a useful tool to study the shape of a deformed nucleus.

ORCID
Volodymyr Yu. Korda, https://orcid.org/0000-0002-9445-0461, **Iryna S. Timchenko,** https://orcid.org/0000-0003-2917-5026

REFERENCES
[1]   M.A. Preston, and R.K. Bhaduri, *Structure of the Nucleus* (Addison-Wesley, Reading, MA, 1975), 716 p.
[2]   W. Greiner, and J. Maruhn, *Nuclear Models* (Springer, Berlin, 1996), 376 p.
[3]   L. Landau, Phys. Z. Sowjet. **11**, 545 (1937). In *Collected Papers of L. D. Landau*, edited by D. Ter Haar (Pergamon, Oxford, 1965), p. 193.
[4]   P. Cejnar, J. Jolie, and R.F. Casten, Rev. Mod. Phys. **82**, 2155 (2010). https://doi.org/10.1103/RevModPhys.82.2155
[5]   A. Bohr, and B. Mottelson, *Nuclear Structure*, Vol. 2, (Benjamin, Reading, MA, 1975).
[6]   R. Lucas, Europhysics News, **32**, 5 (2001); http://dx.doi.org/10.1051/epn:2001101
[7]   D. Warner, Nature, **420**, 614 (2002). https://www.nature.com/articles/420614a
[8]   R.F. Casten, Nature Physics, **2**, 811 (2006). https://www.nature.com/articles/nphys451
[9]   S. Quan, Z.P. Li, D. Vretenar, and J. Meng, Phys. Rev. C, **97**, 031301(R) (2018). https://doi.org/10.1103/PhysRevC.97.031301

[10] M.T. Mustonen, C.N. Gilbreth, Y. Alhassid, and G.F. Bertsch, Phys. Rev. C **98**, 034317 (2018). https://doi.org/10.1103/PhysRevC.98.034317

[11] S.G. Nilsson, "Binding States of Individual Nucleos in Strongly Deformed Nuclei," Mat. Fys. Medd. **29**(16), 1-68 (1955). https://cds.cern.ch/record/212345/files/p1.pdf

[12] E.V. Inopin, E.G. Kopanets, L.P. Korda, V.Ya. Kostin, and A.A. Koval, Voprosy Atomnoi Nauki i Tekhniki, Seriya: Fizika Vysokih Energii i Atomnogo Yadra [Problems of Atomic Science and Technology, Series "Physics of High Energies and Atomic Nucleus"], **3**(15), 31 (1975) (in Russian). https://inis.iaea.org/search/searchsinglerecord.aspx?recordsFor=SingleRecord&RN=9361989

[13] E.G. Kopanets, E.V. Inopin, and L.P. Korda, Izv. Akad. Nauk SSSR, Ser. Fiz. [Bull. Acad. Sci. USSR, Phys. Ser.] **39**, 2032 (1975) (in Russian).

[14] E.G. Kopanets, E.V. Inopin, L.P. Korda, V.A. Kostin, and A.A. Koval, Izv. Akad. Nauk SSSR, Ser. Fiz. [Bull. Acad. Sci. USSR, Phys. Ser.] **40**, 780 (1976) (in Russian).

[15] E.G. Kopanets, E.V. Inopin, and L.P. Korda, Izv. Akad. Nauk SSSR, Ser. Fiz. [Bull. Acad. Sci. USSR, Phys. Ser.] **44**, 1947 (1980) (in Russian). https://www.osti.gov/etdeweb/biblio/5791741

[16] L.P. Korda, and E.G. Kopanets, Voprosy Atomnoi Nauki i Tekhniki, Seriya: Obshchaya I Yadernaya Fizika [Problems of Atomic Science and Technology, Series "General and Nuclear Physics"], **2**(16), 3 (1981) (in Russian).

[17] L.P. Korda, E.G. Kopanets, and E.V. Inopin, Voprosy Atomnoi Nauki i Tekhniki, Seriya: "Obshchaya i Yadernaya Fizika" [Problems of Atomic Science and Technology, Series "General and Nuclear Physics"], **2**(27), 63 (1984) (in Russian).

[18] A.N. Vodin, E.G. Kopanets, L.P. Korda, and V.Yu. Korda, Problems of Atomic Science and Technology, Series "Nuclear Physics Investigations", **2**(41), 66 (2003). https://vant.kipt.kharkov.ua/TABFRAME1.html

[19] V.Yu. Korda, I.S. Timchenko, L.P. Korda, O.S. Deiev, and V.F. Klepikov, Nucl. Phys. **A1025**, 122480 (2022). https://doi.org/10.1016/j.nuclphysa.2022.122480

[20] H.A. Bethe, *Intermediate Quantum Mechanics* (Benjamin, New York, 1964), 416 p.

[21] V.Yu. Korda, A.S. Molev, and L.P. Korda, Phys. Rev. C, **72**, 014611 (2005). https://doi.org/10.1103/PhysRevC.72.014611

[22] V.Yu. Korda, S.V. Berezovsky, A.S. Molev, and V.F. Klepikov, Int. J. Mod. Phys. C, **24**, 1350009 (2013). https://doi.org/10.1142/S0129183113500095

[23] J.H. Holland, *Adaptation in Natural and Artificial Systems* (The University of Michigan Press, Ann Arbor, 1975).

[24] D.E. Goldberg, *Genetic Algorithms in Search, Optimization and Machine Learning* (Addison-Wesley, 1989).

[25] Z. Michalewicz, *Genetic Algorithms + Data Structures = Evolution Programs* (Springer-Verlag, Berlin, 1994).

[26] P.M. Endt, Nucl. Phys. **A633**, 1 (1998). https://doi.org/10.1016/S0375-9474(97)00613-1

[27] M.S. Basunia, Nucl. Data Sheets, **112**, 1875 (2011). https://doi.org/10.1016/j.nds.2011.08.001

[28] C. Ouelet, and B. Singh, Nucl. Data Sheets, **114**, 209 (2013). https://doi.org/10.1016/j.nds.2013.03.001

[29] J. Chen, J. Cameron, and B. Singh, Nucl. Data Sheets, **112**, 2715 (2011). https://doi.org/10.1016/j.nds.2011.10.001

[30] J.R. Morris, D.M. Deaven, and K.M. Ho, Phys. Rev. B, **53**, R1740 (1996). https://doi.org/10.1103/PhysRevB.53.R1740

[31] K. Michaelian, Revista Mexicana de Fisica. **42**, 203 (1996).

[32] C. Winkler, and H.M. Hofmann, Phys. Rev. C, **55**, 684 (1997). https://doi.org/10.1103/PhysRevC.55.684

[33] S.V. Berezovsky, V.Yu. Korda, and V.F. Klepikov, Phys. Rev. B, **64**, 064103 (2001). https://doi.org/10.1103/PhysRevB.64.064103

[34] V.Yu. Korda, A.S. Molev, V.F. Klepikov, and L.P. Korda, Phys. Rev. C, **91**, 024619 (2015). https://doi.org/10.1103/PhysRevC.91.024619

[35] V.Yu. Korda, A.S. Molev, L.P. Korda, and V.F. Klepikov, Phys. Rev. C, **97**, 034606 (2018). https://doi.org/10.1103/PhysRevC.97.034606

[36] Yu.A. Berezhnoy, V.Yu. Korda, and A.G. Gakh, Int. J. of Mod. Phys. E, **14**, 1073 (2005). https://doi.org/10.1142/S0218301305003697

[37] V.Yu. Korda, Int. J. of Mod. Phys. E, **9**, 449 (2000). https://doi.org/10.1142/S0218301300000349

[38] J.C. Tolédano, and P. Tolédano, *The Landau Theory of Phase Transitions* (World Scientific, Singapore, 1987), 472 p.

[39] R.M. Hornreich, M. Luban, and S. Shtrikman, Phys. Rev. Lett. **35**, 1678 (1975). https://doi.org/10.1103/PhysRevLett.35.1678

[40] Y. Ishibashi, and H. Shiba, J. Phys. Soc. Jpn. **45**, 409 (1978). https://doi.org/10.1143/JPSJ.45.409

[41] V. Berezovsky, V.F. Klepikov, V.Yu. Korda, and N.A. Shlyakhov, Int. J. of Mod. Phys. B, **12**, 433 (1998). https://doi.org/10.1142/S0217979298000284

[42] H.Z. Cummins, Phys. Rep. **185**, 211 (1990). https://doi.org/10.1016/0370-1573(90)90058-A

ДЕФОРМАЦІЯ НЕПАРНИХ ЯДЕР ^{27}Al, ^{31}P ТА ^{35}Cl В ОДНОЧАСТИНКОВИХ СТАНАХ

Володимир Ю. Корда^a, Лариса П. Корда^b, В'ячеслав Ф. Клепіков^a, Ірина С. Тімченко^b

^{a}*Інститут електрофізики і радіаційних технологій, Національна академія наук, Харків, Україна*

^{b}*Національний науковий центр "Харківський фізико-технічний інститут", Національна академія наук, Харків, Україна*

Форми непарних ядер s-d-оболонки ^{27}Al, ^{31}P та ^{35}Cl в основних і одночастинкових збуджених станах вилучені з експериментальних даних про енергії, спіни та парності цих станів, а також виміряні імовірності електромагнітних переходів між ними за допомогою недавно розробленого нами еволюційного підходу. Ключовим елементом нашої процедури є еволюційний алгоритм, який приводить популяцію ядерних форм, що погано описують експериментальні дані, до популяції ядерних форм, що добре описують експериментальні дані. Досліджені ядра в їхніх основних станах виявились аномально слабко деформованими, що не притаманно ядрам в середині оболонки. Навіть в їхніх низько лежачих одночастинкових станах ядра ^{27}Al та ^{31}P виявились теж слабко деформованими. Із зростанням одночастинкової енергії збудження зміна стану єдиного нуклона – валентного протона, спін та парність якого визначають спін та парність ядра ^{35}Cl – викликає фазовий перехід із високо симетричної фази – сферичного основного стану – у низько симетричну фазу – деформовані збуджені стани. Кутова частина форми ядер ^{27}Al та ^{31}P описується двома гармоніками – квадрупольною і гексадекапольною. Кутова частина форми ядра ^{35}Cl описується трьома гармоніками – квадрупольною, гексадекапольною і гексаконтатетрапольною, проте внесок гексадекапольної деформації не є незалежним. В теперішній час немає фундаментальної ядерної моделі яка б враховувала або передбачала домінуючу гексаконтатетрапольну деформацію, особливо для легких і середніх ядер. Ми знайшли, що спін та парність ядер ^{27}Al, ^{31}P та ^{35}Cl визначаються спіном та парністю останнього непарного протона. В той же час деякі нуклони остову ядра теж змінюють свої характеристики. Тому електромагнітні переходи між одночастинковими станами ядер ^{27}Al, ^{31}P та ^{35}Cl є багаточастинковими процесами.

Ключові слова: *ядерна деформація; модель деформованих оболонок; одночастинковий стан; ядра s-d-оболонки; еволюційний алгоритм; фазовий перехід*

THE EFFECT OF THE PROTON AND NEUTRON AS PROBE FOR THE NUCLEAR FUSION REACTIONS AT NEAR-BARRIER ENERGIES[†]

M.A. Khuadher*, F.A. Majeed[§]

Department of Physics, College of Education for Pure Sciences, University of Babylon, Iraq
*Corresponding Author e-mail: muntazer.ahmed.kh.1998@gmail.com
[§]e-mail: fmajeed@uobabylon.edu.iq
Received May 5; revised June 15, 2023; accepted June 15, 2023

In this study, quantum mechanical calculations and a semi-classical approach were used to determine fusion the probability (P_{fus}), fusion barrier distribution (D_{fus}), and fusion cross section (σ_{fus}) for the systems $^{28}Si + ^{90}Zr$, $^{28}Si + ^{92}Zr$, $^{28}Si + ^{94}Zr$, $^{41}K + ^{28}Si$, and $^{45}K + ^{28}Si$. The semi-classical approach involved the use of the Wentzel–Kramers–Brillouin (WKB) approximation to describe the relative motion between the projectile and target nuclei, and the Continuum Discretized Coupled Channel (CDCC) method of Alder-Winther (AW) to describe the intrinsic motion of the nuclei. The results showed that the consideration of the coupling-channel calculations for quantum mechanics and a semi-classical approach, and its impact on P_{fus}, D_{fus}, and σ_{fus} for the studied systems involving one neutron or one proton transfer reactions are very important to be considered specifically around and below the Coulomb barrier. The results were compared with the measured data and found in reasonable agreement.
Keywords: *Breakup channel, Elastic channel, Nuclear fusion, Neutron transfer, Proton transfer*
PACS: 34. 85. +x, 24.10.-i, 25.70.Jj

1. INTRODUCTION

Nature displays one of its most impressive processes through the fusion of atomic nuclei. When the two nuclei merge with adequate kinetic energy they are capable of overcoming their electrostatic attraction to one another and producing a new nucleus with a charge and baryon number equal to the total of the original nuclei. The method of fusion depends on the amount of available kinetic energy, and The Coulomb barrier can be crossed or penetrated using quantum mechanical tunneling [1]. In the creation of elements, the involvement of nuclei with a high neutron content is critical, whether it occurs naturally in astronomical events or experiments carried out on Earth. The production of heavy and superheavy nuclei using the neutron-richest projectiles and targets possible is favored by experimental and theoretical data [2-3]. Neutron-rich nuclei fusion is thought to create heat that can cause an X-ray superburst in an accreting neutron star, according to a hypothesis [4]. Where systems rich in neutrons are a rich material for research and exploration. In the investigation of the fusion of $^{58}Ni + ^{64}Ni$ at Q+2n = 3.9MeV, Beckerman et al first noticed the impact of Positive Q-value Neutron Transfer (PQNT) [5] channels on near-barrier fusion cross sections. They directly compared the fusion excitation functions of $^{58,64}Ni + ^{58,64}Ni$ in an experiment, with the symbol "+" notation representing the absorption of neutrons from the target nuclei [6]. According to Broglia et al, the sub-barrier enhancement of fusion observed in $^{58}Ni + ^{64}Ni$ is due to a kinematic effect caused by the transfer of two neutrons during the fusion process, which reduces the neutron transfer cross-section [7] In some cases, the strength of the PQNT channels correlates strongly with the sub-barrier improvement of fusion[8]. In comparison to $^{32}S+^{90}Zr$, the sub-barrier cross sections for $^{32}S+^{96}Zr$ are significantly greater. A coupled-channels calculation that considers the inelastic excitations can explain the sub-barrier improvement in $^{32}S+^{90}Zr$ only. Nonetheless, the unaccounted-for part of $^{32}S+^{96}Zr$ is thought to be connected to intermediate multi-neutron transfers with a positive-Q value. According to the similarities between $^{40}Ca+^{96}Zr$ and $^{32}S+^{96}Zr$, couplings to positive-Q-value multi-neutron transfer channels may have improved sub-barrier fusion [9]. It is noteworthy that the fusion cross sections for the $^{24}O+^{58}Ni$ and $^{40}Ca+^{96}Zr$ systems display different patterns in the vicinity of the barrier due to the contribution of the one-neutron transfer channel. While this channel has negligible impact on the $^{40}Ca+^{96}Zr$ reaction, it plays a significant role in the $^{24}O+^{58}Ni$ reaction. This discrepancy can be attributed to the distinct one-neutron transfer channel's Q-values, which are Q_{1n} = 5.29 MeV and Q_{1n} = 0.508 MeV for $^{24}O+^{58}Ni$ and $^{40}Ca+^{96}Zr$, respectively [10]. A density-constrained Time-Dependent Hartree-Fock (TDHF) [11] approach to fusion theory predicts increased fusion in the $^{24}O + ^{16}O$ system relative to the $^{16}O + ^{16}O$ system due to neutron transfer altering the potential and reducing the barrier. However, the fusion neutron-rich symmetric systems such as $^{24}O + ^{24}O$ is suppressed by a repulsive Pauli potential caused by the overlapping neutron-rich tails. [2] With the addition of one neutron to ^{18}O, the experimental fusion cross-section above the barrier rises by 37%, which is a remarkable outcome. The researcher's analysis showed that the rise in the fusion cross-section for ^{19}O is not the outcome of an odd-even effect, and the improvement in the fusion cross-section of ^{19}O is not a standard excitation.[4] Thought it was because of unpaired neutrons [12]. When comparing neutron-rich and non-neutron-rich systems, the N/Z ratio at the neck region is higher in the former. This increase in the N/Z ratio leads to a decrease in the Coulomb barrier, which enhances the fusion cross-sections in neutron-rich systems[13]. Between interacting nuclei, neutron transfers can form a neck region of nuclear matter that encourages fusion. Once the nuclei are sufficiently close to one another to interact noticeably, or if positive Q-values for neutron transfers, neutron pick-up events

take place [14]. Broad distributions of experimental fusion cross-sections are produced by sequential neutron transfers. Neutron flow may result from the development of a neck between the projectile and target as a result of a collision with a finite Q-value [15]. This could act as fusion's "doorway state". This intermediate state lowers the barrier and makes the fusion process easier at energies below the barrier, significantly increasing fusion cross-sections. An increase in sub-barrier fusion cross-sections has already been shown by experimental findings using (PQNT) [16-17]. It has been proposed by Zagrebaev that the transfer of particles with negative Q values does not increase fusion at energies near or below the barrier [18]. Based on a quantum diffusion approach, Sargsyan and co-workers suggested it if the deformation strength of the nuclei involved in neutron transfer does not change or decrease, neutron transfer channels have little impact on fusion dynamics. Consequently, in some instances, transfer channels may not lead to significant sub-barrier fusion enhancements despite (PQNT) [19]. A universal fusion function approach was used by researchers to analyze the effects of (PQNT) on the fusion process in various systems. They found that significant deformation of the interacting nuclei following neutron transfer is crucial for strong sub-barrier fusion enhancement due to the (PQNT). In contrast, if the deformation of the nuclei is minimal or decreases after neutron transfer, these channels have little effect on the fusion cross-sections [20].

Majeed et al. conducted an extensive study of the nuclear fusion process around and below the Coulomb barrier, the study included weakly bound nuclei ^{6}Li + ^{64}Ni, ^{11}B + ^{159}Tb, and ^{12}C + ^{9}Be using the semi-classical approach and full quantum mechanics, and they reached the results that the inclusion of the breakup channel is very important, To describe σ_{fus} and D_{fus} where results improve around and below the Coulomb barrier for light projectiles [21]. To verify the results, different systems ^{6}Li+^{209}Bi, ^{7}Li+^{209}Bi, and ^{9}Be+^{208}Pb were studied. Similar results were reached in the previous research [22], by Fouad A. Majeed and Yousif A. Abdul-Hussien conducted a study on systems ^{17}F + ^{208}Pb and ^{15}C + ^{232}Th and found that the couple-channel effect between the elastic and continuous channel is very necessary for the calculations of σ_{fus} and D_{fus} where the results improved below and around the Coulomb barrier are very significant about the full quantum mechanics approach, [23]. To confirm the results they reached, they did another study of the systems ^{6}He +^{238}U and ^{8}He +^{197}Au that improved the calculations around and below the Coulomb barrier [23].

The present study aims to investigate the effect of neutron or proton transfer and the impact of coupling between the elastic and breakup channels on the calculations of σ_{fus}, D_{fus}, and P_{fus}, for the systems ^{28}Si + ^{90}Zr, ^{28}Si + ^{92}Zr, ^{28}Si + ^{94}Zr, ^{41}K + ^{28}Si, and ^{45}K + ^{28}Si. And compare the results with the related experimental data.

2. THE SEMICLASSICAL THEORY
2.1 No-Coupling or One-Channel Description

One-dimensional potential models have been utilized to evaluate the fusion Cross-section by employing the semiclassical theory. This model assumes that the degree of freedom of the colliding heavy ions can only be described by their relative motion [25, 26]. The Schrödinger equation is central to the semi-classical theory, which takes into account the energy and angular momentum of the system as well as the energy of the potential of the radial component of relative motion. Quantum tunneling is also considered in this theory. As a result, the semi-classical theory provides a comprehensive framework for understanding the behavior of quantum systems. cross-section of the fusion can be evaluated by implementing the semi-classical theory within the one-dimensional potential model [22].

$$\left(\frac{-\hbar^2 \nabla^2}{2\mu} + V_{(r)} - E\right) \psi_{(r)} = 0. \tag{1}$$

In this context, the system's potential is denoted by $V(r)$, while μ represents the reduced mass of the system. To determine the wave-functions described in equation 1, one can utilize the time-dependent Schrodinger equations. To accomplish this, one can propose a particle trajectory based on Rutherford's usual trajectory. And include the real component of both the Coulomb potential and the centrifugal potential, which is expressed in [26]. This methodology allows for the estimation of said wave-functions.

$$V(r) = V_C(r) + V_N(r) + V_\ell(r). \tag{2}$$

To consider profound absorption in the classically prohibited elastic channel scattering coupled-channel calculations, including the imaginary part of nuclear potential., which is complex, is essential [26].

$$V_N(r) = U_N(r) - iW(r). \tag{3}$$

Researchers have employed the wave expansion technique to investigate the considerable absorption resulting from the interference of (ℓ)waves, which originates from both the actual and imaginary components of the nuclear potential. Previous studies, as per the semi-classical theory, have demonstrated that fusion arises when two nuclei approach each other and pass through the potential barrier to enter the inner region. In this scenario, the WKB method can be utilized to determine the probability of penetration below the barrier. These findings have been documented in multiple sources, including references [25, 27, 28, 29, 30].

$$P_{fus}^{WKB}(\ell, E) = \left[1 + e^{\left(2\int_{r_b^\ell}^{r_a^\ell} K_\ell(r)dr\right)}\right]^{-1} \tag{4}$$

Eqn. 4 can be expressed as where the local wave-function number is ℓ (r), limits, r_a^ℓ and r_b^ℓ are as defined by places of turning to the classical trajectory.

$$P_{fus}^{WKB}(\ell, E) = \left[1 + e^{\frac{2\pi}{\hbar\Omega_\ell}(Vb(\ell) - E)}\right]^{-1} \tag{4}$$

Given that the fusion barrier can be adjusted using a parabolic function, the Hill-Wheeler formula [26] can be employed to depict the likelihood of penetration.

$$P_{fus}^{WH}(\ell, E) = \left[1 + e^{\frac{2\pi}{\hbar\Omega_\ell}(E - Vb(\ell))}\right]^{-1} \tag{5}$$

The fusion barrier cross-section can be calculated using equations [28,31] by employing the (WKB) approximation, where Ω_l and $V_b (l)$ represent the curvature and height parameters of the barrier, respectively. The energy from the projectile bombing the target is indicated by E.

$$\sigma_F(E) = \frac{\pi}{k^2} \sum (2\ell + 1) P_{fus}^{WKB}(\ell, E) \tag{7}$$

$$P_{fus}^\gamma(\ell, E) = \frac{4k}{E} \int \left|u_{\gamma\ell}(k_\gamma, r)\right|^2 W_{fus}^\gamma(r) \tag{8}$$

The radial component of the wave-function for the ℓ partial wave in the γ-channel is denoted by $u_{\gamma l}(k\gamma, r)$, while the potential imaginary part is represented by $W_{fus}^\gamma (r)$.

2.2. The Coupled Channels Formalism

To depict the collision, we're using the projectile-to-target separation vector.$\vec{r}$ and the projectile's appropriate intrinsic degrees of freedom ζ. To simplify, we do not consider the internal arrangement of the target. The Hamiltonian can be expressed as [32].

$$H = H_0(\xi) + V(\vec{r}, \xi) \tag{9}$$

In this study, we ignore the nuclear coupling and focus solely on the interaction between the projectile and the target, which is represented by the term $V(\vec{r}, \xi)$ in the intrinsic Hamiltonian of the projectile denoted as $H_0(\xi)$. We limit our theoretical comparison to the Coulomb dipole term. The equation [32] provides the eigenvectors of $H_0(\xi)$.

$$H_0|\varphi_\beta\rangle = \varepsilon_\beta|\varphi_\beta\rangle \tag{10}$$

The energy of internal motion is denoted by ε_β, and the Alder and Winther (AW) [33] approach involves two main steps. Firstly, classical mechanics is used to model the time growth of variable $\vec{r}$, where the resulting trajectory is influenced by angular momentum ℓ and collision energy E. In the original version of AW, a symmetrized Rutherford trajectory was utilized. However, in our case, the trajectory is determined by solving classical equations of motion with the potential $V(\vec{r}) = \langle\varphi_0 | V(\vec{r}, \xi)\varphi_0\rangle$, where $|\varphi_{\beta0}\rangle$ represents the ground state of the projectile. This transforms the coupling interaction into a time-dependent interaction in the ξ-space, given by $V_\ell(\xi, t) \equiv V(\vec{r}_\ell(t), \xi)$. The second step involves treating the dynamics in the intrinsic space as a problem in time-dependent quantum mechanics. This is achieved by expanding the wave function based on intrinsic eigenstates [33].

$$\psi(\xi, t) = \sum_\beta a_\beta(\ell, t)\varphi_\beta(\xi)e^{-\frac{i\varepsilon_\beta t}{\hbar}} \tag{11}$$

By plugging this spread into the Schrödinger equation for the wave function $\psi(\xi, t)$, we arrive at the AW equations as described in reference [28].

$$i\hbar\dot{a}_\beta(\ell, t) = \sum_\alpha a_\gamma(\ell, t)\langle\varphi_\beta|V_\ell(\xi, t)|\varphi_\beta\rangle e^{\frac{-i(\varepsilon_\beta - \varepsilon_\gamma)t}{\hbar}} \tag{12}$$

To solve these equations, the initial conditions used were $a_\beta(\ell, t \to -\infty) = \delta_{\beta0}$. This signifies that the projectile was in its ground state before the collision ($t \to -\infty$). The resulting population of the channel after the collision corresponds to a specific angular momentum $\ell : P_\ell^\beta = \left|a_\beta(\ell, t \to +\infty)\right|^2$, the cross-section of the angle-integrated [33]

$$\sigma_\beta = \frac{\pi}{k^2}\sum_\ell (2\ell + 1)P_\ell^{(\beta)} \tag{13}$$

To apply this technique to fusion reactions, we begin by utilizing quantum mechanics to compute the fusion cross section in a coupled-channel scenario. To simplify the process, we assume that all channels are bound and have no spins.

The total fusion cross-section can be obtained by adding up the contributions from each channel. By conducting partial-wave expansions, we arrive at the following equation as shown in reference [34].

$$\sigma_F \& = \sum_\beta \left[\frac{\pi}{k^2} \sum_\ell (2\ell + 1) P_\ell^F(\beta) \right]. \tag{14}$$

$$P_\ell^F(\beta) = \frac{4k}{E} \int W_\beta^F(r) \left| u_{\beta\ell}(k_\beta, r) \right|^2. \tag{15}$$

The optical potentials of the imaginary part connected to fusion in the channel $(u_{\beta\ell}(k_\beta, r))$ above have an absolute value of (W_β^F) and the radial wave function for the ℓth partial wave is (β) in the equation above.

One possible way to estimate the likelihood of fusion occurring is by using the following approximation:

$$P_\ell^{(\beta)} \cong \tau_\ell \left| a_\beta(\ell, t_{ca}) \right|^2. \tag{16}$$

Let τ_ℓ denote the transmission factor through the barrier, and $\left| a_\beta(\ell, t_{ca}) \right|^2$ be the probability of finding the system in the channel β at the point of closest approach (t_{ca}). [35-36]

3. Distribution of Fusion Barrier

$$D_{fus}(E) = \frac{d^2 F(E)}{dE^2}. \tag{17}$$

Accurately determining the distribution of the fusion barrier parameter $Dfus$ is crucial, as it is highly sensitive and has been defined in previous research [29, 31]. The function denoted as $F(E)$ represents the distribution of fusion barriers and is defined as follows:

$$F(E) = E\sigma_{fus}(E) \tag{18}$$

Considerable progress has been made in comprehending the fusion reaction by establishing the reaction fusion barrier distribution through experimentation. To determine the uncertainties in numerical fusion barrier calculations, it is possible to refer to the reaction [37, 38].

$$D_{fus}(E) \cong \frac{F(E+\Delta E) + F(E-\Delta E) - 2F(E)}{\Delta E^2} \tag{19}$$

In this case, the cross-sectional data were measured at various excitation energy points, with an interval of ΔE. To determine the statistical error, the relation [29] was utilized.

$$\delta D_{fus}^{stat}(E) \approx \frac{\left[\ [\delta F(E+\Delta E)]^2 + [\delta F(E-\Delta E)]^2 + 4[\delta FE]^2 \ \right]^{\frac{1}{2}}}{\Delta E^2} \tag{20}$$

The uncertainty in the product of $(E\sigma_f)$ for each collision energy, denoted by $\delta F(E)$, is given as [29].

$$\delta D_{fus}^{stat}(E) \cong \frac{\sqrt{6}\delta F(E)}{[\Delta E]^2} \tag{21}$$

4. RESULTS AND DISCUSSION

This section presents the theoretical calculations of the fusion reaction σ_{fus}, the fusion barrier distribution D_{fus} and the fusion probability P_{fus}. These calculations were obtained using the semi-classical theory with a Continuum Discretized Coupled Channel (CDCC) [39] approach to study the effect of calculating the coupling between elastic channels and breakup channels on fusion processes. The calculations were performed using the Sequential Complete Fusion SCF [40] code for semi-classical comparisons, while the quantum mechanical calculations were performed using the CC code for the systems, $^{28}Si + ^{90}Zr$, $^{28}Si + ^{92}Zr$, $^{28}Si + ^{94}Zr$, $^{41}K + ^{28}Si$, and $^{45}K + ^{28}Si$. Table 1 presents the parameters for the Akyüz-Winther potential, with a coulomb barrier.

Table 1. The Coulomb barrier height V_b and The Akyüz-Winther potential parameters

System	Real part			Imaginary part					
	V_o	r_o	a_o	w_o	r_i	a_i	L_{max}	L_{min}	V_b
28Si+90Zr	-146.1	1.055	0.800	-27.7	1.007	0.736	63	0	73.66
28Si+92Zr	-60.1	1.210	0.850	-14.4	1.007	0.736	31	0	72.15
28Si+94Zr	-140	1.100	0.800	-27.0	1.008	0.735	57	0	71.44
41K+28Si	-46.0	1.212	0.655	-15.3	0.983	0.750	46	0	37.48
45K+28Si	-46.9	1.198	0.705	-15.6	0.986	0.748	45	0	36.86

4.1. (^{28}Si+^{90}Zr) reaction

Figure 1. The three drawings below depict the theoretical and experimental σ_{fus}, D_{fus} and P_{fus} for the system, obtained through a combination of quantum mechanical calculations and semi-classical methods. The data used in this study are taken from Ref. [41]. The blue curves correspond to the quantum mechanical calculations with coupling and no-coupling, respectively. The blue curve with the spaces shows the results obtained with no-coupling. Similarly, the red curves, correspond to the semi-classical calculations with and no-coupling, respectively. The dashed red curve shows the results obtained no-coupling. The system's data regarding the position of the Coulomb sub-barrier V$_b$ are sourced from the black arrow. The semi-classical calculations, no-coupling and coupling have a great concurrence with experimental data after exceeding V$_b$, and for below V$_b$, there is no concurrence with experimental data. For no-coupling and coupling quantum mechanical calculation, after exceeding V$_b$ there is a special concurrence.
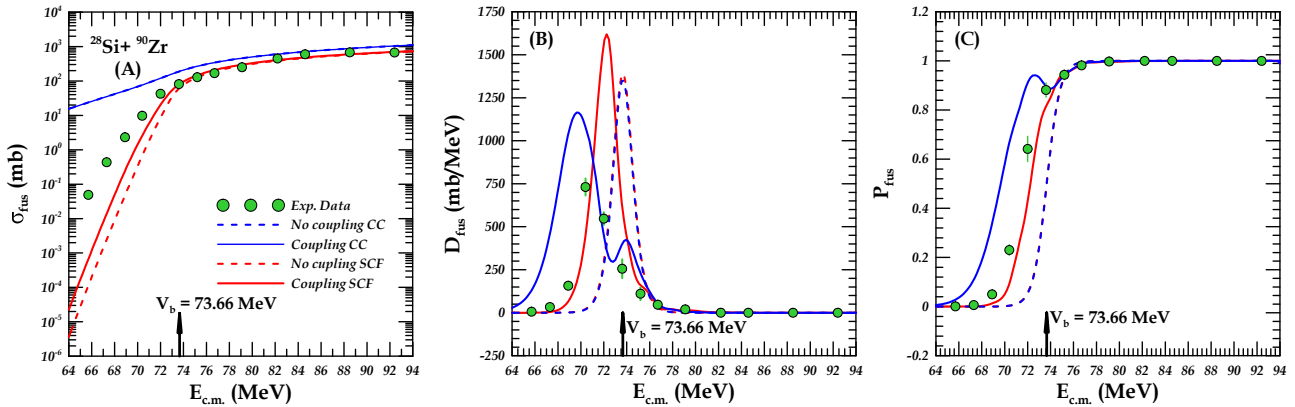
Figure 1. Displays the results of quantum mechanical and semi-classical calculations for the σ_{fus} drawing (A), D_{fus} drawing (B), and P_{fus} drawing (C), alongside experimental data [41] for the system ^{28}Si+^{90}Zr.

4.2 (^{28}Si+^{92}Zr) reaction

Figure 2. The three drawings below depict the theoretical and experimental σ_{fus}, D_{fus} and P_{fus} for the system, obtained through a combination of quantum mechanical calculations and semi-classical methods. The data used in this study are taken from Ref. [42]. The blue curves correspond to the quantum mechanical calculations with coupling and no-coupling, respectively. The blue curve with the spaces shows the results obtained with no-coupling. Similarly, the red curves, correspond to the semi-classical calculations with and no-coupling, respectively. The dashed red curve shows the results obtained no-coupling. The system's data regarding the position of the Coulomb sub-barrier V$_b$ are sourced from the black arrow. The semi-classical calculations, no-coupling and coupling have a special concurrence with experimental data after exceeding V$_b$ and below V$_b$. For no-coupling and coupling quantum mechanical calculation, after exceeding V$_b$ there is a special concurrence.
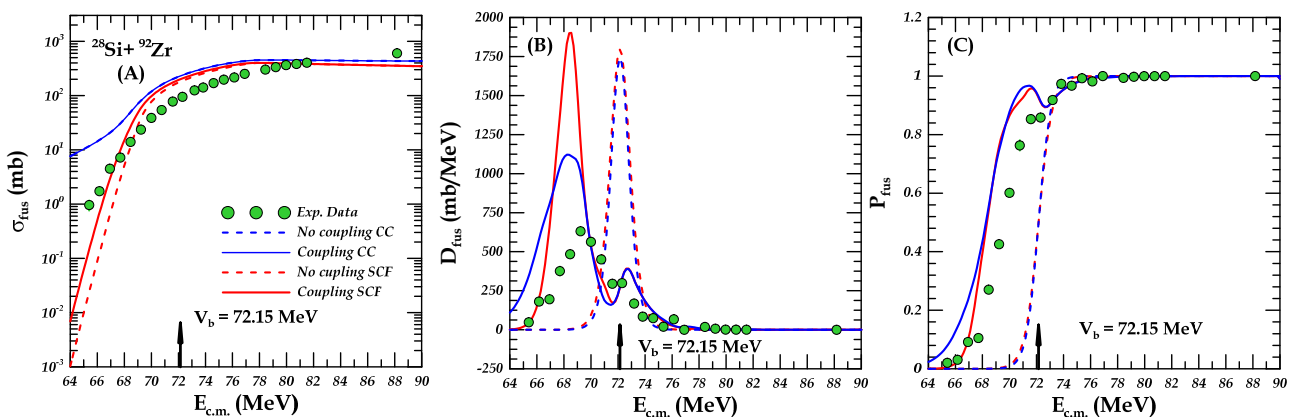
Figure 2. Displays the results of quantum mechanical and semi-classical calculations for the σ_{fus} drawing (A), D_{fus} drawing (B), and P_{fus} drawing (C), alongside experimental data [42] for the system ^{28}Si+^{92}Zr.

4.3. (^{28}Si+^{94}Zr) reaction

Figure 3. The three drawings below depict the theoretical and experimental σ_{fus}, D_{fus} and P_{fus} for the system, obtained through a combination of quantum mechanical calculations and semi-classical methods. The data used in this study are taken from Ref. [41]. The blue curves correspond to the quantum mechanical calculations with coupling and no-coupling, respectively. The blue curve with the spaces shows the results obtained with no-coupling. Similarly, the red curves, correspond to the semi-classical calculations with and no-coupling, respectively. The dashed red curve shows the

results obtained no-coupling. The system's data regarding the position of the Coulomb sub-barrier V_b are sourced from the black arrow. The semi-classical calculations, no-coupling and coupling have a good concurrence with experimental data after exceeding V_b, and for below V_b, there is a special concurrence. For no-coupling and coupling quantum mechanical calculation, there is no concurrence.
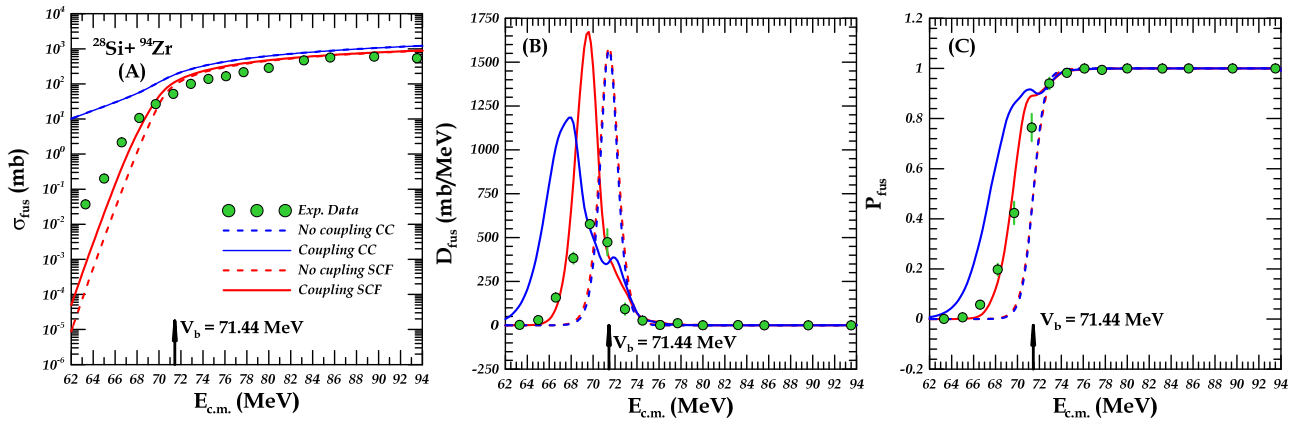
Figure 3. Displays the results of quantum mechanical and semi-classical calculations for the σ_{fus} drawing (A), D_{fus} drawing (B), and P_{fus} drawing (C), alongside experimental data [41] for the system ^{28}Si+^{94}Zr.

4.4. (^{41}K+ ^{28}Si) reaction

Figure 4. The three drawings below depict the theoretical and experimental σ_{fus}, D_{fus} and P_{fus} for the system, obtained through a combination of quantum mechanical calculations and semi-classical methods. The data used in this study are taken from Ref. [43]. The blue curves correspond to the quantum mechanical calculations with coupling and no-coupling, respectively. The blue curve with the spaces shows the results obtained with no-coupling. Similarly, the red curves, correspond to the semi-classical calculations with and no-coupling, respectively. The dashed red curve shows the results obtained no-coupling. The system's data regarding the position of the Coulomb sub-barrier V_b are sourced from the black arrow. The semi-classical calculations, no-coupling have a special concurrence with experimental data after exceeding V_b, and for below V_b there is no concurrence, and for coupling, there is a great concurrence. For quantum mechanical calculation, there is a great concurrence after exceeding V_b.
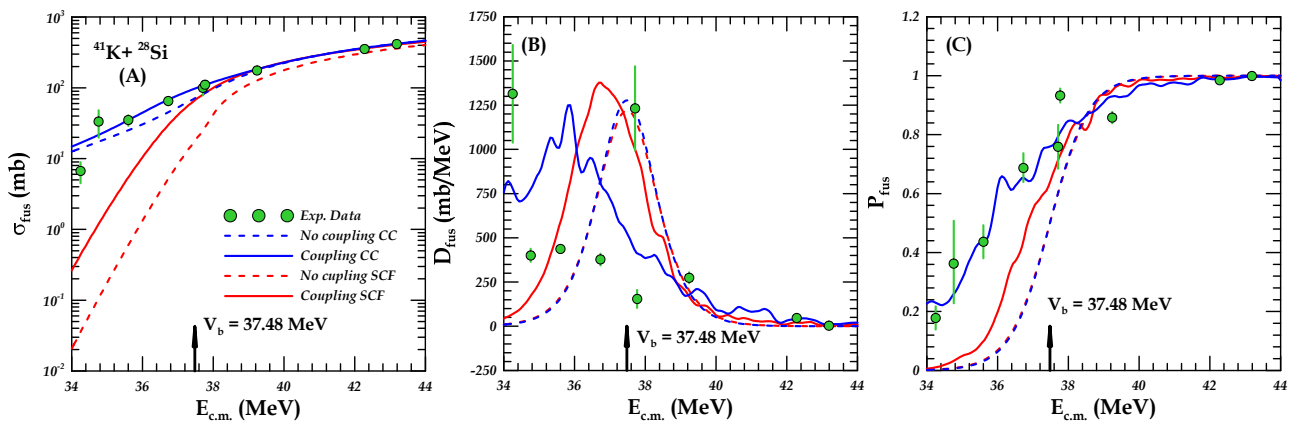
Figure 4. Displays the results of quantum mechanical and semi-classical calculations for the σ_{fus} drawing (A), D_{fus} drawing (B), and P_{fus} drawing (C), alongside experimental data [43] for the system ^{41}K+^{28}Si.

4.5. (^{45}K+ ^{28}Si) reaction

Figure 5. The three drawings below depict the theoretical and experimental σ_{fus}, D_{fus} and P_{fus} for the system, obtained through a combination of quantum mechanical calculations and semi-classical methods. The data used in this study are taken from Ref. [43]. The blue curves correspond to the quantum mechanical calculations with coupling and no-coupling, respectively. The blue curve with the spaces shows the results obtained with no-coupling. Similarly, the red curves, correspond to the semi-classical calculations with and no-coupling, respectively. The dashed red curve shows the results obtained no-coupling. The system's data regarding the position of the Coulomb sub-barrier V_b are sourced from the black arrow. The semi-classical calculations, no-coupling and coupling have a good concurrence with experimental data after exceeding V_b. For no-coupling and coupling quantum mechanical calculation, below V_b there is a great concurrence.
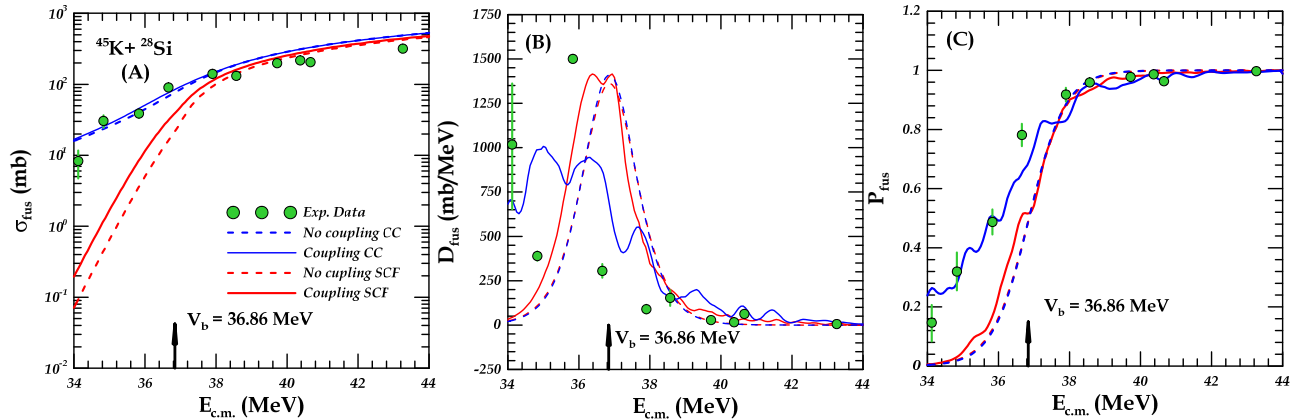
Figure 5. Displays the results of quantum mechanical and semi-classical calculations for the σ_{fus} drawing (A), D_{fus} drawing (B), and P_{fus} drawing (C), alongside experimental data [43] for the system ^{45}K+^{28}Si.

5. CONCLUSION

The effect of channel coupling between elastic channels and breakup channels on calculating fusion cross-section (σ_{fus}), fusion barrier distribution (D_{fus}), and fusion probability (P_{fus}), on systems ^{28}Si + ^{90}Zr, ^{28}Si + ^{92}Zr, ^{28}Si + ^{94}Zr, ^{41}K + ^{28}Si, and ^{45}K + ^{28}Si were investigated in the present study and these systems involved one neutron or one proton transfer reactions. Our theoretical calculations showed that the results improved significantly below the Coulomb barrier, especially the semi-classical calculations. The reason for the improvement below the Coulomb barrier can be attributed to the fact that coupling effects become more significant at lower energies, leading to a more complex interaction between the elastic channels and the breakup channels. Introducing coupling conditions into the calculations takes into account the exchange of flow between these channels, which results in better agreement with the experimental data. On the other hand, the slight overestimation of the results above the Coulomb barrier can be attributed to the fact that the fusion process becomes more controlled by the elastic channel at higher energies, and the coupling effects become less significant. The reason for the overestimation of the cross-section may be the fact that our calculations may not have fully accounted for the effect of the Coulomb barrier on the merger process.

ORCID

M.A. Khuadher, https://orcid.org/0009-0006-5372-547X; **F.A. Majeed,** https://orcid.org/0000-0002-0701-9084

REFERENCES

[1] M. Beckerman, "Sub-barrier fusion of two nuclei," Reports on Progress in Physics, **51**(8), 1047 (1988). https://doi.org/10.1088/0034-4885/51/8/001

[2] J.E. Johnstone, V. Singh, R. Giri, S. Hudan, J. Vadas, R.T. Desouza, D. Ackermann, A. Chbihi, Q. Hourdille, A. Abbott, and C. Balhoff, "Proton and neutron exchange as a prelude to fusion at near-barrier energies," Physical Review C, **106**(1), L011603, (2022). https://doi.org/10.1103/PhysRevC.106.L011603

[3] K. Hammerton, Z. Kohley, D.J. Hinde, M. Dasgupta, A. Wakhle, E. Williams, V.E. Oberacker, A.S. Umar, I.P. Carter, K.J. Cook, and J. Greene, "Reduced quasifission competition in fusion reactions forming neutron-rich heavy elements," Physical Review C, **91**(4), 041602 (2015). https://doi.org/10.1103/PhysRevC.91.041602

[4] S. Hudan, R.T. deSouza, A.S. Umar, Z. Lin, and C.J. Horowitz, "Enhanced dynamics in fusion of neutron-rich oxygen nuclei atbove- energies," Physical Review C, **101**(6), 061601 (2020). https://doi.org/10.1103/PhysRevC.101.061601

[5] H.M. Jia, C.J. Lin, L. Yang, X.X. Xu, N.R. Ma, L.J. Sun, F. Yang, Z.D. Wu, H.Q. Zhang, Z.H. Liu, and D.X. Wang, "A self-consistent method to analyze the effects of the positive Q-value neutron transfers on fusion," Physics Letters B, **755**, 43-46 (2016). https://doi.org/10.1016/j.physletb.2016.01.058

[6] M. Beckerman, M. Salomaa, A. Sperduto, H. Enge, J. Ball, A. DiRienzo, S. Gazes, Y. Chen, J.D. Molitoris, and M. Nai-Feng, "Dynamic influence of valence neutrons upon the complete fusion of massive nuclei," Physical Review Letters, **45**(18), 1472 (1980). https://doi.org/10.1103/PhysRevLett.45.1472

[7] R.A. Broglia, C.H. Dasso, S. Landowne, and A. Winther, "Possible effect of transfer reactions on heavy ion fusion at sub-barrier energies," Physical Review C, **27**(5), 2433 (1983). https://doi.org/10.1103/PhysRevC.27.2433

[8] S. Kalkal, S. Mandal, N. Madhavan, E. Prasad, S. Verma, A. Jhingan, R. Sandal, S. Nath, J. Gehlot, B.R. Behera, and M. Saxena, "Channel coupling effects on the fusion excitation functions for Si28+ Zr90,94 in sub-and near-barrier regions," Physical Review C, **81**(4), 044610 (2010). https://doi.org/10.1103/PhysRevC.81.044610

[9] A.M. Stefanini, L. Corradi, A.M. Vinodkumar, Y. Feng, F. Scarlassara, G. Montagnoli, S. Beghini, and M. Bisogno, "Near-barrier fusion of ^{36}S+^{90,96}Zr: The effect of the strong octupole vibration of ^{96}Zr," Physical Review C, **62**(1), 014601 (2000). https://doi.org/10.1103/PhysRevC.62.014601

[10] V.Y. Denisov, "Subbarrier heavy ion fusion enhanced by nucleon transfer," The European Physical Journal A-Hadrons and Nuclei, **7**, 87-99 (2000). https://doi.org/10.1007/s100500050015

[11] W. Kohn, and L.J. Sham, "Self-consistent equations including exchange and correlation effects," Physical Review, **140**, A1133 (1965). https://doi.org/10.1103/PhysRev.140.A1133

[12] V. Singh, J. Vadas, T. K. Steinbach, B. B. Wiggins, S. Hudan, R. T. deSouza, Z. Lin, C. J. Horowitz, L. T. Baby, S. A. Kuvin, and V. Tripathi, "Fusion enhancement at near and sub-barrier energies in $^{19}O+^{12}C$," Phys. Lett. B, **765**, 99 (2017). https://doi.org/10.1016/j.physletb.2016.12.017

[13] B.A. Bian, F.S. Zhang, and H.Y. Zhou, "Fusion enhancement in the reactions of neutron-rich nuclei," Nucl. Phys. A, **829**, 1 (2009). https://doi.org/10.1016/j.nuclphysa.2009.08.003

[14] C. Beck, "Transfer/Breakup Channel Couplings in Sub-barrier Fusion Reactions," J. Phys. Conf. Ser. **420**, 012067 (2013). https://doi.org/10.1088/1742-6596/420/1/012067

[15] N. Rowley, I.J. Thompson, and M.A. Nagarajan, "Neutron flow and necking in heavy-ion fusion reactions," Phys. Lett. B, **282**, 276 (1992). https://doi.org/10.1016/0370-2693(92)90638-K

[16] R. Pengo, D. Evers, K.E.G. Löbner, U. Quade, K. Rudolph, S.J. Skorka, and I. Weidl, "Nuclear structure effects in sub-barrier fusion cross sections," Nucl. Phys. A, **411**, 255 (1983). https://doi.org/10.1016/0375-9474(83)90392-5

[17] H. Timmers, D. Ackermann, S. Beghini, L. Corradi, J.H. He, G. Montagnoli, F. Scarlassara, A.M. Stefanini, and N. Rowley, "A case study of collectivity, transfer and fusion enhancement," Nucl. Phys. A, **633**, 421 (1998). https://doi.org/10.1016/S0375-9474(98)00121-3

[18] V.I. Zagrebaev, "Sub-barrier fusion enhancement due to neutron transfer," Phys. Rev. C, **67**, 061601(R) (2003). https://doi.org/10.1103/PhysRevC.67.061601

[19] M.S. Gautam, S. Duhan, R.P. Chahal, H. Khatri, S.B. Kuhar, and K. Vinod, "Influence of neutron transfer channels and collective excitations in the fusion of Si^{28} with $Zr^{90,92,94,96}$ targets," Phys. Rev. C, **102**, 014614 (2020). https://doi.org/10.1103/PhysRevC.102.014614

[20] G.L. Zhang, X.X. Liu, and C.J. Lin, "Systematic analysis of the effect of a positive Q-value neutron transfer in fusion reactions," Phys. Rev. C, **89**, 054602 (2014). https://doi.org/10.1103/PhysRevC.89.054602

[21] F.A. Majeed, Y.A. Abdul-Hussien, and F.M. Hussian, "Fusion Reaction of Weakly Bound Nuclei," in: *Nuclear Fusion-One Noble Goal and a Variety of Scientific and Technological Challenges*, edited by I. Girka, (University of Kharkiv, Ukraine, 2019). https://doi.org/10.5772/intechopen.80582

[22] F.K. Ahmed, F.A. Majeed, and T.M. Abbass, *The Effect of Breakup on the Total Fusion Reaction Cross Section of Stable Bound Nuclei*, (University of Babylon, 2012). https://repository.uobabylon.edu.iq/papers/publication.aspx?Pubid=5446

[23] F.A. Majeed, and Y.A. Abdul-Hussien, "Fusion and Breakup Reactions of $^{17}S+^{208}Pb$ and $^{15}C+232Th$ Halo Nuclei Systems," J. Adv. Phys. **11**, 2 (2015).https://rajpub.com/index.php/jap/article/view/495jap

[24] F.A. Majeed, and Y.A. Abdul-Hussien, "Semiclassical treatment of fusion and breakup processes of $^{6,8}He$ halo nuclei," J. Theor. Appl. Phys. **10**(2), 107-112 (2016). https://doi.org/10.1007/s40094-016-0207-y

[25] L.F. Canto, R. Donangelo, and H.D. Marta, "Semiclassical treatment of fusion processes in collisions of weakly bound nuclei," Phys. Rev. C, **73**, 034608 (2006). https://doi.org/10.1103/PhysRevC.73.034608

[26] K. Alder, and A. Winther, *Electromagnetic Excitations*, (North-Holland, Amsterdam, 1975)

[27] P.R.S. Gomes et al., "Effect of the breakup on the fusion and elastic scattering of weakly bound projectiles on Zn 64," Phys. Rev. C, **71**, 034608 (2005). https://doi.org/10.1103/PhysRevC.71.034608

[28] L. F. Canto et al., "Recent developments in fusion and direct reactions with weakly bound nuclei," Phys. Rep. 596, 1-86 (2015). https://doi.org/10.1016/j.physrep.2015.08.001

[29] C.A. Bertulani, and L.F. Canto, "Semiclassical calculation of Coulomb break-up of weakly-bound nuclei," Nucl. Phys. A, **539**, 163-176 (1992). https://doi.org/10.1016/0375-9474(92)90240-K

[30] P. Gomes, T. Penna, R.L. Neto, J. Acquadro, C. Tenreiro, P. Freitas, E. Crema, NC Filho, and M. Coimbra, "Nuclear fusion between heavy ions by the gamma-ray spectroscopy method," Nucl. Instr. and Meth. A, **280**, 395 (1989). https://doi.org/10.1016/0168-9002(89)90940-6

[31] M.S. Hussein, M.P. Pato, L.F. Canto, and R. Donangelo, "Real part of the polarization potential for induced 11 fusion reactions," Physical Review C, **47**(5), 2398-2402 (1993). https://doi.org/10.1103/PhysRevC.47.2398

[32] J.F. Liang, and C. Signorini, "Fusion induced by radioactive ion beams," International Journal of Modern Physics E, 14(8), 1121-1150 (2005). https://doi.org/10.1142/S021830130500382X

[33] K. Alder, and A. Winther, *Electromagnetic Excitations*, (North-Holland, Amsterdam, 1975).

[34] M. Abramowitz, and I.A. Stegun, *Handbook of Mathematical Functions*, (Dover Publications, New York, 1964).

[35] P.R.S. Gomes, J. Lubian, I. Padron, R.M. Anjos, D.R. Otomar, L.C. Chamon, and E. Crema, "Fusion, break-up and scattering bound nuclei," Revista Mexicana de Física, **52**, 23-29 (2006). https://www.scielo.org.mx/scielo.php?pid=S0035-001X2006001000006&script=sci_abstract&tlng=pt

[36] L.F. Canto, R. Donangelo, and H.D. Marta, "Upper bounds for fusion processes in collisions of weakly bound nuclei," Brazilian Journal of Physics, **35**, 884-887 (2005). https://doi.org/10.1590/S0103-97332005000500045

[37] M. Abramowitz, and I.A. Stegun, *Handbook of Mathematical Functions*, National Bureau of Standards, Applied Mathematics Series, vol. 55 (1972).

[38] N. Rowley, G.R. Satchler, and P.H. Stelson, "On the 'distribution of barriers' interpretation of heavy-ion fusion," Physics Letters B, **254**(1-2), 25-29 (1991). https://doi.org/10.1016/0370-2693(91)90389-8

[39] F.M. Nunes, and I.J. Thompson, "Multistep effects in sub-Coulomb breakup," Physical Review C, **59**(5), 2652 (1999). https://doi.org/10.1103/PhysRevC.59.2652

[40] L.F. Canto, R. Donangelo, and H.D. Marta, "Semiclassical treatment of fusion processes in collisions of weakly bound nuclei," Physical Review C, **73**, 034608 (2006). https://doi.org/10.1103/physrevc.73.034608

[41] S. Kalkal, S. Mandal, N. Madhavan, E. Prasad, S. Verma, A. Jhingan, R. Sandal, S. Nath, J. Gehlot, B.R. Behera, and M. Saxena, "Channel coupling effects on the fusion excitation functions for $Si^{28}+Zr^{90,94}$ in sub- and near-barrier regions," Physical Review C, **81**(4), 044610 (2010). https://doi.org/10.1103/PhysRevC.81.044610

[42] J.O. Newton, C.R. Morton, M. Dasgupta, J.R. Leigh, J.C. Mein, D.J. Hinde, H. Timmers, and K. Hagino, "Experimental barrier distributions for the fusion of ^{12}C, ^{16}O, ^{28}Si, and ^{35}Cl with ^{92}Zr and coupled-channels analyses," Physical Review C, **64**(6), 064608 (2001). https://doi.org/10.1103/PhysRevC.64.064608

[43] J.E. Johnstone, PhD thesis, "The influence of shell structure on near-barrier fusion of neutron-rich nuclei", Indiana University, 2022.

**ВПЛИВ ПРОТОНА І НЕЙТРОНА ЯК ЗОНДА ДЛЯ РЕАКЦІЇ ЯДЕРНОГО СИНТЕЗУ
ПРИ НАВКОЛОБАР'ЄРНИХ ЕНЕРГІЯХ**

М.А. Хуадер, Ф.А. Маджид
Факультет фізики, Освітній коледж чистих наук, Вавилонський університет, Ірак

У цьому дослідженні квантово-механічні розрахунки та напівкласичний підхід використовувалися для визначення ймовірності термоядерного синтезу (Pfus), розподілу бар'єрів термоядерного синтезу (Dfus) і поперечного перерізу синтезу (σfus) для систем ^{28}Si + ^{90}Zr, ^{28}Si + ^{92}Zr, ^{28}Si + ^{94}Zr, ^{41}K + ^{28}Si, and ^{45}K + ^{28}Si. Напівкласичний підхід передбачав використання наближення Венцеля–Крамерса–Бріллюена (WKB) для опису відносного руху між снарядом і цільовими ядрами та методу дискретизованого пов'язаного каналу (CDCC) Альдера-Вінтера (AW) для опису власний рух ядер. Результати показали, що врахування розрахунків каналу зв'язку для квантової механіки та напівкласичного підходу та його впливу на Pfus, Dfus та σfus для досліджуваних систем, що включають реакції переносу одного нейтрона або одного протона, є дуже важливим для розгляду зокрема навколо та під кулонівським бар'єром. Результати порівнювали з даними вимірювань і виявили розумну збіг.

Ключові слова: *канал розпаду;пружний канал; ядерний синтез; перенесення нейтронів; перенесення протонів*

NUCLEAR ENERGY LEVELS SCHEME OF 46Cr USING FPD6, FPY, AND KB3G INTERACTIONS†

Hasan A. Kadhim, Firas Z. Majeed

Department of Physics, College of Science, University of Baghdad, Baghdad, Iraq
*Corresponding Author e-mail: hasan.ali2204a@sc.uobaghdad.edu.iq

The 46Cr isotope nuclear energy levels were studied using low-level FP-LS shell inside the shell model calculations. Nuclear energy levels have been calculated using FPD6, KB3G, and FPY interactions in the fp-shell model space and F742 and F7MBZ in the f7/2 model space. The results are compared to one another and to the experimental data that is already accessible and specific outcomes are clearly in agreement. In addition to having a strong arrangement in the reproduced values of the energy levels scheme, the used model space interactions are the two-body matrix element in the fp-shell model space that is best fitted. Particularly below 3 MeV, the general estimation of the replicated data is good. The wave vectors and analysis are modeled in diagrammatic notation, and all inscriptions are given in this style. Utilizing the oscillator's potential, a single particle vector is built, using 40Ca as the core of the fp-shell and f7/2 model space. Results are obtained for all tested nuclei using the OXFORD BUENOS AIRES SHELL (OXBASH) model code.

Keywords: *Nuclear energy levels; FP Shell; FPY; Diagrammatic notation; FPD6; KB3G*
PACS: 21.10.-k, 21.60.-n, 21.60.Cs

1. INTRODUCTION

Many studies have been conducted to comprehend nuclear characteristics and internal composition. Because nuclei are so complicated, no comprehensive theory explains nuclear actions, characteristics, and structures [1]. The shell theory has many advantages and characteristics, such as model independence and applied physical N-N potential, in addition to the conventional Hamiltonian related to various types of eigenvectors and for a wide range of nuclei. The shell theory remains valid because it provides the primary theoretical techniques for achieving all measurable nuclei [1]. To obtain effective N-N matrix elements, excitation energies, binding energies, and spectroscopic factors were computed in the LS shell (1f7/2 1f5/2 2p3/2 2p1/2) [2]. Interactions between PN prompted the existence of an orbital distance at N = 32 in isotope-rich neutrons localized in the nearby magic nucleus 48Ca [3]. Inspections of filled pf-LS shell of A=48 nuclei were conducted [4], and Kuo-Brown (KB) [10] to KB1 and KB3G were changed. The isobaric sequences A = 50, A = 51, and A = 52 were investigated [5] using KB3G, FPD6, and KB3G [6]. The shell theory created a critical technique for carrying out such research. Realistic potentials are established in this theory, and the basis vectors are indicated by precise quantum numbers of parity (π), angular momentum (J), and isospin (T) [7]. Many studies [8] have been done to identify the distribution of Eigen functions and build the framework of the shell model [9].

The nuclear shell theory has been considered a significant theory for understanding nuclear structure [10]. Because of the extreme single-particle motion in spherical symmetry, only including powerful spin-orbit factors allowed the rethink of a wide variety of findings for isotopes near nuclear magic numbers [11]. Calculations were performed in model space of a complete fp-LS shell containing 1f7/2, 1f5/2, 2p3/2, 2p1/2 subshells, and 40Ca as a core. There is no limit to the number of particles that can be excited. A comparison of results with that of his results would thus shed light on the role of intruder g9/2 orbital, appropriate choice of core, and the effect of truncation on the particles to be excited, in addition to testing the suitability of GXPF1A interaction in explaining the experimental data [12]. Within shell model computations, nuclear energy levels, total angular momenta, and even-even parity for nucleons present outside closed and no core for 46Cr, which filled fp-shell (1f7/2, 1f5/2, 2p3/2, 2p1/2) were interesting. The nuclear energy spectrum of 46Cr was calculated using four interactions. The associations of FPD6, FPY, F742, F7MBZ, and KB3G are compared to each other to access experimental data. Shell model calculations were interesting for (42Ca, 44Ca, 46Ca, and 48Ca), which occupied fp-shell (1f7/2, 1f5/2, 2p3/2, and 2p1/2). Calculating the nuclear energy spectra of 42Ca, 44Ca, 46Ca, and 48Ca involved four interactions. The outcomes of the interactions between the FPD6, GXPF1, and KB3G are contrasted with one another and with the existing experimental data. In order to produce model space wave vectors and simultaneously obtain the similar model space effective interaction that was chosen for this investigation, the code OXBASH was used [13].

Nuclear energy levels in 44Sc [14] and 44Ca [15] were studied through a nuclear shell model considering 40Ca as an inert core, adopting FPD6, HW, and FPY as model space effective interactions, and comparing the reproduced data with experimental data. The code OXBASH was used to create model space wave vectors while also receiving the comparable model space effective interaction chosen for this research.

A model space factor has been constructed using F7MBZ that considers the single-particle potential (harmonic oscillator) and elastic magnetic electron scattering form factors for ^{41}Ca with ^{40}Ca as the inert core. The entire theory is then examined using the nuclear shell theory [16] and calculating Ca quadrupole moments (41, 43, 45, and 47) using the shell model [17].

The theoretical level schemes of the selected states of each nucleus that we use for our calculation in the FP-space model for different effective interactions GX1A, KB3G, FPD6, and GX1A often include the spins and association energies of the many levels that have been experimentally identified in ^{52}Ca. Spin spectra of $^{52-54}$Ca and $^{56-58}$Ca are produced for effective interactions [18]. According to the influence of certain physical characteristics, such as the electromagnetic properties effects, such as elastic longitudinal form factors, electric quadrupole moments, and magnetic dipole moments, the nuclear structure of specific cobalt (Co) isotopes with mass number A=56-60 has been examined. By adopting the single-particle wave functions of the harmonic oscillator, calculations involving GXFP1 interaction are presented using the fp model space [19].

This work calculates nuclear energy levels in Cr isotopes using the inert core Ca, the fp shell FPD6, KB3G, and FBY, the 1f7/2 subshell orbit FZMBZ, and F742 [20].

2. THEORY
2.1. Interacting Particles in One and Two Active Orbits
The wave function of two particles may be expressed as a product of a spin and an isospin-dependent portion [21]:

$$\Phi JMTTz\,(1,2) = \Phi JM(j(1)j(2))\Theta TTz(t(1)t(2)). \tag{1}$$

where $j + j = J$, and $t + t = T$ with $T = 0$ or 1 since t = 1/2.
The spin component of Eq. (1) now has a diagrammatic notation, which may be written as [21]:

$$\Phi_J(j(1)j(2)) = \sum \langle jmjm'|JM\rangle \phi_{jm}(1)\phi_{jm'}(2) \equiv \tag{2}$$

$\Phi_{jm}(1)$ and $\Phi_{jm'}(2)$ are the single-particle states for particles 1 and 2 with their angular momenta j coupled to a total J. The coupling yields:

$$P_{12}\Phi_{JM}(j(1)j(2)) = (-1)^{J-2j}\Phi_{JM}(j(1)j(2)) = -(-1)^J\Phi_{JM}(j(1)j(2)) \tag{3}$$

When P_{12}: interchanges operators So, the isospin-dependent part is [21]:

$$\Theta_{TT_Z}((1)t(2)) = \sum \langle tt_z tt'_z|TT_z\rangle \theta_{tt_Z}(1)\theta_{tt'_Z}(2) \equiv \tag{4}$$

The notation has been condensed to include spin and isospin as (j, $\rho \equiv (j, t)$, and $\Gamma \equiv (J, T)$. So, Eq. (1) can be rewritten as:

$$\Phi_\Gamma(1,2) = \tag{5}$$

A circular arc represents the anti-symmetry of a wave function, and one obtains for two particles in two distinct orbits ρ and λ.

$$\Phi_\Gamma^{as}(1,2) \equiv \tag{6}$$

For two particles in the same Orbit, the notation can be extended as follows:

$$\Phi_\Gamma^{as}(1,2) \equiv \tag{7}$$

One can be extended easily to wave functions of more than two particles in one Orbit ρ as

$$\Phi_\Gamma^{as}(1, 2, \ldots, n) \equiv \qquad \qquad \tag{8}$$

2.2 Coefficients of Fractional Parentage

The n-particle function with all particles in one Orbit ρ is given as [20]:

$$\Phi_\Gamma(1, 2, \ldots, n) = \qquad \qquad \tag{9}$$

The group ρ^{n-1} is coupled to J_g, T_g, x_g, with x_g denoting all further quantum numbers needed to specify the state $|\rho^{n-1}\rangle_g$ uniquely. When the operator P_{ij} interchanges all coordinates of particles i and j, then one obtains for $i, j \leq n-1$ dueto the anti-symmetry:

$$P_{ij} \qquad = \qquad = - \qquad . \tag{10}$$

However, the result of the permutation P_{ij} for i or j equal to n cannot be represented in general by a simple expression in terms of the original function, as in Eq (10).

$$\Phi_\Gamma^a(1, 2, \ldots, n) \equiv \qquad \qquad \tag{11}$$

The wave function of eq. (9) due to anti-symmetrization. Also, one can write:

$$\qquad \qquad = \sum \langle \rho^n \Gamma | \} \rho^{n-1} \epsilon \rangle \tag{12}$$

where $\langle \rho^n \Gamma | \} \rho^{n-1} \epsilon \rangle$ represented "coefficients of fractional parentage" or c.f.p. The normalization and orthogonality lead to the states $|\rho^n\rangle_{\Gamma x}$ being denoted by x as:

$$\sum_{\Gamma' x'} \langle \rho^n \Gamma x | \}^{-1} \Gamma' x' \rangle \langle \rho^n \Gamma x'' | \} \rho^{n-1} \Gamma' x' \rangle = \delta_{xx''}. \tag{13}$$

If the particle numbered k is willing to decouple, then the simple reordering based on equation (12) is as follows:

$$\Phi_\Gamma^{as}(1, 2, \ldots, k, \ldots, n) = (-1)^{n-k} \Phi_\Gamma^{as}(1, 2, \ldots, n, k). \tag{14}$$

The completely antisymmetric wave function leads to expansion [21].

$$\qquad = (-1)^{-k} \sum_g \langle \rho^n \Gamma | \} \rho^{n-1} \epsilon \rangle \qquad \tag{15}$$

It is useful to go over the derivation of c.f.p. in detail for the relatively simple case of three identical particles (maximum isospin) in one Orbit with j 7/2. Only for j 7/2 do three particles couple in a novel way to a given total spin J. Using the same diagrammatic representation as in [21], the coupling of three single-particle wave functions to a non-antisymmetrized function of total spin J can be obtained.

3. RESULTS AND DISCUSSION

For ⁴⁶Cr as illustrated in Fig. (1) the scheme is clear, experimental data has the values of ($0^+, 2^+, 4^+, 6^+, 8^+$) with the corresponding values (0.000, 0.892, 1.987, 3.226, 4.817) respectively, the reproduced data for the interaction (FPD6, FPY, F742, F7MBZ, and KB3G) are good in general and have the best sequence and slight differences from that of experimental data. All the ground states are the same, which is (0^+); the first excited state is 2^+, the second is 4^+, the third is 6^+ and the fourth is 8^+ and the order of sequences has coincided with all the reproduced results, but the

differences between interaction to another are obvious, the best results belong to FPD6 AND KB3G but the results of FPY are more shifted upward reflecting that the interaction in the same model space has different actions in the values of the study under respect. The energy levels in the range of E=0 -3 MeV are more interesting and the values higher than this range does not well reproduced because of the model adopted in our study and the interactions, in general do not reflect all the reactions inside the nucleus .shell theory and residual interaction do expect the term of two body matrix element and the fitting parameters, then the interaction succeeded or failed to reproduce the experimental data according to the term constructing the interaction and the range of consideration. Some interactions are best fitted to a range from A=42 to 48 and their fitting parameters are normalized on (A-42) terms which are taken from real (N –N) interaction where the Meson particles are the link between interacting nucleus.

Energy level density, as illustrated in Fig. (2), reveals that the states are condensed in the range of (5-6) MeV and decreased rapidly for all the interactions and the value of energy levels density varies from one interaction to another, but all of them reflect that there is a necessity to modify the analyzers in order to produce the energy level experimentally with hyperfine structure.
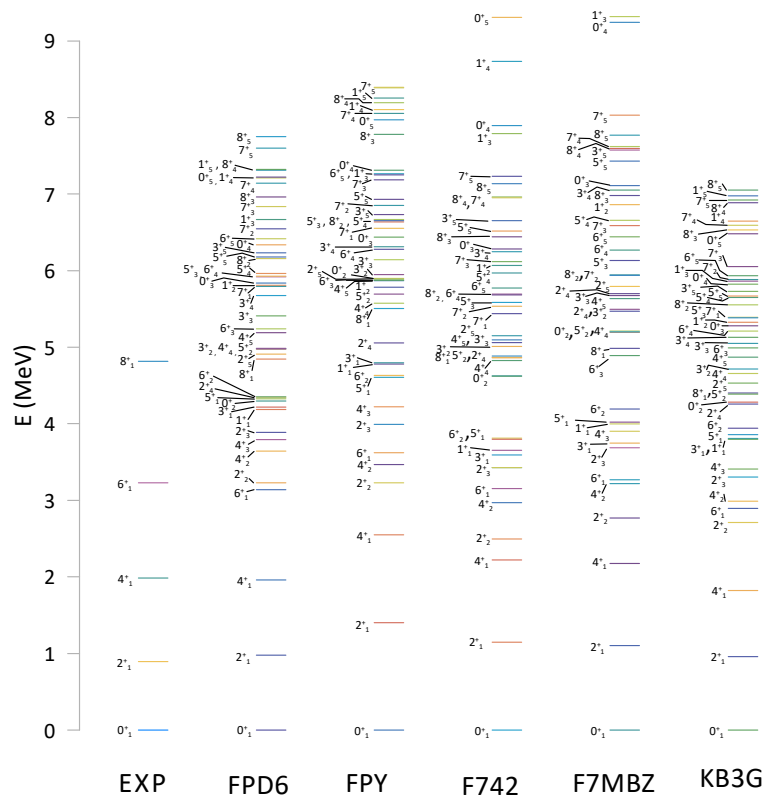
Figure 1. The energy levels scheme of ^{46}Cr by using FPD6, FPY, and KB3G interactions in fp shell model space and F742,and F7MBZ interactions in $1f_{7/2}$ model space with close core ^{40}Ca, positive parity, and ten order.
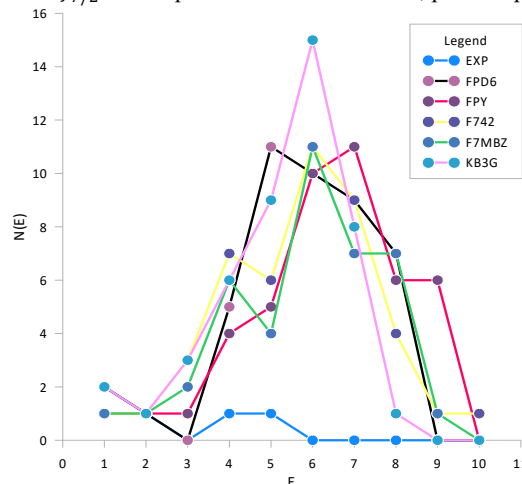
Figure 2. The density of states scheme of ^{46}Cr per 1MeV.

4. CONCLUSIONS

Modern society's effective interaction enhances energy levels and quality. The most suitable choice of interactions in some model spaces and for some isotopes needs to be determined by the values of binding energies and separation energies for both protons and neutrons reproduced by the chosen interaction. Then the interaction will succeed in the model space, according to shell theory. It will still be valid, and the obtained theoretical results will open a straight path for a physicist to modify the analyzers to measure experimental properties not yet reproduced.

ORCID
Hasan A. Kadhim, https://orcid.org/0009-0007-3164-0333; **Firas Z. Majeed,** https://orcid.org/0000-0001-6527-3913

REFERENCES

[1] M. Honma, T. Otsuka, B.A. Brown, and T. Minzusaki, "Effective interaction for pf-shell nuclei," Phys. Rev. C, **65**, 061301(R) (2002). https://doi.org/10.1103/PhysRevC.65.061301

[2] H. Crannell, R. Helm, H. Kendall, J. Oeser, and M. Yearian, "Electron-Scattering Study of Nuclear Levels in Cobalt, Nickel, Lead, and Bismuth," Phys. Rev. **123**(3), 923 (1961). https://doi.org/10.1103/PhysRev.123.923

[3] J.I. Prisciandaro, P.F. Mantica, B.A. Brown, D.W. Anthony, M.W. Cooper, A. Garcia, D.E. Groh, et al., "New evidence for a subshell gap at N=32," Phys. Lett. B, **510**, 17-23 (2001). https://doi.org/10.1016/S0370-2693(01)00565-2

[4] E. Caurier, and A.P. Zuker, Phys. Rev. C, **50**, 225 (1994). https://doi.org/10.1103/PhysRevC.50.225

[5] A. Poves, J. Sánchez-Solano, E. Caurier, and F. Nowacki, Nucl. Phys. A, **694**, 157 (2001). https://doi.org/10.1016/S0375-9474(01)00967-8

[6] W.A. Richter, M.G. Van Der Merwe, R.E. Julies, and B.A. Brown, Nucl. Phys. A, **532**, 325 (1991). https://doi.org/10.1016/0375-9474(91)90007-S

[7] V. Zelevinsky, B.A. Brown, N. Frazier, and M. Horoi, Phys. Rep. **276**, 8 (1996). https://doi.org/10.1016/S0370-1573(96)00007-5

[8] R.R. Whitehead, A. Watt, D. Kelvin, and A. Conkie, Phys. Lett. B, **76**, 149 (1978). https://doi.org/10.1016/0370-2693(78)90262-9

[9] B.A. Brown, G. Bertsch, Phys. Lett. B, **148**(1-3), 5 (1984). https://doi.org/10.1016/0370-2693%2884%2991598-3

[10] J. Suhonen, *From Nucleons to Nucleus Concepts of Microscopic Nuclear Theory*, (Springer, Finland, 2006).

[11] R.D. Lawson, *Theory of the Nuclear Shell Model*, (Clarendon Press, Oxford, New York, 1980).

[12] L. Coraggio, A. Covello, N. Itaco, and T.T.S. Kuo, Prog. Part. Nucl. Phys. **62**, 135 (2009). https://doi.org/10.1016/j.ppnp.2008.06.001

[13] F.Z. Majeed, and S.S. Mashaan, Indian Journal of Natural Sciences, **9**, 50 (2018).

[14] M.K. Hassan, and F.Z. Majeed, East Eur. J. Phys. **1**, 89 (2023), https://doi.org/10.26565/2312-4334-2023-1-10

[15] M.K. Hassan, and F.Z. Majeed, East Eur. J. Phys. **1**, 69 (2023), https://doi.org/10.26565/2312-4334-2023-1-07

[16] R. M. Hussien and F.Z. Majeed, BSJ, 19(6), 1395 (2022)

[17] A. H. Ali, BSJ, 17(2), (2020)507, http://dx.doi.org/10.21123/bsj.2020.17.2.0502

[18] A.M. Ali and A. A. Khamees, IJS, **60**, 60 (2019). https://doi.org/10.24996/ijs.2019.60.1.8

[19] B.S. Hameed, and B.K. Rejah, BSJ, **19**, 1566 (2022). https://dx.doi.org/10.21123/bsj.2022.7537

[20] B.A. Brown et al, OXBASH code, MSUNSCL Report 524 (1988).

[21] P.J. Brussaard, and P.W.M. Glademans, *Shell-model Applications in Nuclear Spectroscopy*, (North-Holland Publishing Company, Amsterdam, 1977).

СХЕМА РІВНІВ ЯДЕРНОЇ ЕНЕРГІЇ ^{47}Ca З ВИКОРИСТАННЯМ ВЗАЄМОДІЙ FPD6, FPY ТА KB3G
Хасан А. Кадхім, Фірас З. Маджід
Факультет фізики, Науковий коледж, Багдадський університет, Багдад, Ірак

Рівні ядерної енергії ізотопу ^{46}Cr досліджувалися з використанням низькорівневої оболонки FP-LS в оболонковій моделі. Рівні ядерної енергії були розраховані з використанням взаємодій FPD6, KB3G і FPY у просторі моделі fp-оболонки та F742 і F7MBZ у просторі моделі f7/2. Результати порівнюються один з одним а також з доступними експериментальними даними, і конкретні результати добре зходяться. На додаток до сильного збігу у відтворених значеннях схеми енергетичних рівнів, використані взаємодії простору моделі є матричним елементом двох тіл у просторі моделі fp-оболонки, який підходить найкраще. Зокрема, нижче 3 МеВ, загальна оцінка відтворених даних добра. Хвильові вектори та аналіз змодельовані у вигляді діаграм, і всі написи наведені в цьому стилі. Використовуючи осциляторний потенціал, будується єдиний вектор частинок, використовуючи ^{40}Ca як ядро простору моделі fp-оболонки та f7/2. Результати отримані для всіх перевірених ядер з використанням коду оболонкової моделі Оксфорд-Буенос-Айрес.
Ключові слова: *рівні ядерної енергії; FP оболонка; FPY; матричне позначення; FPD6; KB3G*

THE INFLUENCE CHANGING OF NUCLEAR POTENTIAL ON QUASI-ELASTIC SCATTERING IN ^{16}O+^{160}Gd AND ^{12}C+^{197}Au SYSTEMS[†]

Farah J. Hamood[§], Khalid S. Jassim*

Department of Physics, College of Education for pure Sciences, University of Babylon, Iraq
Corresponding Author e-mail: khalidsj@uobabylon.edu.iq, [§]e-mail: pure.farah.jabar@uobabylon.edu.iq

In this research, the effect of changing the potential depth V_0 on the Quasi-elastic scattering and barrier distribution calculations have been studied using Wood-Saxon (WS) potential for ^{16}O+^{160}Gd and ^{12}C+^{197}Au systems. The chi square ($\chi 2$) is applied to compare the best fitted value of the diffuseness parameter between the theoretical calculations and the experimental data. The diffuseness parameter which used in this work is to be at standard value 0.63. The χ^2 was applied to most suitable the better fitted value of the potential depth V_0. According to the results, we noticed that some systems achieved a good match between the theoretical calculations and experimental data of Quasi-elastic scattering ($d\sigma qel/d\sigma R$) and the distribution calculations at the standard value of the potential depth or at a value lower than the standard value and no match was achieved at a value greater than the standard value of the potential depth V_0. We conclude that the values of quasi-elastic scattering values increase when the value of potential depth decreases.

Keywords: *Quasi-elastic scattering; Woods-Saxon (WS) potential; Coupled; Heavy-ion system; Surface diffuseness parameter*
PACS: 21.60.-n, 21.10.-k, 21.60.Jz, 25.70.Bc, 25.70.

1. INTRODUCTION

The potential between two nuclei interaction, which comprises the short-range attractive and absorptive nuclear potentials as well as the long-range Coulomb potential, has always been a fundamental topic in nuclear physics. The Coulomb contact between two nuclei is widely understood, but describing the nuclear component is significantly more complex. Over the last few decades, the optical model potential (OMP) has been widely used to characterize the nuclear component, and numerous alternative potential forms have been proposed to replicate a large amount of nuclear reaction data [1][2]. In addition to nuclear reactions driven by light particles, the optical system may also be involved in nuclear reactions between heavy ions. The nuclear potential is often assumed to be of Woods-Saxon type, with three parameters defining it: depth, radius, and diffuseness. The diffuseness parameter defines the nuclear potential's fall-off and hence has a direct impact on the barrier width and coupling strengths, which are first order dependent on the derivative of the potential [3][4][5]. Quasi-elastic scattering is defined as "the sum of elastic scattering, inelastic scattering, and transfer reaction [6][7]. Quasi-elastic scattering is similar to the fusion process [7], which is defined as the combination of two different nuclei to generate a composite system. The Negative of the first derivative of the ratio of quasi-elastic to Rutherford cross-section, dqel/dR, with regard to the energy E, or $D_{qel} = d(dqel/dR)/dE$, is used to determine the quasi-elastic barrier distribution [8]. Several studies on quasi elastic scattering have been studied by Khalid S. Jassim for some heavy ions systems [9]–[11]. They demonstrated the nucleus-nucleus potential for several heavy ions by a comprehensive investigation of the surface characteristics. The nuclear potential has been described using WS, single-channel SC, and coupled-channel CC calculations, which were between the relative motion of colliding nuclei and their intrinsic motions, and they discovered that the best fitted value of the diffuseness parameter was obtained through a coupled-channel calculation with an inert target and excited projectile for the current work.

The aims of the present work is to study the influence changing of nuclear potential (potential depth V_0) on quasi-elastic scattering in systems^{16}O+^{160}Gd ,^{12}C+^{197}Au at surface diffuseness parameter it determined in earlier by the method chi square, we used The CQEL program [12] which contains all orders of coupling and is the most current iteration of the computer code CCFULL, was used to calculate single and coupled channels.

2. THEORY

The nucleus-nucleus potential is made up of two components, the first of which is the nuclear potential V_n, which may be properly and appropriately described by the other two parts of the potential between two nuclei. The form for Woods-Saxon (WS) supplied by [13]:

$$V_N(r) = - \frac{V_\circ}{1+e^{[\frac{r-R_\circ}{a}]}}, \tag{1}$$

where r represents the distance between the projectile's mass number AP and the target's mass number A_T at the center of mass, and R_0 stands for the system's radius: $R_0 = r_0\left(A_T^{\frac{1}{3}} + A_P^{\frac{1}{3}}\right)$. The second portion, which represents the Coulomb

---

potential V_C between two spherical nuclei with uniform charge density distributions when they are not interacting, is given by[13]:

$$V_c(r) = \frac{Z_P Z_T \ e^2}{r}, \tag{2}$$

where r is the distance between the centers of mass of the colliding nuclei, Z_p and Z_T are the atomic numbers of projectile and target, respectively. The Coulomb potential is produced when the nuclei interact, and it is determined by [14]:

$$V_c(r) = \frac{Z_P Z_T \ e^2}{2R_C}\left[3 - \left(\frac{r}{R_c}\right)^2\right], \tag{3}$$

where the projectile and target nuclei are represented by spheres of radii R_c. Two nuclei collide as a result of the nuclear intrinsic motion and the relative motion of their centers of mass, r = (r, r). The following is the Hamiltonian system[15]:

$$H(\vec{r}.\xi) = -\frac{\hbar^2}{2\mu}\nabla^2 + V(r) + H_0(\xi) + V_{coup}(\vec{r}.\xi), \tag{4}$$

where $V(r)$ is the bare potential in the absence of coupling where V(r) = V$_N$(r)+V$_c$(r), H$_0(\xi)$ is the Hamiltonian for the intrinsic motion, and V_{coup} is the stated coupling r stands for the center of mass distance between the colliding nuclei. The Schrodinger equation to wave functions is given by[16]:

$$\left(-\frac{\hbar^2}{2\mu}\nabla^2 + V(r) + H_0(\xi) + V_{coup}(\vec{r}.\xi)\right)\psi(\vec{r}.\xi) = E\psi(\vec{r}.\xi), \tag{5}$$

Internal degrees of freedom have a limited spin in general. the coupling Hamiltonian may be expressed as [15]:

$$V_{coup}(\vec{r}.\xi) = \sum_{\lambda>0.\mu} f_\lambda(r) Y_{\lambda\mu}(\hat{r}).\mathrm{T}_{\lambda\mu}(\xi), \tag{6}$$

The internal coordinate is used to create the harmonics and spherical tensors, which are represented by the notations $Y_{\lambda\mu}(\hat{r})$ and $\mathrm{T}_{\lambda\mu}(\xi)$, respectively. That when it was considered in V(r), the sum of all values of excluding for λ(r) = 0. For a constant total angular momentum J and its z-component M, the expansion basis for the wave function in Eq. (5) is given by [15]:

$$\langle \vec{r}\xi|(nlI)JM \rangle = \sum_{m_1 m_I}\langle lm_l \ Im_I|JM \rangle Y_{lm_l}(\hat{r}) \ \varphi_{nIm_I}(\xi), \tag{7}$$

where l stands for the orbital, I – internal angular momenta, and $\varphi_{nIm_I}(\xi)$ the wave function for the internal motion that is give by the equation below[15] .

$$H_0(\xi) \ \varphi_{nIm_I}(\xi) = \epsilon_n \ \varphi_{nIm_I}(\xi) , \tag{8}$$

The total wave function $\psi(\vec{r}.\xi)$ has been expanded as[16]:

$$\psi(\vec{r}.\xi) = \sum_{n.l.I}\frac{u_{nlI}^J(r)}{r}\langle \vec{r}\xi|(nlI)JM \rangle, \tag{9}$$

The Schrödinger equation [Eq. (3)] can be written as a collection of linked equations for $u_{nlI}^J(r)$:[16]

$$\left[-\frac{\hbar^2}{2\mu}\frac{d^2}{dr^2} + V(r) + \frac{l(l+1)\hbar^2}{2\mu r^2} - E + \epsilon_n\right]u_{nlI}^J(r) + \sum_{\acute{n}.\acute{l}.\hat{I}}V_{nlJ;\acute{n}.\acute{l}.\hat{I}}^J(r)u_{\acute{n}.\acute{l}.\hat{I}}^J(r) = 0 \tag{10}$$

The coupling matrix elements $V_{nlJ;\acute{n}.\ \acute{l}.\hat{I}}^J(r)$, According to [15] are as follows:

$$V_{nlJ;\acute{n}.\acute{l}.\hat{I}}^J(r) = \langle JM \ (nlI)|V_{coup}(\vec{r}.\xi)| \ (\acute{n}.\acute{l}.\hat{I})JM \rangle = \sum_\lambda(-1)^{I-\hat{I}+\acute{l}+J}f_\lambda(r)\langle l||Y_\lambda||\acute{l} \rangle\langle nI||T_\lambda||\acute{n}\acute{I} \rangle \times$$

$$\sqrt{(2l+1)(2I+1)}\begin{Bmatrix} I & \acute{l} & J \\ l & I & \lambda \end{Bmatrix}, \tag{11}$$

Where the reduced matrix elements in Eq. (8) is defined as follows[15]:

$$\langle l_{ml}|Y_{\lambda\mu}|\acute{l}_{m\acute{l}}\rangle = \langle \acute{l}_{m\acute{l}} \ \lambda\mu|l_{ml} \rangle \langle l||Y_\lambda||\acute{l}\rangle, \tag{12}$$

where $V_{nlJ;\acute{n}.\ \acute{l}.\hat{I}}^J(r)$ are separate of the index M, the index has been suppressed as seen in Eq (11). Coupled-channels equations are the name given to the equation (10). For heavy-ion fusion reactions, these equations are usually solved using the incoming wave boundary conditions[16].

$$u_{nlI}^J(r) \sim \mathcal{T}_{nlI}^J \ exp\left(-1\int_{r_{abs}}^r k_{nlI}(\hat{r})d\hat{r}\right).r \leqslant r_{abs} \tag{13}$$

$$\frac{i}{2}\left(H_l^{(-)}(k_{nIr})\delta_{n,n_i}\delta_{l,l_i}\delta_{I,I_i} + \sqrt{\frac{k_{nIi}}{k_{nI}}}S_{lI}^J H_l^{(+)}(k_{nIr})\right) , \ r \longrightarrow \infty , \tag{14}$$

where $k_{nIr} = \sqrt{2\mu(E-\epsilon_{nI})/\hbar^2}$, $k_{nIi} = k = \sqrt{2\mu E/\hbar^2}$ and the following formula defines the local wave number k_{nlI}:

$$k_{nlI}(r) = \sqrt{\frac{2\mu}{\hbar^2}\left(E - \epsilon_{nI} - \frac{l(l+1)\hbar^2}{2\mu r^2} - V(r) - V_{nlJ;nlJ}^J(r)\right)} \tag{15}$$

Following the determination of the transmission coefficients $T_{n_{lIJ}}$, the penetrability through the Coulomb barrier is provided by:

$$P_{lilI}^J(E) = \sum_{n.l.I} \frac{k_{nlI}(r_{abs})}{k} |\mathcal{T}_{nlI}^J|^2 \tag{16}$$

In contrast to the computation of fusion cross sections, the computation of quasi-elastic cross sections often requires a large value of angular momentum in order to yield convergent results. The potential pocket at (r = r$_{abs}$) grows shallow or even disappears for such a large angular momentum. The incoming flux in Eq (13) cannot, however, be clearly identified. The quasi-elastic problem frequently uses the regular boundary conditions at the origin in order to avoid using the incoming wave boundary conditions. When using the standard boundary conditions, a complex potential VN(r) = VN0(r)+iw(r) is needed to simulate the fusion reaction. After obtaining the nuclear S-matrix in Equation (Eq11). The scattering amplitude may be calculated using

$$f_{lI}^J(\theta.E) = i\sum_{Jl}\sqrt{\frac{\pi}{kk_{nI}}}i^{J-l}e^{i[\sigma_J(E)+\sigma_l(E-\epsilon_{nI})]}\sqrt{2J+1}\,Y_{l0}(\theta)\left(S_u^J - \delta_{I.I_2}\delta_{l.l_2}\right) + f_c(\theta.E)\delta_{I.I_2}\delta_{l.l_2} \tag{17}$$

The Coulomb phase shift is σ_l.and given by the equation,

$$\sigma_l = |\Gamma(l+1+i\eta)|, \tag{18}$$

As for f_c, which is the Coulomb scattering amplitude and is determined by[16]:

$$f_c(\theta.E) = \frac{\eta}{2k\sin^2\left(\frac{\theta}{2}\right)}e^{\left[-i\eta\ln\left(\sin^2\left(\frac{\theta}{2}\right)\right)+2i\sigma_0(E)\right]}, \tag{19}$$

where η is the Somerfield parameter which is given by $\eta = Z_1Z_2\,e^2/\hbar v$, and utilizing Equation (16), the differential cross section may be evaluated

$$\frac{d\sigma_{qel}(\theta.E)}{d\Omega} = \sum_{JlI}\frac{k_{nI}}{k}|f_{lI}^J(\theta.E)|^2, \tag{20}$$

May be evaluate the Rutherford cross section.

$$\frac{d\sigma_R(\theta.E)}{d\Omega} = |f_c(\theta.E)|^2 = \frac{\eta^2}{4k^2}\frac{1}{\sin^4\left(\frac{\theta}{2}\right)}, \tag{21}$$

The distribution of the barrier of fusion is defined as [15]:

$$D_{fus}(E) = \frac{d^2}{dE^2}\left[E\,\sigma_{fus}(E)\right], \tag{22}$$

The definition of the total scattering distribution of the barrier of scattering D $_{tot}$ (E) is[15].

$$D_{tot}(E) = -\frac{d}{dE}\left[\frac{d\sigma_{tot}}{d\sigma_R}(E)\right], \tag{23}$$

3. RESULTS AND DISCUSSION

The single-channel and coupled-channel computations were performed with the CQEL program, which is the most recent edition of the computer code CCFULL[12]. To eliminate systematic errors in the current study, the chi square technique χ^2 was used as a normalizing factor between the theoretical calculation and the experimental data. These computations were performed using a WS form for the nuclear potential, which has real and imaginary components. The imagined potential was utilized to explain the relatively low internal absorption following barrier penetration. The parameters of the actual potential were investigated in order to obtain the best fit to the experimental data, which was then replicated for all interactions.

3.1 ^{16}O+^{160}Gd System

In this reaction were processed in two cases, the first case, where both the projectile and target nuclei were considered inert (SC) at three values of the real nuclear potential (potential depth V$_0$) (58.7, 83.7 and 108.7) MeV and we considered the diffusion parameter 0.50 fm. It was previously determined by χ^2 method as the best value for matching the experimental data with the theoretical data. In the second case, the target core ^{160}Gd was rotation this was deduced according to the ratio $E_{4^+}/E_{2^+} = 3.3$ with a deformation coefficient of $\beta_2 = 0.280$ and $\beta_2 = 0.065$. We used the single-quadrupole and third-octupole phonon excitation to the state 2^+ (0.075263 MeV), at coupled-channel (CC). While the projectile nucleus was ^{16}O vibration where $E_{4^+}/E_{2^+} = 1.49$ with a deformation coefficient of $\beta_2 = 0.364$ with single-quadrupole phonon excitation to the state 2^+ (6.9171 MeV) and the radius parameter r$_0$=1.2 fm

Table 1. The values of the **WS** potential's parameters and χ^2 fitting between experimental and theoretical data for the **^{16}O+^{160}Gd reaction**.

System	Channel	a_0 (fm)	r_0 (fm)	V_0 (MeV)	θ_{cm} $(deg.)$	χ^2	
						σ_{qel}/σ_R	D_{qel}
^{16}O+^{160}Gd	SC	0.50	1.2	58.7	170	0.04873	0.0072179
				83.7		0.12627	0.0055259
				108.7		0.27427	0.0074302
	CC	0.50	1.2	58.7	170	0.00522	0.0034521
				83.7		0.01035	0.0034493
				108.7		0.02409	0.0057510

By the comparing between the experimental data and the theoretical calculations, we shown that in Table (1), we notice that the better value for the quasi-elastic scattering $(\frac{d\sigma_{qel}}{d\sigma_R}) = 0.04873$ at the depth potential $V_0 = 58.7$MeV, which was acquired from SC data analysis where the projectile ^{16}O nucleus and target ^{16}Gd nucleus are inert. It was shown by the hard red line in Fig. 1a. (A). This is the curve that is nearest to the curve of the experimental data. The batter value for the distribution $D = 0.0055259$ at the depth potential $V_0 = 83.7$ MeV. According to the coupled-channel calculation with a rotating target (T) and vibrating projectile (P), the best value of $(\frac{d\sigma_{qel}}{d\sigma_R}) = 0.00522$ at the depth potential $V_0 = 58.7$ MeV, was shown by the hard red line in Fig. 1.b (B) We note from the draw It is the curve nearest to the curve of the experimental result, while the best value to the distribution $D = 0.0034493$ at the depth potential V_0=83.7 represented by the green colored curve.
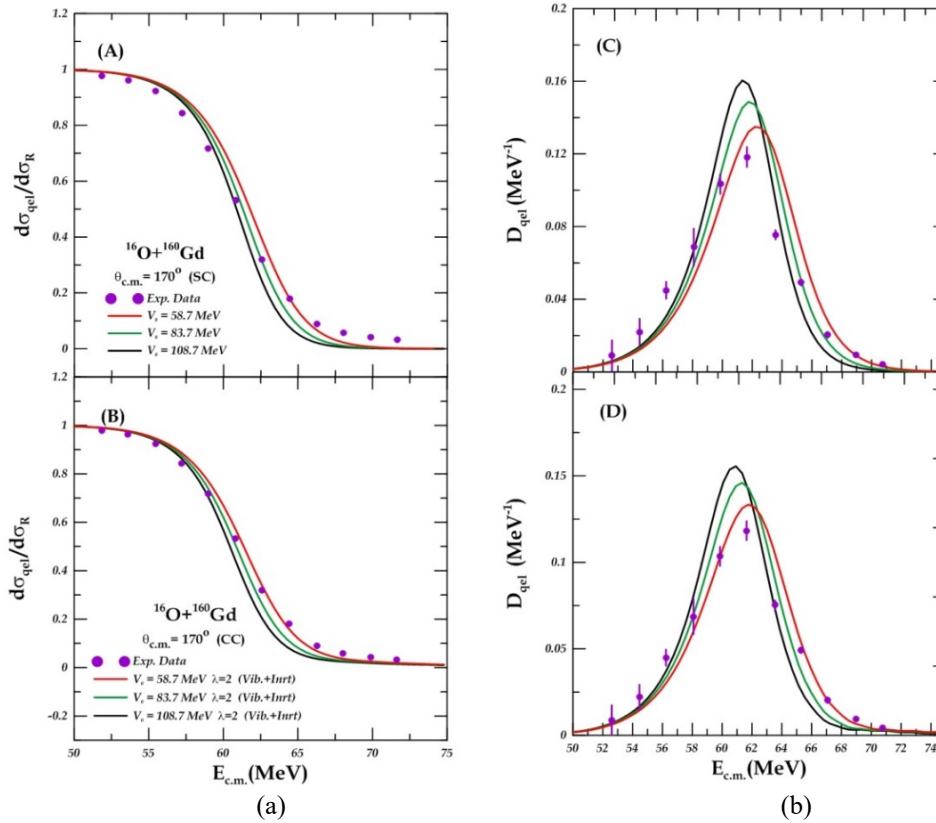
Figure 1a. The ratio of the quasi-elastic scattering to the Rutherford cross sections for ^{16}O+^{160}Gd system at sub-barrier energies. Banal A and B using the single channel and coupled-channels calculations, respectively. **Figure 1.b.** (C, D) shows the distribution at sub-barrier energies, using the single and coupled channels calculations, respectively.

3.2 ^{12}C+^{197}Au system

In this reaction, the results were split into two stages. In the first stage, according to single channel (SC) calculations, the projectile and target nuclei were inert at various real nuclear potentials (potential depth V_0) (48.8, 58.8, and 68.8) MeV, and the diffusion parameter was 0.63 fm, which had previously been determined by the chi-square χ^2 method to be the nearest value between the experimental and theoretical data. In the second stage, at coupled-channel (CC) calculations, the projectile nucleus ^{12}C was rotation where E_{4^+}/E_{2^+}= 2.9 with a deformation coefficient of $\beta_2 = 0.582$ with single quadrupole phonon excitation to the state 2^+ (4.43982 MeV). The target nucleus was ^{197}Au. In the rotation state, this was deduced according to the ratio $E_{5/2^+}/E_{1/2^+}$ = 3.6 with a deformation coefficient of β_2 =-0.131, β_4= - 0.031. We excited the state 2^+ (0.077351 MeV) with single-quadrupole and third-octupole phonons. The radius parameter r_0 is equal to 1.2 fm.

Table 2. The values of the **WS** potential's parameters and χ^2 fitting between experimental and theoretical data for the $^{12}C+^{197}Au$ reaction.

System	Channel	a_0 (fm)	r_0 (fm)	V_0 (MeV)	θ_{cm} (deg.)	χ^2	
						σ_{qel}/σ_R	D_{qel}
$^{12}C+^{197}Au$	SC	0.63	1.2	48.8	180	0.0508598	0.0099349
				58.8		0.1054816	0.0149919
				68.8		0.2342481	0.0349948
	CC	0.63	1.2	48.8	180	0.0133151	0.0230850
				58.8		0.0059362	0.0350599
				68.8		0.0063233	0.0522743

The comparing between the experimental data and the theoretical calculations show in Table (2), from this table, We notice that the best value for the quasi-elastic scattering $\left(\frac{d\sigma_{qel}}{d\sigma_R}\right) = 0.0508598$ at the depth potential $V_0 = 48.8$ MeV, which was obtained from SC data analyses when the projectile ^{16}O nucleus and target ^{197}Au nucleus are inert and it was represented by the hard red line in Fig.2.a (A). This is the curve that is closest to the experimental data curve. The batter value for the distribution D = 0.0099349 at the same depth potential V_0. Then, by using the coupled-channel accounts with a rotating target (T) and vibrating projectile (P), the better value of the quasi-elastic scattering $\left(\frac{d\sigma_{qel}}{d\sigma_R}\right) = 0.0059362$ at the depth potential $V_0 = 58.8$ MeV. It was represented by the hard green line in Fig. 2.b (B) as the figure shows. It is the curve closest to the experimental data curve, with the best value for the distribution D = 0.0230850 at the depth potential $V_0 = 48.8$ MeV represented by the red colored curve.
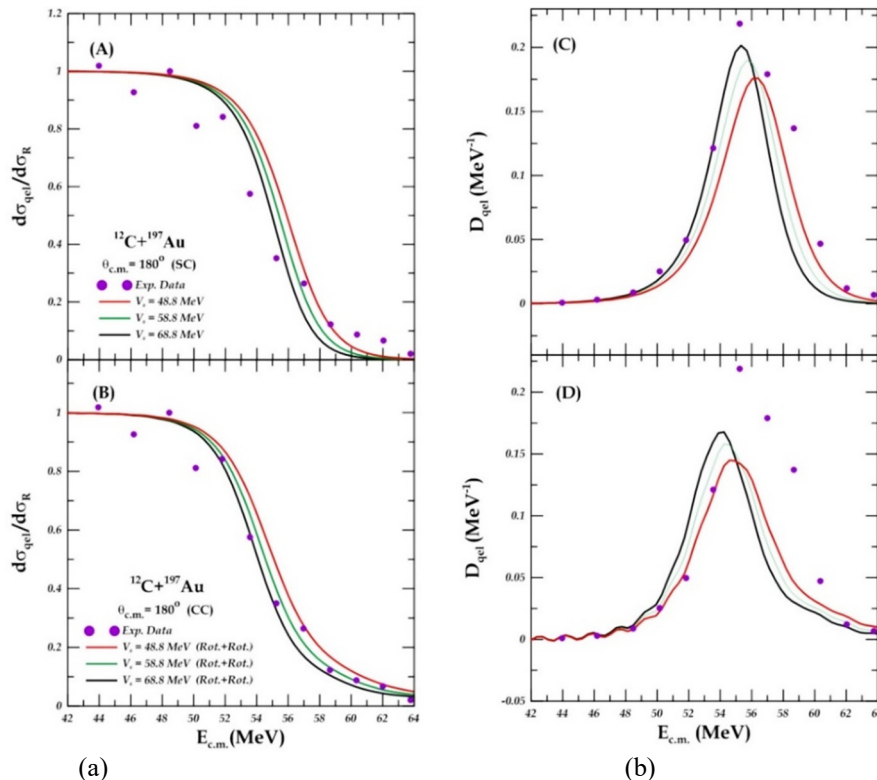
Figure 2.a. The ratio of the quasi-elastic scattering to the Rutherford cross sections for $^{12}C+^{197}Au$ system at sub-barrier energies. Banal A and B using the single channel and coupled-channels calculations, respectively. **Figure 2.b.** (C, D) shows the distribution at sub-barrier energies, using the single and coupled channels calculations, respectively. The experimental data are taken from Ref. [17].

4. CONCLUSIONS

In this research we concluded the following:

1- When the value of the potential depth decreases, it leads to a decrease in the value of the nuclear potential, and thus the height of the potential barrier will increase, the Quasi-elastic scattering calculations will increase, and the potential barrier distribution curve will shift to the right.

2- When the potential depth increases, the nuclear potential also increases, so the potential barrier will decrease and lead to a decrease in semi-elastic scattering calculations and a decrease in the height of the potential barrier distribution and its shift to the left.

ORCID ID

Khalid S. Jassim, https://orcid.org/0000-0002-5990-3277

REFERENCES

[1] M.Y.H. Farag, E.H. Esmael, and H.M. Maridi, "Analysis of proton-Be 9, 10, 11, 12 scattering using an energy-, density-, and isospin-dependent microscopic optical potential," Phys. Rev. C, **90**(3), 034615 (2014). https://doi.org/10.1103/PhysRevC.90.034615

[2] C.J. Lin, H.M. Jia, H.Q. Zhang, F. Yang, X.X. Xu, F. Jia, Z.H. Liu, and K. Hagino, "Systematic study of the surface properties of the nuclear potential with high precision large-angle quasi-elastic scatterings," Phys. Rev. C, **79**(6), 064603 (2009). https://doi.org/10.1103/PhysRevC.79.064603

[3] N.T. Zhang, Y.D. Fang, P.R.S. Gomes, J. Lubian, M.L. Liu, X.H. Zhou, G.S. Li, *et al.*, "Complete and incomplete fusion in the ^{9}Be + ^{181}Ta reaction," Phys. Rev. C, **90**(2), 024621 (2014). https://doi.org/10.1103/PhysRevC.90.024621

[4] V. Avrigeanu, and M. Avrigeanu, "Consistent optical potential for incident and emitted low-energy α particles," Phys. Rev. C, **91**(6), 064611 (2015). https://doi.org/10.1103/PhysRevC.91.064611

[5] T. Furumoto, Y. Sakuragi, and Y. Yamamoto, "Dynamical evolution of heavy-ion scattering in the high-energy region," Prog. Theor. Phys. Suppl. **196**, 219-224 (2012). https://doi.org/10.1143/PTPS.196.219

[6] K. Hagino, "Recent developments in quasi-elastic scattering around the Coulomb barrier," AIP conference proceedings, **891**(1), 80-88 (2007). https://doi.org/10.1063/1.2713503

[7] K. Washiyama, K. Hagino, and M. Dasgupta, "Probing surface diffuseness of nucleus-nucleus potential with quasielastic scattering at deep sub-barrier energies," Phys. Rev. C, **73**(3), 034607 (2006). https://doi.org/10.1103/PhysRevC.73.034607

[8] M. Beckerman, "Subbarrier fusion of atomic nuclei," Phys. Rep. **129**(3), 145-223 (1985). https://doi.org/10.1016/0370-1573(85)90058-4

[9] A.J. Hassan, and K.S. Jassim, "Effect of Surface Diffuseness Parameter on Quasi-elastic Scattering Calculations for ^{6}He+^{64}Zn, ^{7}Li+^{64}Zn and ^{8}Li+^{90}Zr Systems," NeuroQuantology, **18**(9), 40 (2020). https://doi.org/10.14704/nq.2020.18.9.NQ20214

[10] N.H. Hayef, and K.S. Jassim, "Coupled channels for quasi-elastic scattering of determining diffuseness parameters in Woods-Saxon potential for nuclear reaction," in AIP Conference Proceedings, **2414**(1), 030012 (2023). https://doi.org/10.1063/5.0117002

[11] Q.J. Tarbool, K.S. Jassim, and A.A. Abojassim, "Surface diffuseness parameter with quasi-elastic scattering for some heavy-ion systems," Int. J. Nucl. Energy Sci. Technol. **13**(2), 110-119 (2019). https://www.inderscienceonline.com/doi/abs/10.1504/IJNEST.2019.100758

[12] K. Hagino, N. Rowley, and A. T. Kruppa, "A program for coupled-channel calculations with all order couplings for heavy-ion fusion reactions," Comput. Phys. Commun. **123**(1-3), 143-152 (1999). https://doi.org/10.1016/S0010-4655(99)00243-X

[13] R.D. Woods, and D.S. Saxon, "Diffuse surface optical model for nucleon-nuclei scattering," Phys. Rev. **95**(2), 577 (1954). https://doi.org/10.1103/PhysRev.95.577

[14] P. Fröbrich, and R. Lipperheide, *Theory of nuclear reactions*(*Oxford Studies in Nuclear Physics*), vol. 18, 1st ed. (Oxford university Press. Inc., New York, 1996).

[15] K. Hagino, and N. Rowley, "Large-angle scattering and quasielastic barrier distributions," Phys. Rev. C, **69**(5), 054610 (2004). https://doi.org/10.1103/PhysRevC.69.054610

[16] M. Dasgupta, D.J. Hinde, J.O. Newton, and K. Hagino, "The nuclear potential in heavy-ion fusion," Prog. Theor. Phys. Suppl. **154**, 209-216 (2004). https://doi.org/10.1143/PTPS.154.209

[17] M.B. Tsang, *et al.*, "Azimuthal correlations between light particles emitted in ^{12}O induced reactions on ^{12}C and ^{197}Au at 400 MeV," Phys. Lett. B, **148**(4-5), 265-269 (1984). https://doi.org/10.1016/0370-2693(84)90085-6

ВПЛИВ ЗМІНИ ЯДЕРНОГО ПОТЕНЦІАЛУ НА КВАЗІПРУЖНЕ РОЗСІЮВАННЯ В СИСТЕМАХ ^{16}O+^{160}Gd ТА ^{12}C+^{197}Au

Фарах Дж. Хамуд, Халід С. Джасім
Факультет фізики, Освітній коледж чистих наук, Вавилонський університет, Ірак

У цьому дослідженні було вивчено вплив зміни глибини потенціалу V_0 на квазіпружне розсіювання та розрахунки розподілу бар'єрів за допомогою потенціалу Вуда-Саксона (WS) для систем ^{16}O+^{160}Gd і ^{12}C+^{197}Au. Хі-квадрат (χ2) використовується для порівняння найкраще підігнаного значення параметра дифузності між теоретичними розрахунками та експериментальними даними. Параметр дифузності, який використовується в цій роботі, повинен мати стандартне значення 0,63. χ2 було застосовано до найбільш підходящого, краще підігнаного значення потенційної глибини V_0. Відповідно до результатів ми помітили, що деякі системи досягли гарної відповідності між теоретичними розрахунками та експериментальними даними квазіпружного розсіювання ($d\sigma qel$)/$d\sigma R$) і розрахунками розподілу при стандартному значенні глибини потенціалу або при значенні нижче ніж стандартне значення, і не було досягнуто відповідності при значенні, більшому за стандартне значення потенційної глибини V_0. Зроблено висновок, що значення величин квазіпружного розсіювання зростають при зменшенні величини потенціальної глибини.

Ключові слова: *квазіпружне розсіювання; потенціал Вудса-Саксона (WS); спарювання; система важких іонів; параметр дифузності поверхні*

A STUDY THE NUCLEAR POTENTIAL USING QUASI-ELASTIC SCATTERING CALCULATION FOR THE $^{9,10,11}Be+^{208}Pb$ REACTIONS†

Ali A. Rakhees, ⓘ **Khalid S. Jassim***

Department of Physics, College of Education for pure Science, University of Babylon, PO Box 4, Hilla-Babylon, Iraq
*Corresponding Author e-mail: Khalidsj@uobabylon.edu.iq

Specific systematic studies on the nuclear potential parameter for the heavy-ion reactions which includes the systems have been achieved by using large-angle quasi elastic scattering at deep sub-barrier energies close to the Coulomb barrier height.The single-channel (SC) and coupled-channels calculations have been carried out to elicit the nuclear potential. The chi-square method χ^2 has been used find the best value of the nuclear potential in comparison with the experimental data. The best values of the nuclear potential were found from the calculations of the coupled channels for an inert projectile and a vibrating target for systems: $^9Be+^{208}Pb$, $^{10}Be+^{208}Pb$, $^{11}Be+^{208}Pb$, which are equal to 45 MeV, 65 MeV, 53 MeV, respectively.

Keywords: *Coupled-channels calculations; Heavy-ion fusion reactions; quasi-elastic scattering; deep sub-barrier energies*

PACS: specify the PACS code(s) here

1. INTRODUCTION

Knowing the nucleus-nucleus interaction potential is the key ingredient in nuclear reaction analysis [1] and it has played an important role in describing nucleus-nucleus collisions. It has been well recognized that heavy-ion collisions at energies about the Coulomb barrier are strongly influenced by the internal structure of colliding nuclei [2]. The couplings of the relative motion to the substantial degrees of freedom (such as collective inelastic excitation of the colliding nuclei and/or transfer processes) result in a single potential barrier being changed by many distributed barriers.The nucleus-nucleus potential is the cause of the interaction energy of colliding nuclei [5] it has been used to appreciate the cross sections of different nuclear reactions.too,in deformed nucleus interaction the nucleus-nucleus potential depends on the orientation angle of the deformed nucleus prorated to the beam direction. We can define the nucleus-nucleus potential as the sum of the nuclear potential $V_N(r)$ which is less defined and the Coulomb potential $V_C(r)$ which is well-known. By the specific description of the Coulomb or Rutherford scattering. The barrier height of the nucleus-nucleus reaction depends on the ratio between the nuclear and Coulomb potentials, which work at teeny distances between the surfaces of reactant nuclei [6]Ṡo,the nucleus-nucleus potential includes Coulomb and nuclear parts, so that long-range disharmony Coulomb potential acts between the protons in nuclei while the nuclear interaction between nucleons, the nuclear fraction is commonly expressed by the Woods-Saxon (WS) form, which is characterized by the deepness V_o, radius r_o and diffuseness a parameter [2]. The truth is that the WS form of a simple exponential had been exploited to study the surface-characteristic of nuclear potential. Quasi-elastic scattering can be defined as the sum of elastic scattering, inelastic scattering, and transfer reaction, it is very well equivalent to the fusion reaction, which is defined as a reaction where two discrete nuclei integrate to form a compound system [7]. Fusion and quasi-elastic scattering are both considered extensive operations that work in tandem. As a result,these interactions share the same potential and information about the mechanism of interaction, and both are sensitive to channel coupling impacts (due to collective in elastic excitements of colliding nuclei) at energies near the Coulomb barrier [8].

Experimentally, the measurement of quasi-elastic scattering is easier than that of fusion interaction, particularly at deep sub-barrier energies. As well as note that the scattering operation is sensitive fundamentally to the surface area of the nuclear potential, whilst the fusion reaction is also comparatively sensitive to the internal fraction [9]. The experimental measurement process for large-angle quasi-elastic scattering cross sections is more efficient and straight forward than the measurement process for fusion cross sections. At deep sub-barrier energies, the perversion of the rate of the quasi-elastic to the Rutherford cross sections from unity provides a clear way to set the account of the surface diffuseness parameter in the nucleus-nucleus potential [10].

As a result, diffuseness parameter can be defined as a landing of the nuclear potential and thus has a direct impact on the barrier width and coupling strong points,which to first order rely on the derivative of the potential. A coupling channel model is an ideal tool for simultaneously reproducing experimental data for

---

several processes such as elastic and inelastic scattering,particle transfers, and fusion with in a unified framework [11].

The inter-nuclear potential is the most important component in coupled-channels calculations, with nuclear potential influencing barrier width and coupling strengths. The channel coupling is caused by the interaction of the internal degrees of freedom, which include transfer reactions and collective vibrational and rotational motions, with the relative motion of colliding nuclei [12].

The effect of coupling channels can be ignored in nucleus-nucleus collisions at deep sub-barrier energies near the Coulomb barrier because reflection probability is nearly unity at such energies; however, this analysis would be acceptable for spherical nuclei collisions. The use of coupling channel accounts does not play a significant role in determining the best value for the diffuseness parameters at deep sub-barrier energies, but their primary purpose is to achieve the effects of some calculation inputs on the resulting diffuseness parameters. The excitation states of colliding nuclei are critical for performing coupled-channel calculations.[13]
K. Washiyama et al. used large-angle quasi-elastic scattering at energies much less than the Coulomb barrier to investigate the surface characteristics of nucleus-nucleus potential in heavy-ion reactions.As a result, a single-channel potential model was appropriate for describing these energies [2, 14].

The goal of this study is to obtain the nuclear potential parameters for the systems $^{9,10,11}Be + {}^{208}Pb$ by using large-angle quasi-elastic scattering at deep sub-barrier energies close to the Coulomb barrier height,and the single-channels and coupled-channels calculations were performed using the CQEL program, which includes all orders of coupling and is considered the most recent version of computer code CCFULL [15]. The chi-square χ^2 method was used to obtain the best-fitting values of the nuclear potential in comparison to the experimental data [9, 16].

2. THEORY

The nucleus-nucleus potential is divided into two parts nuclear part V_N, which can be well and reasonably described by the Woods-Saxon (WS)form given by [17]:

$$V_N(r) = -\frac{V_o}{1+\exp[\frac{r-R_o}{a}]} \tag{1}$$

where R_0 is a radius parameter of the system, V_o, a and r_o represent the potential depth,surface diffuseness parameter,and radius parameter,respectively, whilst r refers to the center–of–mass distance between the target nucleus of mass number A_T and the projectile nucleus of mass number A_P [18]. From another side,Coulomb part V_C between two spherical nuclei with regular charge density distributions and when they do not interfere is given by [18]:

$$V_c(r) = \frac{Z_P Z_T e^2}{4\pi\epsilon_o r} \tag{2}$$

where Z_p and Z_T represent the atomic number of the projectile and target,respectively, r the distance between the centers of mass of the colliding nuclei. When the nuclei interfere, then the Coulomb potential is given by [19]:

$$V_c(r) = \frac{Z_P Z_T e^2}{8\pi\epsilon_o R_c} \left[3 - \left(\frac{r}{R_c}\right)^2\right] \tag{3}$$

where R_c is the radius of the ball equivalent to the of the target and the projectile. The collision between two nuclei through the presence of coupling between the relative motion of the center of mass of the colliding nuclei $r \rightarrow = (r, \hat{r})$ and the nuclear intrinsic motion ξ. The Hamiltonian for the system is given by [1]:

$$H(\vec{r},\xi) = -\frac{h^2}{2\mu} \nabla^2 + V(r) + H_o(\xi) + V_{coup}(\vec{r}.\xi) \tag{4}$$

where r refers to the center of mass distance between the colliding nuclei, the reduced mass of the system while $V(r)$ is the naked potential in the absence of the coupling where $V(r) = V_N(r) + V_c(r)$,$H_0(\xi)$, represents the Hamiltonian for the intrinsic motion V_{coup} is the mentioned coupling. The Schrodinger equation for the total wave function would be given by [1]:

$$(-\frac{h^2}{2\mu} \nabla^2 + V(r) + H_o(\xi) + V_{coup}(\vec{r}.\xi))\psi(\vec{r}.\xi) = E(\vec{r}.\xi) \tag{5}$$

The internal degree of freedom ξ principally has a limited spin. We can write the coupling Hamiltonian in complications as [1]:

$$V_{coup}(\vec{r}.\xi) = \sum_{\lambda>0.\mu} f_{\lambda\mu}(r)Y_{\lambda\mu}(\hat{r}).T_{\lambda\mu}(\xi) \tag{6}$$

$Y_{\lambda\mu}(\hat{r})$refers to the spherical harmonics and $T_{\lambda\mu}(\xi)$refers to the spherical tensors,which are built from the internal coordinate. The sum is taken over all values of excluding for $\lambda=0$ since it is originally considered in$V(r)$ The expansion basis for the wave function in equation (5) for a fixed total angular momentum J and its z-component M is defined as [20]:

$$\langle \vec{r}\xi|(nlI)JM\rangle = \sum_{m2m1}\langle lm_I m_1|JM\rangle Y_{l_{m1}}(\hat{r})\varphi_{n_{1m1}}(\xi) \tag{7}$$

where l refers to the orbital, Irepresent the internal angular momenta and represents the wave function for the internal motion which fulfills [16]:

$$H_o(\xi)\varphi_{n_{1n2}}(\xi) = \varepsilon_n\varphi_{n_{1m1}}(\xi) \tag{8}$$

The total wave function $\psi(r.\xi)$ has been expanded with this basis as [1]:

$$\psi((\vec{r}).\xi) = \sum_{n\cdot l\cdot I}\frac{u_{n_{lI}}^J(r)}{r}\langle \vec{r}\xi|(nlI)JM\rangle \tag{9}$$

The Schrödinger equation [equation (2)] can then be written as a group of coupled equations for $u_{n_{lI}}^J$(r)[1].

$$[-\frac{h^2}{2\mu}\frac{d^2}{d(r)} + V(r) + \frac{l(l+1)h^2}{2^2} - E + \varepsilon_n]u_{n_{lI}}^J(r) + \sum_{n'.l'.I'}V_{(\ nlI,'_n\ '.l'.I')}^J(r)u_{n\cdot l'\cdot I'}^J(r) = 0 \tag{10}$$

Terms of the coupling matrix elements are given by:[1]

$$V_{(nlI,'_n\ '.l.I')}(r) = \langle JM(nlI)|V_{coup}(\vec{r}.\xi)|(n'.l'.I')JM\rangle = \sum_{\lambda}-1^{1-I'+l'+J}f_{\lambda}(r)\langle lI|Y_{\lambda}|l'\rangle\langle nl|T_{\lambda}|n'l'\rangle$$

$$\times \sqrt{(2l+1)(2I+1)}\begin{bmatrix} I' & l' & J \\ l & I & \lambda \end{bmatrix}$$

(11)

The reduced matrix elements in equation (11) is defined by:[14]

$$\langle l_{ml}|Y_{\lambda\mu}|l'_{ml}'\rangle = \langle l'_{ml}'\lambda\mu|l_{ml}\rangle\langle l||Y_{\lambda}||l'\rangle \tag{12}$$

As can be observed in the equation,the coefficient has been suppressed since it is independent of the coefficient M. Coupled-channels equations are the name given to the equation. These equations are frequently solved using the incoming wave boundary conditions for heavy-ion fusion interactions [14].

$$u_{n_{lI}}^J(r) \sim exp(-1\int_{r_{abs}}^r k_{nlI}(r')dr') \tag{13}$$

$$\rightarrow \frac{i}{2}(\begin{bmatrix} H_l^-(k_{nIr})\delta_{n,n\ i}\delta_{l,l\ i}\delta_{I,I\ i} \\ +\sqrt{\frac{(k_{nIr})}{k_{nl}}}S_{l\ I}^I H_l^+(k_{nIr}) \end{bmatrix}, \rightarrow \infty \tag{14}$$

$$k_{nIr} = \sqrt{2\mu(E - \epsilon_{nl})}/h^2, k_{nIi} = k = \sqrt{2\mu E/h^2} \tag{15}$$

The definition of the local wave number is [9]:

$$k_{nII}(r) = \sqrt{\frac{2\mu}{h^2}(E - \epsilon_{nl} - \frac{l(l+1)h^2}{2\mu r^2} - V(r) - V_{(nlI,'_n\ '.l'.I')}(r)}(16)$$

The penetrability across the Coulomb barrier is calculated using the transmission coefficients and is given by:

A Study the nuclear potential using quasi-elastic scattering calculation...

201
EEJP.3(2023)

$$P^J_{l\,Ili}(E) = \sum_{n\cdot l\cdot I} \frac{k_{nlI}(r_{abs})}{k}|\tau_{nlI}^l|^2 \tag{17}$$

is the wave number for the entrance channel.The fusion cross section for the unpolarized target is given by:

$$\sigma_{fus}(E) = \frac{\pi^2}{k}\sum_{J_{Mli}}\frac{2J+1}{2Ii+1}P^J_{l\,Ili}(E) \tag{18}$$

Equation (17) therefore reads When the initial intrinsic spin=0,the initial angular momentum $=J$,with the coefficients and are suppressed in the penetrability [9]:

$$\sigma_{fus}(E) = \frac{\pi^2}{k}\sum_{J} 2J+1P^J(E) \tag{19}$$

$$f^J_{l\,I}(\theta.E) = i\sum_{J_I}\sqrt{\frac{\pi}{KK_{nl}}}i^{J-1}$$

$$\mathrm{e}^{i\sigma_J(E)+\sigma_l(e-\epsilon_{nl})}\sqrt{2J+1}Y_{l0}(\theta)(S^J_u - \sigma_{I,I\,2}\delta_{ll2}) + f_c(\theta.E)\delta_{I,I\,2}\delta_{ll2} \tag{20}$$

σ_l is the Coulomb phase shift which is given by [9]:

$$\sigma_l = |\Gamma(l+1+i\eta)| \tag{21}$$

While f$_c$ is the Coulomb scattering amplitude which is given by [9]:

$$f_c(\theta.E) = \frac{\eta}{2ksin^2(\frac{\theta}{2})}e^{[-i\eta|nsin^2(\frac{\theta}{2})+2i\sigma_o(E)]} \tag{22}$$

η is the Summerfield parameter,Equation (19) may be used to evaluate the differential cross-section, which is given by [9]:

$$\frac{d\sigma_{el}}{d\Omega}(\theta, E) = \sum_{J_{lI}}\frac{k_{nI}}{k}|f^J_{lI}(\theta, E)|^2 \tag{23}$$

Equation (21) may be used to evaluate the Rutherford cross section [9]:

$$\frac{dR}{d\Omega}(\theta, E) = |f_c(\theta, E)|^2 = \frac{\eta}{4k^2}csc^4\frac{\theta}{2} \tag{24}$$

3. PROCEDURE

The CQEL software,which is regarded as the most recent version of the computer code CCFULL,was used to do the computations for single-channel and coupled-channels. The Schrödinger equation and the linked equations are precisely solved by this program [15]. To prevent systematic mistakes in the current study, the chi-square approach was used as a normalizing factor between the theoretical computation and the experimental results. The nuclear potential, which has both real and fictitious components, was calculated using a WS form [21]. The research was done on the true potential parameters to find the one that suited the experimental data the best, allowing it to be replicated for all interactions [21].

The Woods-Saxon (WS) The radius parameter r_0 is taken to be $1.2fm$, while the values of potential depth V_0 depended on the diffuseness parameter are taken to be $[(45, 50, 60)MeV, (49, 55, 65)MeV$ and $(43, 53, 59)MeV$ for the $^9Be+^{208}Pb$, $^{10}Be+^{208}Pb$ and $^{11}Be+^{208}Pb$ systems, respectively. The radius of the target was taken as $R_T = r_TA^{1/3}$ such that $r_T= 1.16\ fm$ while for the projectile $R_p= r_pA1/3$ so $r_p= 1.22fm$. The beam energies at the center of the reaction target were $88MeV$, $127MeV$ and $140\ MeV$ for ^9Be, ^{10}Be, and ^{11}Be, respectively [21]. The experimental data for the quasi-elastic cross sections at deep sub-barrier energy for all systems were taken from the references [21]. To verify that the calculations are suitably compatible with the available experimental data, we analyze and display the calculated ratio of the quasi-elastic to the Rutherford cross sections as functions of the center of mass energies.

4. RESULT AND DISCUSSION

In the $^9Be+^{208}Pb$ system, the nuclear potential parameter has been discussed in four states, in the first state we considered the projectile ^9Be as well as target ^{208}Pb as inert nuclei (SC). As for the three cases, we assumed the target nucleus ^{20}Pb is vibrational coupling with deformation parameter β_0= 0.055 to the state $2^+(4.085MeV)$ and the projectile ^9Be was inert. We used single-quadruple phonon excitation for the projectile and target nuclei that were vibrationally excited. The values of the nuclear potential parameters (V_0) have been obtained from SC and CC analysis, as well as other parameters of WS potential(radius r_0 and diffuseness a_0) and the values of χ^2 fitting between experimental and theoretical data for the $^9Be+^{208}Pb$ reaction were shown in Table (1).

By looking at the outcomes in Table (1), we find that the better suitable value nuclear potential parameter which has obtained from CC analysis (where the projectile ^9Be was inert and target ^{208}Pb nuclei was vibrational coupling) is $45MeV$ with χ^2=0.00242, this result considered very near for standard value and represented by the solid line in Fig. (1)(B), while the dashed line represents the single-channel accounts with the nuclear potential parameter, was drawn for the comparison, that our calculation outputs bred by all computational models are near one another and in consensus with the experimental outputs. The $\frac{d\sigma_{qel}}{d\sigma_R}$ at the best fitted nuclear potential parameter is $45MeV$, with χ^2=0.00242 using a coupled channel calculation at deep sub-barrier energies. In this reaction, we assumed that projectile ^9Be is inert whilst the target ^{208}Pb is vibrational coupling to the state 2^+. The Figure(C) represents a comparison between the best value of the single channel and the coupling channels, which was found using the chi-square χ^2 code. We concluded that CC and phonon excitation influences augment the calculated cross-sections at energies near the barrier district. It is observed that the influence of vibrational states for the spherical nuclei states for the deformed nuclei, is the effective couplings leading to big fusion cross-sections around the barrier regions.

Table 1. The parameters of the WS potential a_0,r_0,andV_0, as well as the values of χ^2 fitting between experimental and theoretical data for various types of reactions when the excited nuclei are in a vibrational excitation state with a single-quadruple phonon.

System	Case	$r_0(fm)$	$a_0(fm)$	$V_0(MeV)$	χ^2
$^9Be+^{208}Pb$	Single channel		0.63	45	0.00248
				50	0.00257
				60	0.00273
	Inert-Vib.		0.63	45	0.00242
	Inert-Vib.			50	0.00250
	Inert-Vib.			60	0.00257

In the $^{10}Be+^{208}Pb$ system, the nuclear potential parameter has been discussed in four states, in the first state we considered the projectile ^{10}Be as well as ^{208}Pb as inert nuclei, while in the three cases, we assumed the target nucleus ^{208}Pb is vibrational coupling with deformation parameter β_0=0.055 to the state $2^+(4.085MeV)$ and the projectile ^{10}Be was inert. We used single-quadruple phonon excitation for the projectile and target nuclei that were vibrationally excited. The values of the nuclear potential parameters (V_0) have been obtained from SC and CC analysis, as well as other parameters of WS potential (radius r_0 and diffuseness a_0) and the values of χ^2 fitting between experimental and theoretical data for the $^{10}Be+^{208}Pb$ reaction were shown in Table (2).

By observing the results in Table(2),We find that the nuclear potential parameter's more appropriate value,as determined via CC analysis (where the projectile ^{10}Be was inert and target ^{208}Pb nuclei was vibrational coupling) is $65MeV$ with χ^2=0.00550,these results are perceived to be near the conventional value,and represented by the dash dot line in Fig.(2)(B), the Figure (C) represents a comparison between the best value of the single channel and the coupling channels, which was found using the chi-square χ^2 code. We have shown that in heavy ion fusion reactions, higher order couplings to nuclear surface vibrations play an important role.

In the $^{11}Be+^{208}Pb$ system, the nuclear potential parameter has been discussed in four states,in the first state we considered the projectile ^{11}Be as well as ^{208}Pb as inert nuclei, while in the As for the three cases, we assumed the target nucleus ^{208}Pb is vibrational coupling with deformation parameter β_0=0.055 to the state $2^+(4.085MeV)$ and the projectile ^{11}Be was inert. We used single-quadruple phonon excitation for the projectile and target nuclei were vibrationally excited. The values of the nuclear potential parameters (V_0) have been obtained from SC and CC analysis, as well as other parameters of WS potential (radius r_0 and diffuseness a_0) and the values of χ^2 fitting between experimental and theoretical data for the $^{11}Be+^{208}Pb$ reaction were shown in Table (3).

By observing the results in Table(3), we find that the nuclear potential parameter's more appropriate value, as determined via CC analysis (where the projectile ^{11}Be was inert and target ^{208}Pb nuclei was vibrational
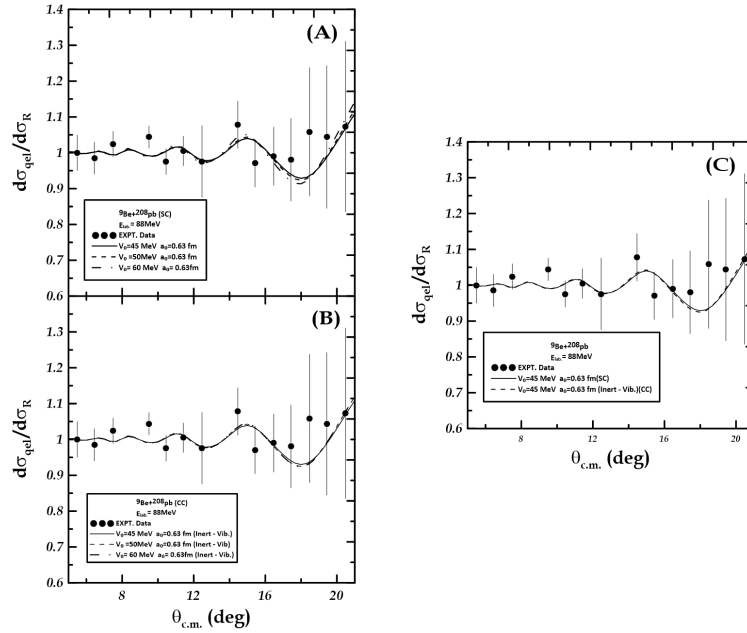
Figure 1. Comparison of accounts for single-channel and kinds of linked channels using experimental data[21]Referred to as points with error bars for the system.In the upper panel (a) the hard and dashed lines represent the results of SC analysis at $V_0 = 45MeV$,$V_0 = 50MeV$ and $V_0 = 60MeV$ respectively,while the hard, dashed and dot-dashed lines in the lower panel (b) represent the results of CC analysis at $V_0 = 45MeV$ (represents the better suitable value of the nuclear potential parameter)$V_0 = 50MeV$ and $V_0 = 60MeV$ respectively (C) comparison between the best value of the single channel and the coupling channels.

Table 2. The parameters of the WS potential a_0,r_0,andV_0, as well as the values of χ^2 fitting between experimental and theoretical data for various types of reactions when the excited nuclei are in a vibrational excitation state with a single-quadruple phonon.

System	Case	$r_0(fm)$	$a_0(fm)$	$V_0(MeV)$	χ^2
$^{10}Be+^{208}Pb$	Single channel		0.63	49	0.00630
				55	0.00576
				65	0.00551
	Inert-Vib.		0.63	49	0.00636
	Inert-Vib.			55	0.00576
	Inert-Vib.			65	0.00550

coupling) is $53MeV$ with χ^2=0.00639, these results are perceived to be near the conventional value, and represented by the solid line in Fig.(3)(B), the figure (C) represents a comparison between the best value of the single channel and the coupling channels, which was found using the chi-square χ^2 code. We have shown that in heavy ion fusion reactions, higher order couplings to nuclear surface vibrations play an important role.

Table 3. The parameters of the WS potential a_0,r_0,andV_0,as well as the values of χ^2 fitting between experimental and theoretical data for various types of reactions when the excited nuclei are in a vibrational excitation state with a single-quadruple phonon.

System	Case	$r_0(fm)$	$a_0(fm)$	$V_0(MeV)$	χ^2
$^{11}Be+^{208}Pb$	Single channel		0.63	43	0.00759
				53	0.00644
				59	0.00647
	Inert-Vib.		0.63	43	0.00756
	Inert-Vib.			53	0.00639
	Inert-Vib.			59	0.00640
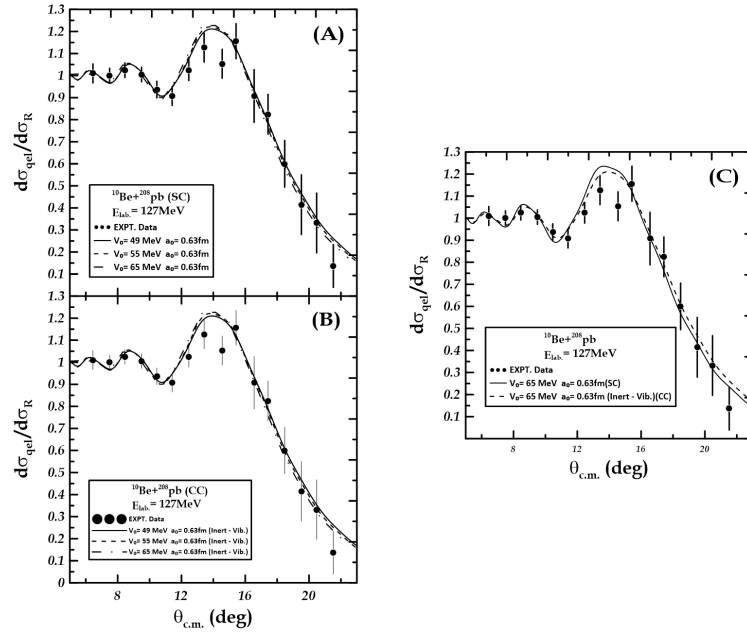
Figure 2. Comparison of accounts for single-channel and kinds of linked channels using experimental data[21]Referred to as points with error bars for the system.In the upper panel (*a*) the hard and dashed lines represent the results of SC analysis at $V_0=49MeV$,$V_0=55MeV$ and $V_0=65MeV$ respectively,while the hard,dashed and dot-dashed lines in the lower panel (*b*) represent the results of CC analysis at $V_0=49MeV$,$V_0=55MeV$ and $V_0=65MeV$ (represents the better suitable value of the nuclear potential parameter) respectively (*C*) comparison between the best value of the single channel and the coupling channels.
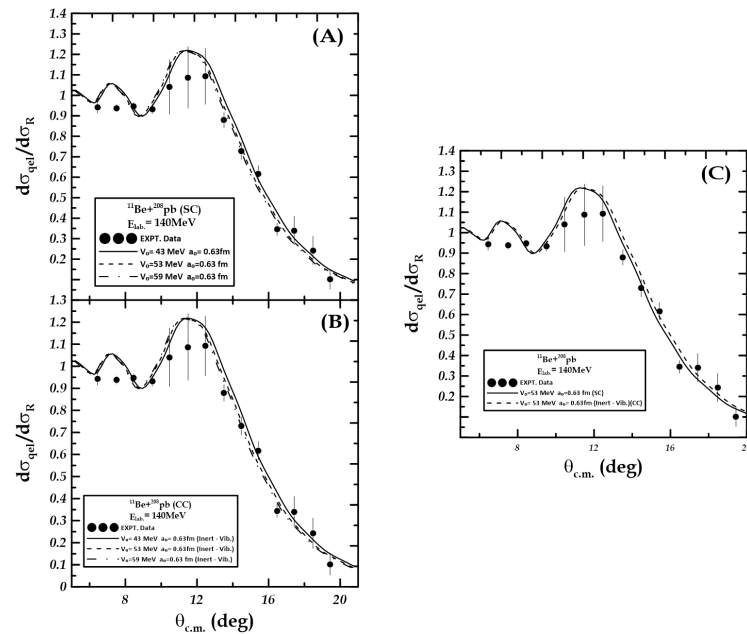
Figure 3. Comparison of accounts for single-channel and kinds of linked channels using experimental data [21]. Referred to as points with error bars for the system. In the upper panel (*a*) the hard and dashed lines represent the results of SC analysis at $V_0 = 43MeV$,$V_0 = 53MeV$ and $V_0 = 59MeV$ respectively, while the hard, dashed and dot-dashed lines in the lower panel (*b*) represent the results of CC analysis at $V_0 = 43MeV$,$V_0 = 53MeV$ (represents the better suitable value of the nuclear potential parameter) and $V_0 = 59MeV$ respectively (*C*) comparison between the best value of the single channel and the coupling channels.

5. CONCLUSION

We found, through micro methodology analyses of the data, that the method of large angle quasi-elastic scattering at deep sub-barrier energies near to the Coulomb barrier height is the perfect instrument for examining the surface property of Inter nucleus potential for the spherical systems discussed in this article. Single-channel

analyses fit experimental data gives nuclear potential parameters for the systems $^9Be+^{208}Pb$,$^{10}Be+^{208}Pb$ and $^{11}Be+^{208}Pb$ respectively, does not differ substantially from the nuclear potential parameter's best fitted value, which was obtained using CC analysis (with an inert projectile and a vibrating target) and is exactly in line with the standard value. All coupling channel accounts produced values that were quite close to the nuclear potential parameter's standard value.

ORCID

Khalid S. Jassim, https://orcid.org/0000-0002-5990-3277

REFERENCES

[1] R. Naik, PhD Thesis, "Studying fusion reactions for effect of P (CN) on heavy nucleus formation and for nuclear structure effects," Oregon State University, 2007.

[2] N.H. Hayef, and K.S. Jassim, "Coupled channels for quasi-elastic scattering of determining diffuseness parameters in Woods-Saxon potential for nuclear reaction," AIP Conference Proceedings, **2414**, 030012 (2023). https://doi.org/10.1063/5.0117002

[3] Z.M. Cinan, B. Erol, T. Baskan, and A.H. Yilmaz, "Heavy-Ion Fusion Reaction Calculations: Establishing the Theoretical Frameworks for 111" In Radionuclide over the Coupled Channel Model," Energies, **14**(24), 8594 (2021). https://doi.org/10.3390/en14248594

[4] F.A. Majeed, K.S. Jassim, and N.H. Abbas, "Role of Coupled-Channels in Heavy Ions Reactions at the Coulomb Barrier," Int. J. Sci. Res. **3**, 315-319 (2014). https://livedna.net/?dna=964.25272

[5] H. Timmers, J.R. Leigh, M. Dasgupta, D.J. Hinde, R.C. Lemmon, J.C. Mein, C.R. Morton, et al., "Probing fusion barrier distributions with quasi-elastic scattering," Nuclear Physics A, **584**(1), 190-204 (1995). https://doi.org/10.1016/0375-9474(94)00521-N

[6] K.S. Jassim, and Q.J. Tarbool, "A Study of the surface diffuseness of inter-nucleus potential with quasi-elastic scattering for the $^{32,34}_{16}S+^{208}_{82}Pb$ reactions," Al-Bahir Journal for Engineering and Pure Sciences, **1**(1-2), 125-140 (2015). https://www.iasj.net/iasj/pdf/a338dda2a3e54bda

[7] H.K. Hagino, and N. Rowley, "Large-angle scattering and quasielastic barrier distributions," Phys. Rev. C, **69**, 054610 (2004). https://doi.org/10.1103/PhysRevC.69.054610

[8] M.M. Evers, Ph.D thesis, "Systematics of near-barrier nuclear reactions using quasi-elastic scattering", The Australian National University, (2010).

[9] Q.J. Tarbool, K.S. Jassim, and A.A. Abojassim, "Surface diffuseness parameter with quasi-elastic scattering for some heavy-ion systems," International Journal of Nuclear Energy Science and Technology, **13**(2), 2019. https://www.inderscienceonline.com/doi/pdf/10.1504/IJNEST.2019.100758

[10] N. Wang, and M. Liu, and Y.-X. Yang, "Heavy-ion fusion and scat- tering with Skyrme energy density functional," Sci. China Series G: Physics, Mechanics and Astronomy, 2009. **52**, 1554–1573 (2009). https://doi.org/10.1007/s11433-009-0205-z

[11] V.I. Zagrebaev, "Understanding the barrier distribution function derived from backward-angle quasi-elastic scattering," Phys. Rev. C, **78**, 047602 (2008), https://doi.org/10.1103/PhysRevC.78.047602

[12] M. Zadro, P. Figuera, A. Di Pietro, M. Fisichella, M. Lattuada, T. Lönnroth, M. Milin, et al., "Quasielastic backscattering and barrier distributions for the 6, 7 Li+ 64 Zn systems," Physical Review C, **87**, 054606 (2013). https://doi.org/10.1103/PhysRevC.87.054606

[13] P.R.S. Gomes, D.R. Otomar, T. Correa, L.F. Canto, J. Lubian, R. Linares, D.H. Luong, et al., "Complete fusion enhancement and suppression of weakly bound nuclei at near barrier energies," J. Phys. G: Nucl. Part. Phys. **39**, 115103 (2012). https://doi.org/10.1088/0954-3899/39/11/115103

[14] Y.Y. Yang, J.S. Wang, Q. Wang, D.Y. Pang, J.B. Ma, M.R. Huang, P. Ma, et al., "Quasi-elastic scattering of ^{10,11}C and ^{10}B from a ^{nat}Pb target," Phys. Rev. C, **90**, 014606 (2014). https://doi.org/10.1103/PhysRevC.90.014606

[15] K. Hagino, N. Rowley, and A.T. Kruppa, "A program for coupled-channel calculations with all order couplings for heavy-ion fusion reactions," Computer Physics Communications, **123**(1-3), 143-152 (1999). https://doi.org/10.1016/S0010-4655(99)00243-X

[16] M. Dasgupta, D.J. Hinde, J.O. Newton, and K. Hagino, "The nuclear potential in heavy-ion fusion," Progress of Theoretical Physics Supplement, **154**, 209–216 (2004). https://doi.org/10.1143/PTPS.154.209

[17] L.R. Gasques, M. Evers, D.J. Hinde, M. Dasgupta, P.R.S. Gomes, R.M. Anjos, M.L. Brown, et al., "Systematic study of the nuclear potential through high precision back-angle quasi-elastic scattering measurements," Phys. Rev. C, **76**, 024612 (2007). https://doi.org/10.1103/PhysRevC.76.024612

[18] M.V. Andres, N. Rowley, and M.A. Nagarajan, "Effect of deformation on the elastic and quasielastic scattering of heavy ions near the Coulomb barrier," Physics Letters B, **202**(3), 292-295 (1988). https://doi.org/10.1016/0370-2693(88)90473-X

[19] W. Reisdorf, "Heavy-ion reactions close to the Coulomb barrier," J. Phys. G: Nucl. Part. Phys. **20**, 1297 (1994). https://doi.org/10.1088/0954-3899/20/9/004

[20] K. Washiyama, K. Hagino, and M. Dasgupta, "Probing surface diffuseness of nucleus-nucleus potential with quasielastic scattering at deep sub-barrier energies," Phys. Rev. C, **73**, 034607 (2006). https://doi.org/10.1103/PhysRevC.73.034607

[21] RIBLL Collaboration, "Scattering of the halo nucleus 11Be from a lead target at 3.5 times the Coulomb barrier energy," Physics Letters B, **811**, 135942 (2020). https://doi.org/10.1016/j.physletb.2020.135942

ВИВЧЕННЯ ЯДЕРНОГО ПОТЕНЦІАЛУ ЗА ДОПОМОГОЮ РОЗРАХУНКУ КВАЗІПРУЖНОГО РОЗСІЮВАННЯ ДЛЯ РЕАКЦІЇ $^{9,10,11}Be+^{208}Pb$

Алі А. Рахіз, Халід С. Джассім

Факультет фізики, Освітній коледж чистої науки, Вавилонський університет, Hilla-Babylon, Iraq

Конкретні систематичні дослідження параметра ядерного потенціалу для реакцій важких іонів, які включають системи, були досягнуті за допомогою великокутового квазіпружного розсіювання при глибоких підбар'єрних енергіях, близьких до висоти кулонівського бар'єру. Для визначення ядерного потенціалу були проведені розрахунки для одноканального (SC) варіанту та варіанту зв'язаних каналів (CC). Методом χ^2 було знайдено найкраще значення ядерного потенціалу в порівнянні з експериментальними даними. Найкращі значення ядерного потенціалу знайдено з розрахунків зв'язаних каналів для інертного налітаючого ядра та коливальної мішені для систем: ^{9}Be+^{208}Pb, ^{10}Be+^{208}Pb, ^{11}Be+^{208}Pb, які дорівнюють 45 MeV, 65 MeV, 53 MeV відповідно.

Ключові слова: *розрахунки зв'язаних каналів; реакції синтезу важких іонів; квазіпружне розсіювання; глибокі підбар'єрні енергії*

INVESTIGATING THE EFFECT OF GRAVITY MODULATION ON WEAKLY NONLINEAR MAGNETOCONVECTION IN A NONUNIFORMLY ROTATING NANOFLUID LAYER[†]

Michael I. Kopp[a]*, Volodymyr V. Yanovsky[a,b]

aInstitute for Single Cristals, Nat. Academy of Science Ukraine, Nauky Ave. 60, Kharkiv 61072,Ukraine
bV.N. Karazin Kharkiv National University, 4, Svoboda Sq., Kharkiv, 61022, Ukraine
*Corresponding Author e-mail: michaelkopp0165@gmail.com
Received July 15, 2023; revised August 2, 2023; accepted August 4, 2023

This paper investigates the impact of gravity modulation on weakly nonlinear magnetoconvection in a nanofluid layer that is nonuniformly rotating. The fundamental equations are obtained for the Cartesian approximation of the Couette flow using the Boussinesq approximation and gravitational modulation. The weakly nonlinear regime is analyzed using the method of perturbations with respect to the small supercritical parameter of the Rayleigh number, considering the effects of Brownian motion and thermophoresis in the nanofluid layer. Heat and mass transfer are evaluated in terms of finite amplitudes and calculated from the Nusselt numbers for the fluid and the volume concentration of nanoparticles. The findings demonstrate that gravitational modulation, nonuniform rotation, and differences in the volume concentration of nanoparticles at the layer boundaries can effectively control heat and mass transfer. Additionally, the negative rotation profile has a destabilizing effect. The study shows that the modulated system conveys more heat and mass than the unmodulated system.

Keywords: *Nanofluid; Nonuniformly rotating layer; Weakly nonlinear theory; Gravity modulation; Non-autonomous Ginzburg-Landau equation*
PACS: 47.32.C, 47.32.cd, 47.90.+a

1. INTRODUCTION

Nanofluids have received significant interest in recent years due to their unique thermal properties, which make them attractive for various applications. Convection in nanofluids is important for analyzing their behavior. The sudden enhancement in thermal conductivity and variety of behavior make it essential to investigate these models. Choi [1] introduced the study of nanofluids as fluids containing a scatter of solid particles with characteristic dimensions of 10 or 100 nm scaled. The use of nanofluids, which have smaller-sized particles providing a larger relative surface area than microsized particles, can improve heat and mass transfer properties and overcome problems such as clogging channels, drastic pressure drops, settling, and premature wear on channels and components. By adding nanoparticles to base fluids, their thermal conductivity can be enhanced by 15-40 %, which is crucial in modern engineering and research. These heat-exchanging situations are found in various fields, including biomechanics, spinning machines like nuclear reactors, food, geophysical problems, chemical processing, and the petroleum industry. Nanofluids have a variety of applications due to their ability to enhance heat and mass transfer using mixed nano-sized particles. These fluids can also control transport processes, making them useful in drug delivery systems.

In recent years, theoretical studies of the Rayleigh-Bénard convection (RBC) in nanofluids have attracted attention due to the potential for improved heat transfer and energy efficiency in various engineering applications. Several studies have investigated the effects of nanoparticle size, concentration, and shape on the onset of convection in Rayleigh-Benard cells. Buongiorno [2] conducted a thorough investigation of convective transport in nanofluids, with a particular focus on elucidating the enhanced heat transfer observed under convective flows. Tzo[3] utilized the transport equations proposed by Buongiorno to explore the onset of convection in a horizontally heated layer using nanofluids. The study revealed that the presence of Brownian motion and thermophoresis in the nanoparticles significantly reduces the critical Rayleigh number, by one to two orders of magnitude, compared to that of a conventional fluid.

Buongiorno and Hu [4], Kuznetsov and Niel [5] studied the effects of nanoparticle concentration on the onset of convection in nanofluids. The presence of nanoparticles in nanofluids can either enhance or suppress the onset of convection, leading to changes in heat and mass transport characteristics. This is attributed to the presence of concentration gradients of the nanoparticles within the fluid. Previous research has consistently shown that the instability of the flow is primarily driven by buoyancy forces, which are independent of the specific effects of Brownian motion and thermophoresis. Therefore, in order to control instability in the medium, it becomes necessary to modify the gravity field in nanofluids.

One of the possible ways to modify the gravitational field in a nanofluid is through its modulation. In general, modulation refers to the deliberate periodic change in certain parameters or conditions that affect convective processes. The study of the effect of modulation on convection is necessary to understand how external disturbances or changes in some parameters can affect the flow and transport phenomena within the system. In the study of RBC, several types of modulation techniques are commonly employed to investigate the influence of external perturbations on the convective flow. Some of the commonly used modulation techniques in RBC include:

---

1. Temperature Modulation: This involves periodically varying the temperature difference across the fluid layer, either by applying a time-dependent boundary temperature or by modulating the heat input or extraction from the system. Temperature modulation can be achieved through various methods, such as sinusoidal variations \cite{6s}, square wave modulation, or modulating the temperature gradient [7].

2. Gravity Modulation: In this technique, the gravitational field acting on the fluid layer is periodically varied. It can be achieved by physically oscillating the entire system or by using time-dependent external forces or fields to induce periodic changes in the effective gravity [8].

3. Rotation Modulation: Rotation modulation involves periodically changing the rotation rate or angular velocity of the system. This can be achieved by modulating the speed of rotation, introducing intermittent rotation, or applying time-dependent torque or angular momentum variations [9].

4. Magnetic field modulation: The modulation of an external magnetic field on RBC refers to the time-dependent variation of the applied magnetic field in a system experiencing convective heat transfer [10].

Currently, researchers extensively utilize these types of modulation to investigate the characteristics of heat transfer in RBC across different media. Due to the vast amount of literature available on this topic, we will provide a concise overview focusing specifically on the impact of gravity field modulation on convective processes.

At present, studies of nanofluids in nonlinear modes of convection under modulation are rapidly developing. Bhadauria and Kiran[11], pioneered the investigation of gravity modulation effects on nanofluid convection in nonlinear modes. Bhadauria et al. [12] investigated the impact of gravity modulation on nanoconvection and observed that modulation plays a role in regulating transport phenomena at finite amplitudes. In addition, Kiran [13] studied the nonlinear thermal instability in a viscoelastic, nanofluid-saturated porous medium under gravitational modulation. Kiran et al. \cite{14s} also investigated the problem of internal heating in a similar way to the work by Bhadauria et al. \cite{12s}. Kiran and Narasimhulu [15]-[16] introduced the concept of out-of-phase modulation and lower boundary modulation in nanoconvection, and their findings revealed that modulation not only influences transport phenomena but also chaotic convection. Furthermore, Kiran et al. [17] explored the effect of throughflow on nanofluid convection and discovered that throughflow, whether inflow or outflow, can either enhance or diminish energy transfer in the medium. More recently, Kiran \cite{18s}-\cite{20s} conducted studies on the impact of g-jitter on RBC and Darcy convection. Kiran et al. [21] investigated the effect of g-jitter on the RBC of nanofluids with the Ginzburg-Landau (GL) model. Using nonlinear analysis, the thermal and concentration Nusselt numbers are calculated depending on other physical parameters. The effect of gravity modulation and rotation on thermal instability in a horizontal layer of a nanofluid was investigated by Manjula et al. [22].

The previous studies discussed concentrated mainly on the problem's plane geometry, using a Cartesian coordinate system. In laboratory experiments, however, the presence of Couette flows between two rotating cylinders with different angular speeds is extremely important. The angular velocity of fluid rotation in this configuration can be described by the relation:

$$\Omega(R) = \frac{\Omega_2 R_2^2 - \Omega_1 R_1^2}{R_2^2 - R_1^2} + \frac{(\Omega_1 - \Omega_2)R_1^2 R_2^2}{R^2(R_2^2 - R_1^2)} = a + \frac{b}{R^2},$$

where $R_{1,2}$ and $\Omega_{1,2}$ represent the inner and outer cylinders' radius and angular velocity, respectively. Chandrasekhar [23] and Velikhov [24] were the first to analyze the stability of such a flow in the presence of a magnetic field in a perfectly conducting medium. Research on magnetic convection in nonuniformly rotating media is currently scarce. This topic was partially explored in our previous articles [25]-[27], which focused on astrophysical applications, and in our nanofluid physics studies [28]. In our research, we suggested using electrically conducting nanofluids to simulate the magnetorotational instability (MRI) in laboratory settings. Theoretical studies conducted in [28] showed that standard MRI, azimuthal MRI, and helical MRI can be implemented in a nonuniformly rotating layer of an electrically conducting nanofluid. We also examined stationary regimes of nonuniformly rotating convection in axial and helical magnetic fields, taking into account temperature and nanoparticle concentration gradients. Our studies aimed to investigate the conditions for stabilizing and destabilizing stationary convection in axial and helical magnetic fields. The absence of a Ginzburg-Landau (GL) model in the existing literature for nonlinear magnetic convection in a nonuniformly rotating nanofluid layer subjected to gravity field modulation has motivated the present study.

The article is structured as follows. Section 1 (Introduction) provides an overview of recent research in this area and also indicates the need for a GL model for nonlinear magnetic convection in a non-uniformly rotating nanofluid layer under the influence of gravitational field modulation. Section 2 describes the problem in detail and derives evolution equations for small perturbations using the Boussinesq approximation. The study is focused on a rotating layer of an incompressible electrically conductive nanofluid in a modulated gravitational field, taking into account a constant temperature gradient and nanoparticle concentration. In Section 3, we study the weakly nonlinear stage of stationary convection in a nonuniformly rotating layer of an electrically conductive liquid in a modulated gravitational field. Using the method of perturbation theory with respect to the small supercritical parameter of the Rayleigh number $\varepsilon = \sqrt{(Ra - Ra_c)/Ra_c}$, we obtained a nonlinear GL equation with a periodic coefficient. In Section 4, we studied linear magnetic convection in a nonuniformly rotating layer of a nanofluid depending on variations in the system parameters.

Further, the results of numerical solutions of the non-autonomous GL equation are presented, showing the dependence of the heat transfer value (Nusselt number Nu) and mass transfer (nano-Nusselt number Nu_ϕ) on the parameters of the nanofluid $(\mathrm{Pr}, \mathrm{Rn}, \mathrm{L}e)$, the profile of the inhomogeneous rotation (Rossby numbers Ro), frequency Ω, and modulation amplitude δ. Conclusions (Section 5) represent the main findings of this paper.

2. GOVERNING EQUATIONS

Let us consider convective flows in a nonuniformly rotating layer of an electrically conductive nanofluid in an externally constant magnetic field and under the influence of gravity field modulation. In order to describe the nonlinear convective flows in the layer, a Cartesian approximation of the Couette flow is used instead of the cylindrical coordinate system (R, φ, z) (see Fig. 1)
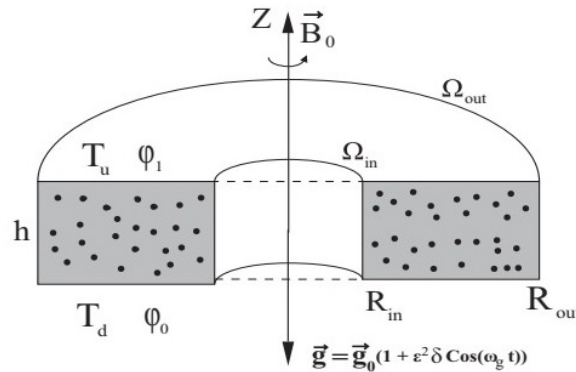
Figure. 1 Electrically conducting nanofluid fills the layer between two rotating cylinders with angular velocities of Ω_{in} and Ω_{out} and is located in an external uniform magnetic field: $\vec{B}_0 = B_0 \vec{e}_z$.

A fixed area of the fluid layer with radius R_0 and angular velocity $\vec{\Omega}$ is considered, and the coordinates $X = R - R_0$, $Y = R_0(\varphi - \varphi_0)$, and $Z = z$ are used to represent the radial, azimuthal, and vertical directions, respectively. The nonuniform rotation of the fluid layer can be locally represented as a rotation with an angular velocity Ω_0 and an azimuthal shear (see Fig. 2), whose velocity profile is locally linear:
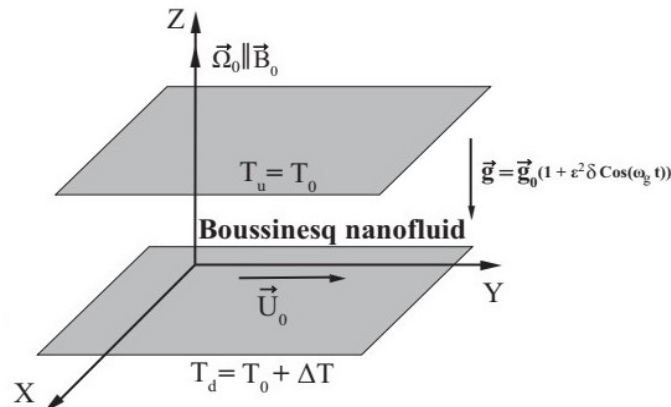
Figure. 2 Cartesian approximation for nonuniformly rotating magnetoconvection under the parametric influence of gravity modulation.

$\vec{U}_0 = -q\Omega_0 X \vec{e}_Y$, where $q = -d \ln \Omega / d \ln R$ is the dimensionless shear parameter determined from the angular velocity profile $\Omega(R) = \Omega_0 (R / R_0)^{-q}$. The shear parameter q is related to the hydrodynamic Rossby number Ro as follows: $q = -2Ro$. Examples of the values of the Rossby parameter include $Ro = 0$ for solid rotation, $Ro = -3/4$ for Keplerian rotation, and $Ro = -1$ for a Rayleigh angular velocity profile $\Omega(R) \sim R^{-2}$.

An electrically conductive nanofluid layer is located between two horizontal planes, $Z = 0$ and $Z = h$, and is heated from below and cooled from above, where $T_d = T_0 + \Delta T$ is the temperature at the lower boundary of the horizontal layer, and $T_u = T_0$ is the temperature at the upper boundary of the horizontal layer (see Fig. 2). We assume that the volume fraction of nanoparticles is also constant at the boundaries and has the corresponding values: ϕ_0 at

$Z = 0$ and ϕ_1 at $Z = h$. If $\phi_1 > \phi_0$, we have a top-heavy configuration of nanoparticles in nanofluid, and otherwise, for $\phi_1 < \phi_0$, we have a bottom-heavy configuration of nanoparticles in nanofluid. Let us consider that the direction of the external constant magnetic field $\vec{B}_0$ coincides with the fluid rotation axis $\vec{\Omega}_0 \parallel OZ$.

The effect of gravity field modulation will be considered based on the equations of magnetohydrodynamics in a rotating coordinate system for an electrically conductive nanofluid in the Boussinesq approximation (see, for example, Kopp et al. [28]):

$$\rho\left(\frac{\partial \vec{v}}{\partial t} - q\Omega_0 X \frac{\partial \vec{v}}{\partial Y} + ((\vec{v}+\vec{U}_0)\nabla)\vec{U}_0 + (\vec{v}\nabla)\vec{v}\right) = -\nabla\left(P + \frac{\mu_e \vec{B}^2}{8\pi}\right) - 2\rho(\vec{\Omega}_0 \times (\vec{v}+\vec{U}_0)) + \frac{\mu_e}{4\pi}(\vec{B}\nabla)\vec{B} + \mu\nabla^2\vec{v} + \tag{1}$$

$$+[\phi\rho_p + (1-\phi)(\rho_f(1-\beta(T-T_u)))]\vec{g}(t)$$

$$\frac{\partial \vec{B}}{\partial t} - q\Omega_0 X \frac{\partial \vec{B}}{\partial Y} + (\vec{v}\nabla)\vec{B} - (\vec{B}\nabla)\vec{U}_0 - (\vec{B}\nabla)\vec{v} = \eta\nabla^2\vec{B} \tag{2}$$

$$(\rho c)_f\left(\frac{\partial T}{\partial t} - q\Omega_0 X \frac{\partial T}{\partial Y} + (\vec{v}\nabla)T\right) = k_f\nabla^2 T + (\rho c)_p\left(D_B\nabla\phi\nabla T + D_T\frac{(\nabla T)^2}{T_u}\right) \tag{3}$$

$$\frac{\partial \phi}{\partial t} - q\Omega_0 X \frac{\partial \phi}{\partial Y} + (\vec{v}\nabla)\phi = D_B\nabla^2\phi + \frac{D_T}{T_u}\nabla^2 T \tag{4}$$

$$div\vec{v} = 0 \quad div\vec{B} = 0 \tag{5}$$

Here $\vec{v} = (u, v, w)$ is the nanofluid velocity, ρ is the nanofluid density, ρ_p is the density of nanoparticles, ρ_f is the density of base fluid at temperature T_u, ϕ is the volume fraction of nanoparticles, $(\rho c)_f, (\rho c)_p$ are the effective heat capacities of the fluid and particle phases, respectively. μ, η and μ_e are the viscosity, magnetic viscosity, and magnetic permeability of nanofluid, respectively. D_B and D_T denote the Brownian diffusion coefficient and thermophoretic diffusion, respectively. The signs of the coefficients D_B and D_T are positive and they are

$$D_B = \frac{k_B T}{3\pi\mu d_p}, \quad D_T = \left(\frac{\mu}{\rho_f}\right)\left(\frac{0.26 k_f}{2k_f + k_p}\right)\phi,$$

where d_p is the diameter of the nanoparticles, k_B is the Boltzmann constant, k_f, k_p are the thermal conductivity coefficients of the base fluid and nanoparticles. The coefficients of magnetic permeability μ_e, magnetic viscosity η and electrical conductivity are

$$\mu_e = \phi\mu_{ep} + (1-\phi)\mu_{ef}, \quad \eta = \frac{1}{4\pi\mu_e\sigma} = \phi\eta_p + (1-\phi)\eta_f, \quad \sigma = \phi\sigma_p + (1-\phi)\sigma_f,$$

where μ_{ep}, μ_{ef} are the magnetic permeability of the nanoparticles and the base fluid, η_p, η_f are the magnetic viscosity of the nanoparticles and the base fluid, σ_p, σ_f are the electrical conductivity coefficients nanoparticles and the base fluid.

In the momentum equation (1), the buoyancy force consists of two distinct components: the temperature variation within the fluid and the distribution of nanoparticles (which are generally heavier than the base fluid). Assuming that the fluid layer undergoes vertical harmonic oscillations with a frequency of ω_g and a small displacement amplitude of $\varepsilon^2\xi$, we can modify the equations of motion in the reference frame associated with the fluid layer. In the equation (1), the acceleration of gravity $\vec{g}(t)$ should be replaced by $\vec{g}_0(1 + \varepsilon^2\delta\cos(\omega_g t))$, where δ is a small amplitude of gravitational modulation. Additionally, the influence of an external magnetic field is incorporated by introducing an additional force known as the Lorentz force, which affects the motion of the electrically conductive nanofluid. Equation (2) represents the description of induced magnetic fields that arise due to convective flows in electrically conductive nanofluids. The equations (3)-(4) are conservation laws for the thermal energy and volume fraction of nanoparticles. Equations (5) describe the solenoidality conditions for the fields $\vec{v}$ and $\vec{B}$. We impose the initial condition on temperature (T) and volumetric fraction of nanoparticles (ϕ) by assuming them to be constant at stress-free boundaries:

$$\vec{v} = 0, T = T_d, \phi = \phi_0, \text{ at } Z = 0$$

$$\vec{v} = 0, T = T_u, \phi = \phi_1, \text{ at } Z = h \tag{6}$$

Equations (1)-(5), along with boundary conditions (6), provide a description of non-uniformly rotating magnetic convection in a nanofluid layer subjected to gravity field modulation. To facilitate the study of this phenomenon, it is advantageous to transform equations (1)-(5) into a dimensionless form by introducing dimensionless variables of the following nature:

$$(x^*, y^*, z^*) = \frac{(X, Y, Z)}{h}, t^* = t\frac{\alpha_f}{h^2}, T^* = \frac{T - T_u}{T_d - T_u} \phi^* = \frac{\phi - \phi_0}{\phi_1 - \phi_0}, \vec{v}^*(u^*, v^*, w^*) = \vec{v}(u, v, w)\frac{h}{\alpha_f}, P^* = \frac{h^2 P}{\alpha_f \mu},$$

$$\vec{B}^*(B_x^*, B_y^*, B_z^*) = \frac{\vec{B}(B_x, B_y, B_z)}{B_0}, \omega_g^* = \omega_g \frac{h^2}{\alpha_f},$$

where $\alpha_f = k_f / (\rho c)_f$ is the coefficient of thermal diffusivity. Upon applying the aforementioned transformations to Eqs. (1)-(6), we obtain the following dimensionless governing system (after omitting the asterisk notation):

$$\frac{1}{Pr}\left(\frac{\partial \vec{v}}{\partial t} + (\vec{v}\nabla)\vec{v}\right) + Ro\sqrt{Ta}\, x\frac{\partial \vec{v}}{\partial y} + \vec{e}_y Ro\sqrt{Ta}\, v_x + \sqrt{Ta}(\vec{e}_z \times (\vec{v} + \vec{U}_0)) = -\nabla\left(P + QPrPm^{-1}\frac{\vec{B}^2}{2}\right) + \nabla^2\vec{v} + \quad (7)$$

$$+QPrPm^{-1}(\vec{B}\nabla)\vec{B} - \vec{e}_z F_m Rm - \vec{e}_z F_m Rn\phi + \vec{e}_z F_m RaT$$

$$\frac{\partial \vec{B}}{\partial t} + PrRo\sqrt{Ta}\, x\frac{\partial \vec{B}}{\partial y} + (\vec{v}\nabla)\vec{B} - Pr\, Ro\sqrt{Ta}\, B_x\vec{e}_y - (\vec{B}\nabla)\vec{v} = PrPm^{-1}\nabla^2\vec{B} \quad (8)$$

$$\frac{\partial T}{\partial t} + PrRo\sqrt{Ta}\, x\frac{\partial T}{\partial y} + (\vec{v}\nabla)T = \nabla^2 T + \frac{N_B}{Le}\nabla\phi\nabla T + \frac{N_A N_B}{Le}(\nabla T)^2 \quad (9)$$

$$\frac{\partial \phi}{\partial t} + PrRo\sqrt{Ta}\, x\frac{\partial \phi}{\partial y} + (\vec{v}\nabla)\phi = \frac{1}{Le}\nabla^2\phi + \frac{N_A}{Le}\nabla^2 T \quad (10)$$

where e_y, e_z are unit vectors along the Y, Z axes, respectively; $F_m = 1 + \varepsilon^2\delta\cos(\omega_g t)$. Then we write the boundary conditions (6) in dimensionless form as

$$\vec{v} = 0, T = 1, \phi = 0, \text{ at } z = 0$$

$$\vec{v} = 0, T = 0, \phi = 1, \text{ at } z = 1 \quad (11)$$

In equations (7)-(10), the following dimensionless parameters are used:

$Pr = \dfrac{\nu}{\alpha_f}$ is the Prandtl number, $Ta = \dfrac{4\Omega_0^2 h^4}{\nu^2}$ is the Taylor number, $Pm = \dfrac{\nu}{\eta}$ is the magnetic Prandtl number,

$Q = \dfrac{\mu_e B_0^2 h^2}{4\pi\mu\eta}$ is the Chadrasekhar number, $Rm = \dfrac{g_0 h^3(\rho_p\phi_0 + \rho_f(1 - \phi_0))}{\mu\alpha_f}$ is the basic density Rayleigh number,

$Ra = \dfrac{\rho_f g_0 \beta h^3 \Delta T}{\mu\alpha_f}$ is the Rayleigh number, $Rn = \dfrac{(\rho_p - \rho_f)(\phi_1 - \phi_0)g_0 h^3}{\mu\alpha_f}$ is the concentration Rayleigh number,

$L_e = \dfrac{\alpha_f}{D_B}$ is the Lewis number, $N_B = (\phi_1 - \phi_0)\cdot\dfrac{(\rho c)_p}{(\rho c)_f}$ is a coefficient characterizing the increment of the density of

nanoparticles, $N_A = \dfrac{D_T(\Delta T)}{D_B T_0(\phi_1 - \phi_0)}$ is a modified diffusion coefficient.

2.1. Basic state
Assume that the basic state is time independent and is given by

$$v_b = 0, P = P_b(x, z), T = T_b(z), \phi = \phi_b(z) \quad (12)$$

Then, by representing all quantities in Eqs. (7)-(10) as the sum of the ground state and perturbed state, we can express them as follows:

$$\vec{v} = \vec{u}(u, v, w), \vec{B} = \vec{B}_0(0, 0, B_0) + \vec{b}(\tilde{u}, \tilde{v}, \tilde{w}), \quad (13)$$

$$P = P_b(x,z) + P', \quad \phi = \phi_b(z) + \phi', \quad T = T_b(z) + T'$$

The equations governing the ground state are given by:

$$\sqrt{Ta}(e_z \times U_0) = -\nabla P_b, \tag{14}$$

$$\frac{dP_b}{dz} = -\mathrm{Rm} - \mathrm{Rn}\phi_b + \mathrm{Ra}T_b, \tag{15}$$

$$\frac{d^2 T_b}{dz^2} + \frac{N_B}{Le}\frac{d\phi_b}{dz}\frac{dT_b}{dz} + \frac{N_A N_B}{Le}\left(\frac{dT_b}{dz}\right)^2 = 0, \tag{16}$$

$$\frac{d^2 \phi_b}{dz^2} + N_A \frac{d^2 T_b}{dz^2} = 0. \tag{17}$$

The geostrophic equilibrium is described by Eq. (14), which balances the Coriolis force with the pressure gradient. The hydrostatic equation (15) ensures that the vertical component of the ground state is satisfied. Equatios (16)-(17) represent the mathematical expressions describing the stationary temperature profile $T_b = T_b(z)$, and the volume fraction of nanoparticles $\phi_b = \phi_b(z)$. Kuznetsov and Nield (2009) further suggested that the magnitude of the second and third terms in Eq. (16) is negligible and can be disregarded. Taking these facts into consideration, Eqs. (16) and (17) can be simplified to:

$$\frac{d^2 T_b}{dz^2} = 0, \quad \frac{d^2 \phi_b}{dz^2} = 0 \tag{18}$$

Equations (13) are solved under the boundary conditions (6), and the resulting solution is as follows:

$$T_b(z) = 1 - z, \quad \phi_b(z) = z \tag{19}$$

As will be shown below, we do not need an explicit form of the pressure $P_b(x,z)$.

2.2 Perturbated State

In this section, we obtain non-linear perturbed state equations used to describe three-dimensional nonuniformly rotating magnetic convection of a nanofluid under the influence of gravity field modulation. By subtracting the equations for the ground state (14)-(15) from Eqs. (7)-(10), we get the equations governing the evolution of perturbations:

$$\frac{1}{\mathrm{Pr}}\left(\frac{\partial \vec{u}}{\partial t} + (\vec{u}\nabla)\vec{u}\right) + \mathrm{Ro}\sqrt{Ta}\,x\frac{\partial \vec{u}}{\partial y} + \vec{e}_y \mathrm{Ro}\sqrt{Ta}\,u + \sqrt{Ta}(\vec{e}_z \times \vec{u}) = -\nabla \tilde{P} + \nabla^2 \vec{u} + \mathrm{QPrPm}^{-1}((\vec{e}_z \nabla)\vec{b} + (\vec{b}\nabla)\vec{b}) -$$
$$-\vec{e}_z F_m \mathrm{Rn}\phi' + \vec{e}_z F_m \mathrm{Ra}T' \tag{20}$$

$$\frac{\partial \vec{b}}{\partial t} + \mathrm{Pr}Ro\sqrt{Ta}\,x\frac{\partial \vec{b}}{\partial y} + (\vec{u}\nabla)\vec{b} - \mathrm{Pr}\,Ro\sqrt{Ta}\tilde{u}\vec{e}_y - (\vec{e}_z\nabla)\vec{u} - (\vec{b}\nabla)\vec{u} = \mathrm{PrPm}^{-1}\nabla^2\vec{b} \tag{21}$$

$$\frac{\partial T'}{\partial t} + \mathrm{Pr}Ro\sqrt{Ta}\,x\frac{\partial T'}{\partial y} + (\vec{u}\nabla)T' - w = \nabla^2 T' + \frac{N_B}{Le}\left(\frac{\partial T'}{\partial z} - \frac{\partial \phi'}{\partial z}\right) + \frac{2N_A N_B}{Le}\frac{\partial T'}{\partial z} \tag{22}$$

$$\frac{\partial \phi'}{\partial t} + \mathrm{Pr}Ro\sqrt{Ta}\,x\frac{\partial \phi'}{\partial y} + (\vec{u}\nabla)\phi' + w = \frac{1}{Le}\nabla^2\phi' + \frac{N_A}{Le}\nabla^2 T' \tag{23}$$

where $\tilde{P} = P' + \mathrm{Q}PrPm^{-1}(\vec{e}_z\vec{b} + (\vec{b}^2/2))$ is the total perturbed pressure.

We will focus on the dynamics of axisymmetric perturbations, which means that all perturbed quantities in Eqs. (20)-(23) will depend solely on two variables, namely, x and z:

$$\vec{u} = (u(x,z), v(x,z), w(x,z)), \quad \vec{b} = (\tilde{u}(x,z), \tilde{v}(x,z), \tilde{w}(x,z))$$

$$\tilde{P} = \tilde{P}(x,z), \quad T' = T'(x,z), \quad \phi' = \phi'(x,z).$$

The solenoidal Eqs. (5) governing the axisymmetric velocity and magnetic field perturbations can be expressed in the following form:

$$\frac{\partial u}{\partial x} + \frac{\partial w}{\partial z} = 0 \; , \quad \frac{\partial \tilde{u}}{\partial x} + \frac{\partial \tilde{w}}{\partial z} = 0 \; . \tag{24}$$

To simplify the expressions of the perturbed velocity components, we can introduce the stream function, denoted as ψ. This allows us to express the components of the perturbed velocity as follows:

$$u = -\frac{\partial \psi}{\partial z} \; , \quad w = \frac{\partial \psi}{\partial x}$$

Similarly, for the perturbations of the magnetic field, we can introduce the current function, denoted as φ. This allows us to express the components of the perturbed magnetic field as:

$$\tilde{u} = -\frac{\partial \varphi_m}{\partial z} \; , \qquad \tilde{w} = \frac{\partial \varphi_m}{\partial x} \; .$$

The Eqs. (20)-(23), expressed in terms of the introduced stream function and current function, will have the following form in the coordinate representation:

$$\left(\frac{1}{\Pr} \frac{\partial}{\partial t} - \nabla^2 \right) \nabla^2 \psi + \sqrt{Ta} \frac{\partial v}{\partial z} - Q \Pr Pm^{-1} \frac{\partial}{\partial z} \nabla^2 \varphi_m + F_m \mathrm{Rn} \frac{\partial \phi'}{\partial x} - F_m Ra \frac{\partial T'}{\partial x} = \tag{25}$$
$$= Q \Pr Pm^{-1} J(\varphi_m, \nabla^2 \varphi_m) - \Pr^{-1} J(\psi, \nabla^2 \psi)$$

$$\left(\frac{1}{\Pr} \frac{\partial}{\partial t} - \nabla^2 \right) v - \sqrt{Ta}(1 + Ro) \frac{\partial \psi}{\partial z} - Q Pr Pm^{-1} \frac{\partial \tilde{v}}{\partial z} = Q Pr Pm^{-1} J(\varphi_m, \tilde{v}) - \Pr^{-1} J(\psi, v) \; , \tag{26}$$

$$\left(\frac{\partial}{\partial t} - Pr Pm^{-1} \nabla^2 \right) \varphi_m - \frac{\partial \psi}{\partial z} = -J(\psi, \varphi_m) \; , \tag{27}$$

$$\left(\frac{\partial}{\partial t} - Pr Pm^{-1} \nabla^2 \right) \tilde{v} - \frac{\partial v}{\partial z} + \Pr Ro \sqrt{Ta} \frac{\partial \varphi_m}{\partial z} = J(\varphi_m, v) - J(\psi, \tilde{v}) \; , \tag{28}$$

$$\left(\frac{\partial}{\partial t} - \nabla^2 \right) T' - \frac{\partial \psi}{\partial x} - \frac{N_B}{Le} \left(\frac{\partial T'}{\partial z} - \frac{\partial \phi'}{\partial z} \right) + \frac{2 N_A N_B}{Le} \frac{\partial T'}{\partial z} = -J(\psi, T') \; , \tag{29}$$

$$\left(\frac{\partial}{\partial t} - \frac{1}{Le} \nabla^2 \right) \phi' + \frac{\partial \psi}{\partial x} - \frac{N_A}{Le} \nabla^2 T' = -J(\psi, \phi') \; , \tag{30}$$

where

$$J(a,b) = \frac{\partial a}{\partial x} \frac{\partial b}{\partial z} - \frac{\partial a}{\partial z} \frac{\partial b}{\partial x} \; , \quad \nabla^2 \equiv \frac{\partial}{\partial x^2} + \frac{\partial}{\partial z^2} \; . \quad J(a,b) \text{ is the Jacobian operator.}$$

In the absence of gravity field modulation, Eqs. (25)-(29) were used to study the weakly nonlinear and chaotic regimes of stationary magnetic convection in a nonuniformly rotating "pure" (without nanoparticles) fluid, which were carried out by Kopp *et al.* [25], [29]-[30]. Magnetic convection in a nonuniformly rotating "pure" (without nanoparticles) fluid under gravity modulation was studied by Kopp *et al.* [31].

3. WEAK NONLINEAR ANALYSIS

In the weakly nonlinear theory of convective instability, the interaction between small amplitude convective cells can be described as follows. Assuming that the amplitude of the convective cells is of the order $O(\varepsilon^1)$, their interaction with each other leads to second harmonic and nonlinear effects of the order $O(\varepsilon^2)$, and subsequently to nonlinear effects of the order $O(\varepsilon^3)$, and so on. In this case, the nonlinear terms in equations (25)-(30) are considered perturbations to the linear convection problem. The Rayleigh parameter Ra, which governs convection, is assumed to be close to the critical value Ra_c. We further assume that the amplitude of the oscillating gravitational field, $\varepsilon^2 \delta g_0$, is of the second order of smallness, $O(\varepsilon^2)$. Therefore, its influence on the nonlinear interaction of convective cells is expected to occur at the third order, $O(\varepsilon^3)$. Given the small influence of unstable modes, our objective is to derive equations that describe the interactions of these modes. The general procedure for constructing a weakly nonlinear theory is as follows. In the weakly nonlinear theory of convective instability, we introduce a small expansion parameter ε^2, which represents the relative deviation of the Rayleigh number Ra from its critical value Ra_c:

$$\varepsilon^2 = \frac{Ra - Ra_c}{Ra_c} \ll 1.$$

The perturbed quantities in the equations of the form $\mathcal{L}U = -N(U \,|\, U)$, where $N(...)$ represents the nonlinear terms, can be expressed as a series expansion in powers of ε:

$$U \rightarrow \varepsilon U^{(1)} + \varepsilon^2 U^{(2)} + \varepsilon^3 U^{(3)} + ...$$

The equations for perturbations in different orders of ε take the following form:

$\varepsilon^1 : \mathcal{L}^{(0)} U^{(1)} = 0$,

$\varepsilon^2 : \mathcal{L}^{(0)} U^{(2)} = -N(U^{(1)} \,|\, U^{(1)})$,

$\varepsilon^3 : \mathcal{L}^{(0)} U^{(3)} = -\mathcal{L}^{(2)} U^{(0)} - N(U^{(1)} \,|\, U^{(2)}) - N(U^{(2)} \,|\, U^{(1)})$.

The solvability condition for this chain of nonlinear equations is known as Fredholm's alternative (see [32]). It can be expressed as:

$$\langle U^\dagger, R.H. \rangle = 0, \tag{31}$$

where $U^\dagger$ is a non-trivial solution of the linear self-adjoint problem $\mathcal{L}^\dagger U^\dagger = 0$, and $\mathcal{L}^\dagger$ is a self-adjoint operator that is defined from the relation:

$$\langle U^\dagger, \mathcal{L}U \rangle \equiv \langle \mathcal{L}^\dagger U^\dagger, U \rangle, \tag{32}$$

where $\langle , \rangle$ denotes the inner product:

$$\langle f, g \rangle = \int\limits_{z=0}^{1} \int\limits_{x=0}^{2\pi/k_c} f \cdot g \, dx \, dz$$

$R.H.$ are the right parts of perturbed equations with non-linear terms.

In the weakly nonlinear theory, we represent all the variables in the Eqs. (25)-(30) using an asymptotic expansion. The Rayleigh number Ra is expanded as

$$Ra = Ra_c + \varepsilon^2 Ra_2 + \varepsilon^4 Ra_4 + ...$$

and the perturbed quantities are expressed as follows:

$$\psi = \varepsilon\psi_1 + \varepsilon^2\psi_2 + \varepsilon^3\psi_3 + ..., \; v = \varepsilon v_1 + \varepsilon^2 v_2 + \varepsilon^3 v_3 + ..., \; \varphi_m = \varepsilon\varphi_1 + \varepsilon^2\varphi_2 + \varepsilon^3\varphi_3 + ..., \; \tilde{v} = \varepsilon\tilde{v}_1 + \varepsilon^2\tilde{v}_2 + \varepsilon^3\tilde{v}_3 + ...,$$

$$T' = \varepsilon T_1 + \varepsilon^2 T_2 + \varepsilon^3 T_3 + ..., \; \phi' = \varepsilon\phi_1 + \varepsilon^2\phi_2 + \varepsilon^3\phi_3 + ...,$$

where Ra_c represents the critical Rayleigh number for convection without modulation. The amplitudes of the perturbed quantities are solely dependent on the slow time variable $\tau = \varepsilon^2 t$. To simplify the analysis, we will consider nonlinear terms only in the equations governing the temperature and volume concentration of nanoparticles (29)-(30). These equations are solved using a perturbation approach by considering various powers of ε. At the lowest order, i.e., ε, the following solution is obtained

$$\hat{L} M_1 = 0 \tag{34}$$

where $M_1 = [\psi_1, v_1, \varphi_1, \tilde{v}_1, T_1, \phi_1]^{Tr}$, $\hat{L}$ is a matrix operator of the form

$$\hat{L} = \begin{pmatrix} a_{11} & a_{12} & a_{13} & a_{14} & a_{15} & a_{16} \\ a_{21} & a_{22} & a_{23} & a_{24} & a_{25} & a_{26} \\ a_{31} & a_{32} & a_{33} & a_{34} & a_{35} & a_{36} \\ a_{41} & a_{42} & a_{43} & a_{44} & a_{45} & a_{46} \\ a_{51} & a_{52} & a_{53} & a_{54} & a_{55} & a_{56} \\ a_{61} & a_{62} & a_{63} & a_{64} & a_{65} & a_{66} \end{pmatrix},$$

where $a_{11} = -\nabla^4$, $a_{12} = \sqrt{Ta}\dfrac{\partial}{\partial z}$, $a_{13} = -Q\Pr Pm^{-1}\dfrac{\partial}{\partial z}\nabla^2$, $a_{14} = 0$, $a_{15} = -Ra_c\dfrac{\partial}{\partial x}$, $a_{16} = Rn\dfrac{\partial}{\partial x}$, $a_{21} = -\sqrt{Ta}(1+Ro)\dfrac{\partial}{\partial z}$,

$a_{22} = -\nabla^2$, $a_{23} = 0$, $a_{24} = -QPrPm^{-1}\dfrac{\partial}{\partial z}$, $a_{25} = 0$, $a_{26} = 0$, $a_{31} = -\dfrac{\partial}{\partial z}$, $a_{32} = 0$, $a_{33} = -PrPm^{-1}\nabla^2$, $a_{34} = a_{35} = a_{36} = 0$,

$a_{41} = 0$, $a_{42} = -\dfrac{\partial}{\partial z}$, $a_{43} = \Pr Ro\sqrt{Ta}\dfrac{\partial}{\partial z}$, $a_{44} = -PrPm^{-1}\nabla^2$, $a_{45} = a_{46} = 0$, $a_{51} = -\dfrac{\partial}{\partial x}$, $a_{52} = a_{53} = a_{54} = 0$,

$a_{55} = -\nabla^2 - \dfrac{N_B}{Le}\dfrac{\partial}{\partial z} + \dfrac{2N_A N_B}{Le}\dfrac{\partial}{\partial z}$, $a_{56} = \dfrac{N_B}{Le}\dfrac{\partial}{\partial z}$, $a_{61} = \dfrac{\partial}{\partial x}$, $a_{62} = a_{63} = a_{64} = 0$, $a_{65} = -\dfrac{N_A}{Le}\nabla^2$, $a_{66} = -\dfrac{1}{Le}\nabla^2$.

The solutions of the system of Eqs. (34) satisfying the boundary conditions (11) are as follows:
$\psi_1 = A(\tau)\sin k_c x \sin \pi z$,

$$v_1 = \frac{A(\tau)\pi\sqrt{Ta}}{a^2}\cdot\frac{(1+Ro)a^4 + \pi^2 QPmRo}{a^4 + \pi^2 Q}\sin k_c x \cos \pi z, \quad \varphi_1 = \frac{A(\tau)\pi Pm}{a^2 \Pr}\sin k_c x \cos \pi z,$$

$$\tilde{v}_1 = -\frac{A(\tau)\pi^2\sqrt{Ta}(1+Ro(1-Pm))Pm}{\Pr(a^4 + \pi^2 Q)}\sin k_c x \sin \pi z, \quad T_1 = \frac{A(\tau)k_c}{a^2}\cos k_c x \sin \pi z,$$

$$\phi_1 = -\frac{A(\tau)k_c}{a^2}(Le + N_A)\cos k_c x \sin \pi z, \quad a^2 = k_c^2 + \pi^2. \tag{35}$$

The critical value of the Rayleigh number Ra_c for steady magnetoconvection in a non-uniformly rotating nanofluid is obtained from the first equation of system (34) and can be expressed as follows:

$$Ra_c = \frac{a^6}{k_c^2} + \frac{\pi^2 a^2}{k_c^2}Q + \frac{\pi^2 a^4 Ta}{k_c^2(a^4 + \pi^2 Q)} + \frac{\pi^2 Ta Ro(a^4 + \pi^2 QPm)}{k_c^2(a^4 + \pi^2 Q)} - Rn(Le + N_A). \tag{36}$$

Expression (36) was first obtained by Kopp *et al.* [28], which agrees very well with the known results. When there are no nanoparticles present $(Rn = 0)$, the expression (36) aligns with the findings reported by Kopp *et al.*[25], [29]. In the absence of rotation $(Ta = 0)$ and a magnetic field $(Q = 0)$, Nield and Kuznetsov [33] derived the expression for the thermal Rayleigh number in the context of stationary motions. Chand [34], on the other hand, investigated a uniformly rotating $Ro = 0$ nanofluid without a magnetic field $Q = 0$ and obtained an expression for the thermal Rayleigh number in the case of stationary convection, considering the top-heavy configuration of nanoparticles. Without rotation $Ta = 0$, expression (36) coincides with the results of Gupta *et al.* [35] and Yadav *et al.* [36]. In the case when there is no heating of the nanofluid $Ra = 0$, then in system, the development of MRI is possible. As established by Kopp *et al.* [28], in the presence of a concentration of nanoparticles, the area of development of the MRI becomes larger compared to a "pure" fluid.

For the second order in ε we get the following equation:

$$\hat{L}M_2 = N_2, \tag{37}$$

where

$$M_2 = [\psi_2, v_2, \varphi_2, \tilde{v}_2, T_2, \phi_2]^{Tr}, \ N_2 = [N_{21}, N_{22}, N_{23}, N_{24}, N_{25}, N_{26}]^{Tr}, \ N_{21} = N_{22} = N_{23} = N_{24} = 0,$$

$$N_{25} = -\left(\frac{\partial \psi_1}{\partial x}\frac{\partial T_1}{\partial z} - \frac{\partial T_1}{\partial x}\frac{\partial \psi_1}{\partial z}\right), N_{26} = -\left(\frac{\partial \psi_1}{\partial x}\frac{\partial \phi_1}{\partial z} - \frac{\partial \phi_1}{\partial x}\frac{\partial \psi_1}{\partial z}\right).$$

The following second-order solutions are obtained using the first-order solutions provided in Eqs. (35):

$$\psi_2 = 0, \ v_2 = 0, \ \varphi_2 = 0, \ \tilde{v}_2 = 0, \tag{38}$$

$$T_2 = -\frac{A^2(\tau)k_c^2}{8\pi a^2}\sin(2\pi z), \ \phi_2 = \frac{A^2(\tau)k_c^2}{8\pi a^2}Le(Le + N_A)\sin(2\pi z).$$

To analyze the intensity of heat transfer, we introduce a horizontally-averaged heat flux at the boundary of the electrically conducting nanofluid layer, known as the Nusselt number:

$$Nu(\tau) = 1 + \frac{\left[\frac{k_c}{2\pi}\int\limits_0^{2\pi/k_c}\left(\frac{\partial T_2}{\partial z}\right)dx\right]_{z=0}}{\left[\frac{k_c}{2\pi}\int\limits_0^{2\pi/k_c}\left(\frac{\partial T_b}{\partial z}\right)dx\right]_{z=0}} = 1 + \frac{k_c^2}{4a^2}A^2(\tau) \tag{39}$$

The nanoparticle concentration Nusselt number, denoted as $Nu_\phi(\tau)$, is defined in the same way as the Nusselt number. It can be expressed as follows:

$$Nu_\phi(\tau) = 1 + \frac{k_c^2 A^2(\tau)}{4a^2}Le(Le + N_A) \tag{40}$$

The heat/mass transfer quotients $Nu(\tau)$ and $Nu_\phi(\tau)$ will be analyzed once the expression for the amplitude $A(\tau)$ is obtained. It can be observed from the asymptotic expansion (33) that the effect of gravity modulation only contributes to the third order in ε. Therefore, in the third order ε, we obtain the following expression:

$$\hat{L}M_3 = N_3, \tag{41}$$

where

$$M_3 = [\psi_3, v_3, \varphi_3, \tilde{v}_3, T_3, \phi_3]^{Tr} \quad , \quad N_3 = [N_{31}, N_{32}, N_{33}, N_{34}, N_{35}, N_{36}]^{Tr}.$$

The terms on the right side of Eq. (41) are defined by the following expression:

$$N_{31} = -\frac{1}{\Pr}\frac{\partial}{\partial\tau}\nabla^2\psi_1 + Ra_2\frac{\partial T_1}{\partial x} + Ra_c\delta\cos(\Omega\tau)\frac{\partial T_1}{\partial x} - Rn\delta\cos(\Omega\tau)\frac{\partial\phi_1}{\partial x}, \quad \Omega = \frac{\omega_g}{\varepsilon^2}, \tag{42}$$

$$N_{32} = -\frac{1}{\Pr}\frac{\partial v_1}{\partial\tau}, \quad N_{33} = -\frac{\partial\phi_1}{\partial\tau}, \quad N_{34} = -\frac{\partial\tilde{v}_1}{\partial\tau}, \tag{43}$$

$$N_{35} = -\frac{\partial T_1}{\partial\tau} - \left(\frac{\partial\psi_1}{\partial x}\frac{\partial T_2}{\partial z} - \frac{\partial T_2}{\partial x}\frac{\partial\psi_1}{\partial z} + \frac{\partial\psi_2}{\partial x}\frac{\partial T_1}{\partial z} - \frac{\partial T_1}{\partial x}\frac{\partial\psi_2}{\partial z}\right), \tag{44}$$

$$N_{36} = -\frac{\partial\phi_1}{\partial\tau} - \left(\frac{\partial\psi_1}{\partial x}\frac{\partial\phi_2}{\partial z} - \frac{\partial\phi_2}{\partial x}\frac{\partial\psi_1}{\partial z} + \frac{\partial\psi_2}{\partial x}\frac{\partial\phi_1}{\partial z} - \frac{\partial\phi_1}{\partial x}\frac{\partial\psi_2}{\partial z}\right). \tag{45}$$

By substituting the expressions for $\psi_1, v_1, \varphi_1, \tilde{v}_1, T_1, T_2, \phi_1$, and ϕ_2 from (35) and (38) into (42)-(45), we can easily obtain expressions for $N_{31}, N_{32}, N_{33}, N_{34}, N_{35}$, and N_{36} in terms of the amplitude $A(\tau)$. Applying the condition for the solvability of the existence of a third-order solution Eq. (32), we find the Ginzburg-Landau equation for stationary convection with time-periodic coefficients in the following form:

$$A_1\frac{\partial A}{\partial\tau} - A_2(\tau)A + A_3A^3 = 0, \tag{46}$$

Where

$$A_1 = \frac{a^2}{\Pr} + \frac{k_c^2}{a^4}Ra_c + \frac{k_c^2}{a^4}RnLe(Le + N_A) - \frac{\pi^2}{a^2}\frac{QPm}{\Pr} - \frac{\pi^2 Ta\left((1+Ro)a^4 + \pi^2 QPm(RoPm - 1)\right)}{\Pr(a^4 + \pi^2 Q)^2} -$$

$$-\frac{\pi^4 TaRoQPm^2}{a^4(a^4 + \pi^2 Q)\Pr}, \quad A_2(\tau) = \frac{k_c^2}{a^2}Ra_c\left(\frac{Ra_2}{Ra_c} + \delta\cos(\Omega\tau)\right) + \frac{k_c^2}{a^2}Rn(Le + N_A)\delta\cos(\Omega\tau), \quad A_3 = \frac{k_c^4}{8a^4}(Ra_c + RnLe^2(Le + N_A)).$$

Obtaining an analytical solution for the non-autonomous Ginzburg-Landau (GL) Eq. (46) with time-varying coefficients is a difficult task. Therefore, we solve this equation numerically using Mathematica software. The initial value $A(0) = A_0$ is set, where A_0 represents the value of the initial amplitude. We assume $Ra_2 \approx Ra_c$, since the nonlinearity is considered near the critical state of convection, i.e., the Rayleigh number in this system is: $Ra \approx Ra_c(1 + \varepsilon^2)$. In the absence of nonuniform rotation and an external magnetic field, the non-autonomous Ginzburg-Landau equation for a non-conductive nanofluid was obtained by Kiran *et al.* [21].

In concluding this section, we note that in the case of an unmodulated system, the Ginzburg-Landau equation given above (47) can be simplified to:

$$A_1 \frac{\partial \tilde{A}}{\partial \tau} - A_2 \tilde{A} + A_3 \tilde{A}^3 = 0, \tag{48}$$

where $\tilde{A}(\tau)$ represents the amplitude of convection for the unmodulated case, and A_1 and A_3 have the same expressions as given in (47), while $A_2 = k_c^2 Ra_2 / a^2 \Pr$. An analytical solution of the equation (48) with a known initial condition $A_0 = A(0)$ can be obtained using the Lagrange method (constant variation), which is expressed as:

$$\tilde{A}(\tau) = \frac{A_0}{\sqrt{\frac{A_3}{A_2} A_0^2 + \left(1 - A_0^2 \frac{A_3}{A_2}\right) \exp\left(-\frac{2\tau A_2}{A_1}\right)}} \tag{49}$$

The thermal and nanoparticle concentration Nusselt numbers in this case can be obtained from Eqs. (39) and (40) by substituting the amplitude of convection (49).

4. RESULTS AND DISCUSSION

The Ginzburg-Landau equation, derived from the perturbation analysis, provides insights into the behavior of the system at finite amplitudes. We utilized a numerical solver, implementing the equation with proper initial conditions to obtain numerical solutions. NDSolve in Mathematica efficiently handles the equation's nonlinear and time-dependent nature. Through setting the appropriate parameters, initial amplitude $A(0) = 0.3$, and gravity modulation strength (δ, Ω), we simulated the system's evolution over time. The external control of convection through the modulation effect is important in the study of thermal instability and therefore has implications for a variety of applications, including the enhancement of heat transfer in industrial processes and the design of thermal management systems.

The graphical representation of the results of our numerical calculations is illustrated in Figs. 3-6.
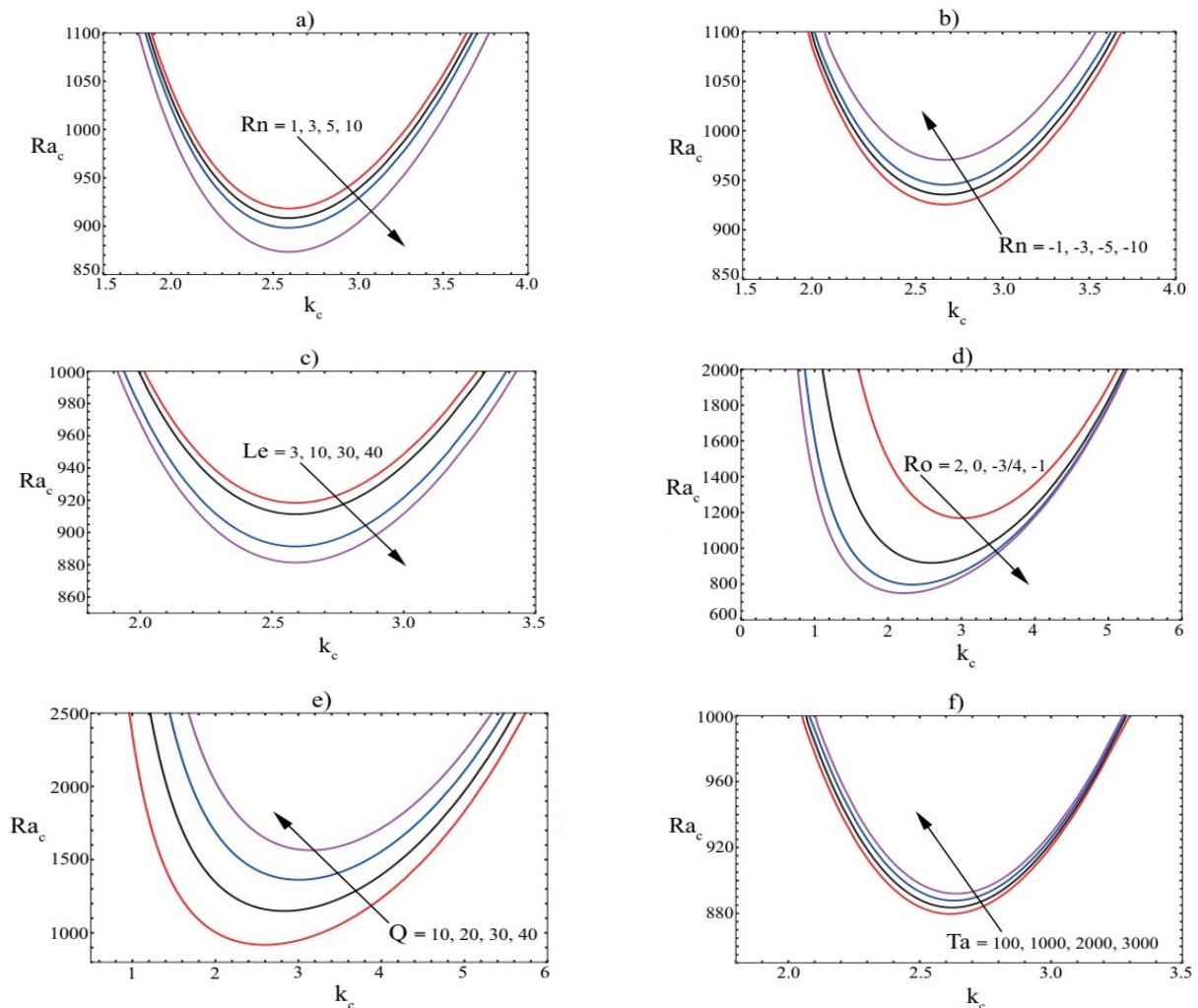
Figure. 3 Plots of the critical Rayleigh number Ra_c versus wave numbers k_c

We analyzed the dependencies of heat transfer Nu and mass transfer Nu_ϕ on the dimensionless time parameter τ. By varying the nanofluid parameters, such as Pr, Rn, Ro, and Le, as well as the modulation parameters (δ, Ω), we could investigate their impact on the heat and mass transfer characteristics. We assume that the fluid layer's viscosity is not high, so moderate Pr values are used in the calculations. δ values are also small due to low amplitude modulation. Additionally, gravity modulation is assumed to have a low frequency Ω, which maximizes its effect on the onset of convection and heat transport at lower frequencies. The stability curves for the stationary Rayleigh number (36) in the linear theory are shown in Fig. 3. From Figs. 3a and 3c, it can be seen that with an increase in parameters $Rn > 0$ (top-heavy configuration of nanofluid) and Le, the minimum values of the Rayleigh numbers decrease. Therefore, an increase in the parameters $Rn > 0$ and Le has a destabilizing effect on the onset of convection. From Fig. 3b, we see that in the case of a bottom-heavy configuration of nanofluid ($Rn < 0$, $N_A < 0$) an increase in the parameters Rn has a stabilizing effect on the onset of convection. Based on Fig. 3d, it can be observed that when the Rossby number has a positive profile ($Ro > 0$), the minimum value of the critical Rayleigh number (Ra_{min}) is higher compared to negative rotation profiles. As a result, negative rotation profiles have a lower threshold for instability development compared to uniform ($Ro = 0$) and nonuniform ($Ro = 2$) rotations. In Fig. 3e, the Rayleigh number is displayed in relation to the dimensionless wavenumber for various vertical magnetic field values (Chandrasekhar number Q). Fig. 3e illustrates that with an increase in magnetic field (Chadrasekhar number Q) values, the Rayleigh number also increases, leading to the stabilization of stationary convection. Fig. 3f illustrates that with an increase in Taylor number Ta values, the Rayleigh number also increases, leading to the stabilization of stationary convection.
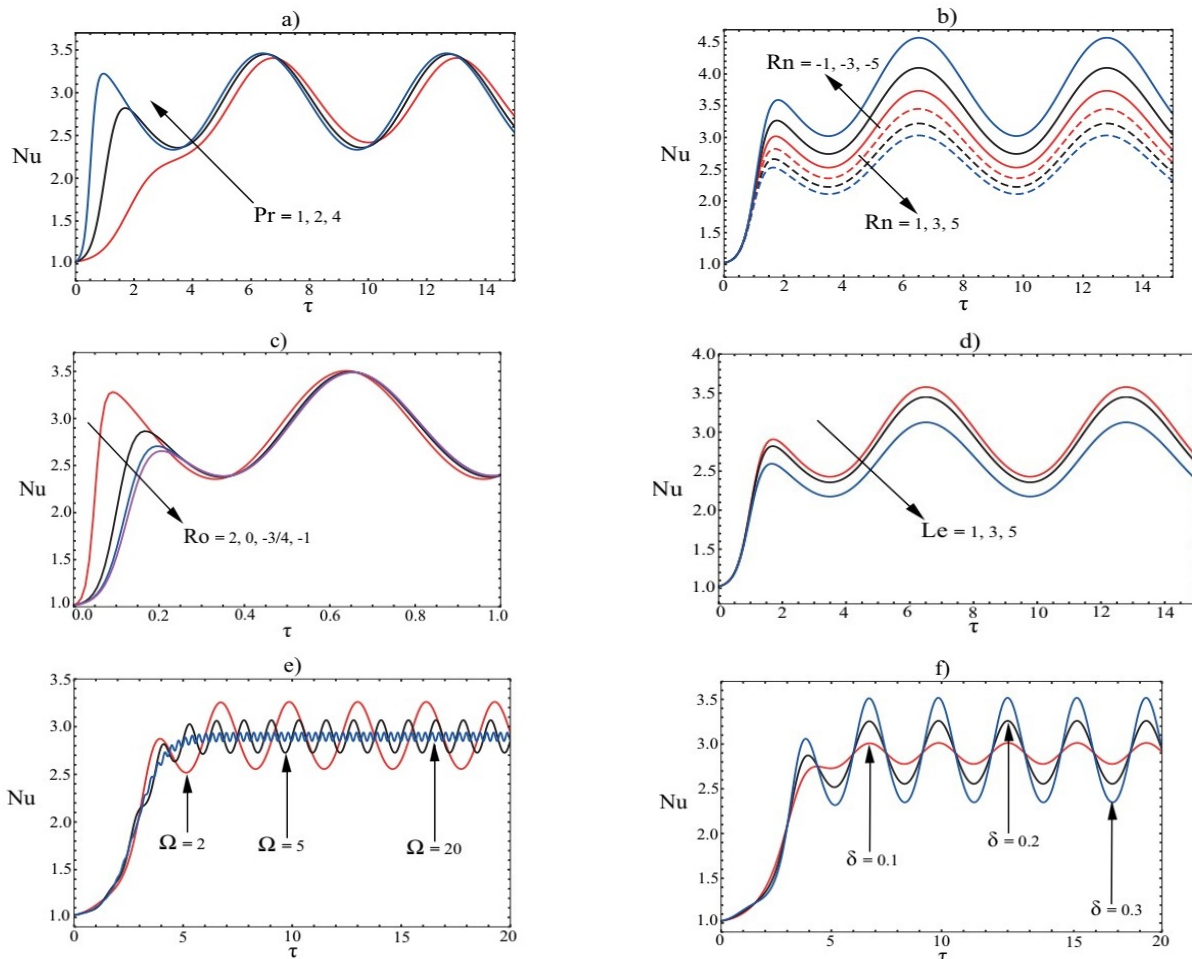
Figure 4. Dependence of the Nusselt number Nu on the time τ for a) Pr, b) Rn, c) Ro, d) Le, e) Ω, f) δ variations

Fig. 4a and Fig. 6a show the effect of Prandtl number Pr variations on heat and mass transfer, assuming the other parameters are fixed: $Rn = 1, Le = 3, Ro = 2, \Omega = 1, \delta = 0.3$. As can be seen from Fig. 4a and Fig. 5a, an increase in the Prandtl number Pr causes a rise in heat and concentration transfer over a brief period of time. As a result, systems with higher Prandtl numbers tend to exhibit more efficient heat transfer characteristics. Therefore, the Prandtl number (Pr) plays a significant role in enhancing heat and concentration transport, especially at low time values. Next, we consider the influence of concentration Rayleigh number Rn on both thermal and concentration Nusselt numbers at fixed

parameters: $Pr = 2, Le = 3, Ro = 2, \Omega = 1, \delta = 0.3$. Similarly, the concentration Rayleigh number Rn has a significant impact on both thermal and concentration Nusselt numbers, leading to enhanced heat and concentration transport in the case of a bottom-heavy configuration of nanofluid ($Rn < 0$, $N_A < 0$), as shown in Figures 4b and 5b. Increasing the concentration of nanoparticles at the lower hot boundary enhances the fluid's thermal conductivity. Nanoparticles typically have higher thermal conductivity than the base fluid, and this higher thermal conductivity aids in conducting heat from the lower hot boundary to the surrounding fluid. As a result, the convective heat transfer is improved, leading to an increase in both the thermal and concentration Nusselt numbers. It is noteworthy that Rn has a dual role in regulating the heat and mass transfer properties of the medium. The positive values of Rn can induce the reverse nature of heat and mass transport within the layer. When the concentration of nanoparticles increases at the upper cold boundary, they can enhance the overall thermal conductivity of the fluid layer. This increased thermal conductivity facilitates heat transfer through conduction, reducing the reliance on convective heat transfer. As a result, the thermal Nusselt number decreases. The presence of nanoparticles can disrupt the fluid flow and impede its motion. This hindered fluid motion reduces the convective heat and mass transfer rates. Consequently, the concentration Nusselt number, which characterizes mass transfer, decreases. It is important to note that these effects can be observed for all profiles of rotation, not just positive profiles.

Figures 4c and 5c exhibit the temporal variations of the Nusselt number Nu and nano-Nusselt number Nu_ϕ for various rotation profiles $Ro = (2, 0, -3/4, -1)$ of the electrically conductive nanofluid subjected to an oscillating gravitational field with a frequency $\Omega = 10$ and an amplitude $\delta = 0.3$ with fixed parameters $Pr = 1, Le = 3$. The results presented in these figures indicate that both heat and concentration transfer in the nanofluid are enhanced when the nanofluid experiences nonuniform rotation characterized by a positive Rossby number $(Ro = 2)$. This demonstrates the useful impact of nonuniform rotation on the overall heat and concentration transport processes within the nanofluid system.
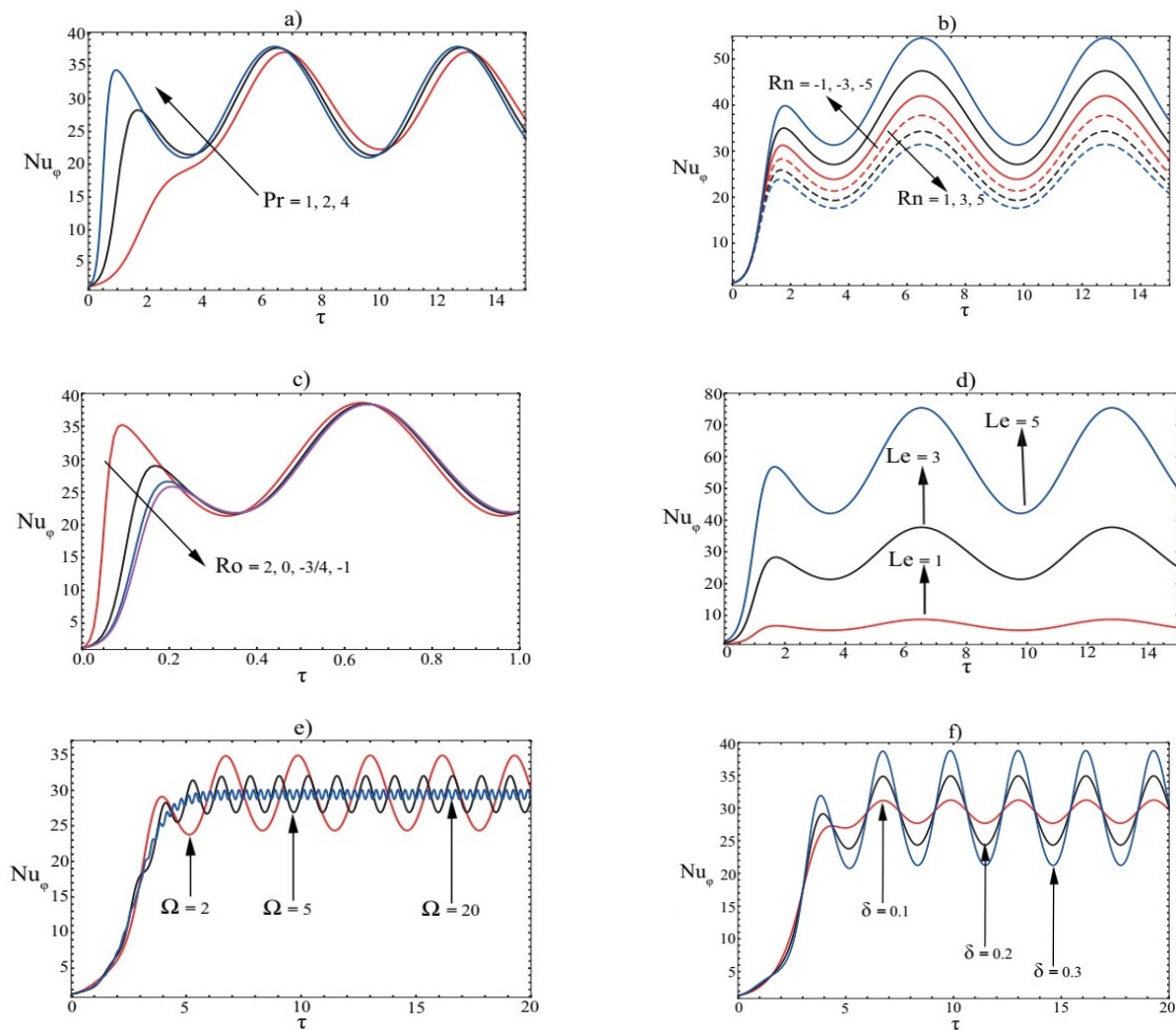
Figure 5. Dependence of the nano-Nusselt number Nu_ϕ on the time τ for a) Pr, b) Rn, c) Ro, d) Le, e) Ω, f) δ variations

On Fig. 4d the effect of variations of the Lewis number Le on heat transfer is shown for fixed other parameters: $\text{Rn} = 1, \text{Pr} = 2, \text{Ro} = 2, \Omega = 1, \delta = 0.3$. It was observed that as the Lewis number increased, the heat transfer decreased. On the contrary, growing Le enhances concentration transport, as depicted in Fig. 5d. These results are in good agreement with the conclusions of the papers by Aleng *et al.* [38], Alam *et al.* [39]. The impact of the modulation frequency Ω is illustrated in Figures 4e and 5e. Specifically, at lower modulation rates, corresponding to low-frequency cases $(\Omega = 2)$, higher heat and mass transfer are achieved compared to higher vibrational rates $(\Omega = 20)$.

Fig. 4f and Fig. 5f depict the influence of the modulation amplitude δ on heat and mass transfer. The range of δ considered in the study is from 0.1 to 0.5, aimed at enhancing heat and mass transfer. It is worth mentioning that the frequency of modulation Ω has a diminishing effect on heat and mass transfer, which aligns with the findings reported by Gresho and Sani [8] and Kopp *et al.* [31] for the case of ordinary fluid. These results highlight the significance of considering low-frequency g-jitter to optimize the transport process. The outcomes obtained from our investigation on nanofluids can also be compared with the studies conducted by Kiran *et al.* [14]-[18] and Bhadauria and Agarwal [40]. Equation (48) provides an analytical expression for the amplitude of convection in the unmodulated case. By utilizing this amplitude, a comparison between the modulated system and the unmodulated system is depicted in Fig. 6. The graph demonstrates that there is a sudden increase in $\text{N}u(\tau)$ and $\text{N}u_\phi(\tau)$ for low values of the time parameter τ, and it stabilizes for higher values of τ. However, in the case of the modulated system, both $\text{N}u(\tau)$ and $\text{N}u_\phi(\tau)$ exhibit oscillatory behavior.
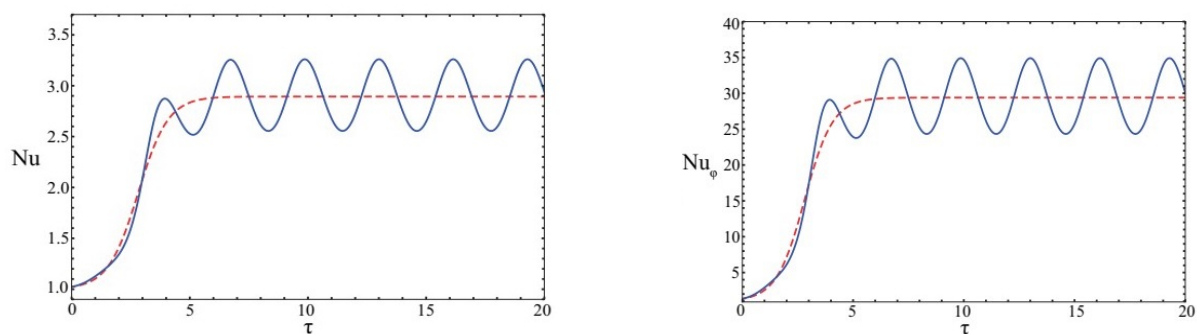
Figure 6. Variations of the Nusselt numbers Nu and Nu_ϕ in the absence of δ (dashed line) and the presence of $\delta = 0.3$, $\Omega = 2$ (solid line) modulation of the gravity field

5. CONCLUSIONS

We have developed a weakly nonlinear theory to investigate the effects of gravity modulation on stationary convection in a nonuniformly rotating electrically conductive nanofluid under a constant vertical magnetic field. Our analysis utilizes perturbation theory with respect to the small supercriticality parameter, $\varepsilon = \sqrt{(Ra - Ra_c)/Ra_c}$, where Ra is the Rayleigh number and Ra_c is the critical Rayleigh number. We consider the small amplitude of the modulated gravity field to be of second order in ε. In the first order of ε, the parametric modulation does not influence the development of convection, leading to results consistent with linear theory. However, in the third order of ε, we obtained a nonlinear Ginzburg-Landau equation with a time-periodic coefficient. Through numerical analysis, we draw the following conclusions based on the obtained results:

- The numbers $\text{Nu}(\tau)$ and $\text{Nu}_\phi(\tau)$ increase when the values of the parameters Pr and $\text{Rn} < 0$ are increased.
- With an increase in the Le number, a decrease in heat transfer and an increase in mass transfer were observed.
- Nonuniform rotation with a positive Rossby number $\text{Ro} > 0$ enhances heat and mass transfer in the nanofluid system.
- Increasing the modulation frequency Ω leads to a decrease in the variations of the Nusselt numbers $\text{Nu}(\tau)$ and $\text{Nu}_\phi(\tau)$, resulting in suppressed heat and mass transfer for both positive $(\text{Ro} > 0)$ and negative $(\text{Ro} < 0)$ rotation profiles.
- Irrespective of the rotation profile, increasing the modulation amplitude δ enhances heat and mass transfer.

These findings provide valuable insights into the behavior of stationary magnetoconvection in a nonuniformly rotating electrically conductive nanofluid under the influence of gravity modulation. Understanding the role of the parameters $\text{Pr}, \text{Rn}, \text{Ro}$, Le, Ω, and δ and their influence on convection is crucial for managing and controlling the behavior of the system to optimize heat and mass transfer.

ORCID
Michael I. Kopp, https://orcid.org/0000-0001-7457-3272, **Volodymyr V. Yanovsky,** https://orcid.org/0000-0003-0461-749X

REFERENCES

[1] S.U.S. Choi, "Enhancing Thermal Conductivity of Fluids with Nanoparticles," In: D. A. Siginer and H. P. Wang, Eds., Developments and Applications of Non-Newtonian Flows, ASME, New York, Vol. 66, 1995, pp. 99-105.

[2] J. Buongiorno. "Convective Transport in Nanofluids," J. Heat Trans. 128, 240-250 (2006). https://doi.org/10.1115/1.2150834

[3] D. Tzou. "Thermal instability of nanofluids in natural convection," Int. J. Heat Mass Transf. **51**, 2967-2979 (2008). https://doi.org/10.1016/j.ijheatmasstransfer.2007.09.014

[4] J. Buongiorno and W. Hu. "Nanofluid coolants for advanced nuclear power plants." Proceedings of ICAPP. Vol. 5. No. 5705. 2005.

[5] D. A. Nield, and A. V. Kuznetsov. "Thermal instability in a porous medium layer saturated by a nanofluid," Int. J. Heat Mass Transfer, 52, 5796-5801 (2009), https://doi.org/10.1016/j.ijheatmasstransfer.2009.07.023

[6] G. Venezian. "Effect of modulation on the onset of thermal convection," J. Fluid Mech. **35**, 243-254 (1969). https://doi.org/10.1017/S0022112069001091

[7] P. K. Bhatia and B. S. Bhadauria. "Effect of Modulation on Thermal Convection Instability," Z. Naturforsch. **55a**, 957-966 (2000). https://doi.org/10.1515/zna-2000-11-1222

[8] P. M. Gresho, R. Sani. "The effects of gravity modulation on the stability of a heated fluid layer," J. Fluid Mech. **40**, 783-806 (1970). https://doi.org/10.1017/S0022112070000447

[9] J. K. Bhattacharjee. " Rotating Rayleigh-Benard convection with modulation," J. Phy. A: Math. Gen. **22**, L1135-L1189 (1989). https://doi.org/10.1088/0305-4470/22/24/001

[10] S. Aniss, M. Belhaq, and M. Souhar. "Effects of a Magnetic Modulation on the Stability of a Magnetic Liquid Layer Heated from Above," J. Heat Transfer **123**, 428-433 (2001), https://doi.org/10.1115/1.1370501

[11] B. S. Bhadauria, and Palle Kiran. "Nonlinear thermal Darcy convection in a nanofluid saturated porous medium under gravity modulation," Advanced Science Letters **20**, 903-910 (2014). https://doi.org/10.1166/asl.2014.5466

[12] B. S. Bhadauria, Palle Kiran, and M. Belhaq. "Nonlinear thermal convection in a layer of nanofluid under g-jitter and internal heating effects," In MATEC Web of Conferences, **16**, 09003 EDP Sciences, 2014. https://doi.org/10.1051/matecconf/20141609003

[13] P. Kiran. "Nonlinear thermal convection in a viscoelastic nanofluid saturated porous medium under gravity modulation," Ain Shams Engineering Journal **7**, 639-651 (2016). https://doi.org/10.1016/j.asej.2015.06.005

[14] P. Kiran, B. S. Bhadauria, V. Kumar. "Thermal convection in a nanofluid saturated porous medium with internal heating and gravity modulation," J. Nanofluids. **5**, 328-339 (2016). https://doi.org/10.1166/jon.2016.1220

[15] P. Kiran, Y. Narasimhulu. "Centrifugally driven convection in a nanofluid saturated rotating porous medium with modulation," J. Nanofluids. **6**, 513-523 (2017). https://doi.org/10.1166/jon.2017.1333

[16] P. Kiran, Y. Narasimhulu. "Internal heating and thermal modulation effects on chaotic convection in a porous medium," J. Nanofluids. ;**7**, 544-555 (2018). https://doi.org/10.1166/jon.2018.1462

[17] P. Kiran, B. S. Bhadauria, R. Roslan. "The effect of throughflow on weakly nonlinear convection in a viscoelastic saturated porous medium," J. Nanofluids. **9**, 36-46 (2020). https://doi.org/10.1166/jon.2020.1724

[18] P. Kiran. "Gravity modulation effect on weakly nonlinear thermal convection in a fluid layer bounded by rigid boundaries," Int. J. Nonlinear Sci. Num. Simul. 2021. https://doi.org/10.1515/ijnsns-2021-0054

[19] P. Kiran. "Nonlinear throughflow and internal heating effects on vibrating porous medium," Alex. Eng. J. **55**, 757-767 (2016). http://dx.doi.org/10.1016/j.aej.2016.01.012

[20] P. Kiran. "Throughflow and gravity modulation effects on heat transport in a porous medium," J. Appl. Fluid Mech. **9**, 1105-1113 (2016). https://doi.org/10.18869/acadpub.jafm.68.228.24682

[21] P. Kiran, S. H. Manjula, and R. Roslan. "Weak nonlinear analysis of nanofluid convection with g-jitter using the Ginzburg-Landau model," Open Physics **20**, 1283-1294 (2022). https://doi.org/10.1515/phys-2022-0217

[22] S. H. Manjula, Palle Kiran, and S. N. Gaikwad. "Study of Heat and Mass Transfer in a Rotating Nanofluid Layer Under Gravity Modulation," J. Nanofluids **12**, 842-852 (2023). https://doi.org/10.1166/jon.2023.1971

[23] S. Chandrasekhar, "On the stability of the simplest solution of the equations of hydromagnetics," Proc. Natl Acad. Sci. USA **42**, 273-276 (1956).

[24] E. P. Velikhov, "Stability of an ideally conducting liquid flowing between cylinders rotating in a magnetic field," Soviet Physics Jetp. **36**, 995-998 (1959).

[25] M. I. Kopp, A. V. Tour, and V. V. Yanovsky. "Magnetic Convection in a Nonuniformly Rotating Electroconducting Medium," JETP **127**, 1173-1196 (2018). http://dx.doi.org/10.1134/S106377611812018X

[26] M. I. Kopp, A. V. Tour, and V. V. Yanovsky, "Magnetic Convection in a Nonuniformly Rotating Electroconducting Medium under the Action of External Magnetic Field Modulation," JETP **130**, 759-782 (2020). https://doi.org/10.1134/S1063776120050052

[27] M. I. Kopp, A. V. Tur, V. V. Yanovsky. "Magnetic convection in a nonuniformly rotating electrically conductive medium in an external spiral magnetic field," Fluid Dyn. Res. **53**, 015509 (2021). https://doi.org/10.1088/1873-7005/abd8dc

[28] M. I. Kopp, A. V. Tour, and V. V. Yanovsky, "Hydromagnetic Instabilities in a Nonuniformly Rotating Layer of an Electrically Conducting Nanofluid," JETP **132**, 960-984 (2021). https://doi.org/10.1134/S1063776121050113

[29] M. I. Kopp, A. V. Tur, V. V. Yanovsky. "Chaotic magnetoconvection in a non-uniformly rotating electroconductive fluids," Problems of Atomic Science and Technology **4**, 230-234 (2018). https://arxiv.org/abs/1805.11894

[30] M. I. Kopp, A. V. Tur, V. V. Yanovsky. "Instabilites in the Non-uniformly Rotating Medium with Temperature Stratification in the External Magnetic Field," East Eur. J. Phys. **1**, 4-33 (2019). https://doi.org/10.26565/2312-4334-2020-1-01

[31] M. I. Kopp, A. V. Tur, V. V. Yanovsky. "Weakly Nonlinear Magnetic Convection in a Nonuniformly Rotating Electrically Conductive Medium Under the Action of Modulation of External Fields," East Eur. J. Phys. 2, 5-37 (2020). https://doi.org/10.26565/2312-4334-2020-2-01

[32] R. Haberman, Elementary Applied Partial Differential Equations with Fourier Series and Boundary Value Problems, 4th ed., Prentice-Hall, Inc., 2004.

[33] D. A. Nield, A. V, Kuznetsov. "The onset of convection in a horizontal nanofluid layer of finite depth," Eur. J. Mech. B/Fluids **29**, 217-223 (2010). https://doi.org/10.1016/j.euromechflu.2010.02.003

[34] R. Chand. "Thermal instability of rotating nanofluid," Int. J. Appl. Math. Mech. 9, 70-90 (2013).

[35] U. Gupta, J. Ahuja, R. K. Wanchoo. "Magneto convection in a nanofluid layer," Int. J. Heat Mass Transf. **64**, 1163-1171 (2013). https://doi.org/10.1016/j.ijheatmasstransfer.2013.05.035

[36] D. Yadav, R. Bhargava, G. S. Agrawal. "Thermal instability in a nanofluid layer with a vertical magnetic field," J. Eng. Math. **80**, 147-164 (2013). https://doi.org/10.1007/s10665-012-9598-1

[37] S. H. Manjula, G. Kavitha, P. Kiran. "Ginzburg Landau Model for Nanofluid Convection in the Presence of Time Periodic Plate Modulation," CFD Letters **15**, 64-79 (2023). https://doi.org/10.37934/cfdl.15.4.6479

[38] N. L. Aleng, N. Bachok, N. M. Arifin. "Flow and Heat Transfer of a Nanofluid over an Exponentially Shrinking Sheet," Indian J. Sci. Technol. **8**, 1-6 (2015). https://doi.org/10.17485/ijst/2015/v8i31/87246

[39] A. Alam, D. N. K. Marwat, A. Ali. "Flow of nano-fluid over a sheet of variable thickness with non-uniform stretching (shrinking) and porous velocities," Adv. Mech. Eng. **13**, 1-16 (2021). https://doi.org/10.1177/16878140211012913

[40] B. S. Bhadauria, S. Agarwal. "Natural convection in a nanofluid saturated rotating porous layer: a nonlinear study," Transp. Porous Med. **87**, 585-602 (2011). https://doi.org/10.1007/s11242-010-9702-9

ДОСЛІДЖЕННЯ ВПЛИВУ ГРАВІТАЦІЙНОЇ МОДУЛЯЦІЇ НА СЛАБОНЕЛІНІЙНУ МАГНІТОКОНВЕКЦІЮ В ШАРІ НАНОРІДІНИ, ЩО НЕРІВНОМІРНО ОБЕРТАЄТЬСЯ

Михайло Й. Копп[a], Володимир В. Яновський[a,b]
[a]*Інститут монокристалів, Національна Академія Наук України*
пр. Науки 60, 61072 Харків, Україна
[b]*Харківський національний університет імені В.Н. Каразіна*
майдан Свободи, 4, 61022, Харків, Україна

В цій роботі досліджується вплив гравітаційної модуляції на слабонелінійну магнітоконвекцію в шарі нанорідіни, що нерівномірно обертається. Отримано основні рівняння для декартової апроксимації течії Куетта з використанням наближення Бусінеска та гравітаційної модуляції. Слабонелінійний режим аналізується методом збурень за малим параметром надкритичності числа Релея з урахуванням ефектів броунівського руху та термофорезу у шарі нанорідіни. Тепломасоперенос оцінюється в термінах кінцевих амплітуд і розраховується за числами Нуссельта для рідини та об'ємної концентрації наночастинок. Отримані дані показують, що гравітаційна модуляція, нерівномірне обертання та відмінності в об'ємній концентрації наночастинок на межах шарів можуть ефективно управляти тепломасопереносом. Крім того, негативний профіль обертання має ефект дестабілізації. Дослідження показує, що модульована система передає більше тепла та маси, ніж немодульована система.

Ключові слова: *нанорідина; шар, що нерівномірно обертається; слабонелінійна теорія; гравітаційна модуляція; неавтономне рівняння Гінзбурга-Ландау*

THE EFFECT OF THERMAL STRATIFICATION ON FLOW PAST AN INFINITE VERTICAL PLATE IN PRESENCE OF CHEMICAL REACTION[†]

 Rupam Shankar Nath[*], **Rudra Kanta Deka**

Department of Mathematics, Gauhati University, Guwahati-781014, Assam, India
*Corresponding Author e-mail: rupamnath23@gmail.com

This study examines how thermal stratification affect the movement of a fluid in presence of first order chemical reaction past an infinite vertical plate. To solve the non-dimensional governing equations in closed form for $Pr = 1$, the Laplace's transform system is applied. Significant findings resulting from thermal stratification are compared to the case of no stratification. The effects of many parameters, including S, K, Gr, Gc, Sc and time on velocity, temperature, concentration, skin friction, Nusselt number, and Sherwood number are explored and graphically displayed. It is shown that the steady state is attained at shorter times as a result of the application of stratification on the flow.

Keywords: *Thermal Stratification; Chemical Reaction; Heat and Mass Transfer; Vertical Plate; Schimdt Number*

PACS: 47.55.P-, 44.25.+f, 44.05.+e, 47.11.-j

1. INTRODUCTION

The phenomena of thermal stratification is widely observed in natural systems like lakes and oceans. The dynamics of the flow can be further complicated by the existence of chemical reactions. In this article, we seek to figure out the effects of thermal stratification on flow dynamics and interactions with chemical reactions.There are numerous applications for this research. It can be utilized to create chemical reactors and heat exchangers that are more effective. It can also be used to investigate the impact of thermal stratification on the performance of cooling systems in electrical equipment.

The combined impact of thermal stratification and chemical reaction flow past an infinite vertical plate has never been studied before, and this study is the first to do so. [1, 2] and [3] investigated unsteady flows in a Stably Stratified Fluid, focusing on infinite plates. Furthermore, buoyancy-driven flows in a stratified fluid were examined by [4] and [5]. [6] came up with an analytical solution to describe how fluid would flow past an infinite vertical plate that had been affected chemically. In their research, [7] and [8] look at what happens when a chemical reaction is applied to an infinite vertical plate under various conditions. [9] and [10] investigate the combined Effects of Chemical Reaction and Thermal stratification on MHD flow for vertical stretching surfaces. Similarly, [11] researched the consequences of non-Newtonian fluid flow over a porous medium on both effects.

In this paper, we derived the special solutions for $Sc = 1$ and classical solutions for the case $S = 0$ (without stratification). These solutions are compared with the primary solutions, and graphs are used to demonstrate the differences. The impacts of physical parameters on velocity, temperature, and concentration profiles, including the thermal stratification parameter (S), thermal Grashof number (Gr), mass Grashof number (Gc), Schimdt number (Sc), Chemical Reaction Parameter (K), and time (t), are explored and presented in graphs. The results of this research have a wide range of applications in a variety of industries and chemical factories. Additionally, this research is to be helpful for chemical processing tasks like fibre drawing, crystal extraction from melts, and polymer manufacturing.

2. MATHEMATICAL ANALYSIS

We investigate the unsteady flow of a viscous in-compressible stratified fluid past an infinite vertical plate with chemical reaction effects. The diffusing species and the fluid are thought to be involved in a first-order chemical reaction. We use a coordinate system in which the x' axis is taken vertically upward along the plate and the y' axis is taken normal to the plate to explore the flow scenario as seen in Fig.1. The temperature T'_∞ and concentration C'_∞ of the plate and the fluid are initially the same. The plate temperature is raised to T'_w and the concentration level is raised to C'_w at time $t' > 0$. Since the plate has an endless length, all flow variables are independent of x' and are solely affected by y' and t'. As a result, we get a one-dimensional flow flow with only one non-zero vertical velocity component, u'. The equations for motion, energy, and concentration are then represented by Boussinesqs' approximation as follows:
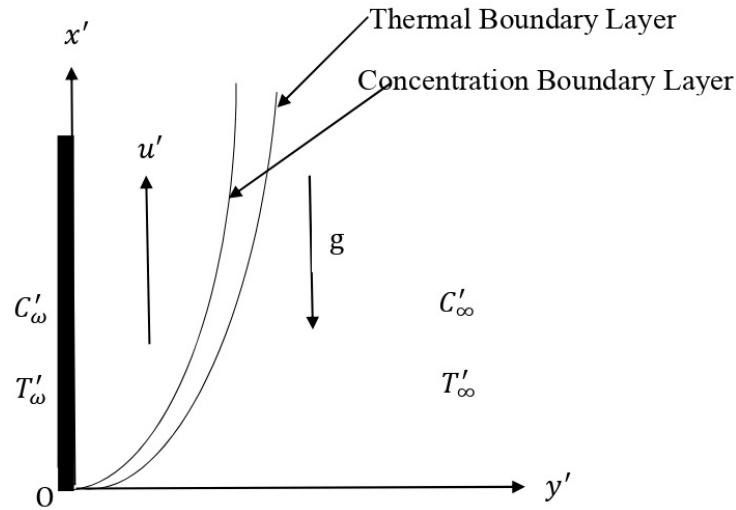
Figure 1. Physical Model and coordinate system

$$\frac{\partial u'}{\partial t'} = g\beta(T' - T'_\infty) + g\beta^*(C' - C'_\infty) + \nu\frac{\partial^2 u'}{\partial y'^2} \tag{1}$$

$$\frac{\partial T'}{\partial t'} = \alpha\frac{\partial^2 T'}{\partial y'^2} - \gamma u' \tag{2}$$

$$\frac{\partial C'}{\partial t'} = D\frac{\partial^2 C'}{\partial y'^2} - K_1 C' \tag{3}$$

with the following initial and boundary Conditions:

$$
\begin{array}{llll}
u' = 0 & T' = T'_\infty & C' = C'_\infty & \forall y', t' \leq 0 \\
u' = 0 & T' = T'_w & C' = C'_w & \text{at } y' = 0, t' > 0 \\
u' = 0 & T' \to T'_\infty & C' \to C'_\infty & \text{as } y' \to \infty, t' > 0
\end{array}
$$

where, $\gamma = \frac{dT'_\infty}{dx'} + \frac{g}{C_p}$ denotes the thermal stratification parameter and $\frac{dT'_\infty}{dx'}$ denotes the vertical temperature convection known as thermal stratification. In addition, $\frac{g}{C_p}$ represents the rate of reversible work done on fluid particles by compression, often known as work of compression. The variable (γ) will be referred to as the thermal stratification parameter in our research because the compression work is relatively minimal. For the purpose of testing computational methods, compression work is kept as an additive to thermal stratification.

Now, we express the reference velocity, length, and time as follows:

$$u_0 = \{g\beta\nu(T'_w - T'_\infty)\}^{1/3}, \quad y_0 = \frac{\nu^{2/3}}{\{g\beta(T'_w - T'_\infty)\}^{1/3}}, \quad t_0 = \frac{\nu^{1/3}}{\{g\beta(T'_w - T'_\infty)\}^{2/3}}$$

and we provide non-dimensional quantities in the following:

$$U = \frac{u'}{u_0}, \quad t = \frac{t'}{t_0}, \quad y = \frac{y'}{y_0}, \quad \theta = \frac{T' - T'_\infty}{T'_w - T'_\infty}, \quad C = \frac{C' - C'_\infty}{C'_w - C'_\infty}, \quad Gr = \frac{g\beta\nu(T'_w - T'_\infty)}{u_0^3}$$

$$Gc = \frac{g\beta^*\nu(C'_w - C'_\infty)}{u_0^3}, \quad Pr = \frac{\nu}{\alpha}, \quad Sc = \frac{\nu}{D}, \quad K = \frac{\nu K_1}{u_0^2}, \quad S = \frac{\gamma\nu}{u_0(T'_w - T'_\infty)}$$

The non-dimensional forms of the equations (1)-(3) are given by

$$\frac{\partial U}{\partial t} = Gr\theta + GcC + \frac{\partial^2 U}{\partial y^2} \tag{4}$$

$$\frac{\partial \theta}{\partial t} = \frac{1}{Pr}\frac{\partial^2 \theta}{\partial y^2} - SU \tag{5}$$

$$\frac{\partial C}{\partial t} \;=\; \frac{1}{Sc}\frac{\partial^2 C}{\partial y^2} - KC \tag{6}$$

Non-dimensional form of initial and boundary Conditions are:

$$
\begin{array}{llll}
U = 0 & \theta = 0 & C = 0 & \forall y, t \le 0 \\
U = 0 & \theta = 1 & C = 1 & \text{at } y = 0, t > 0 \\
U = 0 & \theta \to 0 & C \to 0 & \text{as } y \to \infty, t > 0
\end{array}
\tag{7}
$$

3. METHOD OF SOLUTION

The non-dimensional governing equations (4)- (6) with boundary conditions (7) are solved using Laplace's transform method for $Pr = 1$. Hence, the expressions for concentration, velocity and temperature with the help of [12] and [13] are given by

$$C \;=\; \frac{1}{2}\left[e^{-2\eta\sqrt{ScKt}} erfc\left(\eta\sqrt{Sc} - \sqrt{Kt}\right) + e^{2\eta\sqrt{ScKt}} erfc\left(\eta\sqrt{Sc} + \sqrt{Kt}\right)\right] \tag{8}$$

$$
\begin{aligned}
U \;=\; & \frac{Gc}{2(Sc-1)}\left[C_1\left\{f_1(iA) + f_1(-iA)\right\} + (C_2 - iC_3)\left\{f_2(iA, B + iB_1) + f_2(-iA, B + iB_1)\right\}\right. \\
& + (C_2 + iC_3)\left\{f_2(iA, B - iB_1) + f_2(-iA, B - iB_1)\right\}\right] + \frac{Gc}{2iA}\left[(D_1 - 1)\left\{f_1(iA) - f_1(-iA)\right\}\right. \\
& + (D_2 + iD_3)\left\{f_2(iA, B + iB_1) - f_2(-iA, B + iB_1)\right\} + (D_2 - iD_3)\left\{f_2(iA, B - iB_1)\right.\\
& \left. - f_2(-iA, B - iB_1)\right\}\right] + \frac{iA}{2S}\left\{f_1(iA) - f_1(-iA)\right\} \\
& - \frac{Gc}{(Sc-1)}\left[\frac{C_1}{2}\left\{e^{-2\eta\sqrt{ScKt}} erfc\left(\eta\sqrt{Sc} - \sqrt{Kt}\right) + e^{2\eta\sqrt{ScKt}} erfc\left(\eta\sqrt{Sc} + \sqrt{Kt}\right)\right\}\right. \\
& + (C_2 - iC_3)\left\{f_3(K, B + iB_1)\right\} + (C_2 + iC_3)\left\{f_3(K, B - iB_1)\right\}\right]
\end{aligned}
\tag{9}
$$

$$
\begin{aligned}
\theta \;=\; & \frac{SGc}{2iA(Sc-1)}\left[C_1\left\{f_1(iA) - f_1(-iA)\right\} + (C_2 - iC_3)\left\{f_2(iA, B + iB_1) - f_2(-iA, B + iB_1)\right\}\right. \\
& + (C_2 + iC_3)\left\{f_2(iA, B - iB_1) - f_2(-iA, B - iB_1)\right\}\right] + \frac{SGc}{2(Sc-1)^2}\left[E_1\left\{f_1(iA) + f_1(-iA)\right\}\right. \\
& + (E_2 - iE_3)\left\{f_2(iA, B + iB_1) + f_2(-iA, B + iB_1)\right\} + (E_2 + iE_3)\left\{f_2(iA, B - iB_1)\right. \\
& \left. + f_2(-iA, B - iB_1)\right\}\right] + \frac{1}{2}\left\{f_1(iA) + f_1(-iA)\right\} \\
& - \frac{SGc}{(Sc-1)^2}\left[\frac{E_1}{2}\left\{e^{-2\eta\sqrt{ScKt}} erfc\left(\eta\sqrt{Sc} - \sqrt{Kt}\right) + e^{2\eta\sqrt{ScKt}} erfc\left(\eta\sqrt{Sc} + \sqrt{Kt}\right)\right\}\right. \\
& + (E_2 - iE_3)f_3(K, B + iB_1) + (E_2 + iE_3)f_3(K, B - iB_1)\right]
\end{aligned}
\tag{10}
$$

where,

$$\eta = \frac{y}{2\sqrt{t}}, \quad A = \sqrt{SGr}, \quad B = \frac{ScK}{Sc-1}, \quad B_1 = \frac{A}{Sc-1} = \frac{\sqrt{SGr}}{Sc-1}, \quad C_1 = \frac{B}{(B^2 + B_1^2)}$$

$$C_2 = \frac{-B}{2(B^2 + B_1^2)}, \quad C_3 = \frac{-B_1}{2(B^2 + B_1^2)}, \quad D_1 = \frac{B^2}{(B^2 + B_1^2)}, \quad D_2 = \frac{B_1^2}{2(B^2 + B_1^2)}$$

$$D_3 = \frac{BB_1}{2(B^2 + B_1^2)}, \quad E_1 = \frac{1}{(B^2 + B_1^2)}, \quad E_2 = \frac{-1}{2(B^2 + B_1^2)}, \quad E_3 = \frac{B}{2B_1(B^2 + B_1^2)}$$

Also, f_i's are inverse Laplace's transforms given by

$$f_1(ip) = L^{-1}\left\{\frac{e^{-y\sqrt{s+ip}}}{s}\right\}, \quad f_2(ip, q_1 + iq_2) = L^{-1}\left\{\frac{e^{-y\sqrt{s+ip}}}{s + q_1 + iq_2}\right\}, \quad f_3(p, q_1 + iq_2) = L^{-1}\left\{\frac{e^{-y\sqrt{Sc(s+p)}}}{s + q_1 + iq_2}\right\}$$

We separate the complex arguments of the error function contained in the previous expressions into real

and imaginary parts using the formulas provided by [13].

3.1. Special Case [For Sc=1]

We came up with answers for the special case where $Sc = 1$. Hence, the solutions for the special case are as follows:

$$C^* = \frac{1}{2}\left[e^{-2\eta\sqrt{Kt}}erfc\left(\eta - \sqrt{Kt}\right) + e^{2\eta\sqrt{Kt}}erfc\left(\eta + \sqrt{Kt}\right)\right] \tag{11}$$

$$U^* = \frac{KGc}{2(K^2+A^2)}\{f_1(iA) + f_1(-iA)\} + \frac{iA}{2}\left(\frac{1}{S} + \frac{Gc}{K^2+A^2}\right)\{f_1(iA) - f_1(-iA)\}$$
$$-\frac{KGc}{2(K^2+A^2)}\left[e^{-2\eta\sqrt{Kt}}erfc\left(\eta - \sqrt{Kt}\right) + e^{2\eta\sqrt{Kt}}erfc\left(\eta + \sqrt{Kt}\right)\right] \tag{12}$$

$$\theta^* = \frac{SKGc}{2iA(K^2+A^2)}\{f_1(iA) - f_1(-iA)\} + \frac{1}{2}\left(1 + \frac{SGc}{K^2+A^2}\right)\{f_1(iA) + f_1(-iA)\}$$
$$-\frac{SGc}{2(K^2+A^2)}\left\{e^{-2\eta\sqrt{Kt}}erfc\left(\eta - \sqrt{Kt}\right) + e^{2\eta\sqrt{Kt}}erfc\left(\eta + \sqrt{Kt}\right)\right\} \tag{13}$$

3.2. Classical Case (S=0)

We derived solutions for the classical case of no thermal stratification ($S = 0$). We want to compare the results of the fluid with thermal stratification to the case with no stratification. Hence, the corresponding solutions for the classical case is given by :

$$\theta_c = = erfc(\eta) \tag{14}$$

$$U_c = \frac{Gc}{2KSc}\left[2erfc\left(\eta\right) - e^{-Bt}\left\{e^{-2\eta\sqrt{-Bt}}erfc\left(\eta - \sqrt{-Bt}\right) + e^{2\eta\sqrt{-Bt}}erfc\left(\eta + \sqrt{-Bt}\right)\right\}\right.$$
$$-\left\{e^{-2\eta\sqrt{ScKt}}erfc\left(\eta\sqrt{Sc} - \sqrt{Kt}\right) + e^{2\eta\sqrt{ScKt}}erfc\left(\eta\sqrt{Sc} + \sqrt{Kt}\right)\right\}$$
$$\left.+e^{-Bt}\left\{e^{-2\eta\sqrt{Sc(K-B)t}}erfc\left(\eta\sqrt{Sc} - \sqrt{(K-B)t}\right) + e^{2\eta\sqrt{Sc(K-B)t}}erfc\left(\eta\sqrt{Sc} + \sqrt{(K-B)t}\right)\right\}\right]$$
$$+2t\eta Gr\left\{\frac{e^{-\eta^2}}{\sqrt{\pi}} - \eta\ erfc\left(\eta\right)\right\} \tag{15}$$

3.3. Skin-Friction

The non-dimensional Skin-Friction, which is determined as shear stress on the surface, is obtained by

$$\tau = -\frac{dU}{dy}\bigg|_{y=0}$$

The solution for the Skin-Friction is calculated from the solution of Velocity profile U, represented by (9), as follows:

$$\tau = \frac{Gc}{Sc-1}\left[C_1\left\{\frac{\cos At}{\sqrt{\pi t}} + \sqrt{\frac{A}{2}}(r_1 - r_2) - \sqrt{ScK}\ erf(\sqrt{Kt}) - \sqrt{\frac{Sc}{\pi t}}e^{-Kt}\right\} + 2C_2\left\{\frac{\cos At}{\sqrt{\pi t}} - \sqrt{\frac{Sc}{\pi t}}e^{-Kt}\right\}\right.$$
$$+e^{-Bt}\{(C_2P_1 + C_3Q_1)(r_3\cos B_1t + r_4\sin B_1t) + (C_3P_1 - C_2Q_1)(r_4\cos B_1t - r_3\sin B_1t)\}$$
$$+e^{-Bt}\{(C_2P_2 - C_3Q_2)(r_5\cos B_1t - r_6\sin B_1t) - (C_3P_2 + C_2Q_2)(r_6\cos B_1t + r_5\sin B_1t)\}$$
$$\left.-2e^{-Bt}\sqrt{Sc}\{(C_2P_3 - C_3Q_3)(r_7\cos B_1t - r_8\sin B_1t) - (C_3P_3 + C_2Q_3)(r_8\cos B_1t + r_7\sin B_1t)\}\right]$$
$$+\frac{A}{S}\left\{\frac{\sin At}{\sqrt{\pi t}} - \sqrt{\frac{A}{2}}(r_1 + r_2)\right\} + \frac{Gc}{A}\left[(D_1 - 1)\left\{\frac{-\sin At}{\sqrt{\pi t}} + \sqrt{\frac{A}{2}}(r_1 + r_2)\right\} - \frac{2D_2\sin At}{\sqrt{\pi t}}\right.$$
$$+e^{-Bt}\{(D_2P_1 - D_3Q_1)(r_4\cos B_1t - r_3\sin B_1t) + (D_3P_1 + D_2Q_1)(r_3\cos B_1t + r_4\sin B_1t)\}$$
$$\left.+e^{-Bt}\{(D_2P_2 + D_3Q_2)(r_6\cos B_1t + r_5\sin B_1t) - (D_3P_2 - D_2Q_2)(r_5\cos B_1t - r_6\sin B_1t)\}\right]$$

The solution for the Skin-Friction for the special case is given from the expression (12), which is represented

by

$$
\begin{aligned}
\tau^* \quad = \quad & \frac{KGc}{K^2 + A^2} \left[\frac{\cos At}{\sqrt{\pi t}} + \sqrt{\frac{A}{2}} \, (r_1 - r_2) - \sqrt{K} \, erf(\sqrt{Kt}) - \frac{e^{-Kt}}{\sqrt{\pi t}} \right] \\
& + A \left(\frac{1}{S} + \frac{Gc}{K^2 + A^2} \right) \left[\frac{\sin At}{\sqrt{\pi t}} - \sqrt{\frac{A}{2}} \, (r_1 + r_2) \right]
\end{aligned}
$$

The solution for the Skin-Friction for the classical case is given from the expression (15), which is represented by

$$
\tau_c \quad = \quad \sqrt{\frac{t}{\pi}} Gr + \frac{Gc}{KSc} \left[e^{-Bt} \left\{ \sqrt{Sc(K - B)} \, erf(\sqrt{(K - B)t}) - \sqrt{-B} \, erf(\sqrt{-Bt}) \right\} - \sqrt{ScK} \, erf(\sqrt{Kt}) \right]
$$

3.4. Nusselt Number

The non-dimensional Nusselt number, which is determined as the rate of heat transfer, is obtained by

$$
Nu = - \frac{d\theta}{dy} \bigg|_{y=0}
$$

The solution for the Nusselt number is calculated from the solution of Temperature profile θ, represented by (10), as follows:

$$
\begin{aligned}
Nu \quad = \quad & \frac{\cos At}{\sqrt{\pi t}} + \sqrt{\frac{A}{2}} \, (r_1 - r_2) + \frac{SGc}{A(Sc - 1)} \left[C_1 \left\{ \frac{-\sin At}{\sqrt{\pi t}} + \sqrt{\frac{A}{2}} \, (r_1 + r_2) \right\} - \frac{2C_2 \sin At}{\sqrt{\pi t}} \right. \\
& + e^{-Bt} \left\{ (C_2 P_1 + C_3 Q_1)(r_4 \cos B_1 t - r_3 \sin B_1 t) - (C_3 P_1 - C_2 Q_1)(r_3 \cos B_1 t + r_4 \sin B_1 t) \right\} \\
& \left. + e^{-Bt} \left\{ (C_2 P_2 - C_3 Q_2)(r_6 \cos B_1 t + r_5 \sin B_1 t) + (C_3 P_2 + C_2 Q_2)(r_5 \cos B_1 t - r_6 \sin B_1 t) \right\} \right] \\
& + \frac{SGc}{(Sc - 1)^2} \left[E_1 \left\{ \frac{\cos At}{\sqrt{\pi t}} + \sqrt{\frac{A}{2}} \, (r_1 - r_2) - \sqrt{ScK} \, erf(\sqrt{Kt}) - \sqrt{\frac{Sc}{\pi t}} e^{-Kt} \right\} \right. \\
& + 2E_2 \left\{ \frac{\cos At}{\sqrt{\pi t}} - \sqrt{\frac{Sc}{\pi t}} e^{-Kt} \right\} + e^{-Bt} \left\{ (E_2 P_1 + E_3 Q_1)(r_3 \cos B_1 t + r_4 \sin B_1 t) \right\} \\
& + (E_3 P_1 - E_2 Q_1)(r_4 \cos B_1 t - r_3 \sin B_1 t) + e^{-Bt} \left\{ (E_2 P_2 - E_3 Q_2)(r_5 \cos B_1 t - r_6 \sin B_1 t) \right. \\
& \left. - (E_3 P_2 + E_2 Q_2)(r_6 \cos B_1 t + r_5 \sin B_1 t) \right\} - 2 e^{-Bt} \sqrt{Sc} \left\{ (E_2 P_3 - E_3 Q_3)(r_7 \cos B_1 t - r_8 \sin B_1 t) \right. \\
& \left. \left. - (E_3 P_3 + E_2 Q_3)(r_8 \cos B_1 t + r_7 \sin B_1 t) \right\} \right]
\end{aligned}
$$

The solution for the Nusselt number for the special case is given from the expression (13), which is represented by

$$
\begin{aligned}
Nu^* \quad = \quad & \frac{SKGc}{A(K^2 + A^2)} \left[\frac{-\sin At}{\sqrt{\pi t}} + \sqrt{\frac{A}{2}} \, (r_1 + r_2) \right] + \left(1 + \frac{SGc}{K^2 + A^2} \right) \left[\frac{\cos At}{\sqrt{\pi t}} + \sqrt{\frac{A}{2}} \, (r_1 - r_2) \right] \\
& - \frac{SGc}{K^2 + A^2} \left[\sqrt{K} \, erf(\sqrt{Kt}) + \frac{e^{-Kt}}{\sqrt{\pi t}} \right]
\end{aligned}
$$

The solution for the Nusselt number for the classical case is given from the expression (14), which is represented by

$$
Nu_c = \frac{1}{\sqrt{\pi t}}
$$

3.5. Sherwood Number

The non-dimensional Sherwood number, which is determined as the rate of mass transfer, is obtained by

$$
Sh = - \frac{dC}{dy} \bigg|_{y=0}
$$

The solution for the Sherwood number is calculated from the solution of Concentration profile C, represented by (8), as follows:

$$Sh \quad = \quad \sqrt{ScK} \; erf(\sqrt{Kt}) + \sqrt{\frac{Sc}{\pi t}} e^{-Kt}$$

The solution for the Sherwood number for the special case is given from the expression (11), which is represented by

$$Sh^* \quad = \quad \sqrt{K} \; erf(\sqrt{Kt}) + \frac{1}{\sqrt{\pi t}} e^{-Kt}$$

where,

$$B_2 = \sqrt{B^2 + (A - B_1)^2}, \quad B_3 = \sqrt{B^2 + (A + B_1)^2}, \quad B_4 = \sqrt{(K - B)^2 + B_1^2}, \quad P_1 = \sqrt{\frac{B_2 - B}{2}},$$

$$Q_1 = \sqrt{\frac{B_2 + B}{2}}, \quad P_2 = \sqrt{\frac{B_3 - B}{2}}, \quad Q_2 = \sqrt{\frac{B_3 + B}{2}}, \quad P_3 = \sqrt{\frac{B_4 - (K - B)}{2}}$$

$$Q_3 = \sqrt{\frac{B_4 + (K - B)}{2}}, \quad \sqrt{-B + i(A - B_1)} = P_1 + iQ_1, \quad \sqrt{-B + i(A + B_1)} = P_2 + iQ_2,$$

$$\sqrt{K - B + iB_1} = P_3 + iQ_3, \quad erf(\sqrt{iAt}) = r_1 + ir_2, \quad erf(P_1\sqrt{t} + iQ_1\sqrt{t}) = r_3 + ir_4,$$

$$erf(P_2\sqrt{t} + iQ_2\sqrt{t}) = r_5 + ir_6, \quad erf(P_3\sqrt{t} + iQ_3\sqrt{t}) = r_7 + ir_8$$

4. RESULT AND DISCUSSIONS

In order to better understand the physical significance of the problem, we calculated the velocity, temperature, concentration, Skin friction, Nusselt number, and Sherwood number using the solutions we found in the previous sections, for different values of the physical parameters Gr, Gc, Sc, K, S and time t. Additionally, we represented them graphically in Figures 2-15.
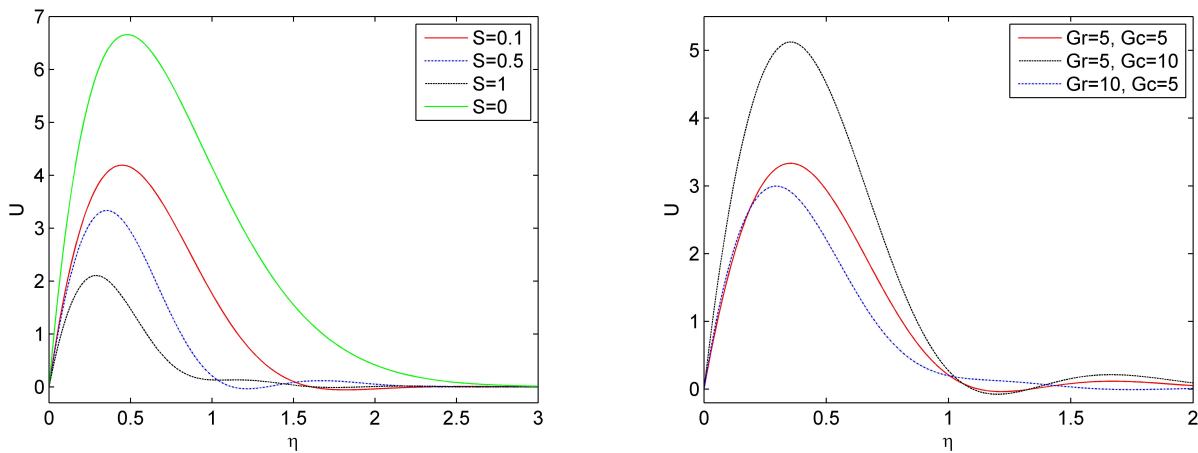
Figure 2. Effects of S on Velocity Profile for $Gr = 5, Gc = 5, t = 1.6, Sc = 0.6, K = 0.2$

Figure 3. Effects of Gr and Gc on Velocity Profile for $S = 0.5, Sc = 0.6, t = 1.6, K = 0.2$

Figure 2 illustrates how the velocity profiles are affected by thermal stratification (S). It can be seen that the velocity is lowered due to thermal stratification. According to Figure 3, increasing Gc results in an increase in velocity, whereas increasing Gr results in a drop in velocity. The fluid's velocity was shown at various values of Sc and K in figures 4 and 5. As Sc and K values grow, the fluid velocity falls.

The influence of thermal stratification on fluid velocity and temperature is plotted against time in Figures 6 and 7. Without stratification, the velocity and temperature grow continuously over time; however, when stratification occurs, they eventually reach a stable condition. This study is more realistic than earlier ones with no stratification because it applies thermal stratification, which lowers velocity and temperature in comparison to the classical scenario ($S = 0$).

Time-varying velocity and temperature patterns are shown in Figures 8 and 9. The velocity is observed to increase with time and diminish to zero as the distance from the plate increases. However, temperatures fall over time and eventually reach absolute zero as one moves away from the plate.

The impact of thermal stratification on the temperature is seen in Figure 10. As the parameters of thermal stratification are raised, it is seen that the temperature drops. Figures 11, 12, and 13 demonstrate the impacts
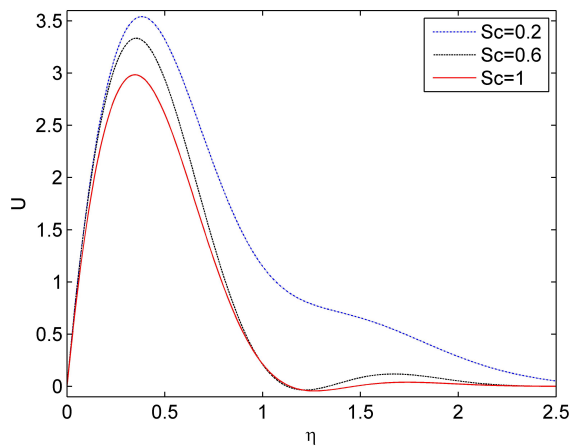
Figure 4. Effects of Sc on Velocity Profile for $Gr = 5, Gc = 5, S = 0.5, t = 1.6, K = 0.2$
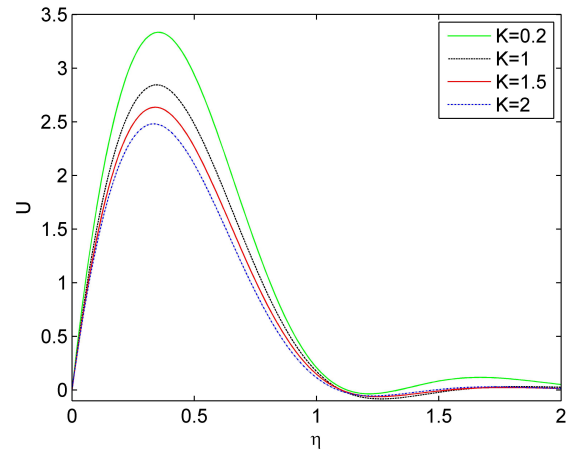
Figure 5. Effects of K on Velocity Profile for $Gr = 5, Gc = 5, S = 0.5, Sc = 0.6, t = 1.6$
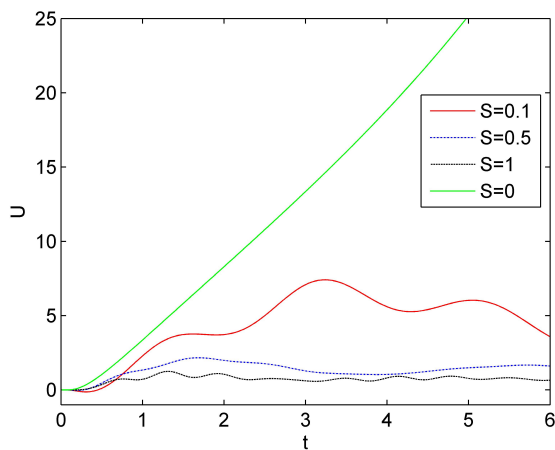
Figure 6. Effects of S on Velocity Profile against time for $Gr = 5, Gc = 5, Sc = 0.6, y = 1.6, K = 0.2$
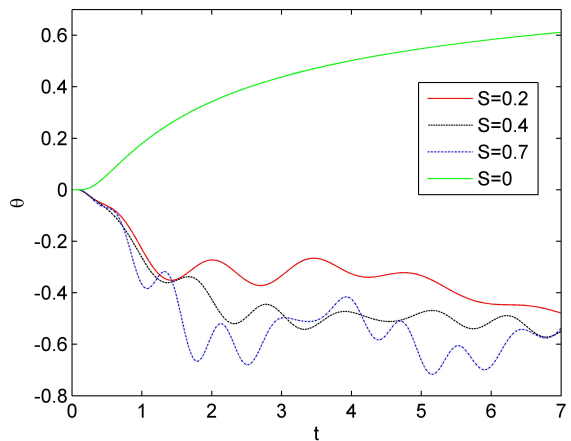
Figure 7. Effects of S on Temperature Profile against time for $Gr = 5, Gc = 5, Sc = 0.6, y = 1.9, K = 0.2$
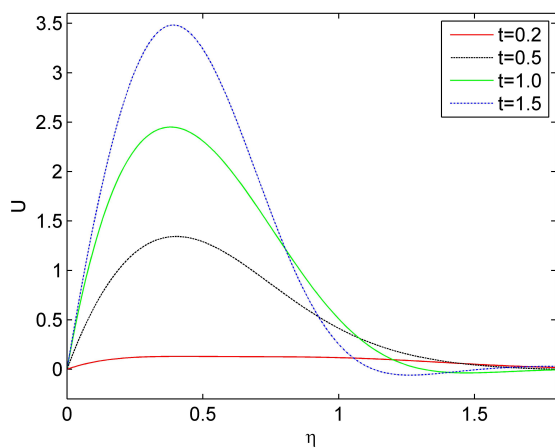
Figure 8. Velocity Profile at different time for $Gr = 5, Gc = 5, S = 0.5, Sc = 0.6, K = 0.2$
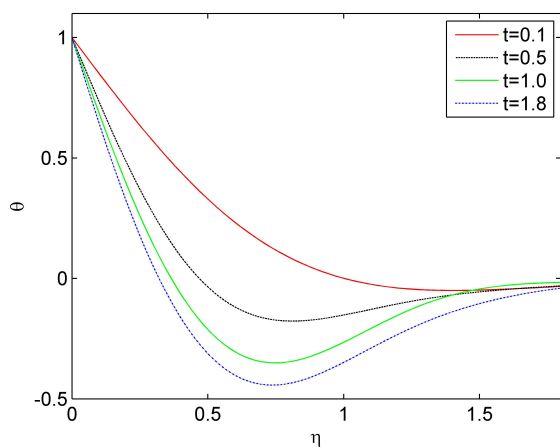
Figure 9. Temperature Profile at different time for $Gr = 5, Gc = 5, S = 0.5, Sc = 0.6, K = 0.2$
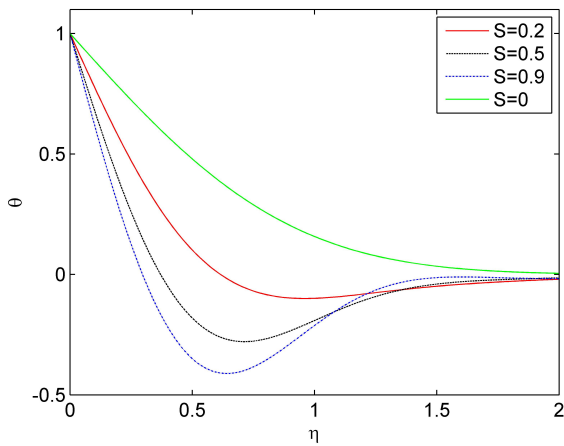
Figure 10. Effects of S on Temperature Profile for $Gr = 5, Gc = 5, , Sc = 0.6, t = 0.6, K = 0.2$
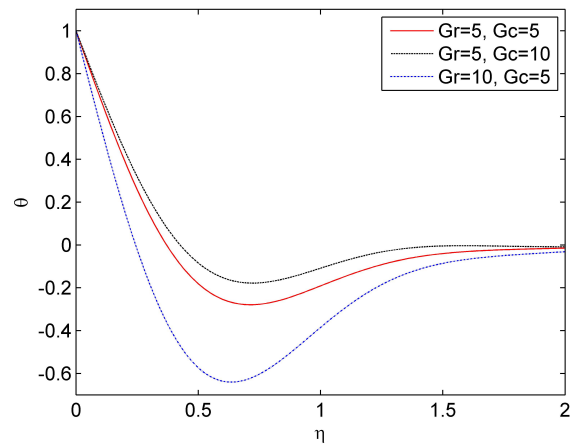
Figure 11. Effects of Gr and Gc on Temperature Profile for $S = 0.5, Sc = 0.6, t = 0.6, K = 0.2$
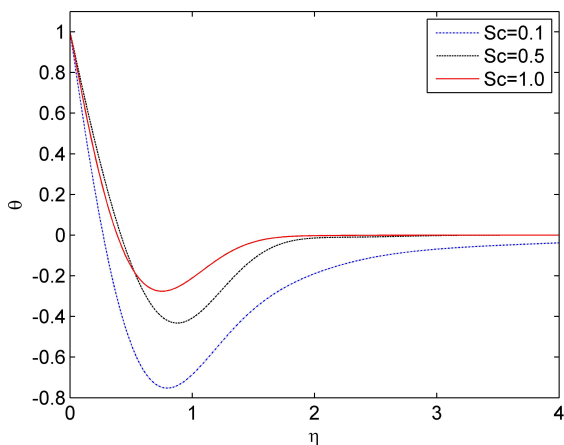
Figure 12. Effects of Sc on Concentration Profile for $Gr = 5, Gc = 5, S = 0.5, t = 1.4, K = 0.2$
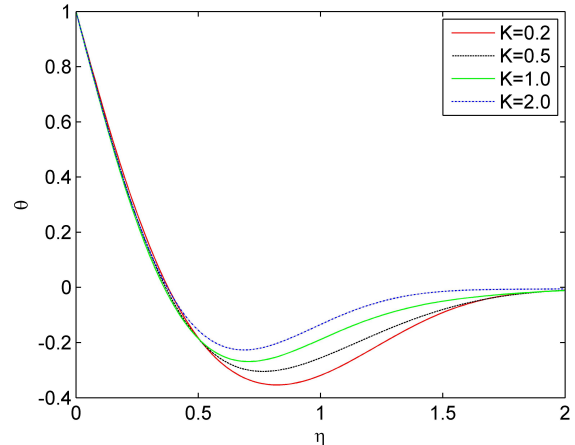
Figure 13. Effects of K on Temperature Profile for $Gr = 5, Gc = 5, S = 0.5, Sc = 0.6, t = 1.4$
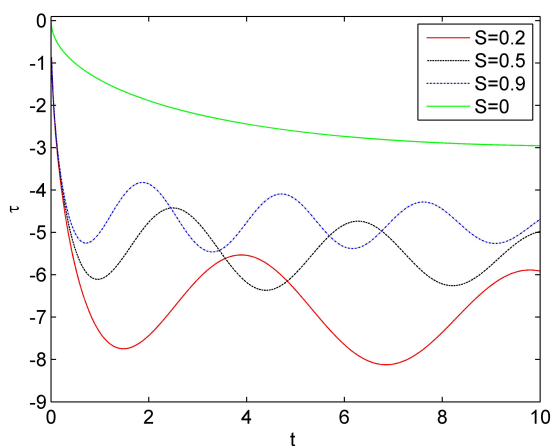
Figure 14. Effects of S on Skin friction for $Gr = 5, Gc = 5, Sc = 0.1, K = 0.2$
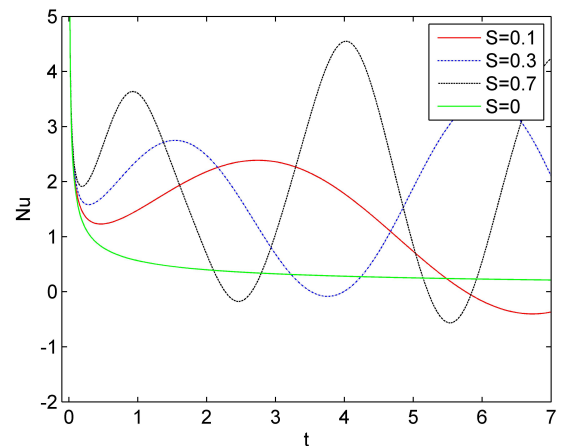
Figure 15. Effects of S on Nusselt Number for $Gr = 5, Gc = 5, Sc = 0.1, K = 0.2$

of Gr, Sc, K and K ,on temperature profile respectively. The temperature drops for higher values of Gc and lower values of Gr, Sc, K.

The effect of Thermal Stratification can be seen in Figures 14 and 15, which show skin friction and the Nusselt number, respectively. In the presence of stratification, they significantly increase in comparison to when there is no stratification.

5. CONCLUSION

We investigated at how chemical reactions affect the flow past an infinite vertical plate when there are different levels of temperature. The results found in the present study are compared to those found in the classical scenario, when stratification does not occur. The velocity of the fluid declines as S, K, Sc, and Gr increase, but it goes up as Gc increases. The application of thermal stratification, which reduces velocity and temperature relative to the classical case ($S = 0$), makes this study more feasible than previous ones. Temperature drops when K, Sc, and Gc drop; conversely, it drops when S, Gr, and time rise. The temperature is maximum at the plate and drops to zero at greater distances from the plate, as demonstrated in research paper [2]. Thermal stratification makes the Nusselt number oscillate more frequently.

ORCID

Rupam Shankar Nath, https://orcid.org/0009-0002-2352-0538; **Rudra Kanta Deka**, https://orcid.org/0009-0007-1573-4890

REFERENCES

[1] E. Magyari, I. Pop, and B. Keller, "Unsteady Free Convection along an Infinite Vertical Flat Plate Embedded in a Stably Stratified Fluid-Saturated Porous Medium," Transp. Porous. Med. **62**, 233–249 (2006). https://doi.org/10.1007/s11242-005-1292-6

[2] A. Bhattacharya, and R. K. Deka. "Theoretical Study of Chemical Reaction Effects on Vertical Oscillating Plate Immersed in a Stably Stratified Fluid," Research Journal of Applied Sciences, Engineering and Technology, **3**(9), 887-898 (2011). https://maxwellsci.com/print/rjaset/v3-887-898.pdf

[3] A. Shapiro, and E. Fedorovich, "Unsteady convectively driven flow along a vertical plate immersed in a stably stratified fluid," Journal of Fluid Mechanics, **498**, 333-352 (2004). https://doi.org/10.1017/S0022112003006803

[4] J.S. Park, and J.M. Hyun, "Technical Note Transient behavior of vertical buoyancy layer in a stratified fluid," International Journal of Heat and Mass Transfer, **41**(24), 4393-4397 (1998), https://doi.org/10.1016/S0017-9310(98)00175-6

[5] J.S. Park, "Transient buoyant flows of a stratified fluid in a vertical channel," KSME International Journal, **15**, 656–664 (2001). https://doi.org/10.1007/BF03184382

[6] U.N. Das, R. Deka, and V.M. Soundalgekar, "Effects of Mass Transfer on a Flow past an Impulsively Started Infinite Vertical Plate with Constant Heat Flux and Chemical Reaction," Forschung im Ingenieurwesen, **60**, 284-287 (1995). https://maxwellsci.com/print/rjaset/v3-887-898.pdf

[7] F.M.N. El-Fayez, "Effects of Chemical Reaction on the Unsteady Free Convection Flow past an Infinite Vertical Permeable Moving Plate with Variable Temperature," Journal of Surface Engineered Materials and Advanced Technology, **2**(2), 100-109 (2012). https://doi.org/10.4236/jsemat.2012.22016.

[8] B.P. Reddy, and J. Peter. "Effects of Chemical Reaction on MHD Flow Past an Impulsively Started Infinite Vertical Plate with Variable Temperature and Mass Diffusion in the Presence of Hall Current," Journal of the Serbian Society for Computational Mechanics, **13**(1), 92-108 (2019). https://doi.org/10.24874/jsscm.2019.13.01.06

[9] M.A. Mansour, N.F. El-Anssary, and A.M. Aly, "Effects of chemical reaction and thermal stratification on MHD free convective heat and mass transfer over a vertical stretching surface embedded in a porous media considering Soret and Dufour numbers," Chemical Engineering Journal, **145**(2), 340-345 (2008). https://doi.org/10.1016/j.cej.2008.08.016

[10] R. Kandasamy, K. Periasamy, and K.K.S. Prabhu, "Chemical reaction, heat and mass transfer on MHD flow over a vertical stretching surface with heat source and thermal stratification effects," International Journal of Heat and Mass Transfer, **48**(21-22), 4557-4561 (2005). https://doi.org/10.1016/j.ijheatmasstransfer.2005.05.006

[11] A.M. Megahed, and W. Abbas, "Non-Newtonian Cross fluid flow through a porous medium with regard to the effect of chemical reaction and thermal stratification phenomenon," Case Studies in Thermal Engineering, **29**, 101715 (2022). https://doi.org/10.1016/j.csite.2021.101715

[12] R.B. Hetnarski, "An algorithm for generating some inverse Laplace transforms of exponential form," Journal of Applied Mathematics and Physics (ZAMP), **26**, 249–253 (1975). https://doi.org/10.1007/BF01591514.

[13] Abramowitz, Milton, I.A. Stegun, and R.H. Romer. "Handbook of mathematical functions with formulas, graphs, and mathematical tables." American Journal of Physics, **56**(10), 958 (1988). https://doi.org/10.1119/1.15378

ВПЛИВ ТЕРМІЧНОЇ СТРАТИФІКАЦІЇ НА ПОТІК ПОВЗ НЕСКІНЧЕННУ ВЕРТИКАЛЬНУ ПЛАСТИНУ ЗА НАЯВНОСТІ ХІМІЧНОЇ РЕАКЦІЇ

Рупам Шанкар Нат, Рудра Канта Дека

Факультет математики, Університет Гаухаті, Гувахаті-781014, Ассам, Індія

У цьому дослідженні досліджується, як теплове розшарування впливає на рух рідини за наявності хімічної реакції першого порядку повз нескінченну вертикальну пластину. Для розв'язування безрозмірних керуючих рівнянь у замкнутій формі при Pr = 1 застосовано систему перетворень Лапласа. Результати, отримані в для умов термічної стратифікації, порівнюються з випадком відсутності стратифікації. Вплив багатьох параметрів, включаючи S, K, Gr, Gc, Sc і часу, на швидкість, температуру, концентрацію, поверхневе тертя, число Нуссельта та число Шервуда досліджується та відображається графічно. Показано, що стаціонарний стан досягається за менший час в результаті застосування стратифікації потоку.

Ключові слова: *термічна стратифікація; хімічна реакція; тепло- та масообмін; вертикальна пластина; число Шмідта*

INVESTIGATION OF THERMAL RADIATIVE TANGENT HYPERBOLIC NANOFLUID FLOW DUE TO STRETCHED SHEET[†]

Muhammad Jawad*,a, Mubeen Alamb, Kottakkaran Sooppy Nisarc

aDepartment of Mathematics, Superior University Lahore, Faisalabad Sub campus, Faisalabad 38000, Pakistan
bDepartment of Mathematics, The University of Faisalabad, Faisalabad 38000, Pakistan
cDepartment of Mathematics, College of Science and Humanities in Alkharj, Prince Sattam Bin Abdulaziz University,
Alkharj 11942, Saudi Arabia
Corresponding Author e-mail: jawadsial37@gmail.com
Received April 29, 2023; revised June 6, 2023; accepted June 8, 2023

The current study illuminates the enactment of tangent hyperbolic nanofluid past a bidirectional stretchable surface. The phenomena of heat and mass transfer with joule heating, chemical reaction and thermal radiation have been debated. For motivation of problem convective boundary conditions and heat source are part of this study. The modeled partial differential equations are mended into ordinary differential equations with the help of appropriate self-similarity transformations. Furthermore, the resulting system of ODEs is numerically handled by using well-established shooting scheme and acquired numerical outcomes are compared with ND Solve command of Mathematica. The Effects of prominent parameters on velocity, temperature and volumetric concentration distribution are inspected through graphs. The influence of emerging parameters involved in this study on flow and heat removal features are deliberated in detail. As we are increasing the values of power-law index n, Prandtl number Pr and Magnetic parameter M, outcomes increment in skin friction coefficient while decline in the Nusselt number is seen.
Keywords: *Shooting Method; Tangent hyperbolic nanofluid; MHD; Joule heating; chemical reaction*
PACS: 44.05.+e, 44.10.+i, 44.30.+v, 47.10.ad

INTRODUCTION

Due to wider applications of non-Newtonian fluid, many researchers paid their attention, in the last few years. The applications of non-Newtonian fluids contain food products, personal protective equipment braking and damping devices, printing technology and drag reducing agents. Shampoo, melted butter, blood, paint, cornstarch, starch suspensions, toothpaste, custard and Ketchup are examples of such type of fluids [1].

One of the most significant kinds of non-Newtonian fluid is Tangent hyperbolic. Kumar et al. [2] reported that the Tangent hyperbolic fluid has capability to illustrate the behavior of shear thinning. Rehman et al. [3] examined the interplay between the stratification of tangent hyperbolic fluid and the combined effects of thermal radiation, and concluded that with the greater value of solar radiation, there are escalations in the fluid temperature. Shafiq et al. [4] discovered the magnetic flow of bio convective tangent hyperbolic fluid containing swimming microorganism with thermal effects and they reported that the temperature field surge for higher value of thermophoresis parameter. Salahuddin et al. [5] examined the tangent hyperbolic due to stretched cylinder across the stagnation point. Naseer et al. [6] exposed the concept of tangent fluid for buoyancy and thermal effects and reported that the temperature function decreased with increasing value of Prandtl number. Prabhakar et al. [7] scrutinized the flow tangent hyperbolic fluid with influence of inclined Lorentz forces due to stretched surface.

Nanofluid is an important category of non-Newtonian fluids having nanometer-sized particles. propylene glycol, water, ethylene glycol etc., are base fluids, to boost the thermal conductivity of base fluid's nanoparticles are used. Nanofluids are the homogeneous typical combination of nanoparticles are usually made by metals (Cu, Zn, Al), nonmetals (nanotubes, boron, carbon) and carbides (SiC, Fe_3C, CaC_2) with base fluids (glycol, water and ethylene glycol) [8]. The inclusion of a modest number of nanoparticles improved the thermal conductivity of heat transfer fluids, according to research by Choi et al. [9]. The concept of increasing the heat conductivity by using nanoparticles was first proposed by Choi and Eastman [10]. Izadi et al. [11] inspected the behavior of nanofluid with laminar forced flow. As noted by Wong et al. [12], they have numerous engineering and biomedical uses, including as in microelectronics, nuclear reactors, process industries, and cancer therapy. Nayak et al. [13] explored the influence of solar radiation on electrical conducting nanofluid dur to vertical sheet.

The study of squeezing flows in several commercial and practical applications in unusual domains including pharmaceutical manufacturing, energy production, polymer exclusion, energy in space technology, nuclear reactors, chemical reactions, and solar energy in space technology aim to slow down and employed other technologies. In industrial applications, squeezing flows are used in lubrication, bearings and motors. Lin et al. [14] exhibited the qualities of electrical conducting squeezed fluid flow among annular vertical plates. Thermal radiation and heat transfer has numerous uses in production procedures, semiconductors, chemical processes, engineering, and other several areas of technology. The micro convection thermal effect in two phase mixtures is, according to Sohn and Chen [15], more potent than it is in a single-phase

fluid. Makinde [16] deliberated the radiative flow of heat transfer free convection in the presence of porous sheet. Hussain et al. [17] premeditated the heat transfer phenomena in squeezing flow with thermal radiation and bio convection between two equivalent plates. Hayat et al. [18] debated the influence of solar radiation in Jeffery squeezing fluid flow. Additional study on the influence of heat transfer process and thermal radiation in fluid flow can be considered in [19-21].

The study of electrically conducting fluids with magnetic field is known as magneto hydrodynamics MHD. Magneto-hydrodynamic flow has many presentations in numerous fields of science engineering like MHD accelerator, power generator, heat exchangers and cooling of reactors as deliberated by Hari et al. [22]. Rashidi et al. [23] determined the electrical conducting flow of nanofluid with nonlinear radiation due to vertical stretched surface. Zhang et al. [24] inspected the radiative flow of MHD nanofluid with heat flux, variable surface and chemical reaction.

The illustration of this investigation is to study the numerical outcomes of electrical conducting fluid flow of hyperbolic nanofluid fluid joule heating and chemical diffusion due to stretching sheet using convective boundary conditions. The couple of nonlinear PDEs of governing model are transformed into a set ODEs by use of appropriate revolution called similarity function. Operating the shooting scheme numerous mathematical outcomes are validated. Furthermore, impression of effective parameters is talk about through graphs in detail.

MATHEMATICAL ANALYSIS

Consider the laminar, 2d electrical conducting tangent hyperbolic nanofluid due to vertical stretched sheet. Moreover, the influence of Joule heating and thermal radiation are part of this investigation. Convective boundary conditions are applied for motivation of problem. Where u and v are component of flow of fluid. MHD effect having strength B_0 is considered perpendicular to the sheet. The governing equation including influence of thermal radiation, browning motion, chemical reaction and thermophoresis are described as [25-33]:

$$\frac{\partial u}{\partial x} + \frac{\partial v}{\partial y} = 0 \tag{1}$$

$$u\frac{\partial u}{\partial x} + v\frac{\partial v}{\partial y} = v(1-n)\frac{\partial^2 u}{\partial y^2} + \sqrt{2}vn\Gamma\left(\frac{\partial u}{\partial y}\right)\frac{\partial^2 u}{\partial y^2} - \frac{\sigma B_0 u}{\rho_f}, \tag{2}$$

$$u\frac{\partial T}{\partial x} + v\frac{\partial T}{\partial y} = \alpha\left(\frac{\partial^2 T}{\partial y^2}\right) + \Lambda\left[D_B\left(\frac{\partial C}{\partial y}\right)\left(\frac{\partial T}{\partial y}\right) + \frac{D_T}{T_\infty}\left(\frac{\partial T}{\partial y}\right)^2\right] + \frac{\sigma B_0^2 u^2}{\rho_f} - \frac{1}{(\rho c)_f}\frac{\partial q_r}{\partial y} + \frac{Q_0}{(\rho c)_f}(T - T_\infty), \tag{3}$$

$$u\frac{\partial C}{\partial x} + v\frac{\partial C}{\partial y} = D_B\frac{\partial^2 C}{\partial y^2} + \frac{D_T}{T_\infty}\left(\frac{\partial^2 T}{\partial y^2}\right) - K_r(C - C_\infty). \tag{4}$$

The associated boundary conditions are given

$$u = u_w, v = 0, -K\frac{\partial T}{\partial y} = h_f\left(T_f - T\right), D_B\frac{\partial C}{\partial y} + \frac{D_T}{T_\infty}\frac{\partial T}{\partial y} = 0, \text{at } y = 0, \Big|$$
$$U \to U_\infty, T \to T_\infty, C \to C_\infty, \text{as } y \to \infty. \tag{5}$$

SIMILARITY TRANSFORMATION

The similarity variables are illustrated as:

$$\psi = \sqrt{avx}f(\eta), \quad \eta = \sqrt{\frac{a}{v}}y, \quad \phi(\eta) = \frac{C - C_\infty}{C_\infty}, \quad \theta(\eta) = \frac{T - T_\infty}{T_f - T_\infty}, u = \frac{\partial \psi}{\partial y}, v = -\frac{\partial \psi}{\partial x}, \tag{6}$$

As a result, Eq. (1) is satisfied identically and equations (2-4) are transformed as:

$$(1 - n)f''' + ff'' - f'^2 - Mf' + nWef'''f'' = 0, \tag{7}$$

$$\left(1 + \epsilon\theta + \frac{4}{3}N_r\right)\theta'' + P_r f\theta' + P_r MEcf'^2 + P_r Nb\ \phi'\theta' + P_r Nt\theta'^2 + P_r\Delta\theta = 0, \tag{8}$$

$$\phi'' + \frac{Nt}{Nb}\theta'' + Sc\ f\phi' + Sck_1\phi = 0, \tag{9}$$

The boundary conditions are converted as:

$$f(0) = 0, \quad f'(0) = 1, \theta'(0) = Bi(\theta(0) - 1), Nb\ \phi'(0) + Nt\theta'(0) = 0, at\ \eta = 0, \Big|$$
$$f'(\infty) \to 0, \quad \theta(\infty) \to 0, \quad \phi(\infty) \to 0, \quad as\ \eta \to \infty. \tag{10}$$

Where

$$\left| Nt = \frac{(\rho c)_p D_T (T_f - T_\infty)}{(\rho c)_f v T_\infty}, \ We = \frac{\sqrt{2} a^{\frac{2}{3}} x \Gamma}{\sqrt{v}}, \ Nb = \frac{(\rho c)_p D_B (C_\infty)}{(\rho c)_f v}, \ S_c = \frac{v}{D_B}, \ \Delta = \frac{Q_0}{a(\rho c)_f}, \right.$$

$$\left. Bi = \frac{h_f}{k} \sqrt{\frac{v}{a}}, \ M = \frac{\sigma B^2_0}{\rho f a}, \ Nt = \frac{(\rho c)_p D_T (T_f - T_\infty)}{(\rho c)_f v T_\infty}, \ Pr = \frac{v}{\alpha}, Nr = \frac{4\sigma^* T^3_\infty}{k^* k}. \right| \tag{11}$$

PHYSICAL QUANTITIES OF INTEREST

The physical quantities are defined as:

$$C_f = \frac{\tau_w}{\rho u_w{}^2}, \ Nu_x = \frac{x q_w}{k(T \to T_\infty)}, \tag{12}$$

where:

$$\left. \begin{aligned} \tau_w &= \mu \left((1-n) \frac{\partial u}{\partial y} + \frac{n\Gamma}{\sqrt{2}} \left(\frac{\partial u}{\partial x} \right)^2 \right), \\ q_w &= -k \left(1 + \frac{16\sigma^* T^3_\infty}{3k^* k} \right) \frac{\partial T}{\partial y}. \end{aligned} \right| \tag{13}$$

The physical quantities in non-dimensional form:

$$\left| \begin{aligned} C_f \sqrt{R} e_x &= \left((n-1) + \frac{n}{2} W_e f''(0) \right) f''(0), \\ Nu_x Re_x^{-1/2} &= - \left(1 + \frac{4}{3} N_r \right) \theta'(0). \end{aligned} \right. \tag{14}$$

Where $Re_x = \frac{ax^2}{v}$ is local Reynolds number.

NUMERICAL SOLUTION

Above equations (7-9) are coupled and highly nonlinear therefore exact solution is not applicable.

$$\left. \begin{aligned} f''' &= \frac{1}{(1-n) + nW_e f''} [f'^2 + Mf' - ff''], \\ \theta'' &= -\frac{Pr}{\left(1 + \epsilon\theta + \frac{4}{3} N_r \right)} [f\theta' + Nb\phi'\theta' + Nt\theta'^2 + MEcf'^2 + \Delta\theta], \\ \phi'' &= \frac{Nt}{Nb} \theta'' - fSc\phi' - Sck_1\phi. \end{aligned} \right| \tag{15}$$

Boundary condition in dimensionless shape is:

$$\left| \begin{aligned} y_1(\eta) &= 0, \ y_2(\eta) = 1, \ y_5(\eta) = Bi(y_4(\eta) - 1), \\ Nby_7(\eta) &+ Nty_5(\eta) = 0, \quad as \ \eta = 0, \\ y_2(\infty) &\to 0, \ y_4(\infty) \to 0, \ y_6(\infty) \to 0, \quad as \ \eta \to \infty \end{aligned} \right. \tag{16}$$

Let us put $f = y_1, f' = y_2, f'' = y_3, f''' = y_3', \theta = y_4, \theta' = y_5, \theta'' = y_5', \phi = y_6, \phi' = y_7, \phi'' = y_7'$. The equations (15) and (16) are written as:

$$\left[\begin{aligned} y_1' &= y_2 \\ y_2' &= y_3 \\ \\ y_3' &= \frac{y_2^2 + My_2 - y_1 y_3}{(1-n) + nWey_3} \\ y_4' &= y_5 \\ y_5' &= \frac{-Pr(y_1 y_5 + Nby_7 y_5 + \Delta y_4 + Nty_5^2 + 2MEcy_2^2)}{\left(1 + \epsilon\theta + \frac{4}{3} Nr \right)} \\ y_6' &= y_7 \\ y_7' &= -Scy_1 y_7 - Scky_7 + \frac{Nt}{Nb} y_5' \end{aligned} \right. \tag{17}$$

$$\left. \begin{aligned} y_1(0) &= 0, \ y_2(0) = 1, \ y_3(0) = l \quad y_4(0) = m \\ y_5(0) &= Bi(t-1), \quad y_6(0) = n \quad y_7(0) = -\frac{Nt}{Nb} Bi(t-1). \end{aligned} \right| \tag{18}$$

<div align="center">

RESULT AND DISCUSSION
</div>

The revelation of the section is to study the numerical outcomes exemplified in the form of graphs. The influence of emerging parameters like power-law index n, Magnetic parameter M, Prandtl number Pr, thermophoresis parameter Nt, thermal radiation parameter Nr, Weissenberg number We and Brownian motion parameter Nb on velocity, temperature and concentration field are discussed. The influence of the power-law index for non-dimensional velocity function is depicted in Figure 1. it is noted that velocity field is decreased as an increment in power-law index n. Because increased magnitude of n decreases fluid flow. The impression of Hartmann number M on velocity profile f' and temperature profile θ are presented in Figures (2-3).
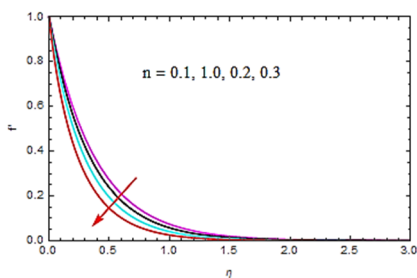
Figure 1. Distribution of f' for power-law index n
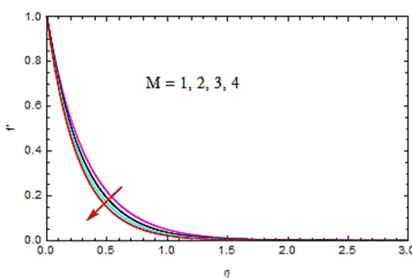
Figure 2. Distribution of f' for Hartmann number M
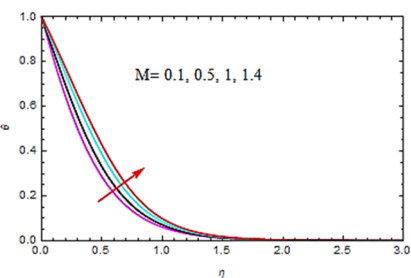
Figure 3. Distribution of θ for Hartmann number M

Figure 2 is plotted to imagine that the flow profile is diminished for improving values of Hartmann number M. In Figure 3, temperature field illustrates growing behavior for the increase of Hartmann number M. Physically, Magnetic field increases Lorentz forces, reducing fluid motion. The impact of Prandtl number Pr on temperature distribution θ and volumetric concentration distribution are exhibited in Figures (4-5).
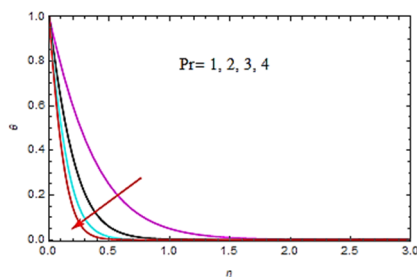
Figure 4. Distribution of θ for Prandtl number Pr
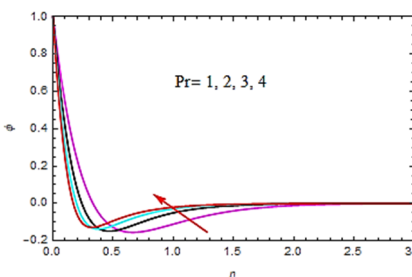
Figure 5. Distribution of ϕ for Prandtl number Pr
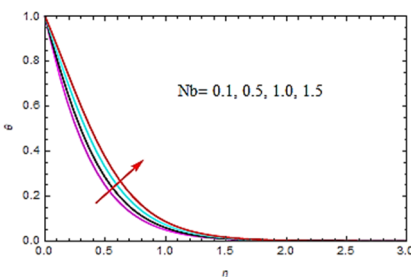
Figure 6. Distribution of θ for Brownian motion parameter Nb

Figure 4 is drawn to explore the influence of the Prandtl number Pr on energy field θ. It is cleared that for increasing value of Prandtl number Pr the energy distribution θ declines. Because of heat transfer rate decreases for increased Pr values. Figure 5, concentration field illustrates growing behavior for the increase of Prandtl number Pr. The impact of Brownian motion parameter Nb on temperature field θ and concentration field are exhibited in Figures (6-7).
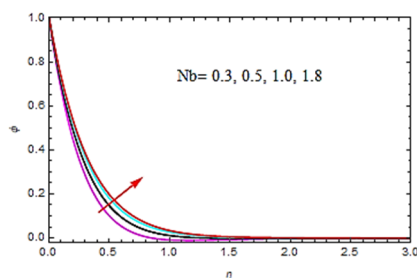
Figure 7. Distribution of ϕ for Brownian motion parameter Nb
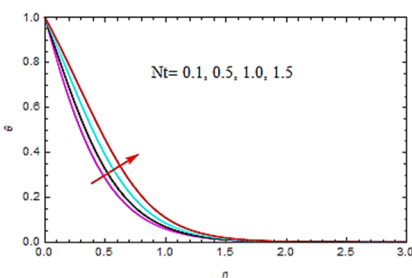
Figure 8. Distribution of θ for thermophoresis parameter Nt
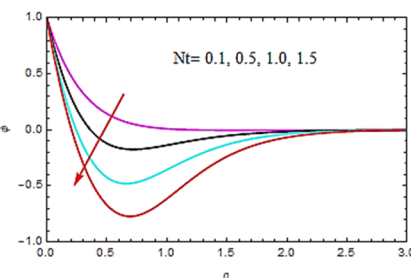
Figure 9. Distribution of ϕ for thermophoresis parameter Nt

Figure 6 is depicted to explore the manipulate of the Brownian motion parameter Nb on energy field θ. It is noted that for increasing value of Brownian motion parameter Nb the energy distribution θ increases. Because of heat transfer rate decreases for increased Nb values. Figure 7, concentration field illustrates growing behavior for the increase of Brownian motion parameter Nb. Figures (8-9) are communicated to imagine the influence of Nt on the energy and concentration distribution. In figures 8, it is observed that temperature function θ establish a growth for rising values of thermophoresis parameter. Figure 9 is drawn to explore the influence of the thermophoresis parameter Nt on concentration field ϕ. It is cleared that for increasing value of thermophoresis parameter Nt the concentration distribution

ϕ declines. Basically, heated particles move away from high temperatures, increasing fluid temperature. Figure 10 characterizes that by improving the values of (seen with the variable thermal conductivity) small parameter ϵ energy distribution θ also augmented. Figure 11 represents that by increasing the value of thermal radiation parameter Nr fluid temperature also increased. Physically, increase in thermal Radiation parameter increases energy flow to fluids). Figure 12 is pinched to investigate the stimulus of the Schmidt Sc on concentration field ϕ. It is evaporated that for increasing value of Schmidt Sc the concentration field ϕ declines.
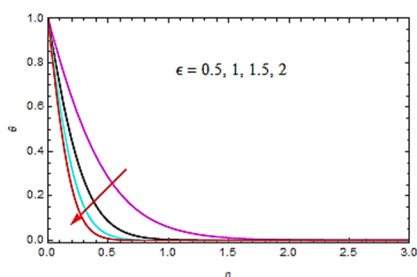
Figure 10. Distribution of θ for small parameter ϵ	**Figure 11.** Distribution of θ for radiation parameter Nr	**Figure 12.** Distribution of ϕ for Schmidt number Sc
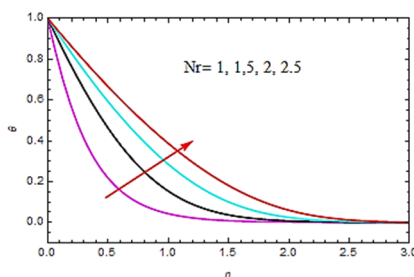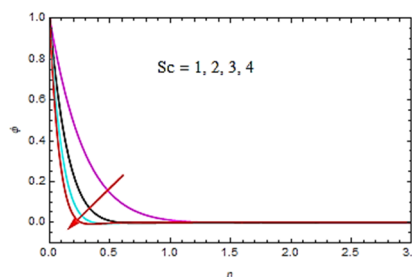
CONCLUSION

In this investigation, tangent hyperbolic flow of nanofluid due to stretched sheet with joule heating, and heat source is examined. Chemical diffusion and thermal radiation are part of this study. First of all, velocity, temperature and volumetric concentration equations are transformed into the set of ODEs by expending similarity variables. The resulting system of ODEs is numerically handled by using well-established shooting scheme and acquired numerical outcomes. These outcomes are useful in the field of engineering and technology due to heat transfer.

The key findings are listed below.

- By increasing the values of power-law index n and Hartmann number M velocity profile declines.
- By increasing values of thermal radiation Nr, thermophoresis parameter Nt and Brownian motion parameter Nb temperature field θ also increases.
- Strong abatement in temperature distribution is noted for raising values of Pr.
- Concentration and temperature and increase by increasing thermophoresis parameter Nt
- Concentration decreases by increasing Schmidt number Sc.

ORCID
Muhammad Jawad, https://orcid.org/0000-0002-9304-615X; **Mubeen Alam,** https://orcid.org/0009-0008-9840-3751
Kottakkaran Sooppy Nisar, https://orcid.org/0000-0001-5769-4320

REFERENCES
[1] T. Hayat, M. Waqas, A. Alsaedi, G. Bashir, and F. Alzahrani., "Magnetohydrodynamic (MHD) stretched flow of tangent hyperbolic nanoliquid with variable thickness," Journal of Molecular Liquids, **229**, 178-184 (2017). https://doi.org/10.1016/j.molliq.2016.12.058
[2] K.G. Kumar, B.J. Gireesha, M.R. Krishanamurthy, and N.G. Rudraswamy, "An unsteady squeezed flow of a tangent hyperbolic fluid over a sensor surface in the presence of variable thermal conductivity," Results in Physics, **7**, 3031-3036 (2017). https://doi.org/10.1016/j.rinp.2017.08.021
[3] K.U. Rehman, A.A. Malik, M.Y. Malik, and N.U. Saba, "Mutual effects of thermal radiations and thermal stratification on tangent hyperbolic fluid flow yields by both cylindrical and flat surfaces," Case studies in thermal engineering, **10**, 244-254 (2017). https://doi.org/10.1016/j.csite.2017.07.003
[4] A. Shafiq, Z. Hammouch, and T.N. Sindhu, "Bioconvective MHD flow of tangent hyperbolic nanofluid with Newtonian heating," International Journal of Mechanical Sciences, **133**, 759-766 (2017). https://doi.org/10.1016/j.ijmecsci.2017.07.048
[5] M. Naseer, M. Yousaf, M.S. Nadeem, and A. Rehman, "The boundary layer flow of hyperbolic tangent fluid over a vertical exponentially stretching cylinder," Alexandria Engineering Journal, **53**, 747-750 (2014). https://doi.org/10.1016/j.aej.2014.05.001
[6] B. Prabhakr, S. Bandar, and R.U. Haq, "Impact of inclined Lorentz forces on tangent hyperbolic nanofluid flow with zero normal flux of nanoparticles at the stretching sheet," Neural Computing and Applications, **29**, 805-814 (2018). https://doi.org/10.1007/s00521-016-2601-4
[7] K. Khanafer, K. Vafai, and M. Lightstone, "Buoyancy-driven heat transfer enhancement in a two-dimensional enclosure utilizing nanofluids," International Journal of Heat and Mass Transfer, **46**, 3639-3653 (2003). https://doi.org/10.1016/S0017-9310(03)00156-X
[8] S.U.S. Choi, Z.G. Zhang, W.Y. a. F.E. Lockwood, and E.A. Grulke, "Anomalous thermal conductivity enhancement in nanotube suspensions," Applied physics letters, **79**, 2252-2254 (2001). https://doi.org/10.1063/1.1408272

[9]   S.U.S. Choi, and J.A. Eastman, "Enhancing thermal conductivity of fluids with nanoparticles," ASME-Publications-Fed, **231**, 99-106 (1995).

[10]   M. Izadi, A. Behzadmehr, and D.J. Vahida, "Numerical study of developing laminar forced convection of a nanofluid in an annulus," International Journal of Thermal Sciences, **48**, 2119-2129 (2009). https://doi.org/10.1016/j.ijthermalsci.2009.04.003

[11]   K.V. Wong, and O.D. Leon, "Applications of nanofluids: current and future," Advances in mechanical engineering, **2**, 519-659 (2010). https://doi.org/10.1155/2010/519659

[12]   M.K. Nayak, N.S. Akbar, V.S. Pandey, Z.H. Khan, and D. Tripathi, "3D free convective MHD flow of nanofluid over permeable linear stretching sheet with thermal radiation," Powder Technology, **315**, 205-215 (2017). http://dx.doi.org/10.1016%2Fj.powtec.2017.04.017

[13]   M. Mahmood, S. Asghar, and M. Hossain, "Squeezed flow and heat transfer over a porous surface for viscous fluid," Heat and Mass Transfer, **44**(2), 165-173 (2007). https://doi.org/10.1007/s00231-006-0218-3

[14]   J.R. Lin, R.F. Lu, and W.H. Liao, "Analysis of magneto-hydrodynamic squeeze film characteristics between curved annular plates," Industrial Lubrication and Tribology, **56**(5), 300-305 (2004). https://doi.org/10.1108/00368790410550714

[15]   M.M. Sohn, and C.W. Chen, "Microconvective thermal conductivity in disperse two-phase mixtures as observed in a low velocity couette flow experiment," Journal of Heat Transfer, **103**(1), 47-51 (1981). https://doi.org/10.1115/1.3244428

[16]   O.D. Makinde, "Free convection flow with thermal radiation and mass transfer past a moving vertical porous plate," International Communications in Heat and Mass Transfer, **32**(10), 1411-1419 (2005). https://doi.org/10.1016/j.icheatmasstransfer.2005.07.005

[17]   S.A. Hussain, S.Muhammad, G. Ali, S.I.A. Shah, M. Ishaq, Z. Shah, H. Khan, M. Tahir, and M. Naeem, "A bioconvection model for squeezing flow between parallel plates containing gyrotactic microorganisms with impact of thermal radiation and heat generation/absorption," Journal of Advances in Mathematics and Computer Science, **27**(4), 1-22 (2018). https://doi.org/10.9734/JAMCS/2018/41767

[18]   T. Hayat, A. Qayyum, F. Alsaadi, M. Awais, and A.M. Dobaie, "Thermal radiation effects in squeezing flow of a jeffery fluid," The European Physical Journal Plus, **128**(8), 1-85 (2013). https://doi.org/10.1140/epjp/i2013-13085-1

[29]   M. Awais, T. Hayat, and A. Alsaedi, "Investigation of heat transfer in flow of burgers fluid during a melting process," Journal of the Egyptian Mathematical Society, **23**(2), 410-415 (2015). https://doi.org/10.1016/j.joems.2014.04.004

[20]   S. Muhammad, S.I.A. Shah, G. Ali, M. Ishaq, S.A. Hussain, and H. Ullah, "Squeezing nanofluid flow between two parallel plates under the influence of MHD and thermal radiation," Asian Research Journal of Mathematics, **10**(1), 1-20 (2018). https://doi.org/10.9734/ARJOM/2018/42092

[21]   C.T. Nguyen, G. Roy, C. Gauthier, and N. Galanis, "Heat transfer enhancement using al2o3–water nanofluid for an electronic liquid cooling system," Applied Thermal Engineering, **27**(8-9), 1501-1506 (2007). https://doi.org/10.1016/j.applthermaleng.2006.09.028

[22]   N. Hari, S. Sivasankaran, M. Bhuvaneswari, and Z. Siri, "Effects of chemical reaction on MHD mixed convection stagnation point flow toward a vertical plate in a porous medium with radiation and heat generation," Journal of Physics: Conference Series, **662**, 012-014 (2015). https://doi.org/10.1088/1742-6596/662/1/012014

[23]   M.M. Rashidi, N.V. Ganesh, A.K. Hakeem, and B. Ganga, "Buoyancy effect on MHD flow of nanofluid over a stretching sheet in the presence of thermal radiation," Journal of Molecular Liquids, **198**, 234-238 (2014). https://doi.org/10.1016/j.molliq.2014.06.037

[24]   C. Zhang, L. Zheng, X. Zhang, and G. Chen, "MHD flow and radiation heat transfer of nanofluids in porous media with variable surface heat flux and chemical reaction," Applied Mathematical Modelling, **39**, 165-181 (2015). https://doi.org/10.1016/j.apm.2014.05.023

[25]   M. Jawad, M.K. Hameed, A. Majeed, and K.S. Nisar, "Arrhenius energy and heat transport activates effect on gyrotactic microorganism flowing in maxwell bio-nanofluid with nield boundary conditions," Case Studies in Thermal Engineering, **41**, 102574 (2023). https://doi.org/10.1016/j.csite.2022.102574

[26]   M. Jawad, M.K. Hameed, K.S. Nisar, and A.H. Majeed, "Darcy-Forchheimer flow of maxwell nanofluid flow over a porous stretching sheet with Arrhenius activation energy and nield boundary conditions," Case Studies in Thermal Engineering, **44**, 102830 (2023). https://doi.org/10.1016/j.csite.2023.102830

[27]   M. Jawad, "Insinuation of Arrhenius Energy and Solar Radiation on Electrical Conducting Williamson Nano Fluids Flow with Swimming Microorganism: Completion of Buongiorno's Model," East European Journal of Physics, (1), 135-145 (2023). https://periodicals.karazin.ua/eejp/article/view/20900/19827

[28]   M. Jawad, "A Computational Study on Magnetohydrodynamics Stagnation Point Flow of Micropolar Fluids with Buoyancy and Thermal Radiation due to a Vertical Stretching Surface," Journal of Nanofluids, **12**, 759-766 (2023). https://doi.org/10.1166/jon.2023.1958

[29]   A. Majeed, A. Zeeshan, M. Jawad, and M.S. Alhodaly, "Influence of melting heat transfer and chemical reaction on the flow of non-Newtonian nanofluid with Brownian motion: Advancement in mechanical engineering," Proceedings of the Institution of Mechanical Engineers, Part E: Journal of Process Mechanical Engineering, 09544089221145527 (2022). https://doi.org/10.1177/09544089221145527

[30]   M. Jawad, F. Mebarek-Oudina, H. Vaidya, and P. Prashar, "Influence of Bioconvection and Thermal Radiation on MHD Williamson Nano Casson Fluid Flow with the Swimming of Gyrotactic Microorganisms Due to Porous Stretching Sheet," Journal of Nanofluids, **11**(4), 500-509 (2022). https://doi.org/10.1166/jon.2022.1863

[31]   A. Majeed, A. Zeeshan, and M. Jawad, "Double stratification impact on radiative MHD flow of nanofluid toward a stretchable cylinder under thermophoresis and Brownian motion with multiple slip," International Journal of Modern Physics B, 2350232, (2023). https://doi.org/10.1142/S0217979223502326

[32]   M. Jawad, K. Shehzad, R. Safdar, and S. Hussain, "Novel computational study on MHD flow of nanofluid flow with gyrotactic microorganism due to porous stretching sheet," Punjab University Journal of Mathematics, **52**(12), 43-60 (2020)". http://pu.edu.pk/images/journal/maths/PDF/Paper_5_52_12_2020.pdf

[33]   M. Jawad, M. Muti-Ur-Rehman, and K.S. Nisar, "Bioconvection Effects on Non-Newtonian Chemically Reacting Williamson Nanofluid Flow Due to Stretched Sheet with Heat and Mass Transfer," East European Journal of Physics, (2), 359-369 (2023). https://periodicals.karazin.ua/eejp/article/view/21555/20220

ДОСЛІДЖЕННЯ ТЕПЛОВИПРОМІНЮВАЛЬНОГО ДОТИЧНОГО ГІПЕРБОЛІЧНОГО ПОТОКУ НАНОРІДИНИ В УМОВАХ РОЗТЯГНЕННЯ ПОВЕРХНІ

Мухаммад Джавад[a], Мубін Алам[b], Коттаккаран Суппі Нісар[c]

[a]Факультет математики, Вищий університет Лахора, Файсалабадський субкампус, Файсалабад 38000, Пакистан
[b]Департамент математики, Фейсалабадський університет, Файсалабад 38000, Пакистан
[c]Факультет математики, Коледж природничих і гуманітарних наук в Алхарджі, Університет принца Саттама бін Абдулазіза, Алхардж 11942, Саудівська Аравія

Поточне дослідження висвітлює потік дотичного гіперболічного нанофлюїду повз двонаправлену поверхню, що розтягується. Обговорювалися явища тепло- та масопереносу з джоулевим нагріванням, хімічними реакціями та тепловим випромінюванням. Для постановки задачі частиною цього дослідження були конвективні граничні умови та наявність джерела тепла. Змодельовані диференціальні рівняння в часткових похідних перетворюються на звичайні диференціальні рівняння за допомогою відповідних самоподібних перетворень. Крім того, отримана система ODE чисельно обробляється за допомогою добре налагодженого метода стрільби, а отримані числові результати порівнюються з командою ND Solve у Mathematica. Вплив основних параметрів на швидкість, температуру та розподіл об'ємної концентрації перевіряється за допомогою графіків. Детально розглянуто вплив нових параметрів, залучених до цього дослідження, на особливості потоку та відведення тепла. Зі збільшенням значень степеневого індексу n, числа Прандтля Pr і магнітного параметра M спостерігається збільшення коефіцієнта шкірного тертя при зниженні числа Нуссельта.

Ключові слова: *метод стрільби; дотична гіперболічна нанорідина; МГД; Джоулеве нагрівання; хімічна реакція*

SLOW ELECTROMAGNETIC SURFACE TM-WAVES IN PLANAR WAVEGUIDE STRUCTURE WITH MU-NEGATIVE METAMATERIAL SLAB[†]

Oleksandr E. Sporov[a], Volodymyr P. Olefir[a],
Mykola O. Azarenkov[a,b], Viktor K. Galaydych[a]*

[a]*V.N. Karazin Kharkiv National University, Kharkiv 61022, Ukraine*
[b]*National Science Center "Kharkiv Institute of Physics and Technology", Kharkiv 61108, Ukraine*
Correspondence Author e-mail: galaydych@karazin.ua

In this work, we study the properties of slow electromagnetic surface TM-waves propagating along the planar waveguide structure involving the mu-negative metamaterial slab. The planar mu-negative metamaterial layer separates two semi-infinite regions: the plasma and the conventional dielectric. All media are assumed to be linear, homogeneous, and isotropic. The dispersion properties, the phase and group velocities, the spatial distribution of the electromagnetic fields of the TM mode in frequency range where the metamaterial has a negative permeability are under the consideration. The properties of this TM-eigenwave of the structure and two other TE modes are compared. It is studied the TM-eigenwave properties variation with metamaterial and plasma-like media properties changing. It is shown that for the considered structure, the properties of the TM mode depend significantly on the parameters of the plasma-like medium.

Keywords: *mu-negative metamaterial; plasma-like media; electromagnetic surface wave; wave dispersion properties; phase and group velocities; spatial wave structure*
PACS: 52.35g. 52.50.Dg

1. INTRODUCTION

In recent years, there has been an intensive study of the properties of metamaterials. These composite materials make it possible to create incredible combinations of electrodynamics parameters that are not found in nature [1-4]. Most often it was about the so-called "left-handed material" because in the unbounded medium, the vectors of the electric field, magnetic field, and wave vector of a plane waves form the left triple. This is valid for the double negative metamaterials, in which the both permittivity and permeability are negative. The properties of surface electromagnetic waves in the metamaterials were studied [5-13]. Mainly it was studied such double negative metamaterials.

It is an obvious fact that creation of material with only negative permeability is easier that for the double negative ones [14]. In a number of works [15-17] the properties of surface electromagnetic waves in such mu-negative metamaterials have been studied. The application areas of the considered modes are very wide from the signal transmission and processing, the sensing and detection, the particles accelerators, the photovoltaic and many others [18-20].

In the present work, it has been studied slow electromagnetic waves that propagate in planar waveguide structures involving both mu-negative metamaterial and plasma.

2. TASK SETTING

Let's study the properties of the electromagnetic eigenwaves that propagate in the waveguide structure that consists of semi-infinite region of plasma-like media ($x \leq 0$), the region of mu-negative metamaterial slab with thickness d ($0 \leq x \leq d$) and the semi-infinite region of conventional dielectric ($x \geq d$) (Fig. 1).
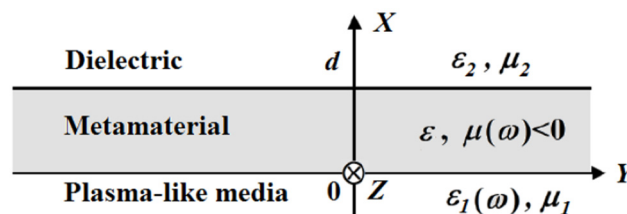
Figure 1. The studied waveguide structure

All media that construct the studied waveguide structure are considered to be homogeneous and isotropic. The plasma-like media is characterized by the wave frequency dependent permittivity $\varepsilon_1(\omega) = 1 - \omega_p^2/\omega^2$, where ω_p is effective plasma frequency, ω is the wave frequency and by the constant permeability $\mu_1 = 1$. The mu-negative

metamaterial is characterized by the constant permittivity ε and the permeability that depends on the wave frequency and commonly expressed with the help of experimentally obtained expressions:

$$\mu(\omega) = 1 - \frac{F\omega^2}{\omega^2 - \omega_0^2}, \tag{1}$$

here ω_0 is the characteristic frequency of metamaterial, $\omega_0 / 2\pi = 4$ *GHz* and $F = 0{,}56$ [14]. It was studied further the frequency region where $\mu(\omega) < 0$.

On other side of the mu-negative metamaterial slab the semi-infinite region of conventional dielectric with the constant permittivity ε_2 and permeability $\mu_2 = 1$ is located.

To study the propagation of the electromagnetic wave along the described structure it was assumed that the dependence of the wave components on time t and coordinate and z is expressed the following form:

$$E, H \propto E(x), H(x) \exp[i(k_3 z - \omega t)], \tag{2}$$

here x is coordinate perpendicular to the wave propagation direction and to the metamaterial slab. It was also assumed that wave disturbance tends to zero far away from the metamaterial slab: $\lim_{x \to \pm\infty} E(x), H(x) \to 0$.

For such case the system of Maxwell equations can be divided into two subsystems: one for the waves of H - type (*TE*-wave) and another – the waves of E - type (*TM*-wave). Taking into the account the boundary conditions (the continuity of the tangential electric and magnetic wave field components at the plasma-like medium - metamaterial interface and at the metamaterial – conventional dielectric interface) one can obtain the dispersion equation for the E - type wave in the following form:

$$\frac{h_1 h_2 \varepsilon_0^2 + \kappa^2 \varepsilon_1 \varepsilon_2}{\kappa \varepsilon_0 (h_2 \varepsilon_1 + h_1 \varepsilon_2)} \tanh(d\kappa) + 1 = 0, \tag{3}$$

here $h_1 = \sqrt{k_3^2 - \varepsilon_1 k^2}$, $h_2 = \sqrt{k_3^2 - \varepsilon_2 k^2}$, $\kappa = \sqrt{k_3^2 - \varepsilon_0 \mu(\omega) k^2}$, $k = \omega / c$, were c is the speed of light in vacuum.

The wave field components of the E -wave is naturally normalized on the $H_y(0)$ wave component. In the plasma-like region ($x \le 0$) these E -wave field components are expressed:

$$E_x^P(x) = \frac{e^{h_1 x} k_3}{\varepsilon_1 k}, \quad H_y^P(x) = e^{h_1 x}, \quad E_z^P(x) = i \frac{e^{h_1 x} h_1}{\varepsilon_1 k} \tag{4}$$

The normalized E -wave field components in the region of metamaterial slab ($0 \le x \le d$) can be written as:

$$E_x^M(x) = \frac{k_3}{k\varepsilon_0}\left(C_{1E} e^{\kappa x} + C_{2E} e^{-\kappa x}\right), \quad H_y^M(x) = C_{1E} e^{\kappa x} + C_{2E} e^{-\kappa x}, \quad E_z^M(x) = \frac{i\kappa}{k\varepsilon_0}\left(C_{1E} e^{\kappa x} - C_{2E} e^{-\kappa x}\right) \tag{5}$$

here C_{1E} and C_{2E} – are E -wave field constants.

In the dielectric region ($x \ge d$) the normalized wave field components have the form:

$$E_x^D(x) = \frac{k_3}{k\varepsilon_2} B_E e^{-h_2 x}, \quad H_y^D(x) = B_E e^{-h_2 x}, \quad E_z^D(x) = -\frac{ih_2}{k\varepsilon_2} B_E e^{-h_2 x}, \tag{6}$$

here B_E is E - wave field constant. The constants C_{1E}, C_{2E}, B_E are also find from the boundary conditions and have the following form:

$$C_{1E} = \frac{h_1 \varepsilon_0 (h_2 \varepsilon_0 - \varepsilon_2 \kappa)}{\kappa \Psi_E}, \quad C_{2E} = -\frac{h_1 \varepsilon_0 (h_2 \varepsilon_0 + \varepsilon_2 \kappa)}{\kappa \Psi_E} e^{2\kappa d}, \quad B_E = -\frac{2 h_1 \varepsilon_2 \varepsilon_0}{\Psi_E} e^{(h_2 + \kappa) d} \tag{7}$$

here $\Psi_E = \varepsilon_1 \left((1 + e^{2\kappa d}) h_2 \varepsilon_0 + (-1 + e^{2\kappa d}) \varepsilon_2 \kappa\right)$.

According to the similarly approach the dispersion equation for the wave of H - type can be obtained in the following form:

$$\frac{h_1 h_2 \mu^2(\omega) + \kappa^2}{(h_1 + h_2) \kappa \mu(\omega)} \tanh(d\kappa) + 1 = 0. \tag{8}$$

The wave field components of the H -wave is naturally normalized on the $E_y(0)$ wave component. In the plasma region ($x \le 0$) the H -wave field normalized components have the following form:

$$H_x^P(x) = -\frac{k_3}{k}e^{h_1 x}, \quad E_y^P(x) = e^{h_1 x}, \quad H_z^P(x) = -\frac{ih_1}{k}e^{h_1 x} \tag{9}$$

The normalized components of the H-wave in the region of metamaterial slab ($0 \le x \le d$) can be written as:

$$H_x^M(x) = \frac{k_3}{k\,\mu(\omega)}\left(C_{1H}e^{\kappa x} + C_{2H}e^{-\kappa x}\right), \quad E_y^M(x) = C_{1H}e^{\kappa x} + C_{2H}e^{-\kappa x}, \quad H_x^M(x) = -\frac{i\,\kappa}{k\,\mu(\omega)}\left(C_{1H}e^{\kappa x} - C_{2H}e^{-\kappa x}\right) \tag{10}$$

here C_{1H} and C_{2H} – are H-wave field constants.

In the dielectric region ($x \ge d$) the wave field components, normalized on the $E_y(0)$, can be written as:

$$\begin{cases} E_y(x) = B_H\,e^{-h_2 x}, \\ H_x(x) = k_3\,B_H\,e^{-h_2 x}\,/\,k, \\ H_z(x) = i\,B_H\,h_2 e^{-h_2 x}\,/\,k, \end{cases} \tag{11}$$

here B_H is H-wave field constant. The constants C_{1H}, C_{2H} and B_H can be also find from the boundary conditions and have the following form:

$$C_{1H} = \frac{h_1\,\mu(\omega)\left(h_2\,\mu(\omega) - \kappa\right)}{\kappa\,\Psi_H}, \quad C_{2H} = -\frac{h_1\,\mu(\omega)\left(h_2\,\mu(\omega) + \kappa\right)}{\kappa\,\Psi_H}e^{2\kappa d}, \quad B_H = -\frac{2\,h_1\,\mu(\omega)\,\varepsilon_0}{\Psi_H}e^{(h_2+\kappa)d} \tag{12}$$

here $\Psi_H = \kappa\left[(-1 + e^{2\kappa d})\kappa + (1 + e^{2\kappa d})h_2\,\mu(\omega)\right]$.

3. MAIN RESULTS

To study the eigenwaves of the considered structure, let us use the following normalized variables and structure parameters: the normalized frequency $\Omega = \omega/\omega_0$ and the normalized wave number $\beta = k_3 c/\omega_0$, normalized metamaterial slab thickness $\tilde{d} = \omega_0 d/c$ and normalized plasma frequency of the plasma-like media $\Omega_p = \omega_p/\omega_0$. Further study is carried out for the waveguide structure with the fixed normalized metamaterial slab thickness $\tilde{d} = 2.2$ and the permittivity $\varepsilon = 1$. The dispersion properties of the E- and H- eigenwaves of the structure with conventional dielectric permittivity $\varepsilon_2 = 1$ and for two values of the plasma frequency $\Omega_p = 1.5$ and $\Omega_p = 2.0$ are shown in the Fig. 2, 3, respectively. The dashed lines on these both figures correspond to the condition $h_2(k_3, \omega) = 0$ and the region of the study corresponds to the region of the slow surface waves.
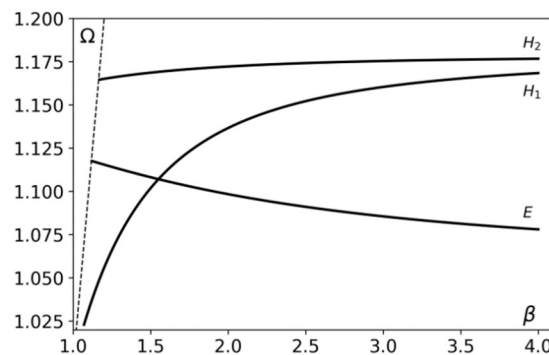
Figure 2. The dependence of the normalized frequency Ω on the normalized wave number β for normalized metamaterial slab thickness $\tilde{d}$, $\varepsilon_2 = 1$ and normalized plasma frequency $\Omega_p = 1.5$

In the studied waveguide structure only one E-wave and two H-waves can exist. In out further consideration the wave of H-type with lower frequency will be noted as H_1-wave, and the wave of such polarization with larger frequency will be noted as H_2-wave. The analysis of the dispersion properties of the eigenwaves of the considered structure shows that the variation of the normalized plasma frequency Ω_p has the greatest influence on the wave of E-type (see Fig. 2, 3). When Ω_p frequency value increases from 1.5 up to 2.0, the eigenfrequency of the E-wave also significantly increases with the changing of wave character – from backward wave for $\Omega_p = 1.5$ to forward wave for $\Omega_p = 2.0$.
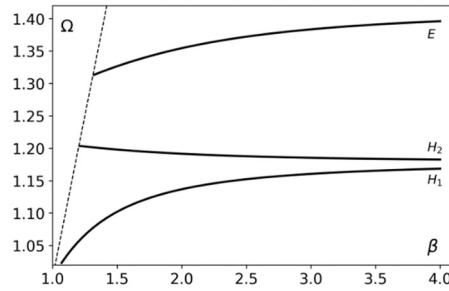
Figure 3. The dependence of the normalized frequency Ω on the normalized wave number β for normalized metamaterial slab thickness $\tilde{d} = 2.2$, $\varepsilon_2 = 1$ and normalized plasma frequency $\Omega_p = 2.0$

By changing the normalized plasma frequency Ω_p, it is also possible to influence the H_2 - wave characteristics, especially in the region of the smallest possible values of the normalized wave number β. With this mentioned increase of the Ω_p value, the H_2 - frequency in the region of small possible values of the normalized wave number increases more than with larger values $\beta = 4$. As a result of such Ω_p growth, not only the H_2 - wave frequency increases, but also changes the wave dispersion type, which becomes the reversed from the straight one. The indicated increase of the plasma frequency Ω_p practically does not change the dispersion of the H_1 - wave. Such influence of the plasma-like medium on the properties of the considered eigenwaves can be explained by analyzing the spatial distribution of the electromagnetic field components of the eigenwaves of the studied structure.

The Fig. 4a, 4b, 4c present the structure of wave field components for all three eigenwaves of the structure with parameters that are equal to parameters of the Fig. 3 and for the axial wave number $k_3 = 4.0$. The normalized frequency Ω of the E - eigenwave is approximately equal to 1.39597 (Fig. 4a). The frequency of H_2 - eigenwave is approximately equal to 1.18341 (Fig. 4b) and approximately equal to 1.1676 for the H_1 - wave (Fig. 4c).
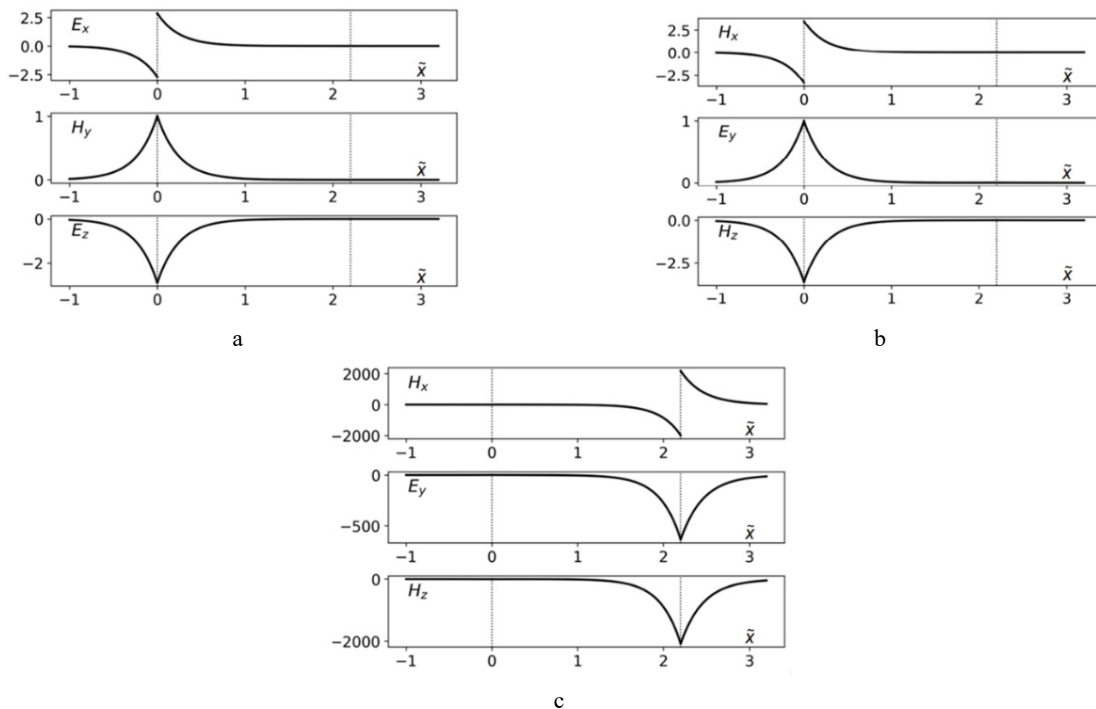
Figure 4. Spatial distribution of wave field components

a - the E - wave, normalized by the $H_y(0)$, $\tilde{x} = \omega_0 x / c$ - normalized x coordinate; b - the H_2 -wave, normalized by the $E_y(0)$; c - the H_1 -wave, normalized by the $E_y(0)$. The structure parameters corresponding to Fig. 3

Both the E - and H_2 - einegwaves of the structure are localized at the metamaterial - plasma-like medium interface. Thus, the significant influence of the plasma frequency value on these waves is quite understandable. As for the field of H_1 - wave, it is localized at the interface of the metamaterial - conventional dielectric interface $x = d$ and is practically equals to zero at the metamaterial's left boundary $x = 0$ (recall that the study is done for the normalized width of the

metamaterial $\tilde{d} = 2.2$). This is the physical reason for the fact that properties of the plasma-like medium practically do not influence on the H_1- wave properties. The spatial structure of the E - wave field that is presented in the Fig. 3a, explains the fact that its properties practically does not depend on the dielectric constant ε_2 of the conventional dielectric which restricts the metamaterial at $x = d$.

Let us note that the obtained strong influence of the plasma frequency on the E - wave properties requires a detailed analysis of the dependence of the frequency range of the E - wave existence, upon the parameters of the structure, are especially upon the normalized plasma frequency. This study can be done with the help of Fig. 5 which shows the dispersion of E - wave for different values Ω_p in the structure with $\tilde{d} = 2.2$, $\varepsilon_2 = 1$.
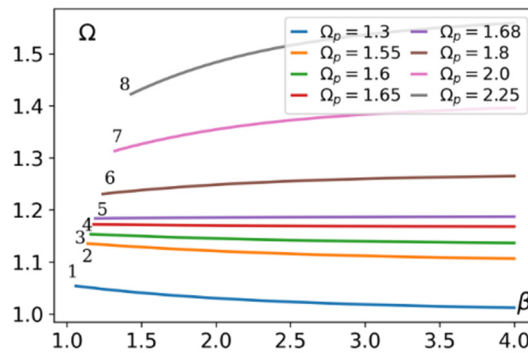
Figure 5. The dependence of the normalized frequency on the normalized wave number for normalized metamaterial slab thickness $\tilde{d} = 2.2$, $\varepsilon_2 = 1$ under different values of the normalized plasma frequency Ω_p

For the considered waveguide structure, the increase of the parameter Ω_p value in the range $1 < \Omega_p \leq 2.255$ leads to the oncoming of the dispersion curve to some curve. Next, let us determine how the region of wave existence in frequency and wavenumber spaces changes its size due to an increase in the normalized plasma frequency of the plasma-like medium Ω_p . The carried-out study has shown that in the case when $\Omega_p = 1.3$ the interval of normalized eigenwave frequencies is {1.01195, 1.026}. The corresponding normalized wave numbers β relates to the interval {2.28, 4.0}.

With a further increase of Ω_p value up to 2.0, one can observe the shift of the wave frequency range to more high frequency region {1.36531, 1.39598}, but at the same time corresponding region of wave numbers does not change. With further plasma frequency Ω_p growth up to the 2.2 values, the shift of the wave frequency range towards the higher frequencies' interval {1.47631, 1.50728}. It is important that at the same time the range of allowed normalized wavenumber values of the E - wave significantly reduces to the interval {2.28, 3.04}. This means that with an unchanged lower limit of the possible β values, the upper limit of the range of β values becomes significantly smaller. When Ω_p value increases and becomes approximately equal to 2.255 the width of both wave frequency range {1.50624, 1.50749} and wavenumber range {2.28, 2.3}.

Thus, with the increase of the normalized plasma frequency Ω_p the frequency of the E - eigenwave increases. At the same time, in the considered waveguide structures with $\varepsilon_2 = 1$ the frequency of the E - wave in the case when $\Omega_p < 1,6$ is less than the frequency of the H_1 - wave. In the case when $\Omega_p > 1,68$ the frequency of the E - wave is greater than the frequency of the H_2 - wave.

The carried out study have shown it is possible to find such normalized plasma frequency Ω_p value at which the frequency of the E - wave can coincide with the frequency of the H_1 - wave or with the frequency of the H_2 - wave that have the different polarization than the E - wave. At the same time it is necessary to note that frequencies of H_1 - and H_2 - waves with the same polarization belong to different frequency ranges.

So, it is necessary to mention that it is possible the situation when electromagnetic waves of different polarization can simultaneously propagate in the considered three-component waveguide structure composed of linear media. In particular, a situation is possible when the E - wave and H_2 - wave which localized at the boundary between the metamaterial and the plasma-like medium can simultaneously propagate in the structure (Fig. 6). Vertical dashed lines show the bounds of the frequency intervals in which the eigenwaves of the considered planar waveguide structure can propagate.

It should be noted that the overlap of the frequency ranges where H_1 and H_2 - type waves exist means that H_1 - and H_2 - wave with the same frequency but different wavelengths and significantly different spatial field structure can simultaneously propagate in the considered structure.

There is also possible the situation when a E - wave that propagates at the metamaterial - plasma-like medium interface can simultaneously propagate with H_1 - wave that propagates at the metamaterial - conventional dielectric interface.
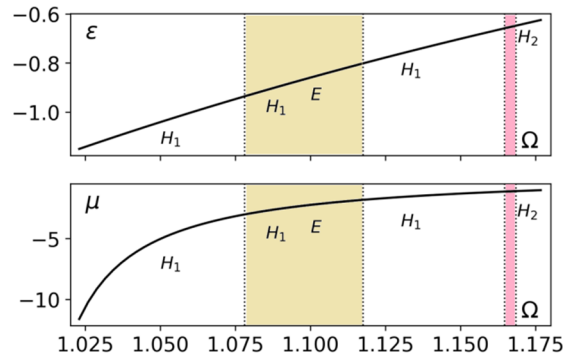
Figure 6. The dependence of the dielectric permittivity of the plasma-like medium $\varepsilon_1(\Omega)$ and the magnetic permeability $\mu(\Omega)$ of the metamaterial on normalized frequency Ω for the structure parameters $\tilde{d} = 2.2$, $\varepsilon_2 = 1$, $\Omega_p = 1.5$

So, let us note the important feature of this structure: due to changing the plasma frequency of plasma-like medium it is possible to provide a single-mode regime and it is possible to provide corresponding polarization of the eigenwaves that can propagate in the considered planar waveguide structure. From the point of view of the further possibility of application both similar waveguide structures and eigen-waves propagating in them, in addition to polarization, dispersion, spatial distribution of wave field components, it is important to analyze the influence of the normalized plasma frequency Ω_p on the phase and group velocity of the E - wave.

The Fig. 7 presents the dependence of the normalized phase velocity $\tilde{V}_{ph} = \omega/(k_3 c)$ and the normalized group velocity $\tilde{V}_{gr} = (d\omega/dk_3)/c$ of the E - wave for different values of the normalized plasma frequency from the normalized wave frequency Ω. It is necessary to note the convenience of Fig. 7, the upper part of which shows the dependency $\tilde{V}_{gr}(\Omega)\big|_{\Omega_p}$ with the horizontal line $\tilde{V}_{gr}(\Omega) = 0$, that separates the regions with different types of E - wave dispersion. It is presented how the increase of Ω_p value leads to the change of the dispersion type. For the chosen parameters set the value $\Omega_p = 1.68$ is the value of group velocity sign changing. With the Ω_p value increase from 1 up to limiting value 1.68, the normalized group velocity, remaining negative, goes to zero. At the same time, the wave frequency range essentially decreases. When Ω_p value is greater than $\Omega_p > 1.68$ the signs of the group and phase velocities coincide. The further increase of the plasma frequency Ω_p value up to 2.255 leads to the increase the E - wave group velocity.
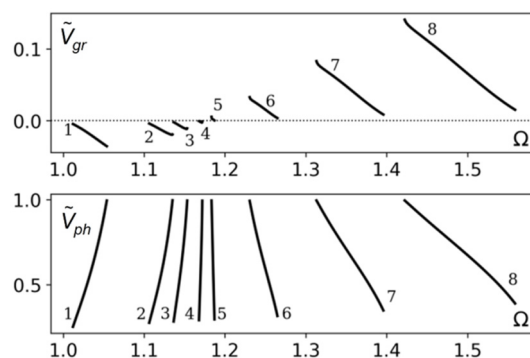
Figure 7. The dependence of the normalized phase velocity $\tilde{V}_{ph} = V_{ph}/c$ and the normalized group velocity $\tilde{V}_{gr} = V_{gr}/c$ of the E - wave on the normalized frequency for the structure parameters $\tilde{d} = 2.2$, $\varepsilon_2 = 1$ under different values of the normalized plasma frequency Ω_p

At the same time the phase velocity of the E - wave for plasma frequency range $\Omega_p < 1.68$ increases from the minimum value at the lower limit of the frequency range up to the speed of light in a vacuum at the upper limit of the frequency range. In the region when $\Omega_p > 1.68$, the phase velocity of the E - wave decreases from a maximum value (close to the speed of light in a vacuum) at the lower limit of the frequency range to some minimum velocity value at the frequency range upper limit, which increases with the growth of Ω_p value.

The calculations have shown that for the considered waveguide structure the influence of the dielectric constant ε_2 of a conventional dielectric on the E - wave properties are practically absent.

CONCLUSIONS

The study has shown the possibility of one E - eigenwave and two H - eigenwaves propagation in a planar structure that is constructed with the metamaterial slab bounded on one side by a semi-infinite plasma-like medium, and on the other side by a conventional dielectric.

For the considered waveguide structure, it is determined the normalized plasma frequency Ω_p region in which the E - wave can propagates.

It is shown that the increase of Ω_p value leads to the significant increase of the E - eigenwave frequency. It is also defined range of Ω_p parameter values, where the wave dispersion changes its type.

It was found out that the E - eigenwave is localized at the metamaterial - plasma-like medium interface, where the H_2 - wave is also localized.

It is also shown the possibility of plasma frequency of the plasma-like medium Ω_p usage to ensure a single-mode regime and to select the polarization of the eigenwave in the considered planar waveguide structure.

It was also was determined the influence of Ω_p value as on the phase $\tilde{V}_{ph}(\Omega)$ and group $\tilde{V}_{ph}(\Omega)$ velocities of the E - eigenwaves, as on the regions of its wave numbers and frequencies, where the metamaterial possesses negative magnetic permeability.

The results obtained and presented in the article can be useful for modeling and creating modern devices based on metamaterials.

ORCID
Oleksandr Sporov, https://orcid.org/0000-0002-4610-9656; **Volodymyr Olefir**, https://orcid.org/0000-0002-8022-2556
Mykola Azarenkov, https://orcid.org/0000-0002-4019-4933; **Viktor Galaydych**, https://orcid.org/0000-0002-2255-9716

REFERENCES
[1] I. Shadrivov, M. Lapine, and Y. Kivshar, *Nonlinear, tunable and active metamaterial*, (Springer, 2015), 324 p.
[2] L. Solymar, and E. Shamonina, *Waves in Metamaterials*, (Oxford University Press, Oxford, 2009).
[3] M.I. Stockman, K. Kneipp, S.I. Bozhevolnyi, S. Saha, A. Dutta, J. Ndukaife, N. Kinsey, *et al*., Journal of Optics, **20**(4), 043001 (2018). https://doi.org/10.1088/2040-8986/aaa114
[4] F. Capolino, editor, *Theory and Phenomena of Metamaterials*, (CRC Press, Boca Raton, 2009). https://doi.org/10.1201/9781420054262
[5] R. Ruppin, "Surface polaritons of a left-handed medium", Phys. Lett. A, **277**(1), 61–64 (2000). https://doi.org/10.1016/S0375-9601(00)00694-0
[6] I.V. Shadrivov, A. Sukhorukov, and Y. Kivshar, "Guided modes in negative-refractive-index waveguides", Phys. Rev. E, **67**(5), 057602 (2003). https://doi.org/10.1103/PhysRevE.67.057602
[7] G. D'Aguanno, N. Mattiucci, M. Scalora, and M.J. Bloemer, "TE and TM guided modes in an air waveguide with negative-index material cladding", Physical Review E, **71**(4), 046603 (2005). https://doi.org/10.1103/PhysRevE.71.046603
[8] Y. He, Z. Cao, and Q. Shen, "Guided optical modes in asymmetric left-handed waveguides", Optics Communications, **245**(1-6), 125-135 (2005). https://doi.org/10.1016/j.optcom.2004.09.067
[9] B. Wu, T. Grzegorczyk, Y. Zhang, and J. Kong, "Guided modes with imaginary transverse wave number in a slab waveguide with negative permittivity and permeability", J. Appl. Phys. **93**(11), 9386-9388 (2003). https://doi.org/10.1063/1.1570501
[10] C. Hermann, A. Klaedtke, C. Jamois, and O. Hess, "Surface plasmon polaritons in generalized slab heterostructures with negative permittivity and permeability", Physical Review B, **73**(8), 085104 (2006). https://doi.org/10.1103/PhysRevB.73.085104
[11] V.K. Galaydych, N.A. Azarenkov, V.P. Olefir, and A.E. Sporov, "Surface electromagnetic waves on boundary between lossy dielectric and left-handed material with gain", Problems of Atomic Science and Technology, **1**, 96 (2017), https://vant.kipt.kharkov.ua/ARTICLE/VANT_2017_1/article_2017_1_96.pdf
[12] S.M. Vukovic, N.B. Aleksic, and D.V. Timotijevic, "Guided modes in left-handed waveguides", Optics Communications, **281**(6), 1500-1509 (2008). https://doi.org/10.1016/j.optcom.2007.11.010
[13] V.K. Galaydych, N.A. Azarenkov, V.P. Olefir, and A.E. Sporov, "Modelling of the electromagnetic surface waves propagation on the interface between the left-handed metamaterial and the dissipative dielectric", Problems of Atomic Science and Technology, **6**, 109 (2018). https://vant.kipt.kharkov.ua/ARTICLE/VANT_2018_6/article_2018_6_109.pdf
[14] J.B. Pendry, A.J. Holden, D.J. Robbins, and W.J. Stewart, "Magnetism from conductors and enhanced nonlinear phenomena", IEEE Trans. MTT, **47**(11), 2075-2084 (1999). https://doi.org/10.1109/22.798002
[15] V. Galaydych, and N. Azarenkov, "Slow surface electromagnetic waves on a mu-negative medium", Applied Physics B, **128**(7), 132 (2022). https://doi.org/10.1007/s00340-022-07854-3
[16] V. Galaydych, A. Sporov. V. Olefir, and N. Azarenkov, "Slow surface eigenmodes directed by the mu-negative metamaterial slab," East European Journal of Physics, 3, 77-83 (2022). https://doi.org/10.26565/2312-4334-2022-3-10
[17] V. Galaydych, and N. Azarenkov. "Surface polaritons in a vacuum gap inside mu-negative medium", Applied Physics A, **129**, 466 (2023). https://doi.org/10.1007/s00339-023-06751-6
[18] M. Stockman, "Applied optics. Nanoplasmonic sensing and detection", Science, **348**(6232), 287-288 (2015). https://doi.org/10.1126/science.aaa6805

[19] S. Antipov, W. Liu, W. Gai, J. Power, and L. Spentzouris, "Double-negative metamaterial research for accelerator applications", Nuclear Instruments and Methods in Physics Research A, **579**(3), 915-923 (2007). https://doi.org/10.1016/j.nima.2007.04.158

[20] S. Boriskina, G. Hadi, and C. Gang, "Plasmonic materials for energy: From physics to applications", Materials Today, **16**(10), 375-386 (2013). https://doi.org/10.1016/j.mattod.2013.09.003

ПОВІЛЬНІ ЕЛЕКТРОМАГНІТНІ ТМ-ХВИЛІ В ПЛАНАРНІЙ ХВИЛЕВОДНІЙ СТРУКТУРІ З ШАРОМ MU-НЕГАТИВНОГО МЕТАМАТЕРІАЛУ

Олександр Є. Споров[a], Володимир П. Олефір[a], Микола О. Азарєнков[a,b], Віктор К. Галайдич[a]

[a]Харківський національний університет імені В.Н. Каразіна, 61022, Харків, Україна
[b]Національний науковий центр «Харківський фізико-технічний інститут», 61108, Харків, Україна

В роботі досліджуються властивості повільних електромагнітних поверхневих ТМ-хвиль, що поширюються вздовж планарної хвилеводної структури, до складу якої входить мю-негативна пластина метаматеріалу, що розділяє дві напівнескінченні області: плазму та звичайний діелектрик. Усі середовища вважаються лінійними, однорідними та ізотропними. Розглядаються дисперсійні властивості, фазова та групова швидкості, просторовий розподіл електромагнітного поля ТМ-хвилі в інтервалі частот, де метаматеріал має негативну магнітну проникність. Проведено порівняльний аналіз властивостей власних хвиль структури: однієї ТМ моди та двох ТЕ мод. Досліджено вплив параметрів структури на характеристики її власних хвиль. Показано істотну залежність властивостей ТМ моди структури, що розглядається, від параметрів плазмоподібного середовища. Отримано, що збільшення значення плазмової частоти плазмоподібного середовища призводить до значного збільшення частоти власної ТМ-хвилі. Було визначено діапазон значень плазмової частоти, за яких ця хвиля змінює тип дисперсії. Визначено, що власна E-хвиля локалізована на межі розподілу між мета матеріалом та плазмоподібним середовищем, де також локалізована H_2-хвиля - одна з хвиль з TE поляризацією та частотою дещо більшою за частоту H_1-хвилі. Було показано можливість забезпечення одномодового режиму та вибору потрібної поляризації власної хвилі в розглянутій планарній хвилеводній структурі за рахунок вибору значення плазмової частоти плазмоподібного середовища. Було вивчено також вплив цієї частоти на значення як фазових, так і групових швидкостей власних E-хвиль. Отримані результати можуть бути корисними для моделювання та створення сучасних пристроїв на основі метаматеріалів.

Ключові слова: *мю-негативний метаматеріал; плазмоподібні середовища; електромагнітна поверхнева хвиля; хвильові дисперсійні властивості; фазові та групові швидкості; просторова хвильова структура*